Exploring the Self-Aggregation of Short Peptides in Aqueous Environment for Various Applications

Thesis Submitted

By

Basab Kanti Das
Roll No. 166122035
Department of Chemistry
Indian Institute of Technology Guwahati
Guwahati, Assam-781039
India

A Thesis Submitted for the partial fulfilment
Of The requirements of the degree of

Doctor of Philosophy

In

Chemistry

IIT Guwahati, August, 2021

Dedicated

To

My Parents

Declaration

I hereby declare that all the matters embodied in the thesis result from the experiments and investigations performed by me in the Department of Chemistry, Indian Institute of Technology, Guwahati, India, under the supervision of Prof. Debapretim Das. In keeping with the general practice of reporting scientific observations, due acknowledgements have been made wherever the work described is based on the findings of the other investigators.

Basab Kanti Das.

(**Basab Kanti Das**)

भारतीय प्रौद्योगिकी संस्थान गुवाहाटी
INDIAN INSTITUTE OF TECHNOLOGY GUWAHATI

Dr. Debapratim Das
Professor
Department of Chemistry
Ph: + 91 361 258 3301
Fax: + 91 361 258 2349
E-mail: ddas@iitg.ac.in

To whom it may concern

This is to certify that the thesis entitled as '**Exploring the self-aggregation of short peptides in aqueous environment for various applications'** submitted by Mr. Basab Kanti Das (Roll No. 166122035) for award of PhD degree to IIT Guwahati, is absolutely based on his own research work and that neither this thesis nor any part of it has been submitted for any degree/diploma or academic award anywhere.

25-08-2021

(Debapratim Das)

Acknowledgements

The thesis is the last milestone of my PhD journey. Indeed, it is the most crucial academic documentation of my scientific activities. These endeavours only became prosperous by the immense support and encouragement from numerous people, including my lab mates, friends, families, and other well-wishers. By their inspirations and motivations, I have kept myself always on track. So, here at the beginning, I am privileged to have an excellent opportunity to express my gratitude to one and all who extended their helping hands several times to reach my destination.

Prior to all, I would like to express my heartfelt gratitude to my supervisor, Prof. Debapratim Das, for selecting me and sparing me a student position in his lab. No doubt to say that the journey never finds an end without his kind guidance, scholarly imputes, constant and unconditional support throughout my research period. Besides that, his brilliant ideas, scientific expertise, and positive vibes have gifted wings to my perplexed ideas to overcome many hurdles in the journey. It will be my great pleasure and dearest anticipation to follow his scientific footprints and convictions in future. Thank you so much, Sir, for staying beside me always whenever and wherever I required. Apart from being a successful academician and teacher, he is a generous person, an admirable speaker with having an excellent sense of humour which I would like to imbibe in my character.

I find myself very fortunate to have humble doctoral committee members: Prof. A.S. Achalkumar (Chairperson), Dr. Kalyan Raidongia and Dr. Sunanda Chatterjee. At different periods, they have encouraged me by their helpful scientific suggestions and insightful thoughts.

After supervisor, my seniors had many influences on my journey. At the day of joining, I was introduced to the three musketeers (Dr. Sahnawaz Ahmed, Dr. Nilotpal Singha and Dr. Bapan Pramanik) our lab. Unfortunately, I have got a very short period of time to work under Sahnawaz da, but Bapan da and Nilotpal da immensely helped me from instrument handling, data analysing, designing molecules to proper executions. I am also thankful to Dr. Shubhajit Ghosh and Dr. Tanur Sinha for caring support and encouragement during their presence. A big thanks also goes to my batchmate, Ms. Payel Dowari for her enormous cooperation in various experiments. Besides seniors, I must mention my juniors especially,

Mr. Saurav Das and Mr. Sumit Chowdhuri. They have assisted a lot during accomplishing my projects. I have got assistance also from other juniors, Mr. Priyam Das, Ms. Tanushree Das and Mr. Supriya Halder. All my labmates have given me an amazing and joyous environment to alleviate the various difficulties in research life. I must anticipate, all the golden lab-memories will strengthen myself to face dark times in future.

I would like to express my sincere thanks to ours collaborators, Prof. Oren Scherman and Prof. Anindita Ukil for their assistance for my different projects.

My special thanks also go to my friends Tanumay, Dipanjan, Asesh, Rabi and Kaushik da for their company and support in the department and hostel. I extend my sincere acknowledgements to all the members and technical staff of my department and C.I.F. for their direct or indirect help. I am immensely helpful to IIT Guwahati for providing the doctoral fellowship with consistency and the opportunity to be a part of India's one of the finest educational institute.

Last but not least, I have got ample motivation and assistance from my family members to focus on my research carrier entirely.

Abstract

The thesis "**Exploring the Self-Aggregation of Short Peptides in Aqueous Environment for Various Applications"** deals with the design and applications of new short aggregating peptide with the different non-covalent interactions.

Chapter 1 is a brief introduction of peptide based aggregations with up to date literature review.

Chapter 2 describes the combination of cation-π and charge-transfer interactions within a donor-acceptor pair to form self-healing hydrogel.

Chapter 3 depicts the light-induced syneresis by a water insoluble peptide-hydrogel and effective removal of small molecule waste contaminants.

Chapter 4 deals with charge transfer complexation aided control over the reaction pathway.

Chapter 5 illustrates protection and glutathione responsive delivery of proteins by an ultrashort peptide hydrogel.

List of Abbreviations

NDI	Naphthalene Diimide
NDA	Naphthalene Dianhydride
NMR	Nuclear Magnetic Resonance
NOESY	Nuclear Overhauser Effect Spectroscopy
ESI-MS	Electrospray Ionization Mass Spectroscopy
MALDI	Matrix-assisted Laser Desorption Ionization
TOF	Time of Fight
LC-MS	Liquid Chromatography-Mass Spectrometry
UV-Vis	Ultraviolet-Visible Spectroscopy
FL	Fluorescence Spectroscopy
LVR	Linear Viscosity Region
λ_{max}	Wavelength at which absorbance is maximum at absorption spectra.
MAC	Maximum Aggregation Concentration
MeOH	Methanol
EtOH	Ethanol
ACN	Acetonitrile
Calcd.	Calculated
H_2O	Water
DMSO	Dimethyl Sulfoxide
DMF	Dimethylformamide
DIPEA	Diisopropyl Ethylamine
DCM	Dichloromethane
TEA	Triethylamine
NaOH	Sodium Hydroxide
FESEM	Field Emission Scanning Electron Microscope
FETEM	Field Emission Transmission Electron Microscope
AFM	Atomic Force Microscope
FTIR	Fourier-transformation Infrared Spectroscopy
DLS	Dynamic Light Scattering
Tris	Tris(hydroxymethyl) aminomethane
PBS	Phosphate Buffer Saline
CD	Circular Dichroism
G′	Storage Modulus
G″	Loss Modulus
MGC	Minimum Gelation Concentration
T_g	Gel Melting Temperature
D_2O	Deuterium Oxide
d_6-DMSO	Deuterated Dimethyl Sulfoxide

$CDCl_3$	Deuterated Chloroform
mg	Milligram
mm	Millimetre
nm	Nanometer
μm	Micrometer
mL	Millilitres
μL	Microlitre
mM	Millimolar
μM	Micromolar
ppm	Parts per million
HRTEM	High Resolution Transmission Electron Microscope
DFT	Density Functional Theory
Phe	Phenylalanine
Trp	Tryptophan
Tyr	Tyrosine
Cys	Cysteine
Lys	Lysine
Gly	Glycine
Py	Pyrene
PXRD	Powder X-Ray Diffraction
TCEP	Tris(2-carboxyethyl)phosphine hydrochloride
GSH	Glutathione
DTT	Dithiothreitol
HPLC	High Performance Liquid Chromatography
HBTU	Hexafluorophosphate Benzotriazole Tetramethyl Uronium
HOBT	Hydroxybenzotriazole
HFIP	Hexafluoro-2-propanol
TFA	Trifluoroacetic acid
TES	Triethylsilane
BSA	Bovine Serum Albumin
RNase A	Ribonuclease A
CR Lipase	Lipase from *Candida rugosa*
FITC	Fluorescein isothiocyanate
RhB	Rhodamine B
MB	Methylene Blue
EBT	Eriochrome Black-T
MO	Methyl Orange
Neu R	Neutral Red
Wt%	Weight Percent (W/V)

Submitted Synopsis report

Chapter 1

Self-Assembly of Peptides

Peptides self-assemble into a varied collection of nanostructures.[1] The peptide assemblies and the soft-materials generated thereof are of high interest in material science and especially in Bio-materials owing to their biocompatibility, biodegradability and stimuli responsive property.[2] Supramolecular assemblies of amino acids, peptides and proteins is governed by different noncovalent interactions. Hydrogen bonding, π-π stacking, salt-bridge, etc., are the common noncovalent supramolecular forces responsible for forming different secondary structures in peptides and proteins. These secondary structures/small aggregates further assemble in a concentration dependent manner to generate higher order assemblies. The hierarchical assembly leads to soft-materials with interesting properties. However, rational design is the key to construct such materials.[2]

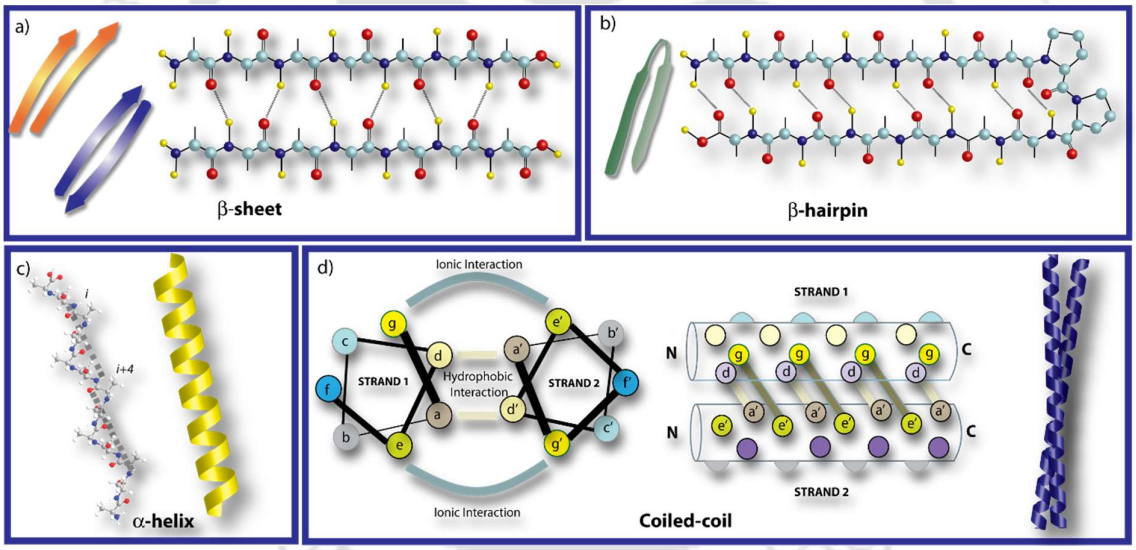

Figure 1.1 Illustrations of the molecular self-assembly involved in the formation of different secondary structures peptides: (a) β-sheet, (b) β-hairpin, (c) α-helix and (d) coiled-coil.

Unusual Supramolecular Interactions

Along with the above mentioned non-covalent interactions, some other weak interactions are found to exist in nature. These interactions are rarely reported in the context of peptide assemblies but we believe that incorporation of such interactions can lead to newer and unusual properties of the soft-materials.

Charge Transfer Interaction

Charge transfer (CT) interaction within organic molecules happens when an electron-deficient moiety and a p-electron cloud close proximity. Typically, the electron-rich π-ring partially donates its electron density to the electron-deficient group, thereby stabilizing the complex. Though it is commonly observed in the case of self-assemblies of other types of organic molecules, [3-5] in the case of peptides, one has to rationally introduce both electron-deficient and electron-rich groups to achieve CT interaction.[6-8]

Cation-π Interaction

Apart from the conventional non-covalent interactions, peptides and proteins also utilize other types of supramolecular interactions for their assembly and functions.[9, 10] Important to mention, the assembled structure of the proteins and the peptide chains could be stabilized influentially by the cation-π interaction between different amino acid residues. The π-electron rich moieties like Phenylalanine and Tryptophan reported binding with the same interactions with charged amine groups of the Lysine and arginine units. Phosphatidylethanolamine (PE), and phosphatidylcholine (PC), interact with interfacial Tryptophans via cation-p interactions.[11] However, these types of supramolecular interactions are not very common, and it is important to rationally design the peptide sequences to incorporate such interactions in the self-assembly process.

Peptide-Based Hydrogels

Gels are semisolid viscous materials having 3D hierarchical network structures capable of immobilizing a large amount of solvent. In recent years, the interest in small peptide-based supramolecular hydrogels has risen substantially. The aggregating short peptides easily form the secondary conformations of the peptides resulting in various nanostructures such as fibre, tube, belt, ribbon, tape.[12-16] It is noteworthy that various supramolecular interactions crucially assist in forming the superior hierarchical assembly from smaller peptide chains during the hydrogelation process. These interactions are vulnerable to certain conditions known as the stimulus or the triggering forces, and often the gels are termed 'smart gels'.

Unusual hydrogels

Response to some particular stimuli like, change in pH, temperature, a chemical, light etc. are important for the application of smart aggregates. However, along with interesting response to these stimuli, some unusual properties are also observed for different peptide based systems.[17-21] Syneresis is one such property where expulsion of the solvents from the gel is exhibited, followed by contraction of the volume of the gel with time.[22] In literature, very few examples of syneresis are reported to date for small molecular weight hydrogels. A substantial effort is required to understand this phenomenon and design peptide hydrogels with such property.

Applications of peptide hydrogels

Peptide based hydrogels have found several applications over the years. In the present thesis, the designed peptide hydrogels have been utilized for protein delivery and pollutant removal. Here is a brief about these two applications.

Delivery Vehicle

Delivery of different therapeutic agents including drugs, proteins, peptide, hormones etc. has marked an important position in the treatment of cancer and other deadly diseases.[23,24] Compared to regular cells, cancer cells provide several special functions (e.g., hypoxia, acidic pH, and improving permeability and retention effects) that can be completely exploited during the design of drug delivery vehicles.[25] Hydrogels, having diverse size and shape, from nanogel to microscopic gel, can exhibit different type of release mechanism in presence of various stimuli.[26] The successful delivery of drugs using peptide hydrogels can be accredited to the four subsequent reasons; facile targeting, biocompatibility and biodegradability, easy drug encapsulation, and sustained release of cargoes in physiological conditions.[27,28]

Pollutant Removal

Dyes are extensively used in many industries including textile, leather, cosmetics, paper, printing, plastic, pharmaceuticals, foods, and others to colour their products.[29] Due to the limited resources of the waste management most of the wasted toxic dyes mixed with the river water and slowly deteriorate the essential ecosystem of water organisms. So, the

separation of the toxic organic dyes is a very important issue for the coming days. In a classic example, Banerjee and his team have nicely exploited the self-shrinking peptide hydrogel of lapidated diphenylalanine to separate various organic dyes and toxic metal atoms from water.[30]

Aim of the Thesis

The aim of the present thesis is to understand the mechanism of self-assembly of some amino acid or peptide based small molecules to prepare new soft materials with some new properties. In this regard, four different peptide based self-assemblies have been constructed and utilized for different applications.

1. Combing of cation–π and CT interactions to create a self-healing hydrogel.

2. Designing a azobenzene functionalised peptide hydrogel for the light induce syneresis and removal of model organic dyes from water.

3. Utilisation of charge transfer pair toward synthesizing unsymmetric disulphides in a simple way from two different thiols.

4. Protection and intracellular delivery of the proteins by glutathione responsive ultrashort peptide hydrogel.

Chapter 2: Combing Cation-π and Charge-Transfer Interactions within a Donor-Acceptor Pair to Form Self-Healing Hydrogel

Herein, we present a rational design to incorporate a combination of CT and Cation-π interactions within a D–A pair. A pyrene – peptide conjugate (**PyFFK**, Scheme 2) exhibits a combination of cation–π and CT interactions with a cationic naphthalenediimide (**NDTA**) molecule in water (Scheme 2.1). Nuclear Overhauser effect spectroscopy NMR along with other techniques and density functional theory calculations reveal the involvement of these interactions. The π-planes of pyrene and NDI adopt an angle of 56° to satisfy both the interactions (Figure 2.1A), whereas β-sheet formation by the peptide sequence facilitates self-assembly. Notably, the binary system forms a self-supporting hydrogel (Scheme 2.1) at a higher concentration. The hydrogel shows efficient self-healing and injectable property (Figure 2.1B). Broadly, we demonstrate a pathway that should prove pertinent to various

areas, ranging from understanding biological assembly to peptide-based functional soft materials.

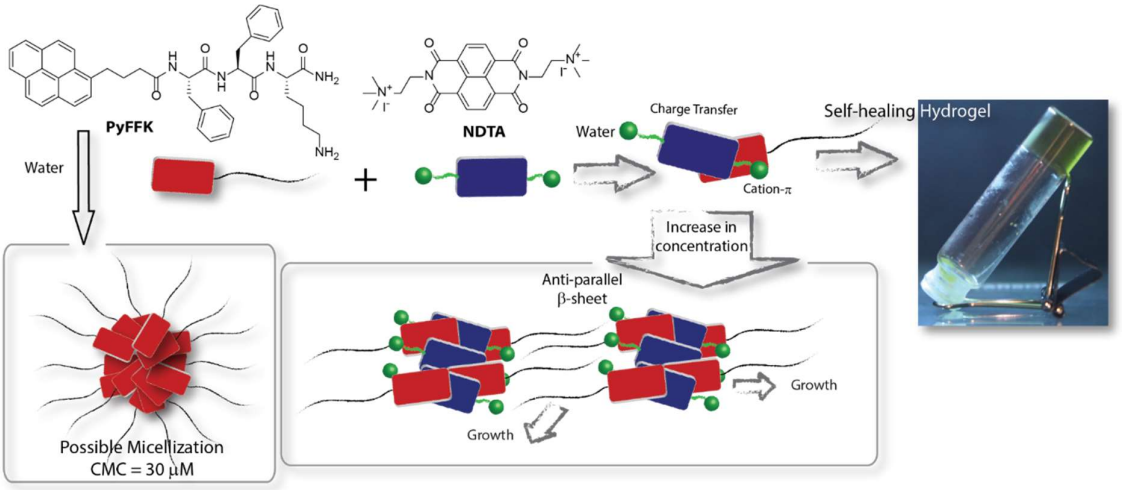

Scheme 2.1 Chemical structures of compounds under investigation in this study (**PyFFK** and **NDTA**) and schematic presentation of the involvement of cation–π and CT interactions between **PyFFK** and **NDTA**, and subsequent formation of a self-healing hydrogel at a higher concentration.

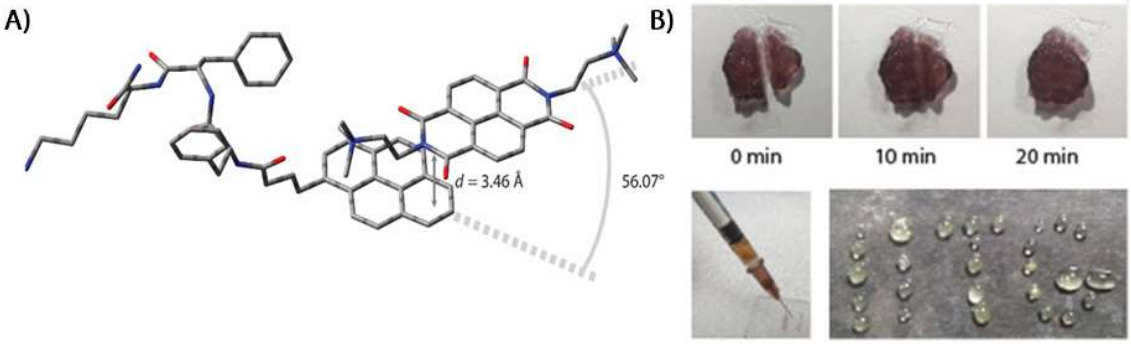

Figure 2.1 (A) Optimized structure of **PyFFK-NDTA** complex. (B) Macroscopic self-healing property of the hydrogel at 0-20 min and photographs of Injectibility where the syringe containing the hydrogel and drops of liquids which turned into hydrogel immediately after coming out of the needle.

Chapter 3: Light-Induced Syneresis by a Water Insoluble Peptide-Hydrogel and Effective removal of Small Molecule Waste Contaminants.

An azobenzene functionalised short peptide (**Azo-KC**, Scheme 3.1A) based hydrogel exhibits aqueous insolubility, thixotropy and efficient light induced syneresis. Upon irradiation with UV light, the hydrogel shrinks and expels ~50% of the solvent (Scheme 3.1B). Syneresis is caused by light-triggered *trans–cis* isomerisation of the azobenzene

moiety of the peptide (Scheme 3.1C). The hydrogel and it's syneresis mechanism is studied in detail. The expulsion of solvent was effectively exploited in the removal of low molecular weight contaminants in water (Figure 3.1).

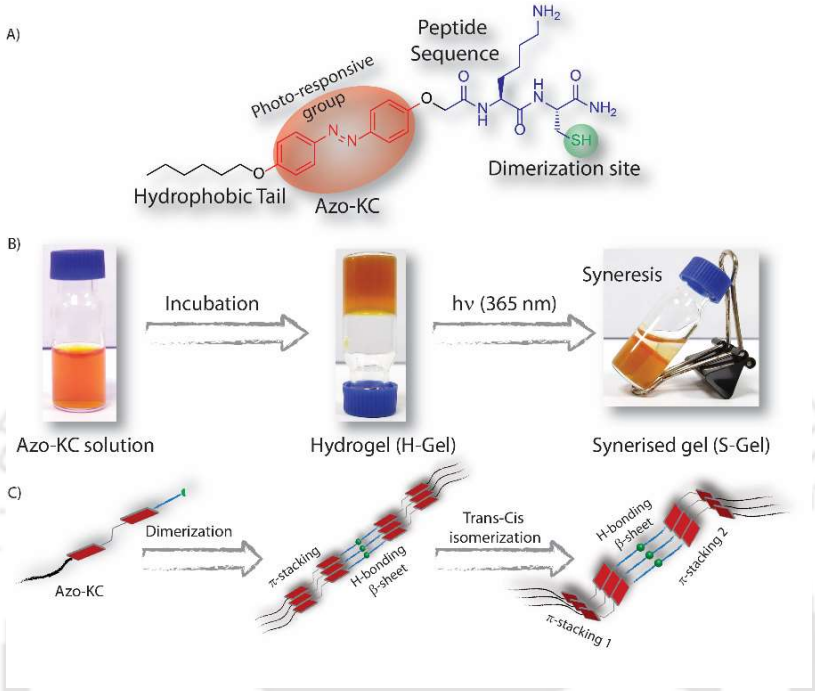

Scheme 3.1 (A) Chemical structure of **Azo-KC**. (B) Photographs of the **Azo-KC** solution, hydrogel formed by the solution (H-gel) and syneresis (S-gel) upon irradiation with UV light. (C) Possible molecular arrangements.

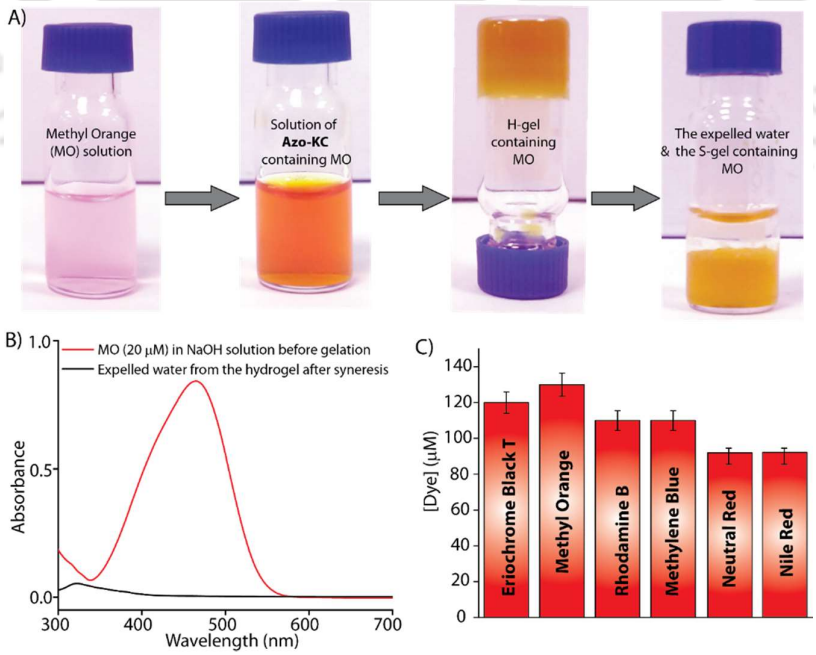

Figure 3.1 (A) Photographs showing MO removal from hydrogel upon UV light induced syneresis. (B) UV-Vis spectra of MO and the expelled water from (A). (C) Maximum initial dye concentrations for different dyes, which can be completely removed through syneresis of the hydrogel.

Chapter 4: Charge Transfer Complexation Aided Control over the Reaction Pathway

A conceptually new strategy to exploit CT complexes toward chemo-selective products by means of seizing the dynamic character of CT complexes is reported here (Scheme 4.1A). Aqueous CT complexes of donor (**PyKC**) and acceptor (**NDA-1**) molecules bearing reactive thiol groups were frozen instantly and cryo-desiccation to get the alternate D–A assembly in the solid state (Scheme 4.1A and B). Oxidation of reactive thiols in an oxygen rich solvent in the solid state resulted in the formation of the asymmetric disulfide exclusively (>98%). CT complexation and appropriate molecular arrangements are the key factors behind successful execution that was confirmed by different analytical experiments (Figure 4.1). The strategy paves the way to prepare unsymmetrical disulfide molecules from two dissimilar thiols.

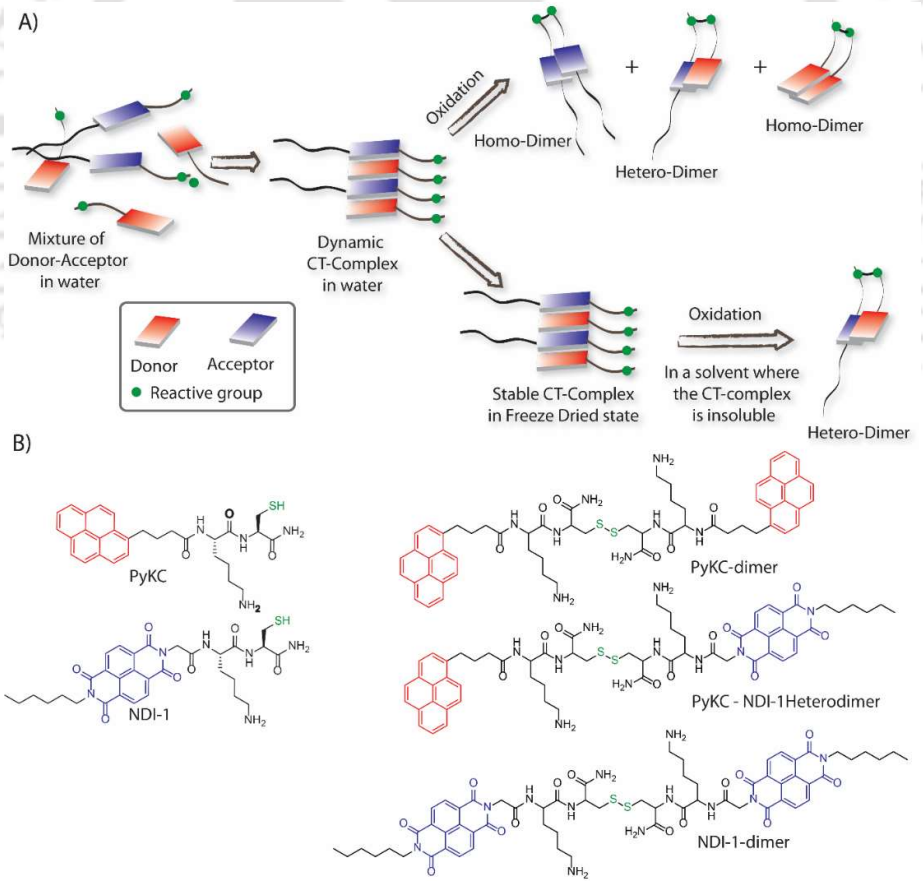

Scheme 4.1 (A) Schematic presentation of the CT-complexation driven protocol to control the chemo-selectivity. (B) Chemical structures of different thiol substrates used for the study and their homo and heterodimers.

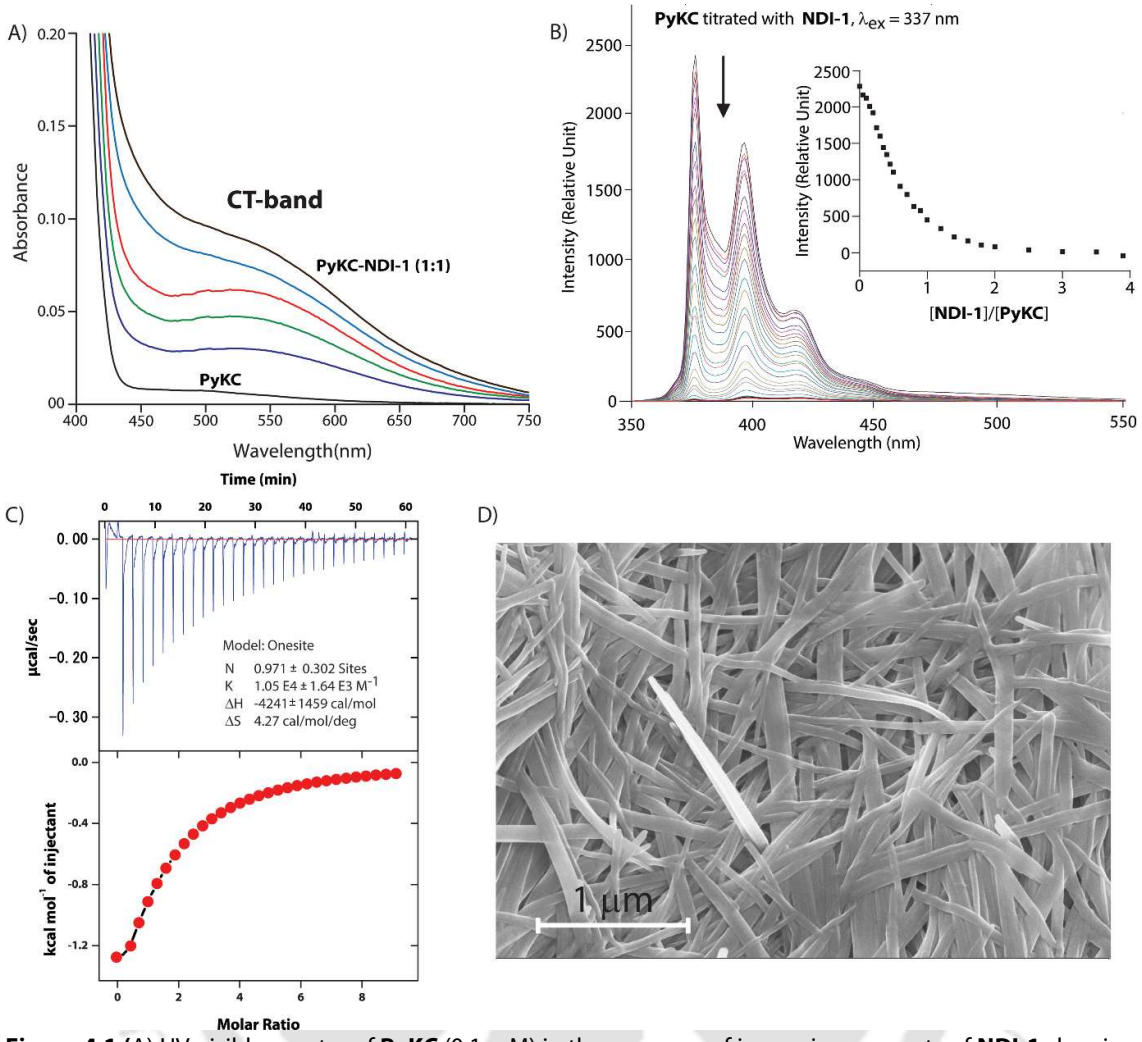

Figure 4.1 (A) UV-visible spectra of **PyKC** (0.1 mM) in the presence of increasing amounts of **NDI-1** showing the appearance of the CT-band. (B) Emission spectra of PyKC when titrated with NDI-1 showing the quenching of the emission. Inset: the changes in emission intensity at 376 nm against the molar ratio of **PyKC** and **NDI-1**. (C) Thermogram (top) and binding isotherm (bottom) of titration of PyKC with NDI-1 at 298 K. (D) FESEM image of a freeze dried sample of an aqueous mixture of **PyKC** with **NDI-1** (1: 1).

Chapter 5: Protection and Glutathione Responsive Delivery of Proteins by a Ultrashort Peptide Hydrogel

In this work, we have demonstrated a composite hydrogel by combining two different short peptides, **PyKC** and **PyKRGD** (Scheme 5.1A and B). The characterization of the composite gel (Scheme 5.1C) shows that the presence of **PyKRGD** in the mixture could not impart much changes in the gel character of **PyKC**. Importantly, like **PyKC**, the composite gel also showed insolubility in aqueous buffers of varying pH and thixotropic and injectability property. Moreover, the hydrogel showed response to GSH which disrupts the hydrogel by

breaking disulphide linkages of **PyKC** dimer. **PyKC** was found to be non-toxic to different cell lines. Based on these results, the composite hydrogel was used for in-vitro protein release studies using four different fluorophore labelled proteins in response to GSH concentration. In presence of 10 µM GSH, a sustained release of ~ 50% of the loaded proteins within 7 days were observed (Figure 5.1).

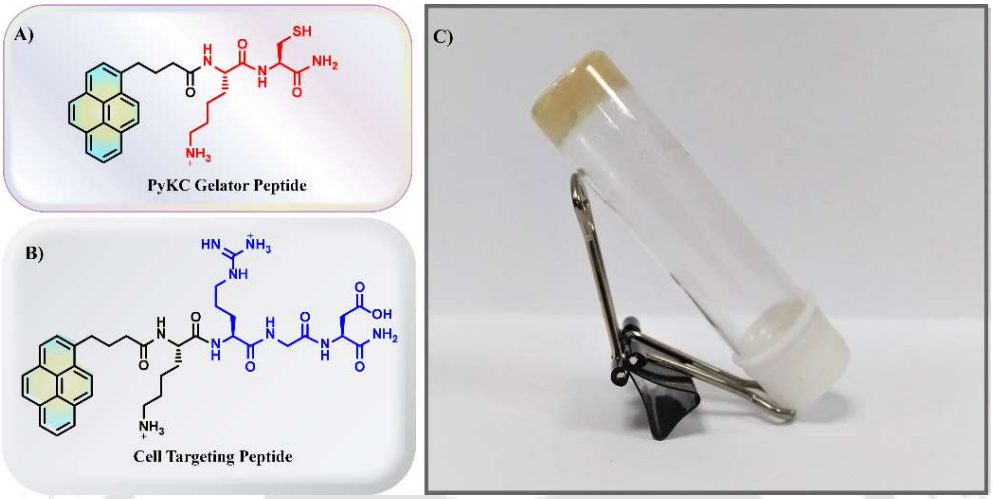

Scheme 5.1 A). and B). Chemical structures of the peptides and C). Picture of the composite hydrogel.

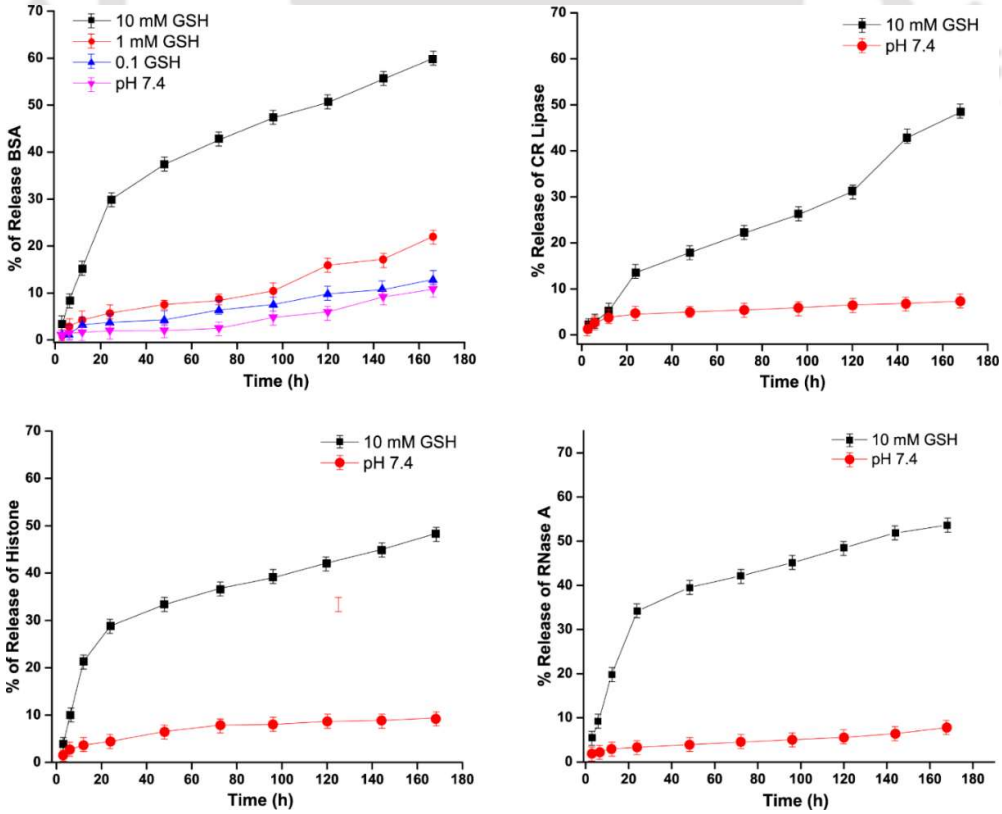

Figure 5.1 Release profile of the various proteins upon Glutathione (GSH) treatment, (A) BSA-FITC with different concentration of GSH, (B) CR lipase, (C) Histone and (D) RNase A respectively.

References

1. Dasgupta, A.; Das, D., *Langmuir* **2019,** *35*, 10704-10724.
2. Dasgupta, A.; Mondal, J. H.; Das, D., *RSC Advances* **2013,** *3*, 9117-9149.
3. Jalani, K.; Kumar, M.; George, S. J., *Chem. Commun.* **2013,** *49*, 5174-5176.
4. Jain, A.; Dhiman, S.; Dhayani, A.; Vemula, P. K.; George, S. J., *Nat. Commun.* **2019,** *10*, 450.
5. Wang, C.; Guo, Y.; Wang, Z.; Zhang, X., *Langmuir* **2010,** *26*, 14509-14511.
6. Shin, Y.-g. K.; Newton, M. D.; Isied, S. S., *J. Am. Chem. Soc.* **2003,** *125*, 3722-3732.
7. Yu, J.; Horsley, J. R.; Abell, A. D., *RSC Advances* **2017,** *7*, 42370-42378.
8. Bartocci, S.; Berrocal, J. A.; Guarracino, P.; Grillaud, M.; Franco, L.; Mba, M., *Chem. Eur. J.* **2018,** *24*, 2920-2928.
9. Lucas, X.; Bauzá, A.; Frontera, A.; Quiñonero, D., *Chem. Sci.* **2016,** *7*, 1038-1050.
10. Grauffel, C.; Yang, B.; He, T.; Roberts, M. F.; Gershenson, A.; Reuter, N., *J. Am. Chem. Soc.* **2013,** *135*, 5740-5750.
11. Petersen, F. N.; Jensen, M.; Nielsen, C. H., *Biophys. J.* **2005,** *89*, 3985-96.
12. Han, T. H.; Kim, J.; Park, J. S.; Park, C. B.; Ihee, H.; Kim, S. O., *Adv. Mater.* **2007**, *19*, 3924-3927.
13. Ryu, J.; Park, C. B., *Angew. Chem., Int. Ed.* **2009**, *48*, 4820–4823.
14. Cui, H.; Muraoka, T.; Cheetham, A. G., *Nano Lett.* **2009**, *9*, 945–951.
15. Aggeli, A.; Bell, M.; Boden, N.; Keen, J. N.; Knowles, P. F.; McLeish, T. C. B.; Pitkeathly, M.; Radford, S. E., *Nature* **1997**, *386*, 259–262.
16. Zhang, S.; Holmes, T.; Lockshin, C.; Rich, A., *Proc. Natl. Acad. Sci. U. S. A.* **1993**, *90*, 3334–3338.
17. Singha, N.; Srivastava, A.; Pramanik, B.; Ahmed, S.; Dowari, P.; Chowdhuri, S.; Das, BK.; Debnath, A.; Das, D., *Chem. Sci.* **2019**, *10*, 5920-5928.
18. Xing, R.; Li, S., Zhang, N.; Shen, G.; Mohwald, H.; Yan, X., (2017). *Biomacromolecules* **2017**, *18*, 3514-3523.
19. Jonker, A. M.; Löwik, D. W.; Van Hest, J. C., (2012). *Chem. Mater.* **2012**, *24*, 759-773.
20. Draper, E. R.; McDonald, T. O., Adams, D. J., (2015). *Chem. Commun.* **2015**, *51*, 6595-6597.
21. Clarke, D. E.; Parmenter, C. D.; Scherman, O. A., (2018). *Angew. Chem. Int. Ed.* **2018**, *57*, 7709-7713.
22. Pearse, M. J.; Mackinlay, A. G., *J. Dairy Sci.* **1989**, *72*, 1401-1407.
23. Rosen, H.; Abribat, T., *Nat. Rev. Drug Discov.* **2005,** *4*, 381-385.
24. Langer, R., *Nature* **1998,** *392*, 5-10.
25. Tran, S.; DeGiovanni, P.-J.; Piel, B.; Rai, P., *Clin. Trans. Med.* **2017,** *6*, 1-21.
26. Raizada, A.; Bandari, A.; Kumar, B., *Int. J. Pharm. Res. Dev.* **2010,** *2*, 9-20.
27. Mondal, S.; Das, S.; Nandi, A. K., *Soft Matter* **2020,** *16*, 1404-1454.
28. Li, J.; Mooney, D. J., *Nat. Rev. Mater.* **2016,** *1*, 1-17.
29. Okesola, B. O.; Smith, D. K., *Chem. Soc. Rev.* **2016,** *45*, 4226-4251.
30. Basak, S.; Nandi, N.; Paul, S.; Hamley, I. W.; Banerjee, A., *Chem. Commun.* **2017,** *53*, 5910-591

Contents

Chapter 1: Introduction

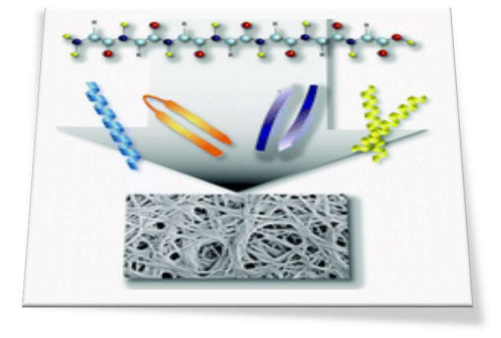

1.1 Prelude

"Supramolecular chemistry has grown in importance because it goes beyond the molecule — the focus of classical chemistry. It also offers a fresh interface with biological and materials science." – G. R. Desiraju[1].Traditional chemistry deals with strong covalent bonds while supramolecular chemistry explains the weak, reversible, noncovalent interactions between two interacting molecules in space.[2, 3] Back in 1894, this subject was apparently introduced through Emil Fischer's discovery of the famous 'Lock and Key' model for the enzyme-substrate mechanism.[1] Subsequently, various important concepts are embraced by supramolecular scientists and researchers such as molecular assembly, molecular recognition, host-guest chemistry, and most recently chemical machinery, dynamic covalent chemistry, systems chemistry, etc., where the major inspiration comes from the interplay of noncovalent interactions in natural systems.

Nature ubiquitously uses molecular self-assembly for the formation of essential functional bio-molecules like proteins, nucleic acids, polysaccharides, etc., for maintenance and advancement of life. Peptides, covalently cross-linked poly-amino acid chains, are the key constructor of proteins. Different supramolecular interactions within the peptide chain lead to different secondary, tertiary and quaternary structures. The folding of these long peptides results into active functional proteins.[4] The presence of various functional groups within the natural amino acids and the possible tenability of supramolecular interactions within short peptides make them ideal candidates for supramolecular assemblies. The hierarchical assembly of short peptides results in various functional soft-materials that found applications in a variety of fields including, drug delivery, protein delivery, wound healing, nanofabrication, conducting materials, tissue engineering, to name a few.[5-7] We envisioned that judicially exploiting the self-assembly process of short designer peptides could be useful for constructing novel soft materials for various applications. The present thesis primarily deals with the self-aggregation of short peptides in aqueous environments while we have utilized our best academic efforts to culminate certain new scientific information in this subject.

1.2 Propensity of Peptides toward Aggregation

Peptides self-assemble into a varied collection of nanostructures. The peptide assemblies are of key interest in material science and especially in Bio-materials because they play an important role in fabricating nano-architectures with biocompatibility and bio-degradability. The various secondary structures (α-helix, β-sheet, coils etc.) generated within a protein structure can be easily incorporated in short peptide sequences by applying rational design of the peptides. The key component of peptides, i.e., amino acids, possess a wide variety of functionalities that can be fine-tuned to construct short sequences with a high level of self-aggregation propensity. The balanced design of peptides leads to hierarchical assembly of these secondary structures leading to higher-order aggregates that provide the required properties for targeted application of the soft materials.

1.2.1 Noncovalent Interactions Involved in Self-Aggregation of Peptides

Self-aggregation of peptides essentially relies on the hydrogen bonding ability, hydrophobic side chains of amino acids, electrostatic interactions between charged side chains, π–π stacking of the aromatic residues and other synthetically incorporated supramolecular forces. Below is an overview of the various noncovalent forces that allow the self-aggregation of short peptide sequences.

1.2.1.1 Hydrogen Bonding

Hydrogen bonding is the most crucial supramolecular interaction behind the self-assemblies of short peptides. The presence of hydrogen bond donor (amide-N*H*) and acceptor (amide carbonyl) groups in the peptide backbone allow the peptide molecule to assemble easily. The most effective way of utilizing the hydrogen bonding ability can be found in various secondary structures formed by proteins and peptides.

β-sheet or β-pleated sheet is the most commonly found secondary structure in proteins. Beta sheets consist of laterally connected β-strands by at least two or three backbone hydrogen bonds, resulting in a pleated sheet (Figure 1.1a).[8] Sometimes, two β-strands are connected with a loop and form hairpin-like structures called β-hairpins (Figure 1.1b). β-hairpins are also stabilized through hydrogen bonding between the strands. The higher secondary structure of proteins that are heavily relying on hydrogen bonding is the α-helix

(Figure 1.1c). The α-helices are formed by winding the polypeptide backbone into a right-handed helix and are stabilized by internal hydrogen bonding. In proteins, α-helices gain additional stabilization through hydrophobic effect and van der Waals' forces. Another interesting secondary structure developed are the coiled-coils (Figure 1.1d), where multiple α-helices are joined together through favourable interactions at the helix surfaces. In these cases, though the helices are stabilized by hydrogen bonding, the interaction between the helices is governed by hydrophobic interactions.

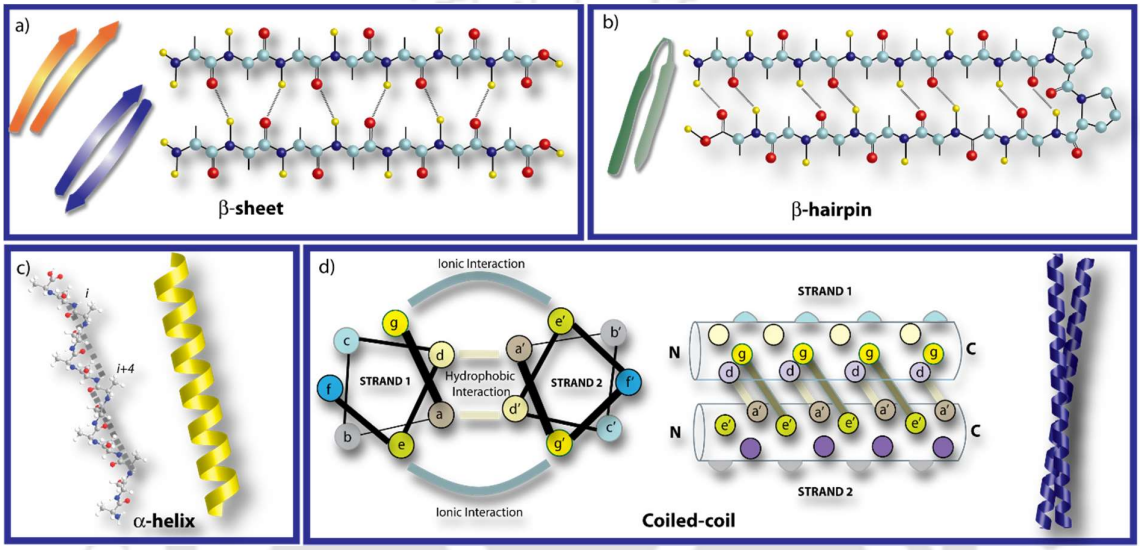

Figure 1.1 Graphical presentation of various types of secondary structures adopted by peptides. Figure adapted from reference 8.

1.2.1.2 Hydrophobic Interaction

The hydrophobic characters in a peptide sequence mainly arise from the presence of hydrophobic side chains of the amino acids. Proper arrangement of the amino acids can lead to a completely hydrophobic face of the peptide secondary structures. An arrangement of alternating hydrophilic and hydrophobic amino acids in the primary sequence of a peptide leads to the formation of two distinctly different faces where one side of the backbone is hydrophobic while the other face remains hydrophilic. Such an arrangement leads to the formation of β-sheet. Similarly, for α-helix formation, proper positioning of hydrophobic amino acids in the sequence is essential. Even in the formation of coiled-coil structures, several α-helices get joined through hydrophobic interactions. A peptide sequence containing hydrophobic and hydrophilic groups can be considered "peptide amphiphile" (PA, Figure 1.2).[8] The appropriate hydrophilic-lipophilic balance or

HLB[9] is one of the key parameters that control the self-assembling property of the peptide. PAs can be classified into two broad categories,[10, 11]

a) **Amphiphilic peptides:** Here, the PA is made of amino acids only, and because of the positioning of the amino acids, the peptides behave like an amphiphile.
b) **Lipidated Peptides:** In this case, a hydrophobic chain is attached to an essentially hydrophilic peptide sequence, and appropriate HLB is attained. The hydrophobic chain (group) and the peptide sequence can be considered the tail and head of a surfactant.

   In addition, PAs can also be constructed using host-guest chemistry, as shown in Figure 1.2. In these cases, a hydrophilic peptide sequence is conjugated with a lipid chain using macrocyclic hosts like Cucurbiturils (CB), Cyclodextrin etc. and are termed as supramolecular peptide amphiphiles (SPA).[12-14]

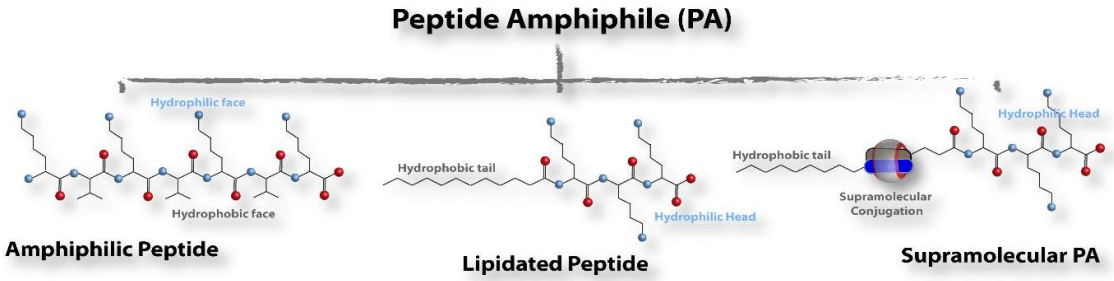

Figure 1.2 Classification of peptide amphiphile. Figure was adapted from reference 11.

1.2.1.3 Ionic Interaction

Ionic interactions between charged side chains (sometimes called salt bridges) play a critical role in forming secondary and tertiary structures of peptides and proteins. The α-helices are stabilized by the ionic interactions between the $(i)^{th}$ and $(i+4)^{th}$ residues of the sequence (Figure 1.1). Similarly, in the case of self-aggregation of short sequences, proper sequencing of the peptides can allow two molecules to bind together through ionic interactions, leading to a hierarchical aggregation of higher orders.[15, 16]

1.2.1.4 π–π Stacking

π–π stacking is one of the key supramolecular interactions. Figure 1.3 shows different types of π–π stacking possible between two π rings. This particular interaction is at commonplace in supramolecular assemblies. Tryptophan (Trp), Phenylalanine (Phe) and Tyrosine (Tyr) is

the only natural amino acids that possess aromatic rings, and appropriate arrangements of these amino acids in the peptide sequences lead to effective π–π interaction leading to self-assemblies of peptides and proteins. In addition to that, other aromatic moieties like, Fmoc, naphthalene, pyrene, anthracene, naphthalene diimide (NDI), perylene diimide (PDI) are also frequently conjugated to synthetic peptides in order to create self-assembling sequences.[17-23]

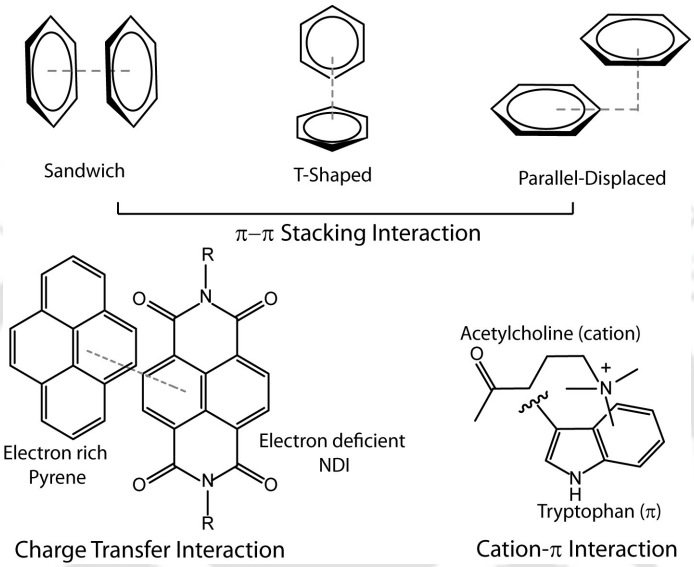

Figure 1.3 Pictorial presentation of π–π stacking, charge transfer and cation-π interactions.

1.2.1.5 Charge Transfer Interaction

Charge transfer (CT, Figure 1.3) interaction within organic molecules happens when an electron-deficient moiety and a π-electron cloud come to close proximity. Typically, the electron-rich π-ring partially donates its electron density to the electron-deficient group and thereby stabilizes the complex. Though it is commonly observed in the case of self-assemblies of other types of organic molecules,[24-26] in case of peptides, one has to rationally introduce both electron-deficient and electron-rich groups to achieve CT interaction.[27 28, 29] Nevertheless, it is important to state that presence of CT interactions in case of peptide self-assemblies are scarcely observed.

1.2.1.6 Cation-π interactions

Cation–π interactions are results of closed-shell cations interacting with neutral π systems. Cation–π interactions are omnipresent in biological systems and have been utilized by

several proteins to stabilize the tertiary or quaternary structures.[30-37] For example, Phosphatidylethanolamine (PE), and phosphatidylcholine (PC) interact with interfacial Tryptophans via cation-π interactions.[38] Following the discovery of cation–π interaction by Kebarle in 1981,[39] MeotNer *et al.* reported organic cations NH_4^+ and $MeNH_3^+$ with C_2H_4 and benzene derivatives showed that these interactions are stronger than typical hydrogen bonds.[40] Since then, this particular interaction has been utilized in several contemporary fields, including chemistry, materials science, and related areas.[41-43] However, the design and syntheses of systems capable of exhibiting cation–π interactions are challenging tasks, especially in organic soft materials. Recently, Price *et al.* showed that placing a negatively charged amino acid in close proximity to π-electron-rich Phe in a reverse turn results in a favourable interaction that increases the conformational stability significantly.[44] However, these types of supramolecular interactions are not very common, and it is important to rationally design the peptide sequences to incorporate such interactions in the self-assembly process.

1.3 Short Peptide-Based Self-Assemblies

1.3.1 The Hierarchical Assembly Process

The aggregation of peptides is a hierarchical process.[45] The process can be explained with the help of Figure 1.4. As can be seen, under an appropriate environment, peptides form secondary structures utilizing supramolecular interactions. These secondary structures further assemble in a concentration-dependent manner, leading to various nanostructures like tube, fibres, belt, sheet, spheres etc.[46-50] With further enhancement in the concentration, these nanostructures can grow in three dimensions to thicker and bigger architectures. The process can continue if these nanostructures possess sufficient functional groups at the surface to exert noncovalent interactions and lead to network-like structures. In many cases, the formed network can encapsulate the solvent through cohesive forces and form a semi-solid material called gel. Based on the type of solvent used, the gels can be divided into two groups, organogel (with organic solvent) and hydrogel (in an aqueous medium).

Since the present thesis partially deals with short peptide-based hydrogels, a brief discussion on peptide hydrogels is provided in the following sub-section.

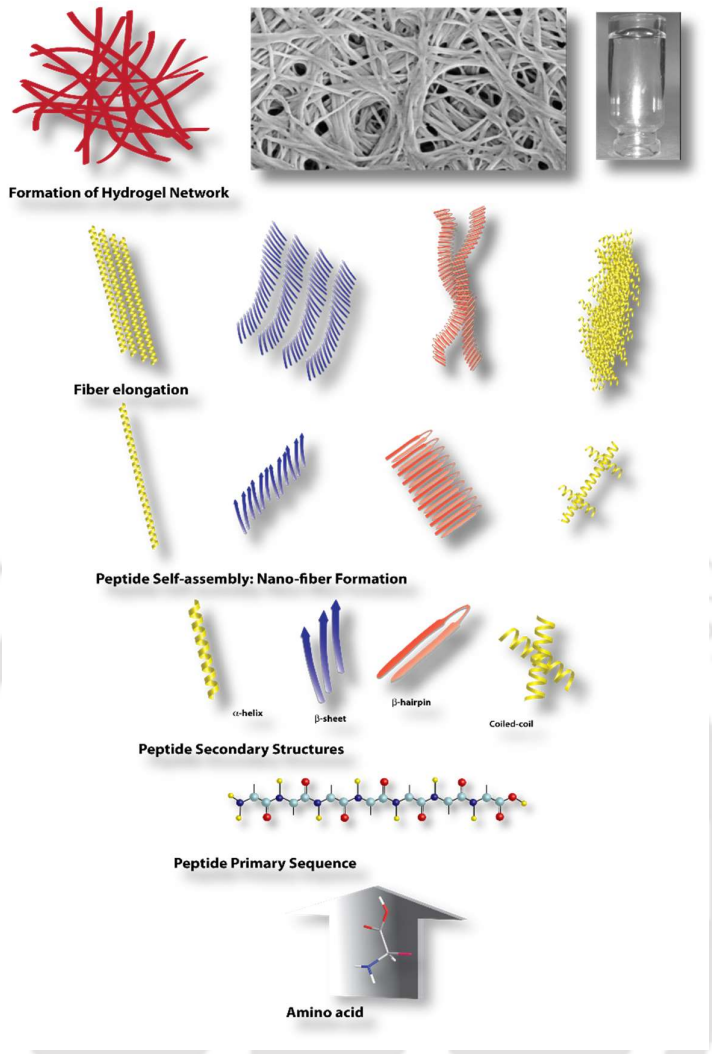

Figure 1.4 Graphical presentation of the hierarchical assembly of peptides. Adapted from Reference 8.

1.3.2 Short Peptide Based Hydrogels

As mentioned before, supramolecular hydrogels are one of the most superior outcomes of the self-assembly processes of short peptides in the aqueous medium. Over the years, with many such examples, in-depth knowledge and information are gathered about the assembly process and mechanism for supramolecular hydrogels. The accumulated knowledge certainly helps us design a small molecule or peptide that may lead to hydrogels. However, there is always a high possibility of failure. It is extremely important to understand the purpose of creating such soft materials and design the molecules accordingly. The appropriate balance and positioning of the different noncovalent

interaction sites are of the utmost importance. Here is a brief discussion on different short-peptide hydrogels based on their designing principles.

Designing a smart peptide with rationally selected amino acids to attain the precise balance in hydrophilicity and hydrophobicity is essential to construct such strong self-assembly driven hydrogels.[32] The self-assembly of peptides leading to hydrogelation is a hierarchical process, the so-called "Bottom-up" route as described before. To construct such assemblies, chemists relied upon the peptide sequences to form various secondary structures. These secondary structures consequently lead to the hydrogel networks formation through higher-order assemblies.

1.3.2.1 Hydrogels Formed by Different Secondary Structures

Amongst the various secondary structures formed by peptides, β-sheets are the most commonly used to construct hydrogels. Even extremely short peptides (2-3 amino acids) also show the tendency to form β-sheet like assemblies. Boden and co-workers proposed some simplistic models to form elongated βsheets from a peptide sequence, leading to various kinds of higher order assemblies, including hydrogels.[46] The proposed criteria are,

- Cross-strand attractive forces between side chains.
- Lateral recognition between adjacent β-strands to constrain their self-assembly to one dimension and avoid heterogeneous aggregated β-sheet structures.
- Strong adhesion of solvent to the surface of the sheets to control solubility.

Following these assumptions, this group reported several peptides (1.1-1.6 Figure 1.5) which form hydrogels in water.[46-48] The hydrogels were achieved from β-sheet formation by the peptides. A series (1.7-1.10, Figure 1.5) of amphiphilic and acidic antiparallel β-sheet forming peptides (AAβPs) have been prepared by Rapaport *et al.* at neutral pH showing scaffold for bone forming cells.[49] Zhang *et al.* have reported a series (1.11-1.16, Figure 1.5) of β−sheet forming amphiphilic peptides containing periodic repeats of alternating ionic hydrophilic and hydrophobic amino acids. These short (8 to 16 aa) peptides form stable β-sheets which further aggregate to higher order nano scaffolds.[50, 51]

Short Name	Sequence	Number
P_{II} - I	CH_3CO-QQRQQQQQQQ-NH_2	1.1
P_{II} - II	CH_3CO-QQRFQWQFEQQ-NH_2	1.2
P_{II} – 4	CH_3CO-QQRFEWEFEQQ-NH_2	1.3
P_{II} – 8	CH_3CO-QQRFOWOFEQQ-NH_2	1.4
P_{II} – 9	CH_3CO-SSRFEWEFESS-NH_2	1.5
P_{II} – 12	CH_3CO-SSRFOWOFESS-NH_2	1.6
P_{LD}-5	$PD(LD)_5P$	1.7
P_{ED}-5	$PE(LE)_5P$	1.8
P_{FD}-5	$PD(FD)_5P$	1.9
P_{FE}-5	$PE(FE)_5P$	1.10
EAK8	H_2N- AEAEAKAK-$CONH_2$	1.11
EAK12	H_2N-AEAEAKAKAEAE -$CONH_2$	1.12
EAK16	H_2N-AEAEAKAKAEAEAKAK-$CONH_2$	1.13
KLD12	CH_3CO-KLDLKLDLKLDL-NH_2	1.14
RADA16-I	CH_3CO-RADARADARADARADA-NH_2	1.15
RADA16-II	CH_3CO-RARADADARARADADA -NH_2	1.16
	IDIDI	1.17
	DDIII	1.18
	DIIID	1.19

Figure 1.5 Some β-sheet forming peptide sequences.

Recently, Scherman and his group reported a series of β–sheet forming peptides (1.17-1.19, Figure 1.5) that self-assemble to form hydrogels.[52] They have shown that by changing the charge distribution of the peptide sequence, the stiffness of the hydrogels can be tuned across two orders of magnitude (2–200 kPa). Interestingly, peptide 1.18 formed the hydrogel with highest stiffness reported for any peptide based hydrogel so far. There are several other reports of β-sheet forming peptides which form hydrogels. However, it is beyond the scope of this literature survey to discuss all of them.

Another interesting secondary structure that has been extensively exploited to construct short peptide based hydrogels is β-hairpin. Schneider and his group first reported the 20 aa sequence containing alternate Val and Lys units with ^{D}Pro-^{L}Pro in the middle of the sequence (MAX1, 1.20, Figure 1.6).[53] The alternate VK repeat helps in forming the β-sheet while the ^{D}Pro-^{L}Pro dyad provides the Type–II β-turn to the sequence. These hairpin structures consequently assemble further to form the hydrogel network. Utilizing this concept, the same group have reported several interesting hydrogels of β-hairpin peptides. Some of the representative examples are shown in Figure 1.5 (1.20 – 1.26, Figure 1.6).[54-57]

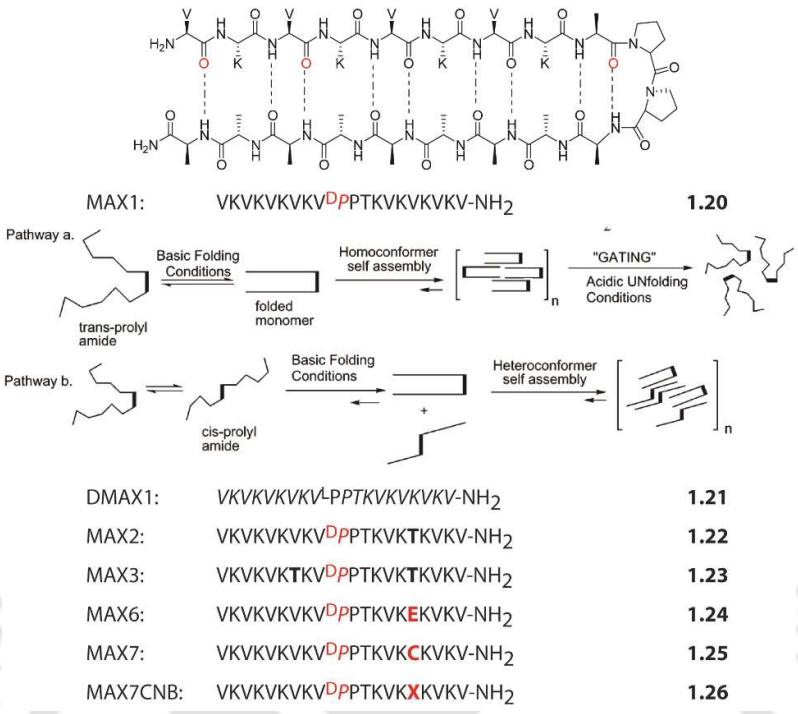

Figure 1.6 Some β-hairpin forming peptide sequences.

α-helix and coiled coil peptides are not very common when it comes to the formation of hydrogel network. However, there are some specific examples where hybrid hydrogels are prepared using coiled-coil motifs as cross-linkers for synthetic polymers. An artificial protein was reported by Tirrell and co-workers that forms reversible hydrogels in response to changes in pH and temperature (1.27**,** Figure 1.6). Kopeĉek *et al.* reported a rationally designed coiled coil domain. A polyelectrolyte middle domain (B), consisting of Ala-Gly repeats was flanked between two terminal coiled-coil segments A and C (1.28 – 1.31, Figure 1.7). All these peptides formed hydrogels at high concentration is PBS buffer and water.

Figure 1.7 Peptide sequences with α-helical motifs.

1.3.2.2 Stimuli Responsiveness of Peptide Hydrogels

As discussed earlier, Various supramolecular interactions assist in the formation of the superior hierarchical assembly from smaller peptide chains resulting various peptide based assemblies like gels, vesicles, nanosheets, nanoaggregates, etc. These interactions are vulnerable to certain conditions which are known as the stimulus or the triggering forces and often the gels are termed as 'smart gels'. From the thermodynamic point of view, the stimuli are obligatory to shift the thermodynamic equilibrium for the transition of the phases of the hydrogel. The stimuli responsiveness of the peptide hydrogels is judicially utilized in various fields like targeted drug delivery, wound healing, pollutant removal, logic gate, and artificial intelligent.[58-60] The mechanical strengths, stiffness and other rheological properties of the peptide based hydrogels are depended on the degree of supramolecular interactions that various physiochemical triggers can easily tune, likes pH, temperature, ionic strength and other parameters. Besides that, hydrogels can be designed by proper peptide sequences so that they specifically respond towards the various physiological stimulants of unhealthy cells or tissues e.g., tumour tissue microenvironment exhibits low pH, low oxygen content (hypoxia), elevated levels of reactive oxygen species (ROS), over-expressed receptors and hydrolytic enzymes.[61, 62] Hence, peptide based hydrogels hold importance over other material based congeners. So far, it is also important to structurally engineer the peptide sequences in the hydrogels for the sustained release of the therapeutic agents which is both economically and biologically more advantageous over burst release. In the next section, different stimuli responsiveness of the peptide hydrogels has been discussed from their design strategy to successive application.

1.3.2.2.1. pH Responsiveness

pH portrays the most crucial effect on the construction or the degradation of the peptide hydrogels. The polar groups in the peptide backbone are very much responsive towards the pH changes, the H-bonding interactions among various groups, and the water molecules that change gradually with the change of pH that leads to the proper fibrilar conformation of the gelator molecule from a homogeneous solution. In literature, most of the primary amine containing hydrophobic peptides are reported to gel at a relatively higher pH. The hydrogels which are formed in physiological pH are suitable for certain biological applications due to their content features of natural biomaterials.

Schneider and co-workers[63] showed in their pioneering work that MAX1, a 20 residue peptide (Figure 1.8) comprising β-sheet forming alternating Valine and Lysine residues adjoining a type II' β-turn including tetrapeptide (V^DPPT) that folded into an amphiphilic β-hairpin under basic aqueous solutions affording a hydrogel with the shear-thinning property. The peptide folded in a manner that the outer face of the peptide was lined with a hydrophobic valine unit and lysine residues participated in hydrogen bonding in the inner face of the peptide. Lowering the pH of the gel, intramolecular H-bonding was cleaved off that unstructured the β-hairpin structure resulting in the dissolution of the hydrogel. Later on, Ulijn and co-worker[64] demonstrated a pH switchable hydrolase by attaching a Histidine residue with a Ser-Gly spacer at the N-terminus of the MAX1 peptide (Figure 1.8).

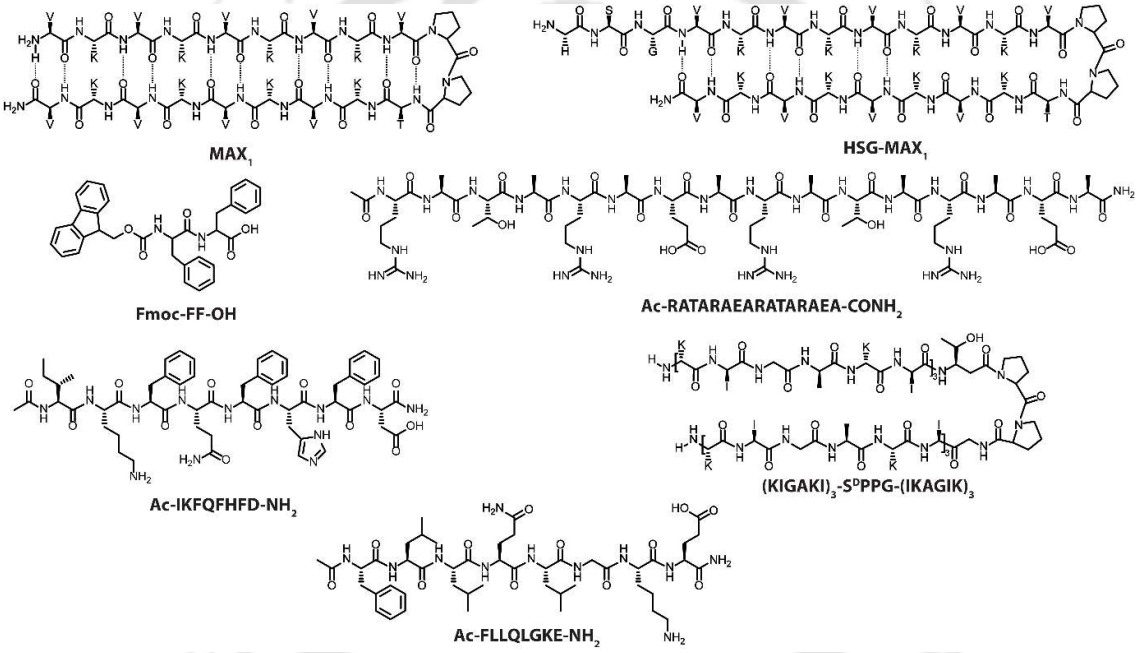

Figure 1.8 Chemical structures of some pH responsive peptide gelators.

The catalytic activity of the hydrogel was found to be maximum at the gel state in pH 9. After acidifying, the gel immediately turned into the sol and the activity was reduced by many folds. In another report by the same group, they have shown pH dependent self-assembly of a short peptide gelator Fmoc-FF (Figure 1.8).[65, 66] At higher pH, most of the molecules remain ionized showing no assembly at all. At the pH range of 10.2 to 9.5, both the protonated and unprotonated molecules are present and they pair up into the β-sheet fibrils which result in a transparent hydrogel over critical gelation concentrations. Another change of the self-assembly occurs lowering the pH 9.5-6.2 where the reduction of the fiber

surface charge directs the peptide to self-assemble laterally through hydrophobic interactions and form large rigid ribbons that precipitate from the homogeneous solution. Kinoshita and Tan *et al.* demonstrated a 16 residue peptide gelator (Ac-RATARAEARATARAEA-$CONH_2$, Figure 1.8) which produces an elastic and thixotropic hydrogel at neutral pH.[67] The strong electrostatic interaction between the positively charged Arg and negatively charged Glu leads to the β sheet formation disturbed in both acidic and basic conditions. Therapeutically, the biocompatible hydrogel is utilized by the release of vitamin B_1 in the acidic environment. Li *et.al.* reported a zwitterionic octapeptide (IKFQFHFD, Figure 1.8) which exhibits switchable antimicrobial properties.[67,68] At neutral pH (7.4), the peptide is electrically neutral, and the intermolecular electrostatic attraction between Asp and Lys units leads to hydrogelation. Due to lower pH (5.5) in the chronic wound environment, the fibrilar network of the hydrogel destabilizes and the activated release of the cationic antimicrobial peptide was observed. Moreover, the hydrogel was also loaded with a photothermal agent, cypate, and a procollagen component, proline to achieve pH-activated synergistic biofilm disruption and wound healing. The pH switchable property of the hydrogel not only facilitated programmable and targeted drug release but also assisted in reducing toxicity to normal tissues and avoid undesirable side effects. Zhao and his team synthesized a new self-assembling peptide consisting of a tetrapeptide(T^DPPG) linker flanked by two antibacterial peptide sequences (KIGAKI, Figure 1.8).[69] Increasing the pH, the designed peptide can undergo an abrupt structural transition from a random coiled structure to a stable unimolecular β hairpin conformation which subsequently drives to an elastic hydrogelation. The potential bacterial inhibition of the peptide hydrogel is confirmed by the antibacterial assay against *Escherichia coli*. Ghosh *et al.* reported a pH responsive hydrogel of a hexapeptide (FLLQLGKE, Figure 1.8), which can entrap a water soluble molecule, Calcein within the fibrilar network and release it at lower pH (5.5) with good biocompatibility.[70] At physiological pH (7.4), an entangled fibrous network with β-sheet secondary structure efforts the hydrogel formation after a single heating cooling cycle. The ionic interactions between the Lys and Asp residues in β sheets are perturbed by lower pH causing an immediate breakdown of the hydrogel.

1.3.2.2.2. Redox Responsiveness

Redox reaction is a type of chemical reaction that involves transfer of electrons between two species. For many decades, chemists keep trying to understand the details of the

change of oxidation state that directs the feasibility of a chemical reaction. In the biological perspective, amongst several chemical reactions that are going on every moment within a cell, most of them fall in the category of redox reaction.[71] Intracellular redox reactions control the signalling pathway of cell division, proliferation, and apoptosis by altering protein structure and function. Moreover, the redox reactions by normal metabolism or external stress generate reactive oxygen species (ROS) which can regulate the intracellular redox balance and eventually the fate of the cell. Many organelles within cells are known to generate ROS such as mitochondria, lysosome, peroxisome, cytosol, plasma membrane, and endoplasmic reticulum.[72] Redox responsive materials could be an easy solution to the challenge for the balance of the perfect cellular oxidative stress. From a chemist's perspective, peptides functionalised with the redox-active groups can be an effective tool to regulate the fate of a cell leading to its death or resurgence. In the next segment, we have demonstrated some redox responsive peptides and their applications.

Zhang and his team reported a very simple strategy where they functionalized ferrocene with phenylalanine (Figure 1.9) to develop a self-supporting hydrogel.[73] This ultra-short peptide-based hydrogel collapsed to liquid upon treatment with Ce^{4+} oxidant. Apart from that, the hydrogel responded to pH, temperature, and mechanical shaking which made the gel multi-responsive. Density Functional Theory (DFT) calculations suggested that the fiber network was formed by the organization of antiparallel dimerization of the molecule where the axe-shaped ferrocene moiety stacked above the phenyl group of the next molecule to form a brick-like dimer. The porous nature of hydrogel was utilized for the sustained release of two trivial aromatic dyes, rhodamine B and methylene blue indicating the potency as a drug delivery vehicle. In another report, the same group demonstrated the nanowire forming capability of the ferrocene-attached diphenylalanine peptide.[74] An immunosensor was prepared using glucose oxidase on the gold nanorod surface that catalyzed glucose oxidation in the presence of ferrocene moiety with high sensitivity and good selectivity towards anti-TNF-antibody.

The thiol group of cysteine is commonly reported for its rapid disulfide formation capacity in the design of redox-sensitive systems. The disulfide linkages are generally very stable in physiological conditions but they can be easily reduced using various reducing agents such as TCEP, DTT, Glutathione (GSH), etc. In earlier reports, we have found the pioneering

hydrogel of dibenzoylcystine (DBC) (Figure 1.9) responses in presence of above mentioned reducing agent intruding the self-assembly process to an out of equilibrium direction.[75] Glutathione is a tripeptide that is known as the master antioxidant inside the cell. The intracellular concentration of the glutathione is nearly 0.5 to 10 mM whereas in the extracellular milieu it falls to 2-20 μM.[76] This particular difference in the glutathione level is always maintained inside the cell to judiciously control the various oxidative stress for the proper functioning of enzymes and proteins

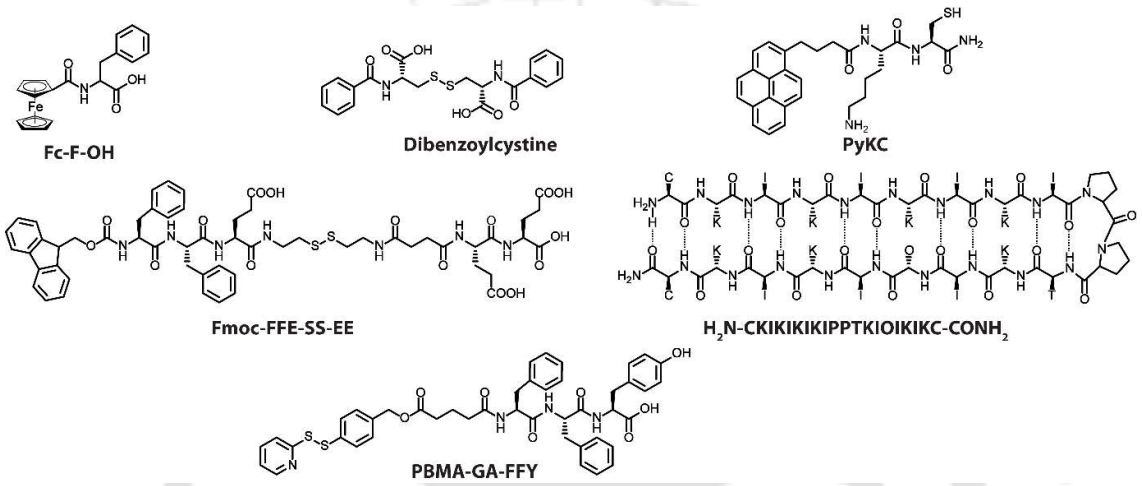

Figure 1.9 Chemical structures of some redox responsive peptide gelators.

. Recently, our group has also reported a pyrene functionalised short peptide, PyKC (Figure 1.9) that formed hydrogel via sulfide bond formation which was nicely utilised for the protection and storage of enzymes.[77] This hydrogel was melted in presence of different reducing agents by collapsing the disulfide bonds. In another example, Yang *et.al.* have demonstrated the disulfide reduction strategy for hydrogel formation as an efficient 3D cell culture medium of 3T3 cells.[78] In the presence of GSH, the Fmoc-FFE-ss-EE progelator (Figure 1.8) released Fmoc-FFE-s resulting in stable gelation in DMEM cell-culture medium for more than six months. Inspired the MAX1 peptide (Figure 1.9), Wu and Ge *et.al.* designed a pH and redox dual responsive peptide IC1-R wherein the Val and Lys residues in MAX1 (Figure 1.9) are replaced with Iso and ornithine residues respectively to improve the pH responsiveness.[79] In addition, two Cys residues were introduced to both the terminus of the peptide in order of redox responsiveness. Under the neutral condition, the peptide undergoes β-sheet folding along with spontaneous intramolecular disulfide-bonding and forms a hydrogel. The hydrogel was employed in the presence of GSH at pH 5.8 for the

controlled release of paclitaxel that effectively implemented for the inhibition of tumour proliferation with good biocompatibility and biodegradability. Yang *et al.* adopted a self-immolation approach to introduce redox responsiveness in peptide hydrogels and designed a GSH responsive self-immolating group (PBMA) capped peptide gelator PBMA-GA-FFY (Figure 1.9) which could form a hydrogel in PBS at physiological pH.[80] In the presence of GSH, the PBMA group underwent a thioquinone methide cascade reaction wherein the cleavage of the disulfide bond triggered a 1, 6-elimination self-immolative step and destabilized the gelator molecule leading to the dissolution of the hydrogel. The hydrogel showed effective encapsulation and GSH triggered sustained and tunable release of a model drug, Congo red.

1.3.2.2.3. Light Responsiveness

On the research of exploring various stimuli-responsive soft materials, photoresponsive hydrogels and polymers are of particular interest for material science and engineering due to their non-invasive and non-contaminating mode of applications directed towards the desired locations with easy regulation of the irradiations.[81, 82] Light provides the required amount of energy for the chemical changes within the responsive groups that successively lead the molecular organization to a reversible spatio-temporal transformation. Based on the previous studies, we have understood that the photo-switchable peptide hydrogels could be a primary point of interest for stimuli-responsive materials[83] for numerous applications[84], so herein, we have divided our discussion into two categories based on the functional units. In the first section, certain reports are presented mainly focusing on the well-known azobenzene group and then a few other promising light-responsive units linked different peptides and their hydrogelation properties are discussed.

The azobenzene functionalised peptides can assemble into a hydrogel network by the intermolecular π–π stacking of the phenyl rings and the hydrogen bonding interaction among the peptide backbones while the light mediated conformational switching from E to Z isomer displaced the phenyl rings leading to collapse of the network structure.[85] Zhang extensively reported a series of peptides where the azobenzene substituted dipeptides could not form hydrogels due to their solubility issues, exceptionally a few examples with charged sidechains such as Azo-Phe-Glu, Azo-Glu-Tyr are prone to hydrogelation after dropping the pH of the medium.[86] Interestingly, the tripeptide hydrogel Azo-Lys-^{D}Phe-^{D}Ala

(Figure 1.10) has reported a response towards light and heat. Having the D-peptide analogues[87] it could easily behave as a ligand for recognising vancomycin as its receptor. In the same report, they also have utilised the gelation ability of Azo-Gln-Phe-Ala (Figure 1.9) for the encapsulation of vitamin B_{12} and UV light mediated control release in water. Xu and his team have shown the first example of enzyme triggered hydrogelation of a photo responsive peptide (Nap-FFK(Azo)Y-PO_3H_2, Figure 1.10).[88], in the presence of alkaline phosphatase, the tyrosine was dephosphorylated and a self-supporting hydrogel was gradually formed at pH 9 buffer that responded reversibly in the presence of UV light. Notably, Nilsson reported the self-assembly of an inter-placed azobenzene derivative ([3-(3-aminomethylphenylazo)]phenyl acetic acid, AMPP) within $(RADA)_4$ peptide (Figure 1.10) that readily resulted a self-supporting photo responsive hydrogel in saline.[89] The *trans*-form of AMPP helped the peptide form a β arc resulting in a network of cross- β fibrils, and in the presence of light, the isomerised cis form of AMPP directed the peptide to the discrete β hairpin structures.

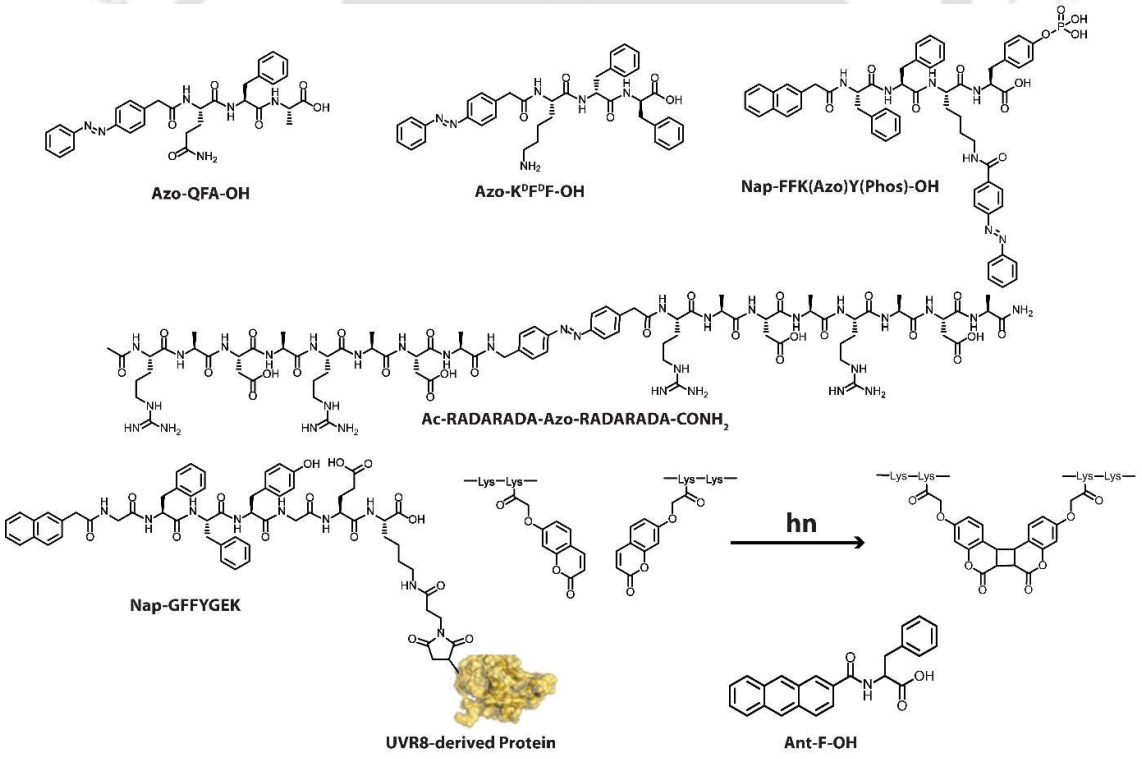

Figure 1.10 Chemical structures of some light responsive peptide gelators.

Beyond azobenzene derivatives, Yang reported a fascinating study of a photoresponsive UVR8-derived protein along with the conjugation of an aggregating peptide (Nap-

GFFYGEK, Figure 1.10).[90] The hydrogel formed by the peptide and its protein conjugate showed a reversible photo regulation of gel to sol phase that has been utilized for protein delivery and cell separation. Another new strategy was designed by the Ohkawa group where they employed few poly-lysine backbones with coumarin units (Figure 1.10) affording the head-to-head cycloaddition for light-induced hydrogelation.[91] In recent times, Webb *et al*. showed the hydrogel of amino acids modified with N-terminal anthracene group (Figure 1.10) as cell culture medium.[92] The photo dimerization of the anthracene resulted in the disassembly of the gel phase which helped in the recovery of the cells from the 3D culture.

1.3.2.2.4. Other Biomolecule Responsive

To name a few essential biomolecules, undoubtedly enzymes remains on the top position in the queue. Enzymes control the catalytic conversion of the required substrates for various cellular processes resulting the self-assembly of smaller molecules to larger bio macromolecules. Nowadays, biocatalyst or enzyme instructed self-assembly (EISA) is a hot topic for the hydrogelation of different small molecules like peptide and lipids. Moreover, using proper condition along with appropriate designing of peptides, hydrogels could be made responsive towards the overexpressed enzyme of a specific tissues or organs in order to achieve a targeted delivery of the necessary cargos. In a classic example, Chen *et al*. designed a peptide gelator, (Ac-I_3SLKG-NH_2, Figure 1.11) that responded in presence of matrix metalloproteinase-2 enzyme (MMP-2).[93] MMP-2 is generally upregulated in cancer cells and it has a strong affinity for the sit specific cleave of S-L bond. They have encapsulated FITC labelled anticancer peptide G(IIKK)$_3$I-NH_2 (FITC-G_3) into the hydrogel network and incubated with HeLa cells which are known to overexpress MMP-2. The enzymatic degradation of the hydrogel released the anticancer peptide which strikingly inhibited the cancer cell proliferation. Tyrosinase is also one such enzyme which is upregulated during tumorigenesis of malignant melanoma and specifically catalyses the oxidation of tyrosine. Utilising this fact, Yang et.al. designed a tyrosine rich peptide gelator (Ac-YYYY-OMe, Figure 1.11) which could form hydrogel at physiological pH but melted in response to tyrosinase enzyme due to the lack of π-π interaction after oxidation.[94] The hydrogel was applied for the in vitro release of a model drug, Congo red which could be a promising platform for the sustained release of therapeutics under tumour

microenvironments. In another example, Xu et.al. designed a azobenzene functionalised peptide hydrogelator (Nap-FFK-Azo, Figure 1.11) to utilise its response towards the colon specific overexpression of azo reductase.[95] The anti-inflammatory prodrug, olsalazine was directly attached to the peptide backbone and the peptide-prodrug conjugate assembled in a mildly acidic solution to form hydrogel. In presence of enzyme, the azo linkage was reduced that triggered the gel to sol transition and eventually released the active drug, mesalazine (or 5-aminosalicylic acid) at the site of inflammation.

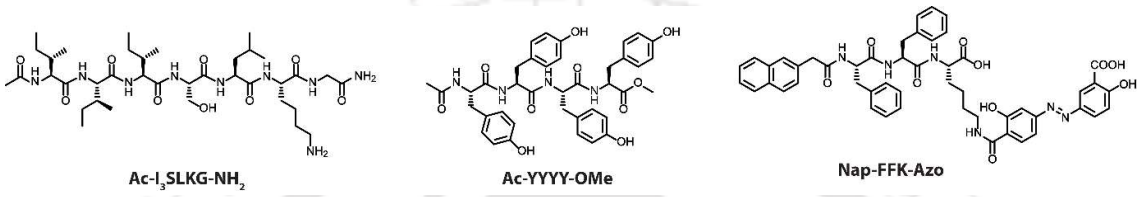

Figure 1.11 Chemical structures of some biomolecule responsive peptide gelators.

Another essential biomolecule is glucose which is the primary source of energy for all living organisms. Qian *et.al.* introduced a safer method for the delivery of insulin for the treatment of hyperglycaemia where blood glucose is elevated due to misbalance of insulin.[96] They have employed the modified MAX1 peptide (Figure 1.8) for hydrogelation. The hydrogel was used to encapsulate glucose oxidase (GOx), catalase, and insulin. In a higher concentration of glucose, GOx converts glucose to gluconic acid and H_2O_2; the subsequent drop of pH initiates the hydrogel dissolution following the release of insulin. The unwanted side product, H_2O_2 was further decomposed by the catalase enzyme forming H_2O and oxygen which helped back the GOx catalysis.

1.3.2.3 Unusual Properties of some Peptide Hydrogels

Although, for more than five decades, the science behind the small-molecule hydrogels and their applications have been explored in detail, somehow their unorthodox emergences and fortuitous happenstances will rejuvenate the interest of the subject for the coming days. The incisive investigation of such mere serendipitous observations assists in the advancement of science and technology at the greater service of mankind. After the diligent discussion of constructive parameters responsible for the self-assembling property of the peptide-based hydrogelators, herein we have intended to exemplify some unexpected properties of peptide hydrogels that have inspired us to fulfil the thesis work.

Temperature is one of the key features for the regulation of the various supramolecular interaction during hydrogel formation. Elevation in temperature results in the better solubility of the compounds to the oversaturated region so that gelation happens upon cooling. On the other hand, hydrogels melt beyond a certain temperature (T_g) due to the disruption of the required noncovalent interactions for molecular assembly. Interestingly, Xu *et al.* reported a short peptide (Fmoc-^{D}Ala-^{D}Ala) undergo hydrogelation upon increasing temperature.[97] Upon further increment, the gel expelled water and eventually collapsed into precipitates like lower critical solution temperature (LCST) polymer. Ultrasound is commonly used for better dissolution and dispersion of the solid lumps into solutions. At higher concentrations, hydrophobic peptides can be transformed into organogels by sonication. Gu and his team designed a hydrogelator with Lysine connected with 7-carboxyl methoxycoumarin and hydrazine as lipophilic and water-soluble moieties.[98] Only upon ultrasound treatment, the hydrogelator exhibited rapid hydrogel formation that was utilized for the mitigation and proliferation of 3T3 fibroblast cells. Deming and co-worker prepared an injectable hydrogel from a class of amphiphilic diblock co-polypeptides with hydrophobic leucine. They charged Lysine, aspartate residues that exhibited atypically high salt stability, as an ideal candidate for the successive cell culture and tissue engineering applications.[99, 100]

Gazit reported an ultra-short peptide-based hydrogelator, Fmoc-Lys(Fmoc)-Asp which showed the lowest critical gelation concentration (CGC) ever, 0.002 wt%. this hypergelator also exhibited unusual and unprecedented two-step self-assembly processes.[101] Time-dependent TEM images revealed a morphological transition from sphere to fiber with the advancement of time. The dissolution of the preformed plaques helped in the increment of the peptide local concentration along with the propensity of fiber formation by both intermolecular and intramolecular π stacking interactions that gradually led to the transformation from a turbid solution to a transparent hydrogel. The hydrogel was utilised as biocompatible support for 2D/3D cell culture and further composited with a conducting polymer for efficient binding and sensing of DNA. In another interesting report, Mazzenga *et al.* showed a short octapeptide (Ac-GLYGGYGV-NH_2) with the gelation ability in water where the mechanical response of the gel state was tuned at varying concentration.[102] The maximum storage modulus was found at 35.5 kPa, representing the gel among the stiffest biopolymeric hydrogels. Using various spectroscopic techniques, it was confirmed that the

peptide assembled into an unusual 3_{10} monomeric helices at the dilute condition and upon gelation, the helices to antiparallel β-sheet transformation induced the inherent mechanical stiffness.

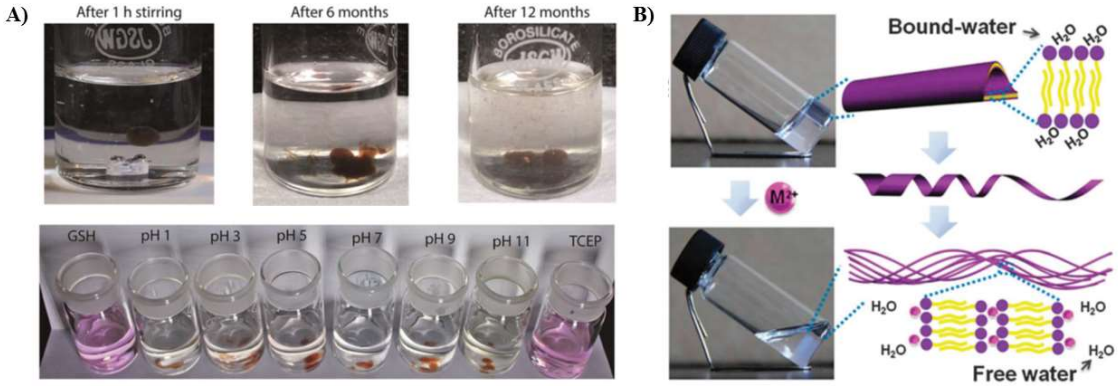

Figure 1.12 A) Unusual dissolution property of PyKC hydrogel in water and various buffer. Adapted from reference 82. B) Shrinking ability of the lipidated glutamic acid dendron hydrogel in presence of bivalent metal ion. Adapted from reference 109.

As discussed earlier, our group has reported a simplistic design of tripeptide gelator, PyKC (Figure 1.11A) which could form a highly robust and water-insoluble hydrogel, a very rare property found among the low molecular weight gelator.[77] The hydrogel was formed by the cysteine mediated dimerization and the π-π stacking between the aligned pyrene units in a manner so that it could restrict the 'to and from' movement of both the solute and the solvent molecules. The unique property of the hydrogel was applied for the facile storage and long-term protection of the enzymes from pH, heat, and other denaturing agents.

Liu and his group reported the exceptional aggregating nature of the lapidated glutamic acid dendron that could hierarchically assemble into nanotubes through H-bonding interactions over a wide pH range.[103] With the addition of bivalent metal ions, the molecule efficiently gelled the water with a very low CGC value, 0.08 wt%.[104] The metal trigger hydrogel displayed a continuous shrinkage (Figure 1.11B) for several hours which was reversibly shifted back to the initial gel state by heating and the cycle could be continued many times. Later on, in another report, they have utilised the amphiphilic gelator to co-assemble with a pyridinyl derivative of azobenzene.[105] Over time, the composite hydrogel underwent an inherent contraction to the shrunken gel which was reversibly moved back to the original gel state expending light and heat. From a different perspective, Das *et al.* have engaged a stearylated histidine amphiphile for a self-supporting hydrogel formation

following a dissipative self-assembly pathway.[106] EDC was employed to fuel up the gelation by the p-nitrophenolate linkage formation whereas the aggregated imidazole moieties of histidine units co-operatively catalysed off the ester linkage leading to the breakdown of the gel structure.

1.4 Applications of Peptide Self-Assemblies

Undoubtedly, the peptides can be rationally designed and modified to get a smart functional soft material. Hydrogel is one such example that is being utilized by mankind in many ways starting from domestic to industrial applications. In this report, various applications of peptide-based self-assemblies mostly hydrogels have been discussed below**.**

1.4.1 Tissue Engineering

Tissue engineering is one of the important therapeutical implementations of soft materials in the biomedical field that ensues with the advancement of science in the last couple of decades. [107, 108] Tissue engineering primarily entails the use of cells mounted on tissue scaffolds in the creation of new viable tissue for treatment.[109] The application of this field is now not only limited to the regeneration of the cells or tissues, rather recent advancements have been extended towards the repair or replacement of some essential body parts such as artificial bladders[110, 111], bioartificial heart[112], cartilage[113], artificial bone marrow[114, 115], blood vessels[116], and in vitro mussel meat[117] for food industries. Tissue engineering is also used for regenerative therapeutics where stem cells are instructed to produce tissues. [118] Usually, Hydrogel entraps a large volume of water inside the fibrilar network where the cells and tissues can be successfully grown and protected with proper environments.[119, 120] On this occasion, Peptide-based hydrogels can be an easy choice for mimicking the extracellular matrix (ECM) where the cells compatibly adhere and proliferate like the in vivo microenvironments. [5, 121] In the next portion, we have exemplified some successfully applied peptides for tissue engineering.

One of the most discussed peptide hydrogels as a 3D nanofibrous biocompatible scaffold is the RADA-16 family. [122] The ion-rich backbone of the peptide was assembled to form a stable β-sheet and further assemble into a cross-linked network that could mimic the ECM of the tissue cells. For example, three different peptide hydrogels of the same family

have been used for the growth of human adipose stem cells with proper biologically active sequences (SKP, FHR, PRGD). Another classic example of the peptide hydrogel for tissue engineering purposes is the EAK-16 peptide.[123] This peptide sequence spontaneously assembled to a β-sheet through ionic interactions. With suitable modification in peptide, the hydrogel was used as an artificial ECM for different cells like SMMC7721 cells[124], thymic epithelial cells[125], etc. Moreover, Peptide hydrogels with sufficient mechanical strength are very much familiar platform for the Bone tissue engineering (BTE) process where stem cells (osteoblast or chondrocytes) are seeded and cultured into a 3D scaffold. RADA, FEFEFKFK based hydrogels were successfully applied for this purpose due to their biomineralisation capability and required functionality.[126, 127] Stupp reported the biomineralization hydroxyapatite (HA) on peptide amphiphile-based cross-linked nanofibers that resembled with the alignment of HA crystals in bone and the collagen fibrils.[128]

1.4.2 Drug Delivery

Delivery of different therapeutic agents including drugs, proteins, peptide, hormones etc. has marked an important position in the treatment of cancer and other deadly diseases.[129, 130] Compared to regular cells, cancer cells provide several special functions (e.g., hypoxia, acidic pH, and improving permeability and retention effects) that can be completely exploited during the design of drug delivery vehicles.[131] Hydrogels, due to having diverse sizes and shapes, from nanogel to microscopic gel, can exhibit different types of release mechanisms in various stimuli.[132] The successful delivery of drugs using peptide hydrogels can be accredited to the four subsequent reasons; facile targeting, biocompatibility and biodegradability, easy drug encapsulation, and sustained release of cargoes in physiological conditions.[32, 133] In the following paragraph, we discussed some peptide hydrogels as delivery vehicles of various essential cargos.

Xu reported the enzyme-activated self-assembly of a D-tripeptide ($^{D}F^{D}F^{D}Y$) hydrogel that could resist the dissolution in presence of endogenous peptidases and eventually inhibited the growth of cancer cells.[134] Later on, they reported the hydrogelation of another modified D-peptide (Nap-$^{D}F^{D}F^{D}K^{D}Y$(Phospho)) triggered by enzymatic dephosphorylation and utilized this hydrogel to obstruct the growth of Hela cells.[135] Yang and co-workers demonstrated a D-amino acid-based peptide, Nap-G$^{D}F^{D}F^{D}$YGRGD, was used for delivery of 10-hydroxycamptothecin (HCPT) in mouse model.[136] Another brilliant example of an

injectable hydrogel (Fmoc-FFRGDF) that was applied during the surgery of rabbit eyes (Figure 1.13), resulting in a sustained release of the anti-proliferating model drug, 5-fluorouracil to inhibit the scleral flap fibrosis.[137] Zhang *et al.* reported in their pioneering work about the encapsulation and release kinetics of various proteins (lysozyme, trypsin inhibitor, BSA, and IgG) from RADA peptide (Ac-$(RADA)_4$-$CONH_2$) hydrogel.[138]

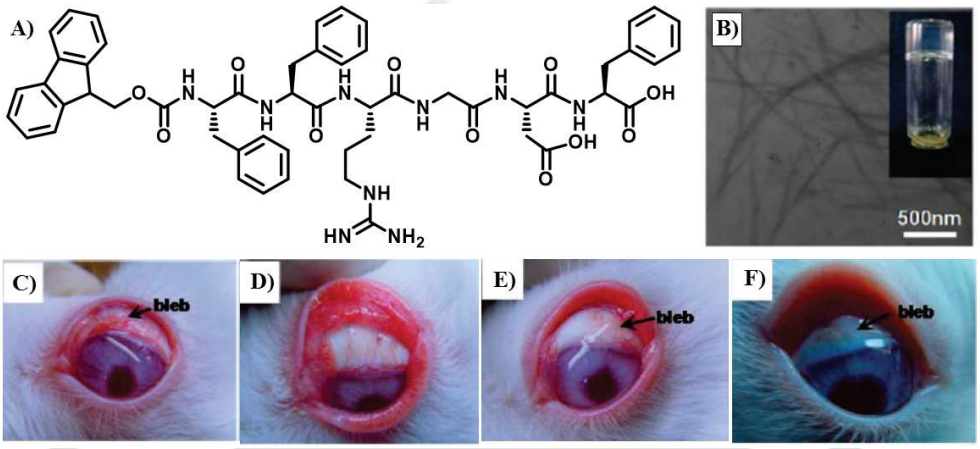

Figure 1.13 A) Molecular structure of Fmoc-FFRGDF peptide hydrogelators, B) Optical and TEM image of the peptide hydrogel. C-F) Effect of the hydrogel mediated release of 5-fluorouracil drug to inhibit the scleral flap fibrosis. Photo images of the rabbit eyes that underwent filtering surgery alone at postoperative condition (C) 7 days, (d) 28 days. (I) 28 days with exposure 5-fluorouracil, (F) 28 days with 5-fluorouracil loaded peptide hydrogel. All pictures were undertaken from reference 142.

Oppenheim and co-workers used self-assembling cationic peptide hydrogels (HLT_2) that can encapsulate plasmid DNA preventing its enzymatic degradation and fragmentation.[139] The syringe delivery of the DNA encapsulated hydrogel into mice was found to promote increased lymphoproliferation producing an enhanced immune response. Schneider et.al reported a unique strategy for time staggered sequential co-delivery of Erlotinib (ERL, an EGFR inhibitor) and DOX (loaded inside vesicles) using an injectable hydrogel. They have incorporated MAX8 peptide for the hydrogel formation with different charged/neutral liposomes as the DOX encapsulating modules. The rapid release of ERL followed by the sustained release of DOX combinedly resulted in the apoptotic extermination of cancer cells.[140]

1.4.3 Nano-Reactor and Nano-Template

For several decades, it has been a quest to imitate the different cellular uphill reactions to be carried out in the harsh external environment for better scientific assistance towards humanity. [141] A cell is the most complex nanoreactor having no match yet with other artificial lab-based analouges.[141, 142] Peptide-based assembled materials are designed to emulate various emerging functions of necessary enzymes for their close structural correspondence. Contextually, in the preliminary reports, Escuder and Miravet demonstrated that the catalytic efficiency of the peptides could be multi-fold amplified in their gel state.[143, 144] In most cases, they employed amphiphilic peptides that were comprised of Pro-Val dipeptide bridged by an alkyl chain and could catalyse the aldol and nitro-aldol reactions in aqueous as well as organic solvents. Recently, Smith *et al.* [145] synthesised lapidated glutamine amide, which can catalyse the aldol reaction between cyclohexane and 4-nitrobenzaldehyde in the solution state. The benzaldehyde-modified Schiff base derivative along with the precursor molecule resulted a dynamic hydrogel that efficiently catalysed the prebiotically relevant aldol dimerization of glycoaldehyde to produce erythrose and threose. Xu and co-workers[146] have shown that the hydrogel nanofibers combining the single amino acid derivatives of Fmoc-Lys and Fmoc-Phe can easily immobilize hemine chloride, increasing the catalytic activity for peroxidation of pyrogallol substrate in water or organic media. They further modified[147] their hydrogel nanoreactor with the appropriate distal substituents tailored towards the iron centre like natural heme proteins resulting a catalytic activity nearly 90% of the nascent activity of horseradish peroxide (HRP). In this regard, Das and team successfully utilized the short peptides based cross-β-amyloid nanotubular fibrils for two or three step cascade transformation resembling to the complex biocatalytic reaction networks.[148-150]

Self-assembled materials are very much beneficial template for nanofabrication is that the self-assembly process can be fine-tuned and consequently nano-materials of different shape and sizes can be prepared from the same material. Peptide-based materials play a superior role in this regard owing to their easily tunable functionality and morphology. [151-153] The nanostructures fabricated from peptides are gaining attention owing to their simple chemical and biological modification and easy availability for bottom-up fabrication.[8] Peptide Self-assemblies can produce various nanostructures like fiber, tubes, tapes, belts,

ribbon etc.[10] In the presence of appropriate precursors, these shapes can be used as a template to produce the nano-materials. As a nanofabrication technique, Gazit[154] exploited the self-assembly of diphenylalanine motif that is of special interest for their significant intervention during the fibrilization of the Aβ sequence. The hollow and monodispersed nanotubes were taken within a hot silver solution in presence of a reducing agent. Eventually, the reduction of the silver assisted to form a uniform nanowire inside the nanotubes which was procured after proteinase k mediated dissolution of the peptide mould. Banerjee and the group[155] showed a simplistic pathway using the hydrogel matrix of pyrene appended tryptophan for the facile synthesis of gold nanoparticles. Graphene oxide nanosheets were also composited inside the hydrogel that helped in the reduction of the gold. The triple hybrid system of nanofibers, nanosheets, and nanoparticles resulted in a better stiffness and catalytic property in the hydrogel. Our group also reported one such example in the formation of a hollow single-walled silica nanotube from a simple peptide amphiphile-based hydrogel (Figure 1.14).[156]

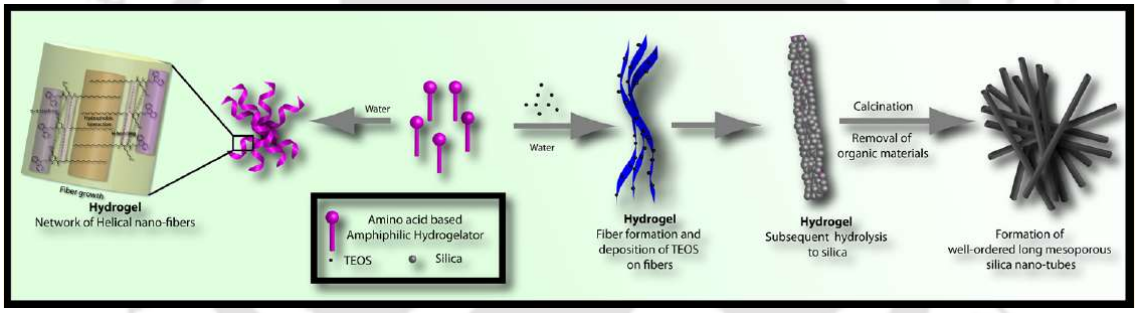

Figure 1.14 A lysine peptide based amphiphilic hydrogel utilised as an effective template for the synthesis of the single walled silica nanotubes. Adapted from reference 157.

1.4.4 Encapsulation and Protection of Bio-molecules

Proteins are essential biomolecule for life, but it has limited application due to the denaturation propensity of the tertiary structure even in the acute change in the environment (pH, temperature, salt ions, etc.). So, the storage of proteins and enzymes without compromising biological activity is a very challenging job. Various methods, including immobilization of proteins on a solid support[157], chemical modification[158], using molecular chaperons[159] or polymeric hydrogels[160], etc., have been applied for this purpose. However, the reported methods usually lack efficiency and could not provide long endurance to the proteins under antagonistic conditions.[161]

Previously, we have already discussed the unique solvent stability and the stimuli responsiveness of the PyKC gelator.[77] Based on the special features, a new strategy was undertaken where the hydrogel was used to store various enzymes with their desired activity for a long time in the exposure of heat, pH, salt, and another denaturing stimulus. A tightly entangled network can be a suitable hiding place for a biomolecule where due to limited space availability, the biomolecules cannot unwind themselves and thereby remain protected. Different reducing agents (TCEP, GSH) were used to recover the encapsulated native proteins as the hydrogel was formed by disulfide linkage of the cysteine unit. Notably, Yang, Wang, and their team reported that the treatment of alkaline phosphatase followed by Ca^{2+} mediated cross-linking on the mixture Nap-GFFY(p) peptide and sodium alginate could result in a mechanically stable hybrid hydrogel formation.[162] This double network hydrogel was used to immobilize enzymes with good preservation of their activities. In another report, Millar demonstrated a promising protein-peptide conjugate synthesised by the thiol-ene reaction between the aggregating octapeptide, VKVKVEVK and the biocatalyst pentaerythritol tetranitrate reductase (PETNR).[163] Above CGC, the hydrogel was found to happen wherein the activity and structural integrity of the PETNR was retained after exposure to high temperatures (90^0C) and long-term storage (up to 1 year). Recently, another excellent example of enzyme protection, especially for an oxygen-sensitive one, was illustrated by Abramovich.[164] They engaged the well-known Fmoc-FF hydrogel for the encapsulation of [FeFe]-hydrogenase, a potent catalyst for H_2 evolution. Generally, this class of hydrogenase enzymes irreversibly react with oxygen and lose most of their activity without proper protection. The hydrogel was substantially capable of lessening the flow O_2 inside and proficiently sheltered the sensitive enzyme under the 3D fibrous network.

1.4.5 Pollutant Removal

Water pollution is being one most severe concerns of human health in the contemporary world.[165, 166] Dyes are extensively used in many industries, including textile, leather, cosmetics, paper, printing, plastic, pharmaceuticals, foods, and others, to colour their products. Due to the limited resources of waste management, most of the wasted toxic dyes mixed with the river water slowly deteriorate water organisms' essential ecosystem. So, the separation of the toxic organic dyes is a significant issue for the coming days. Banerjee and his team have shown in many reports that peptide-based hydrogels can be utilized to

separate various organic dyes inside the hydrogel network. In one such report[167] from the same group, they have nicely exploited the self-shrinking behaviour of a peptide gelator of lapidated diphenylalanine in water. The peptide was gelled by the immediate assembly of the Phe-Phe unit, and the attached long lipid tails further lump together strongly with time leading to the obvious shrinking of the gel (Figure 1.15). Generally, this gel property of expelling the trapped water is known as 'syneresis', which helped them separate various organic dyes and toxic metal atoms.

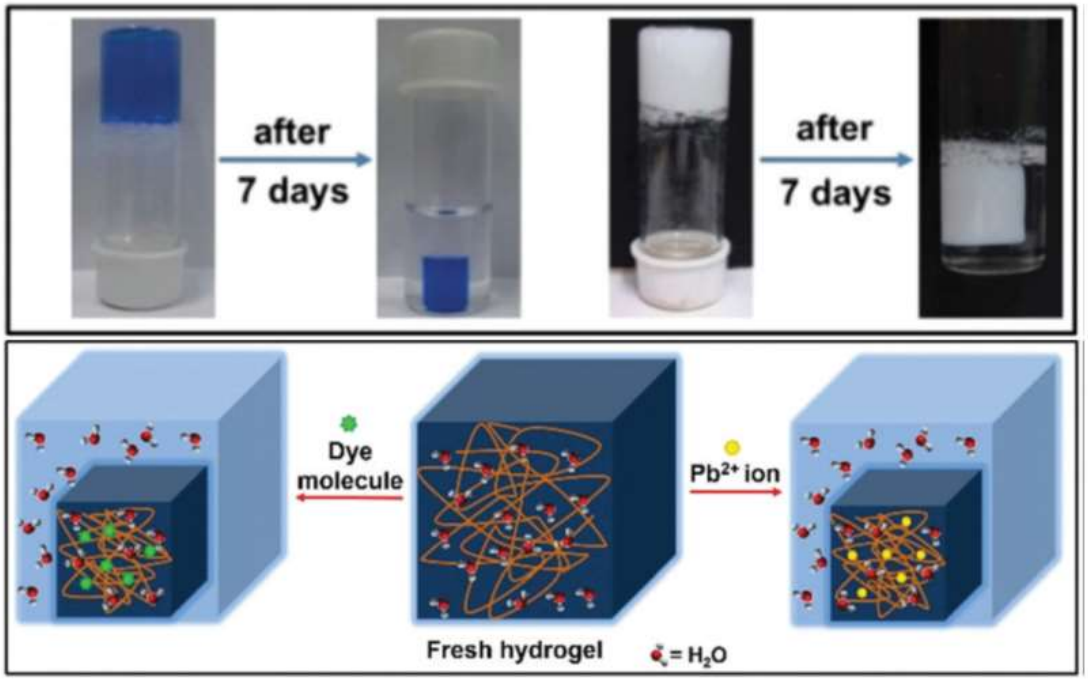

Figure 1.15 Photographs and schematic illustrations of the removal of the dye (Brilliant blue) and Pb^{2+} ions by syneresis of the peptide hydrogel. Adapted from reference 168.

1.5 The Present Thesis

Based on the previously reported information and understandings, we are motivated to design some aggregating peptides and fully explore different self-assembly processes and their utilization towards profound applications. In most cases, we have adopted the minimalistic and straightforward approach for the preparation of required materials to follow the recent trend of 'complex emergence out of the small molecular assembly'. In this way, firstly, we have focused on the uncharted chemistry of charge transfer (CT) mediated self-assembly of peptides as the CT interactions are yet mainly limited to the small organic chromophores and a few synthetic polymers. Secondly, we have continued the exploration of the cysteine-based short peptides and their assembly phenomena comprising the synergistic combination of covalent and supramolecular interactions. Altogether, all the studies have resulted in the formation of the utmost features and unique applications. In the next section, the fundamental key points of my research works are sequentially highlighted, which are elaborately discussed in the subsequent chapters of the thesis.

Chapter 2. Here, we presented the first example of the combination of cation–π and CT interactions to create a self-healing hydrogel. The organisation of the PyFFK peptide serves special orientation between the molecules, which creates the combination of the two interactions together. The angular placement of 56° between the Pyrene ring and NDI revealed with the help of DFT calculations and the combination of two different interactions well-justified NOESY experiments. With an increase in concentration, the 1:1 mixture of PyFFK and NDTA forms a self-supporting hydrogel having excellent self-healing and injectability

Chapter 3. A conceptually new strategy to exploit CT complexes toward chemo-selective products by means of seizing the dynamicity of CT complexes is reported here. Aqueous CT complexes of donor and acceptor molecules bearing reactive thiol groups were frozen instantly and cryo-desiccated to get the alternate D–A assembly intact in the solid-state. Oxidation of reactive thiols in an oxygen-rich solvent in the solid-state resulted in the formation of the heterodimer exclusively.

Chapter 4. We have presented a small peptide (AzoKC) based hydrogel, which displayed insolubility in water and buffers of different pH (1-13). The hydrogel was found to be

thixotropic in nature and exhibited efficient syneresis upon irradiation with UV light. The syneresis is stimulated through light-induced *trans-cis* isomerisation of the gelator molecule, which rearranged within the gelled state and expelled the excess unwanted water. The syneresis process was successfully utilised to remove model dyes from water efficiently.

Chapter 5. Herein**,** we have developed a composite hydrogel using the previously reported PyKC hydrogelator and the cell-targeting PyKRGD peptide. The hydrogel was found to be robust and especially responsive towards the biological antioxidant glutathione. Different spectroscopic studies revealed the hydrogel could be employed for the entrapment and protection of various proteins and enzymes released in a sustained manner in the in vitro conditions. Further, the application of the hydrogel was successfully extended to the intracellular delivery of the cargo proteins.

Chapter 2- Combining Cation-π and Charge-Transfer Interactions within a Donor-Acceptor Pair to Form Self-Healing Hydrogel

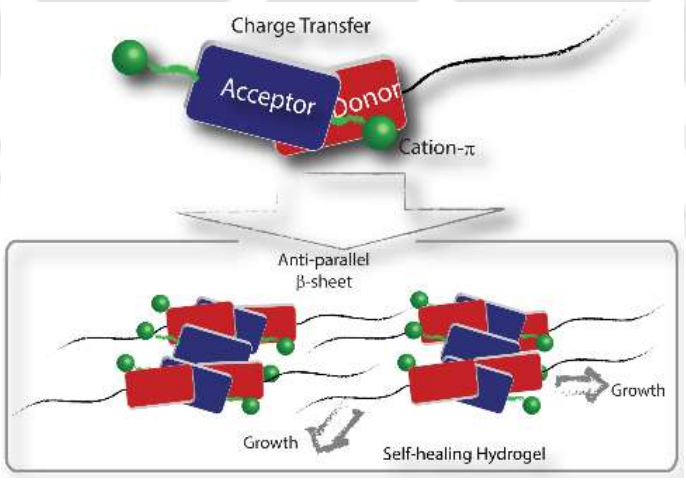

भारतीय प्रौद्योगिकी संस्थान गुवाहाटी
Indian Institute of Technology Guwahati

2.1 Introduction

Apart from the commonly used non-covalent forces like hydrogen bonding, π-π stacking, hydrophobic interactions etc., some other interactions, namely, charge transfer (CT) and cation–π interactions, have appeared as forces of immense importance toward constructing functional materials in recent years. Cation–π interactions are results of closed shell cations interacting with neutral π systems. Cation–π interaction was discovered by Kebarle in 1981[168] and first synthetic example was reported by Moetner *et al.* between organic cations NH_4^+, and $MeNH_3^+$ with C_2H_4 and benzene derivatives.[169] Since then, cation–π interaction has been utilized in several contemporary fields including chemistry, materials science and related areas.[4,170-175]

On the other hand, charge-transfer interaction between electron rich donor (D) and electron deficient acceptor (A) have gained enormous attraction over the last few decades. Alternately arranged D-A assemblies are important toward creating systems applicable to organic-electronics.[176, 177] The directional movement of their high-density charge carriers in an alternate D-A assembly results in better conductivity.[178, 179] However, CT-interaction mediated assemblies of alternate donor and acceptor molecules in solution is difficult to accomplish owing to the dynamic nature of assemblies which lead to orthogonal self-assembly of individual components. Although both these interactions are well known since long time, their combined participation within a D-A pair have never been observed. Cooperativity between π-stacking and cation-π interaction has been demonstrated through systematic quantum chemical studies by Sastry *et al.*[180] However, any experimental evidence on combination of CT and cation-π interaction remained uncharted.

In this regard, naphthalenediimide (NDI, acceptor) and pyrene (Py, donor) are one of the mostly studied D-A pairs.[181, 182] Wilson *et al.* demonstrated the strongest binding between NDI and Py amongst a pool of D-A pairs.[183] The frontier orbital symmetry plays a crucial role for the CT interaction between NDI and Py.[184] HOMO of Py and LUMO of NDI were observed to be in harmony to create a face-to-face stacking or the so called parallel sandwich packing.[33] However, Wilson *et al.* also demonstrated, by X-ray diffraction experiments, an angle of about 53° for NDI–Py packing.[185] Using density functional theory (DFT) calculation Lin and his group showed that the parallel sandwich configuration with rotation angles

larger than 50° are the relative stable structures of NDI–Py dimers.[33] X shaped face to face CT stacking between naphthalene and NDI was also reported by Zhang *et al.*[24]

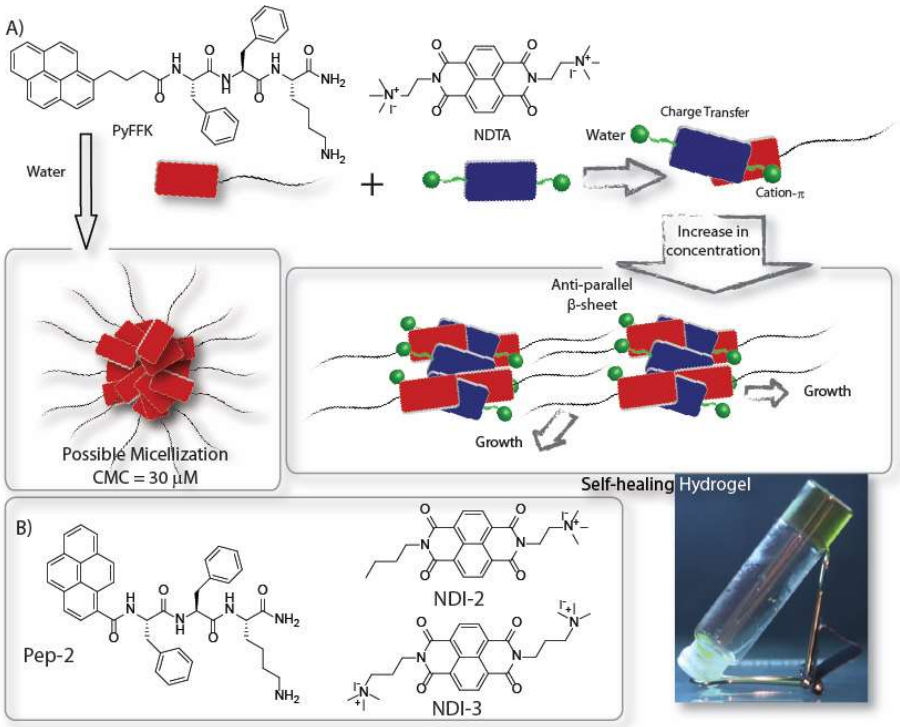

Scheme 2.1 (A) Chemical structures of compounds under investigation in this study (**PyFFK** and **NDTA**) and schematic presentation of the involvement of cation-π and CT interaction between **PyFFK** and **NDTA** and subsequent formation of a self-healing hydrogel at higher concentration. (B) Chemical structures of other supporting molecules investigated in this study.

We anticipated that with the possible slipped sandwich packing, a rational design of molecules can create assemblies involving both cation-π and CT interactions within a D-A pair. In an attempt to combine these two important supramolecular interactions, a short self-assembling peptide sequence (**PyFFK**, Scheme 2.1) bearing pyrene and a di-cationic NDI derivative (**NDTA**) were designed. The well-established D-A pair of Pyrene-NDI are used for CT interaction while FFK sequence was introduced for the anti-parallel β-sheet formation.[186] We assume that, formation of β-sheet by the FFK units may not leave any space for the cationic sites on **NDTA** to arrange themselves within the molecular packing when CT interaction is active. The only possible hypothesis was the involvement of cation-π interaction in combination with the CT interaction as shown in Scheme 2.1. Indeed, an angular slipped sandwich arrangement between pyrene and NDI units was established with the combined operation of cation-π and CT interactions. The assembly at a higher concentration also formed hydrogel with efficient self-healing property.

2.2 Results and discussion

2.2.1 Self-Assembly of PyFFK and NDTA in Water.

Having synthesized both the molecules, before validating our hypothesis, we wanted to understand the self-assembly of individual molecules in water. **PyFFK** showed two prominent absorption bands at 337 and 355 nm and a concentration dependent absorption profile of **PyFFK** showed an inflection point at ~50 μM for absorption at these wavelengths (Figure 2.1A and B). When excited at 337 nm, **PyFFK** showed three prominent emission bands at 378, 392 and 417 nm that correspond to the pyrene, group (Figure 2.1B and C). Interestingly, no excimer band could be observed in the measured concentration range (above which the viscosity enhanced and caused irreproducible data). One possibility behind the absence of excimer band could be the interaction of pyrene with amide function at the peptide end.

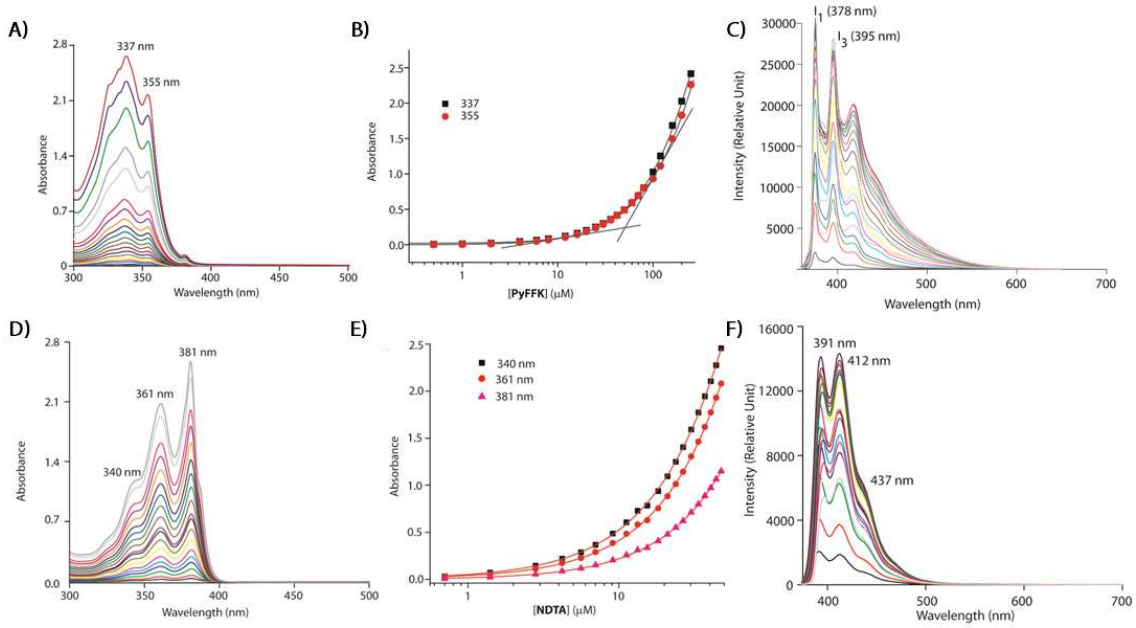

Figure 2.1 (A) UV-Visible absorption spectra of **PyFFK** with increasing concentration. (B) Plot of absorption against concentration of **PyFFK** showing CAC. (C) Emission spectra of **PyFFK** with increasing concentration, λ_{ex} = 337 nm. (ϵ = 11830 $M^{-1}cm^{-1}$), [**PyFFK**] = 0.05 -250 μM. (D) UV-Visible absorption spectra of **NDTA** with increasing concentration. (E) Plot of absorption against concentration of **NDTA** showing the critical aggregation concentration. (F) Emission spectra of **NDTA** with increasing concentration λ_{ex} = 360 nm (ϵ = 29720 $M^{-1}cm^{-1}$), [**NDTA**] = 0.05 -100 μM.

Photophysical and aggregation behavior of **NDTA** was previously reported by us and some other groups.[36, 37] It was observed that aqueous solution of **NDTA** shows an absorption band

with vibronic features at ~341, 361 and 381 nm (CAC ~ 10 μM, Figure 2.1D and E) and emission bands at 391, 412 and 437 nm when excited at 360 nm (Figure 2.1F).

However, powder XRD (PXRD) of a dried film of **PyFFK** showed a π-π stacking distance of 4.8 Å (Figure 2.2A) which is significantly higher than the typical π-π stacking distance between pyrene rings to generate an excimer band.[38, 39] The interplanar distance in the aggregated state of **NDTA** was measured to be 3.92 Å from PXRD studies (Figure 2.2A). Microscopic images of a dried sample of **PyFFK** revealed formation of sheet like morphology by the molecules in solution (Figure 2.2B).

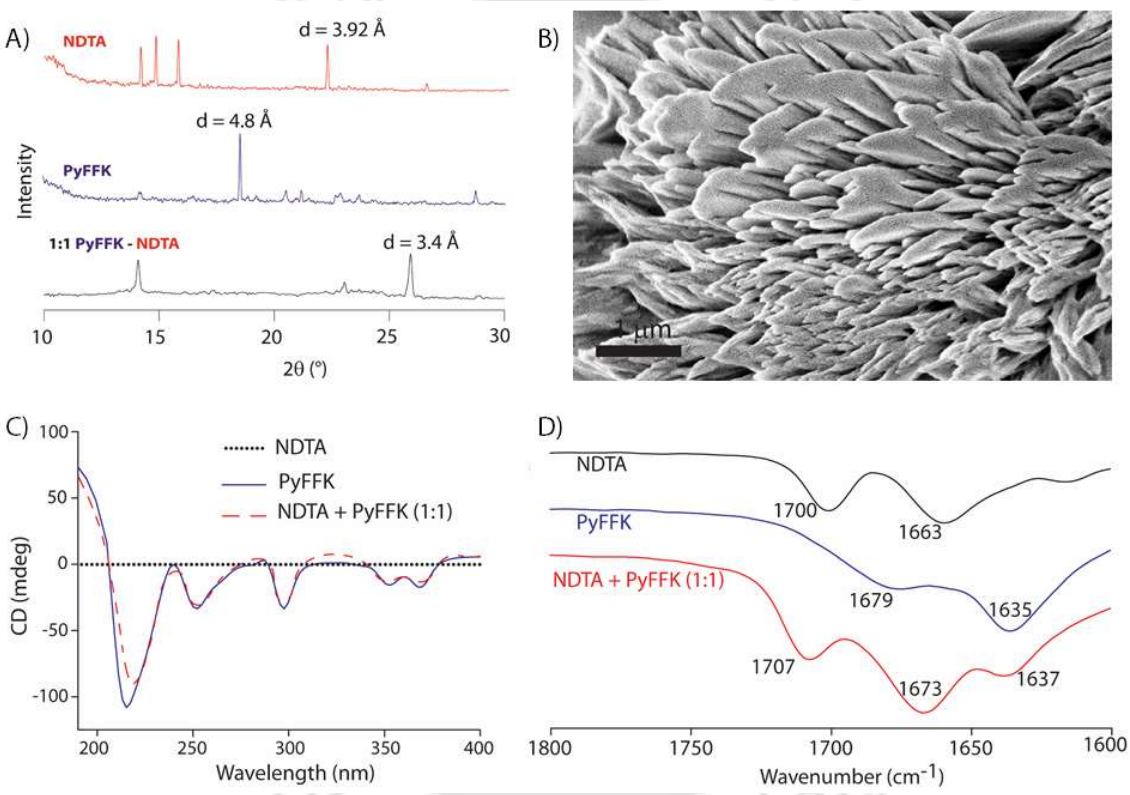

Figure 2.2 (A) PXRD data of dried samples of aqueous solutions of **PyFFK**, **NDTA**, and their 1:1 mixture measured at room temperature. (B) FESEM images taken from dried PyFFK, (C) Circular dichroism, and (D) FTIR spectra of PyFFK, NDTA, and their 1:1 mixture. For all studies, [PyFFK or NDTA] = 0.12 mM.

Though identification of any clear secondary structure formation by a small peptide is difficult, the negative band at ~ 217 nm in circular dichroism (CD) spectra revealed the possible formation of β-sheet like structure (Figure 2.2C). [40] Three negative signals (288, 338, and 355 nm) in the pyrene absorption region suggest the formation of left-handed helical aggregates.[187] Notably, the NDTA molecule is CD inactive, as can be seen from Figure 2.2C. The β-sheet like aggregation was further supported by FTIR spectra of an aqueous solution

of **PyFFK,** which displayed two peaks at 1679 and 1635 cm^{-1} (Figure 2.2D) in the carbonyl region, confirming the antiparallel nature of the β-sheet.[39, 42, 43] The self-aggregation of **PyFFK** is schematically presented in Scheme 2.1. In Figure 2.2, the results from the **PyFFK** and **NDTA** (1:1) mixtures are elaborately discussed in the succeeding sections.

2.2.2 Charge Transfer Interaction.

Before evaluating the binding pattern, we wanted to find the binding affinity and stoichiometry between **PyFFK** and **NDTA**. ITC experiment was employed for that purpose. As can be seen from Figure 2.3A, the molecules bind in equimolar ratio with binding constant of $K = (2.81 \pm 2.40) \times 10^5\ M^{-1}$.

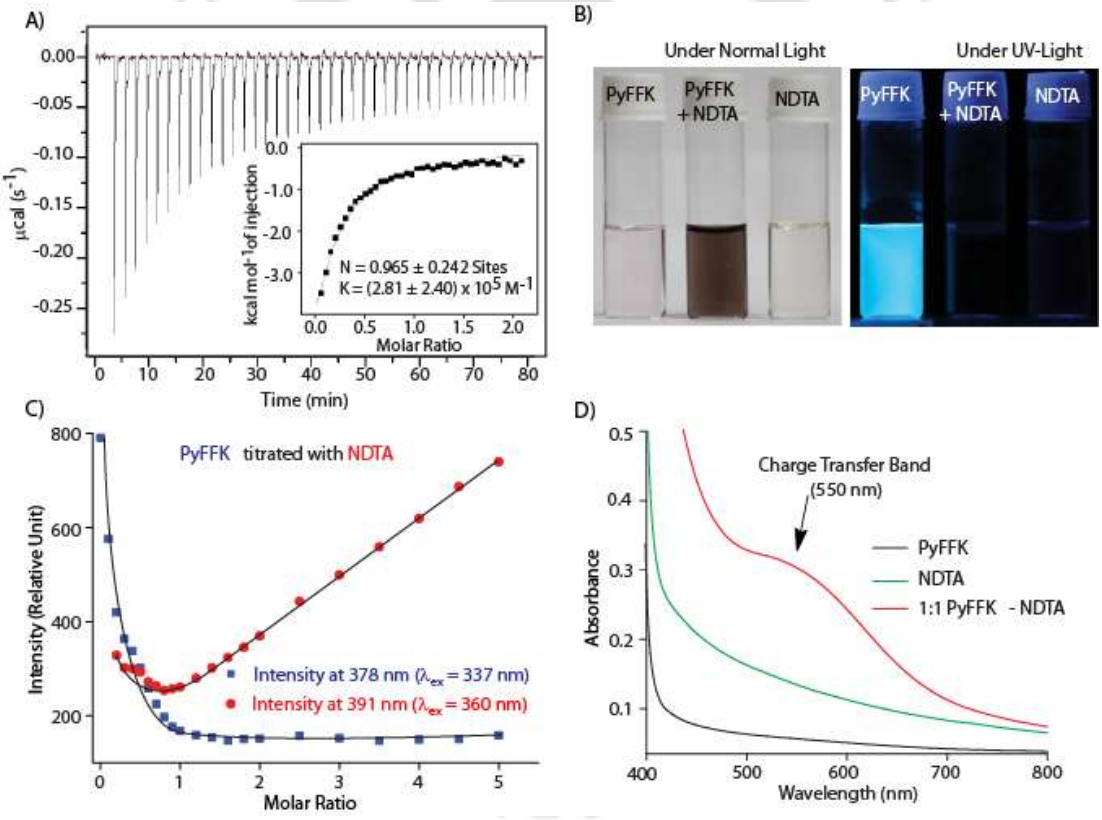

Figure 2.3 (A) Binding isotherm and thermogram (inset) as obtained from ITC measurement showing 1:1 binding between **PyFFK** (0.1 mM) and **NDTA** (1 mM). (B) Photographs of solutions of **PyFFK** and **NDTA** and their 1:1 mixture in water under normal and UV light. (C) Changes in emission intensities of **PyFFK** and **NDTA** with molar ratio during titration of a 1 μM solution of **PyFFK** by **NDTA** (1mM). λ_{ex} = 337 nm. (D) UV-Visible spectra of **PyFFK**, **NDTA**, and a 1:1 mixture of **PyFFK** and **NDTA** showing the appearance of a CT band at 550 nm in case of the mixture. These studies were performed at 2 mM concentrations of individual molecules.

The calculated thermodynamic parameters suggest a thermodynamically favorable complexation between **PyFFK** and **NDTA** (ΔG = -25.36 kJ mol^{-1}, ΔH = -15.45 $kJmol^{-1}$ and ΔS = 0.033 $kJmol^{-1}K^{-1}$). The results obtained from ITC experiments indicate a possible enthalpy

driven binding process. Moreover, the binding constant is ~ two orders of magnitude higher than the usually found values for similar NDI and pyrene pairs in aqueous medium.[26,188] An equimolar mixture of **PyFFK** and **NDTA** in water produced a clear brown colored solution (Figure 2.3B). The generation of the brown color from colorless **PyFFK** and yellowish **NDTA** solutions indicated a possible binding between them.

One of the most prominent feature of CT interaction is the appearance of a broad and weak CT band at a higher wavelength compared to the absorption maxima for the donor and acceptor. The CT band in the absorption spectra of a D-A dyad is associated with an optical transition from the ground state to the CT excited state.[189] In the present case, the CT band was observed for a 1:1 mixture at 550 nm (Figure 2.3D). All these experimental evidence confirm the formation of a 1:1 CT complex between **PyFFK** and **NDTA** in water. Notably, the higher binding constant as obtained from ITC suggests that in addition to the CT interaction, some additional stabilizing force is also in operation. Titration of **PyFFK** with **NDTA** resulted in continuous decrease in the emission intensity for **PyFFK** (378 nm) up to 1 equivalent of **NDTA** and remained constant thereafter (Figure 2.3C). Importantly, the emission peak related to NDI group (391 nm) started appearing only after this ratio suggesting a 1:1 binding between these two components. Though all these results indicate a 1:1 binding between **PyFFK** and **NDTA** as well as CT interaction, none of them are conclusive for CT interaction.

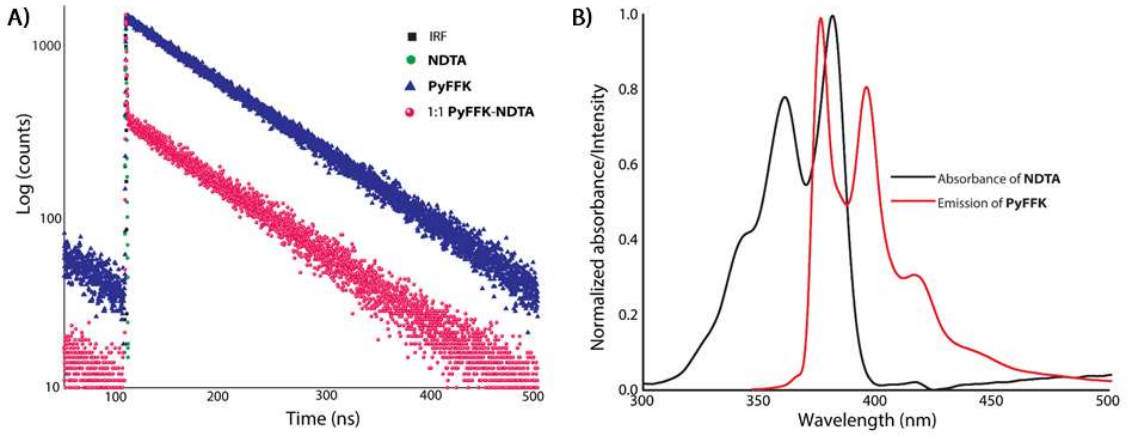

Figure 2.4 (A) Life time measurements for **NDTA**, **PyFFK** and 1:1 **PyFFK-NDTA** mixtures measured at room temperature. λ_{ex} = 336 nm; λ_{em} = 378 nm. ϵ for **PyFFK** and **NDTA** at 336 nm are 11830 $M^{-1}cm^{-1}$ and 12310 $M^{-1}cm^{-1}$ respectively. (B) Normalized absorption spectrum of **NDTA** and emission spectrum of **PyFFK** showing the overlapping region for possible FRET (Förster resonance energy transfer).

Indeed, the quantum yield of 0.18 (for **PyFFK**) dropped to 0.07 in presence of equimolar **NDTA**. The fluorescence life time also decrease from 102.16 ns for **PyFFK** to 88.23 ns for the 1:1 mixture (Figure 2.4A). As the absorption spectra of **NDTA** overlaps with the emission spectra of **PyFFK** (Figure 2.4B), the decrease in lifetime can be a result of possible FRET between the D-A pair.

Next, the CD, FTIR and PXRD analyses of the 1:1 mixture of **PyFFK** and **NDTA** were recorded to get further insight into the packing. PXRD data showed a distance of 3.4 Å between two π-planes in the self-assembly (Figure 2.2A). Notably, this interplaner distance is significantly lower than that observed in case of **PyFFK** suggesting a possible π-π (or in this case, a CT) interaction between pyrene and NDI groups. CD spectra (Figure 2.2C) was very similar to that of **PyFFK** suggesting that the presence of **NDTA** could not impart any effect on the secondary structure of the peptide. The FTIR spectra also supports the same as peaks corresponding to the antiparallel β-sheet (1637 and 1673 cm^{-1}) were present along with other peaks arising from the imides of **NDTA** (Figure 2.2D).[35, 39, 41] It is to be noted that the signal at 1673 cm^{-1} is an overlap of the imide peak from **NDTA** and the signal from the β-sheet formed by **PyFFK**. As a result, the signal become intense and broad as well.

2.2.3 Cation-π Interaction between PyFFK and NDTA.

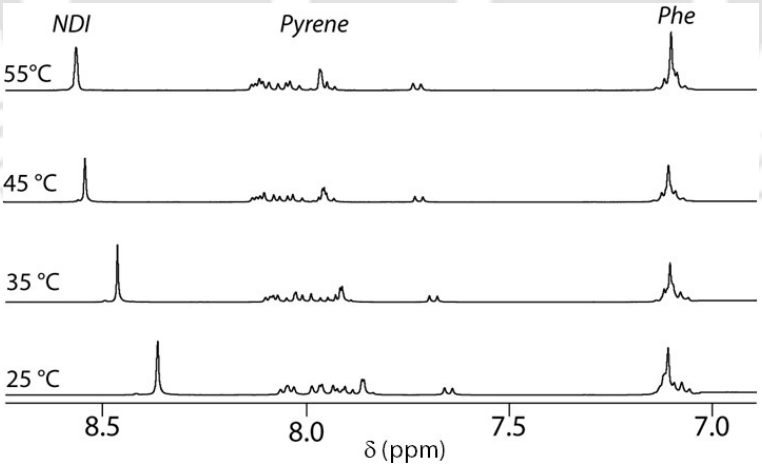

Figure 2.5 ^{1}H NMR spectra of a 12.15 mM 1:1 solution of **PyFFK**-**NDTA** in 1:1 DMSO-d_6 – D_2O at different temperatures.

To gain structural information and test our hypothesis of involvement of CT and cation-π interactions, we used ^{1}H NMR spectroscopy and NOESY experiment. Before that, a temperature dependent study of the 1:1 mixture of **PyFFK-NDTA** (12.15 mM) showed a

down-field shift of the pyrene and **NDTA** protons with increase in temperature but no movement of the Phe protons was observed (Figure 2.5). Comparison of ^{1}H NMR spectra of **NDTA**, **PyFFK** and 1:1 mixture of the components is shown in Figure 2.6A. It can be seen that, all the proton signals from NDI and pyrene units were up-field shifted in the 1:1 mixture while no movement was recorded for the Phe protons from the peptide. The unchanged signals from Phe units along with CD and FTIR results confirm that the presence of **NDTA** does not affect the orientation of the peptide sequence.

A clear picture of the molecular arrangement could be obtained from a NOESY spectra of 1:1 mixture where the spatial interaction of a particular proton within up to 5 Å can be detected. For a better understanding of the NOESY spectra, we concentrated on the interactions of the pyrene protons (p1-p9, Figure 2.6B) with all the protons of NDI (n1-n4). Figure 2.7C shows the interaction of aliphatic protons of **NDTA** with pyrene protons. Cross peaks between n2→p1-6, n3→p1-4 and n4→p1-4 were observed. Interestingly, no cross peak obtained between any of these **NDTA** protons (n2-4) and p7-9 which indicates that these protons situated further from each other. Importantly, the methyl protons of the quaternary ammonium segment of **NDTA** are situated in close proximity to a portion of the pyrene ring (n4→p1-4). Figure 2.7D shows the interaction between aromatic protons of both components. Cross peaks were observed between n1→p5-9 with very weak to no interaction between n1→p4. Most importantly, no signal could be found between n1 and p1 which confirms the fact that this region of pyrene ring is far from the NDI core. The intensities of the cross-peaks are extremely important as the signals are generated from spatial interactions of the protons, the closer they are more intense will be the cross-peaks. In the present case, the intensity of the cross-peaks between n1 and pyrene protons follow the order, p9-7 > p6-7 > p4 (extremely low). The difference in intensities of cross-peaks n1→p4 > n1→ p4 > n1→ p3 (no cross-peak) clearly indicate non-identical interactions of p4 and p3 with n1. Such a situation could arise only when the π-planes arrange themselves in an angular position. Combining these results, the picture of the spatial arrangement could be visualized as drawn in Figure 2.7B. A partial overlapping of the π-systems as well as an angular position between the π-plane axes is confirmed. A strong interaction between n4 → p1-2 can only be generated when the ammonium cation is close to the π-plane of pyrene and execute a cation-π interaction.

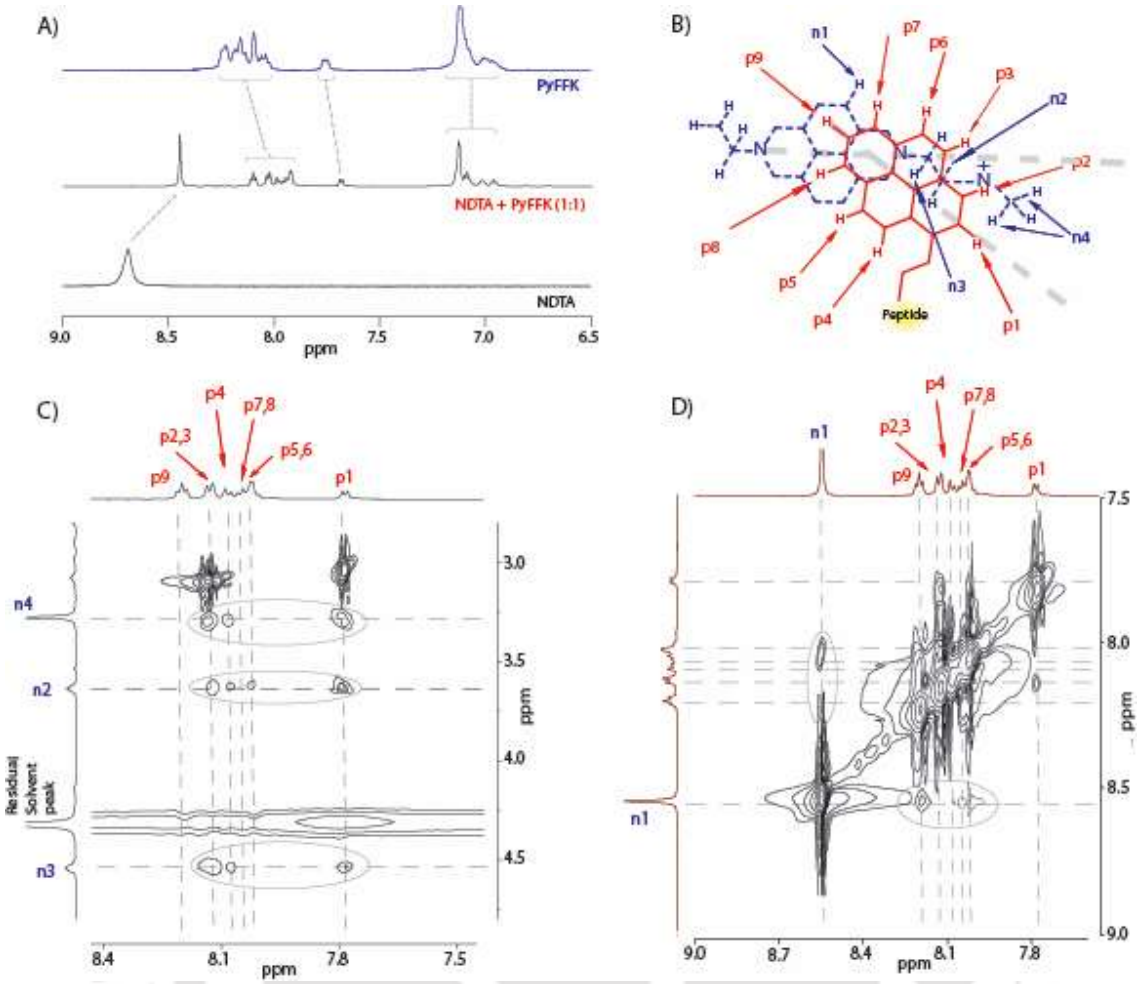

Figure 2.6 (A) ^{1}H NMR spectra of **PyFFK**, **NDTA**, and their 1:1 mixture displaying the up-field shifts of aromatic protons due to CT complexation. (B) Proposed packing arrangement of pyrene and NDI in the 1:1 complex of **PyFFK** and **NDTA**. The proton numbers mentioned should be used to read (C) and (D). (C) And (D) partial NOESY NMR of a 1:1 mixture of **PyFFK** and **NDTA** showing the cross-peaks to identify the interaction of different protons of the individual molecules. For all studies, [**PyFFK** or **NDTA**] = 12.15 mM.

As single crystals could not be developed after several attempts, to validate the observed results, we relied on DFT calculation. The geometries of individual components (**PyFFK** and **NDTA**) were first calculated at the DFT/B3LYP level with a 6-31G (d,p) basis set. The optimized structures of individual molecules were subsequently used to get the complex between **PyFFK** and **NDTA**. The energy optimized complex (Figure. 2.7A) showed a partial stacking between the π-planes of Py and NDI. The HOMO on **PyFFK** and LUMO on **NDTA** are in harmony with an angular slipped sandwich configuration as can be seen from Figure 2.7B. Interestingly, the angle (56.07 °) between the π-planes were found to be very similar to that observed by Wilson[34] and calculated by Lin.[33] The calculated arrangement closely fits with the observation from NOESY experiment. Notably, the smallest interplaner distance

between pyrene and NDI was calculated as 3.46 Å which is in very good agreement with the PXRD data of 3.4 Å. Moreover, the closest distance obtained between the ammonium nitrogen and the π-ring of pyrene was 3.54 Å. An ammonium cation and a π-ring situating at this proximity is an ideal situation for a cation-π interaction.

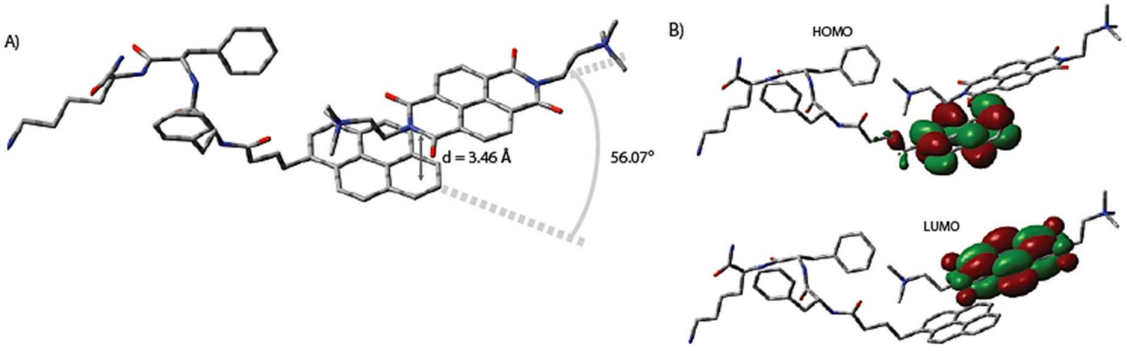

Figure 2.7 (A) Optimized structure of **PyFFK**-**NDTA** complex. (B) HOMO and LUMO of the optimized structure as shown in (A).

As pointed out before, the binding constant obtained from the ITC measurement (Figure 3A) is considerably higher than the usually obtained values for both CT complexes as well as cation-π complexes in water (both fall in the range of 10^3 M^{-1}).[8,17,26] This higher binding constant can be rationalized if both these interactions are present in the system. The overall binding process can be summarized as, A) the extreme end of the pyrene ring of **PyFFK** is stacked with the π-system of NDI core of **NDTA** via CT interaction and, B) the portion of pyrene connected to the peptide sequence is interacting with **NDTA** through cation-π interaction. Both these interactions are complementing each other to form a stable 1:1 complex. The situation is described pictorially in Scheme 2.1.

2.2.4 Hydrogelation of the 1:1 Complex.

Peptides containing conjugated aromatic groups are well known to form hydrogels and several CT induced hydrogelation is also reported in literature.[27,41, 190-193] We observed that at relatively higher concentration, the viscosity of the solutions increased which was an indication of possible hydrogel formation. In case of **PyFFK**, though the viscosity increased with concentration, it remained in solution state even up to its maximum solubility in water. Interestingly, the equimolar mixture of the components, formed a self-supporting hydrogel at individual concentrations of 12.15 mM (1 wt% of **PyFFK** and 0.84 wt% for **NDTA**, Scheme 2.1). As controls, equimolar combinations of **Pep-2** – **NDTA**, **PyFFK – NDI-2**, and **PyFFK** –

NDI-3 (Scheme 2.1) were tested but none of these pairs resulted in hydrogel even at their highest soluble concentrations. Interestingly, in all three cases, though CT interactions were observed from the absorption spectroscopy, no clear evidence for cation-π interactions were found. The absence of cation-π interaction in these systems can be attributed to the differences in spacers (between Pyrene and FFK or NDI and NMe_3^+ groups) in cases of **Pep-2** – **NDTA** and **PyFFK** – **NDI-3** combinations. In case of **PyFFK** – **NDI-2**, the non-availability of the second quaternary ammonium group probably did not allow the molecules to arrange themselves in a way to facilitate the cation-π interaction. Nevertheless, the inability to from hydrogel by these composition explains the importance of the combination of CT and cation-π in the **PyFFK** – **NDTA** system to form higher order assembly. Notably, this is the first example of a hydrogel formation assisted by a combination of CT and cation-π interaction.

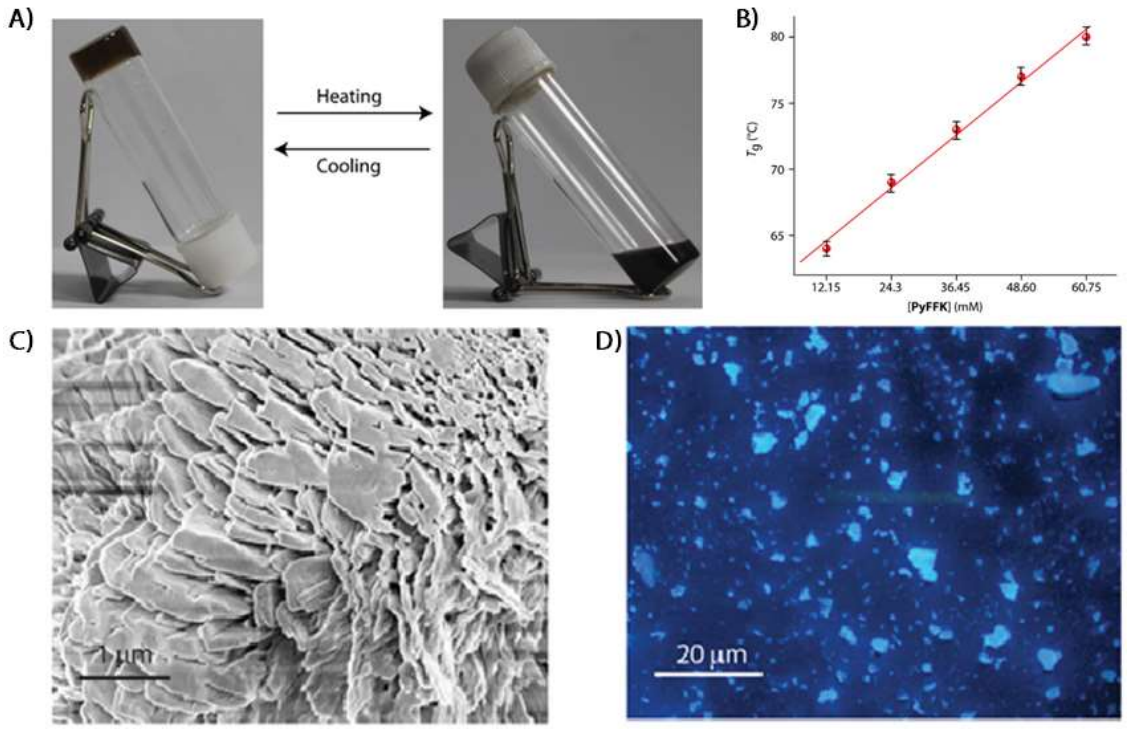

Figure 2.8 (A) Pictures of a hydrogel and its sol state prepared from 1:1 **PyFFK**-**NDTA** showing thermo-reversibility. (B) Dependence of T_g with concentration of **PyFFK**. (C) FESEM, and (D) fluorescence microscopic an aqueous 1:1 mixture of **PyFFK** and **NDTA**. All experiments were carried out at room temperature. [**PyFFK** or **NDTA**] = 12.15 mM.

Since, MGC of the hydrogel was obtained as 12.15 mM for individual components, unless otherwise mentioned, all the experiments were carried out at this concentration. The hydrogel showed thermo-reversibility and that is confirmed by repeating the gel-sol-gel

cycle several times. The gel to sol transition temperature (T_g) for a 12.5 mM hydrogel was measured as ~ 64 °C. The T_g was found to be linearly dependent on the concentration and is in good agreement with previous reports (Figure 2.8A and B).[194] Furthermore, the hydrogel was found to be stable over a long period of time (more than 6 months) under ambient temperature. Morphology of the hydrogel was analysed using FESEM and fluorescence microscopic techniques and sheet like structures similar to **PyFFK** were observed (Figure 2.8C and D). The observed sheets were more than 2 μm long in two dimensions while the width of them were < 100 nm. As shown in Scheme 2.1, the complex between **PyFFK** and **NDTA** can elongate in two directions and thus can form large sheet like structures and entrapment of water molecules within these sheets results in formation of hydrogel.

2.2.5 Self-Healing and Injectability of the Hydrogel.

The mechanical property of a hydrogel is one of the most important parameters which determines its applicability. For that purpose, rheology of the hydrogel was tested. From the strain sweep experiment of the gel it was observed that the gel can retain its viscoelastic property up to 10% strain under the fixed angular frequency of 1 rad s^{-1} at 25 °C (Fig. 2.9A). The storage modulus, G′ is greater than the loss modulus, G″, *i.e.* G′>G″, within the applied range of 0.07-10 % strain for this particular gel and beyond that, the gel turns into sol, i.e. G″>G′. However, the gel is found to be frequency independent over the applied region 0.1-1000 rad s^{-1} confirmed from frequency sweep experiment, where both the G′ and G″ values are higher as well as the gap between these two parameters are quite high over the full region (Figure 2.9B). Moreover, the steadiness of the G′ value and all these results suggesting that the gel is stable and strong in nature.

The strain–dependent measurement showed that the material exhibits a yield strain and transforms to a quasi-liquid, which reveals the beginning of deformation of the hydrogel, an essential behavior for the injectable gels. However, it is also important to verify the recovery of the gel state from the quasi-liquid state upon removal of the mechanical strength. A time dependent strain sweep was performed by alternating the applied strains at a fixed angular frequency of 1 rad s^{-1}.

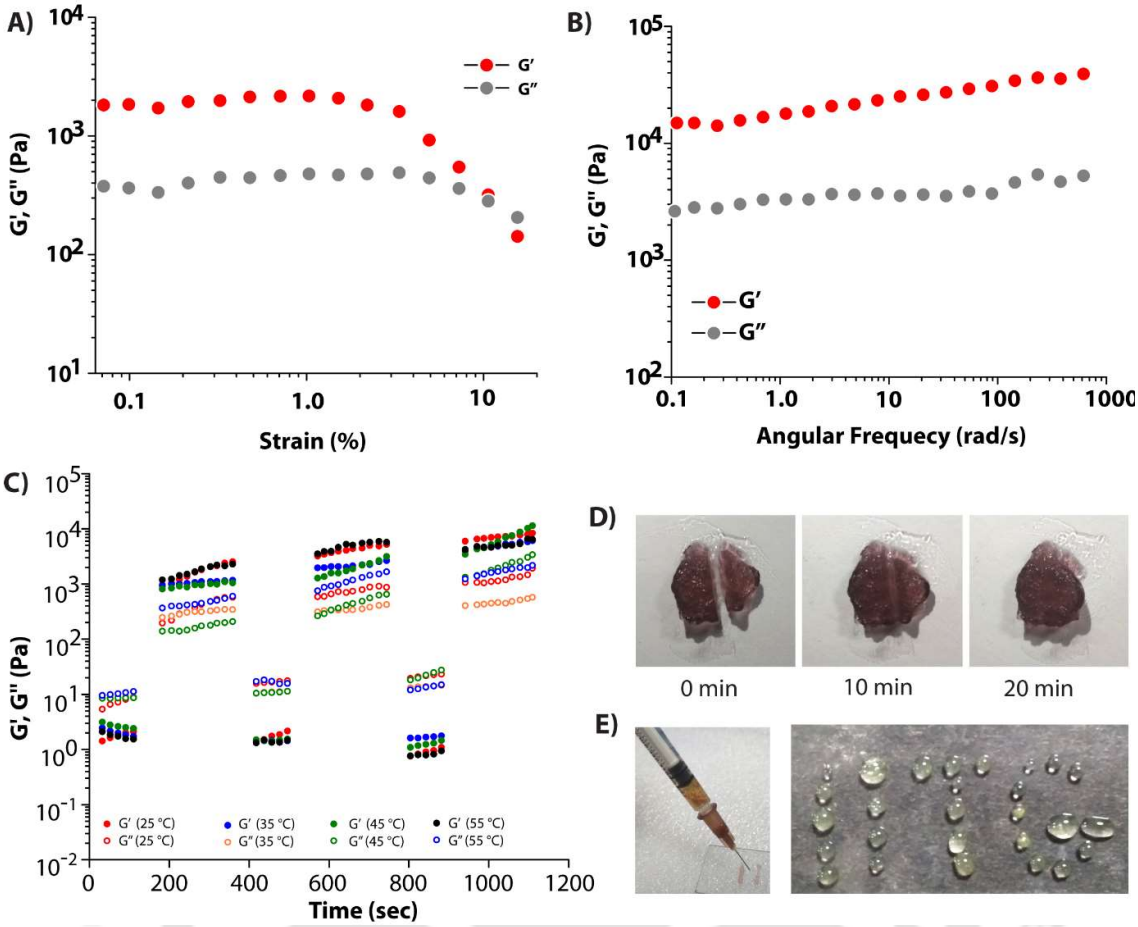

Figure 2.9 (A-B) Changes in storage and loss modulus as a function of (A) shear strain (amplitude sweep at frequency of 1 rad s^{-1}) and (B) frequency (at 0.1% constant strain). (C) The damage-healing property of hydrogel demonstrated by the continuous step strain measurements at different temperature. (D) Macroscopic self-healing property of the hydrogel at 0-20 min. (E) Injectibility: photographs of the syringe containing the hydrogel and drops of liquids which turned into hydrogel immediately after coming out of the needle. All experiments were carried out with 12.15 mM **PyFFK-NDTA** hydrogel.

The strain–dependent measurement showed that the material exhibits a yield strain and transforms to a quasi-liquid, which reveals the beginning of deformation of the hydrogel, an essential behavior for the injectable gels. However, it is also important to verify the recovery of the gel state from the quasi-liquid state upon removal of the mechanical strength. A time dependent strain sweep was performed by alternating the applied strains at a fixed angular frequency of 1 rad s^{-1}. At higher strain (γ = 100%), the gel loses its viscoelastic property and interestingly, in every successive step, it regains its initial viscoelastic nature almost completely while coming back to a lower strain (γ = 0.1%, Figure 2.9C). Such recovery of the mechanical properties for a gel is termed as self-healing or thixotropic behavior. In the present case, when a strain (γ= 100 %) much higher than the yield strain (γ = 10%) is applied, the sol state appears (G″>G′); however, when a strain (γ =

0.1 %) much lower than the yield strain is applied on that deformed gel it goes back to its initial gel state (G'>G", G' ~ 10^3 Pa). This alternate change of strains was repeated four times and the gel has shown excellent recovery each time demonstrating that the hydrogel possesses a rapid self-healing property. Moreover, the same experiment was performed at different temperature and similar thixotropic behavior was observed even at 55 °C demonstrating that the hydrogel retains its self-healing property at elevated temperature as well. Measurements above this temperature could not be performed considering the measured T_g of 64 °C for 12.15 mM hydrogel.

Both, self-healing and injectability of the hydrogel were physically tested as can be seen from Figure 2.9D and E. A piece of the hydrogel was cut into two pieces and kept side-by-side which healed completely within 20 min (Figure 2.9D). Figure 2.9E shows that up on pressing the plunger of a syringe containing the hydrogel, the gel melts into liquid and comes out of the needle which immediately returns back to the gel state as the pressure is released.

2.3 Conclusion

In summary, we have presented an electron donor-acceptor pair which bind to each other using a combination of cation-π and CT interactions. Pyrene of **PyFFK** and the NDI unit of **NDTA** form a 1:1 complex where parts of the π-rings are stacked together through CT interaction while the cationic section of **NDTA** interacts with the other half of pyrene π-system through cation-π interaction. In this process, organization of the peptide sequence of **PyFFK** creates a spatial arrangement between the molecules which favors this combination of interactions to act together. The π-planes of pyrene and NDI are positioned in an angular sandwich arrangement at an angle of 56°. With increase in concentration, the 1:1 mixture of **PyFFK** and **NDTA** formed a self-supporting hydrogel. Increase in concentration lead to the growth of the aggregates in two dimensions and results in larger sheets where water molecules are trapped between these sheets to form the hydrogel. The hydrogel showed excellent self-healing and injectability and holds promise for future applications. Broadly, the work reports the first example of the combination of cation- and CT interactions in action together to create a self-healing hydrogel. These results open up the possibility to utilize these non-covalent interactions together within appropriately

engineered molecules to create new-generation soft materials with desired mechanical properties.

2.4 Experimental section

2.4.1 General Information and materials

Rink amide MBHA resin and protected amino acids and coupling reagents were purchased from Novabiochem. All other chemicals and reagents were obtained from Sigma-Aldrich (USA). HPLC-grade DMF, DCM, and ACN were procured from Spectrochem (India) and Fisher Scientific (India), respectively. To prepare samples, Milli-Q water with a conductivity of less than 2 $mScm^{-1}$ was used. Chromatographic purifications were performed on a Luna 5 µm (C18) column (Phenomenex) using a Dionex Ultimate 3000 HPLC. UV-Visible spectra were recorded on a PerkinElmer Lambda 750 spectrometer, while fluorescence measurements were performed on a Cary Eclipse (Agilent) spectrophotometer. Standard 10 mm-path quartz cuvettes were used for all spectroscopic measurements. ^{1}H NMR and ^{13}C NMR were recorded with a Bruker Ascend 400 MHz (Bruker, Coventry, UK) spectrometer and referenced to deuterated solvents. ESI-MS were performed with a Q-tof-Micro Quadrupole mass spectrophotometer (Micromass). Lifetime measurements were done using Edinburgh FSP920 spectrophotometer (pulse width of < 570 ps).

2.4.2 ITC Experiment

The binding constant, stoichiometry and thermodynamic parameters of **PyFFK** with **NDTA** were determined by isothermal titration calorimetry using a Nano-ITC instrument from MicroCal. For the experiment, the temperature was fixed at 298 K. All solutions were prepared in milliQ water and degassed prior to titration. A 0.1 mM **PyFFK** solution was titrated with 1 mM solution of **NDTA**. Heats of dilution were checked by titration of **PyFFK** into a water solution and subtracted from the normalized enthalpies. The first data point was removed from the data set for curve fitting. The data were fitted to a theoretical titration curve by one set of sites binding model using a software supplied by Microcal.

2.4.3 NMR Studies

As the pyrene protons did not appear in D_2O, the NMR studies were performed in 1:1 DMSO-d_6 – D_2O mixture. In this solvent composition, the UV-Visible spectra showed the presence of CT-band and ESI-MS also confirmed the presence of 1:1 complex of **PyFFK** and **NDTA**. All studies were performed at 12.15 mM (MGC) concentrations of individual molecules. The peaks corresponding to the Pyrene unit of **PyFFK** and NDI unit of **NDTA** were identified using COSY and TOCSY NMR of the 1:1 mixture of these two compounds. All 2D NMR studies were performed on a 600 MHz (Bruker, Coventry, UK) spectrometer and the raw data were processed with the supplied software.

2.4.4 UV–Visible and Fluorescence Spectroscopic Studies

Concentrated stock solutions (5 mM) of **PyFFK** and **NDTA** were prepared in 10 mL volumetric flasks by weighing appropriate amounts of the compounds and dissolving in water. These stock solutions were diluted to the concentrations required for the experiment.

2.4.5 CD Spectroscopy

The CD spectra of all the samples were recorded on a J-1500 (JASCO, U.S.A.) instrument at room temperature. The data were collected at 1 nm intervals with 2 nm band width. All measurements were done in 0.2 cm path length cuvette with 400 µL sample volume. Each CD profile is an average of 3 scans of the same sample collected at a scan rate 100 nm min^{-1}, with a proper baseline correction from the respective solvents. Scans were performed over 190 to 650 nm. All studies were performed at 0.125 mM concentrations of individual molecules.

2.4.6 FTIR Spectroscopy

Aqueous solutions of the samples were placed between two CaF_2 windows and the FTIR spectra were recorded at room temperature on a Nicolet IS10 spectrometer. The baseline was subtracted from the obtained absorbance intensity in each case. All studies were performed at 0.125 mM concentrations of individual molecules.

2.4.7 Quantum Yield Measurement

The fluorescence quantum yields of **PyFFK** and 1:1 mixture of **PyFFK-NDTA** were determined by Parker-Rees method using quinine sulphate as a standard fluorophore. The Parker-Rees equation is written as follows,

$$\phi_u = (A_s F_u n_u^2 / A_u F_s n_s^2)\phi_s \qquad (1)$$

where, ϕ_s = Quantum Yield of standard fluorophore = 0.54 in 0.1(M) H_2SO_4, ϕ_u = Quantum Yield of unknown fluorophore, A_s = the absorbance of standard fluorophore at the excitation wavelength, A_u = the absorbance of unknown fluorophore at the excitation wavelength, F_s = the area of integrated fluorescence intensity of the reference sample when excited at the same excitation wavelength, F_u = the total area of integrated fluorescence intensity for the unknown sample when excited at the same excitation wavelength, The refractive indices of the solvents for the unknown and the standard samples are denoted by n_u and n_s respectively. To minimize the reabsorption of the fluorescence light passing through the samples their absorption maximum was kept below 0.1. For **PyFFK**, the absorbance was monitored at 337 nm (ϵ = 11830 $M^{-1}cm^{-1}$) and for **NDTA**, the absorbance was monitored at 360 nm (ϵ = 29720 $M^{-1}cm^{-1}$).

2.4.8 Preparation of Hydrogel

In a typical experiment, 10 mg of **PyFFK** and 8.4 mg of **NDTA** were taken in 1 mL of water in a glass vial. The mixture was vortexed followed by sonication for 30 seconds to dissolve the solid completely. The vial was allowed to stand at room temperature without any disturbance. After 12h, a transparent gel was obtained that did not flow downward upon inversion of the glass vial.

2.4.9 Determination of Sol–Gel Transition Temperature (T_g)

T_g was determined using standard ball dropping method. A small steel ball was placed on top of the hydrogel sample (equal volume). The samples were placed in a water bath and the bath was heated at a rate of 0.5 °Cmin^{-1}. The temperature at which the steel ball drops to the bottom was noted as T_g. The experiments were performed in triplicate.

2.4.10 PXRD Analyses

For XRD measurements, a few drops of the solutions/gel were placed on silicon surfaces, and the solvents were evaporated at room temperature. These samples were used for XRD measurements on a Bruker D2 Phaser X-ray diffractometer (30 kV, 10 mA). The Bragg peak λ was extracted from the XRD data and the layer thickness *d* could be obtained according to the Bragg equation $d = \lambda/2\sin\theta$, λ = 0.15405 nm. All studies were performed at 12.5 mM concentrations of individual molecules.

2.4.11 FESEM and AFM

The FESEM samples were prepared by casting 10 µL of **PyFFK** solution and 1:1 mixture of **PyFFK**-**NDTA** (incubated for at least 24 h) on a silicon wafer and air dried for at least 1 day. FESEM images were taken on a Gemini SEM 300 (Sigma Zeiss) instrument. Atomic Force Microscope images were taken on Nanosurf Flex-Axiom (Nanosurf, Switzerland). All studies were performed at 12.5 mM concentrations of individual molecules.

2.4.12 FETEM

5 µL of **PyFFK** solution and 1:1 mixture of **PyFFK**-**NDTA** (incubated for at least 24 h) were cast on carbon coated copper grid (300 mesh Cu grid with thick carbon film from Pacific Grid Tech, USA) and allowed to air dry for 2 minutes and then the excess sample was bloated with a tissue paper. The grid was then air dried for 1 day. The samples with desired solvent were prepared and incubated for at least 2 days before casting on the grid. FETEM images were taken in JEOL 2100F microscopes. All studies were performed at 12.5 mM concentrations of individual molecules.

2.4.13 Rheology

The viscoelastic properties of the hydrogel were characterized using rheometer (Anton-Paar MCR 102) equipped with a 20mm parallel plate measuring system at 25 °C. A strain sweep test was performed first to identify the LVR over a range from 0.1 to 100 % strain at a fixed oscillatory frequency of 1 rad s^{-1}. The LVR can be defined as where strain has no impact upon G′ and G″. Further, the mechanical strength of the gel was determined from oscillatory test i.e. frequency sweep, which was carried out under an appropriate strain (γ = 0.1 %) selected from the LVR with the frequency ranging from 0.1 to 100 rad s^{-1} at 25 °C. To investigate the

thixotropic and self-healing property of the gel (2 wt %), a cyclic dynamic strain sweep experiment was carried out at a constant angular frequency of 1 rad s^{-1}. In this experiment, a higher strain (γ = 50 %) and a lower strain (γ = 0.1 %) were applied on the gel alternatively over a period of 3136 seconds and four successive cycles.

2.4.14 DFT Calculations

The M06 family of functions were chosen over other conventional DFT functions as they are proven to be more accurate toward geometries and energy calculations for a variety of dispersion dominated systems like DNA base pair stacks. HOMO and LUMO orbital energies of the **PyFFK**, **NDTA** and the complex **PyFFK**-**NDTA** (1:1) were obtained using the density functional theory (DFT) at the B3LYP/6-31G(d,p) accuracy level using the Gaussian 09 package of programs.

2.4.15 Synthesis of materials

2.4.15.1 General synthesis of the peptides (PyFFK and Pep-2)

The peptides were synthesized on Rink amide MBHA resin using standard Fmoc (9-fluorenylmethoxycarbonyl) solid phase peptide synthesis (SPPS) method. In a typical coupling, 3 equiv. of protected amino acid (with respect to the loading of the resin), 3 equiv. of HBTU, and 6 equiv. of DIPEA were taken in 5 mL of DMF (for 0.1 mmol scale with respect to the resin loading) and stirred for 5 minutes prior to addition of the mixture to the resin. The reaction mixture was shaken for 60 min and the resin was washed several times with DMF. The Fmoc-deprotection was achieved by treatment of the resin with 20% piperidine/DMF (5 mL, 5 minutes, three times) followed by thorough washing of the resin with DMF. The Fmoc-deprotection and coupling steps were repeated until the designed peptide sequence was obtained. After the final Fmoc-deprotection, the peptide loaded resin was washed several times with DMF followed by DCM and dried under reduced pressure. The dried resin was then treated with a mixture of 95% TFA in DCM containing 1% TES and stirred for 1 h. The resin was finally washed with DCM several times. The cleavage cocktail and the washings combined were concentrated to a minimum volume on a rotary evaporator. The cleaved peptide was then precipitated from cold dry ether, centrifuged and lyophilized to get the crude peptide. Purification was done in a semi-preparative HPLC using a Luna 5 μm (C18) column (Phenomenex) and an eluent of acetonitrile and water starting

at 20% ACN in H_2O reaching at 100% ACN in 8.9 mins (for **PyFFK)**, and 8.1 mins **(**for **Pep-2)** to complete the chromatogram in 20 mins.

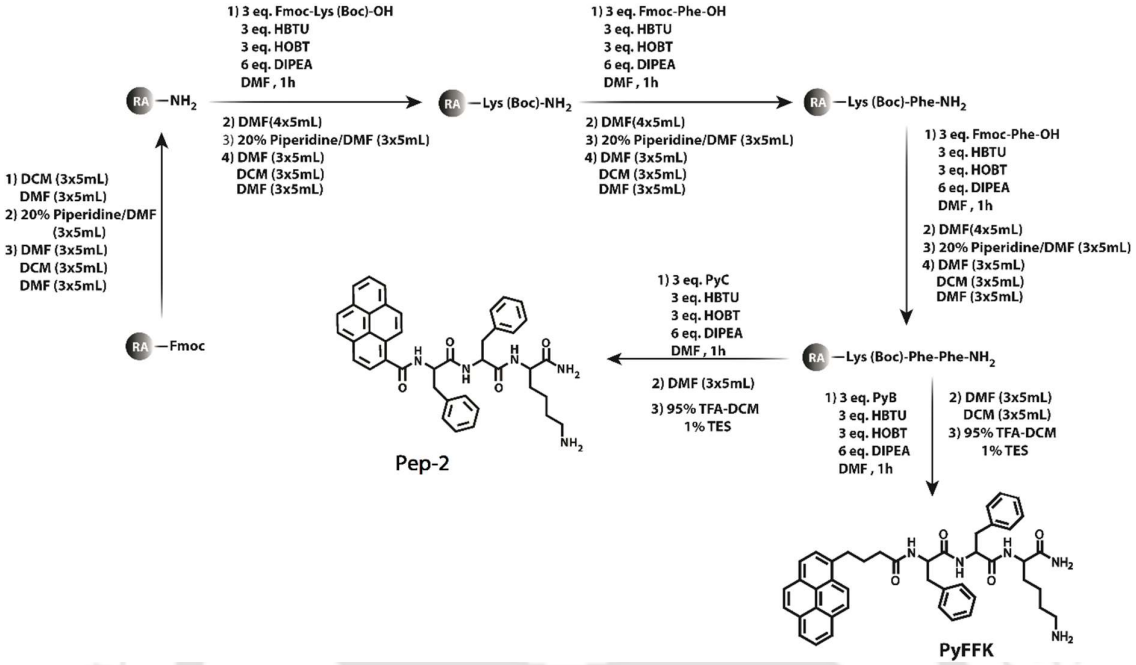

Scheme 2.2 Synthetic routes for **PyFFK** and **Pep-2.**

PyFFK: Yield = 70%. ^{1}H NMR (400 MHz, DMSO-d_6) δ (ppm)= 8.31 – 8.24 (m, 3H), 8.23 – 8.16 (m, 2H), 8.13 (d, J= 2.0 Hz, 1H), 8.12 – 8.07 (m, 2H), 7.99 (d, J= 8.2 Hz, 1H), 7.83 (d, J= 7.8 Hz, 1H), 7.65 (s, 2H), 7.24 – 7.16 (m, 8H), 7.11 – 7.06 (m, 3H), 4.62 – 4.48 (m, 2H), 4.16 (td, J= 8.4, 5.1 Hz, 1H), 3.13 (t, J= 7.7 Hz, 2H), 3.06 (dd, J= 14.0, 4.8 Hz, 1H), 2.96 (dd, J= 14.0, 4.1 Hz, 1H), 2.85 (dd, J= 14.0, 9.0 Hz, 1H), 2.70 (dd, J= 15.8, 5.5 Hz, 3H), 2.17 (t, J= 7.2 Hz, 2H), 1.85 (q, J= 7.6 Hz, 2H), 1.66 (s, 1H), 1.50 (q, J= 7.5 Hz, 3H), 1.35 – 1.21 (m, 2H). ^{13}C NMR (100 MHz, DMSO-d_6) δ (ppm)= 173.23, 172.01, 171.49, 170.63, 137.56, 136.55, 130.89, 130.43, 129.22, 129.10, 128.03, 127.97, 127.52, 127.46, 127.15, 126.51, 126.16, 124.91, 124.79, 123.55, 53.95, 52.08, 37.23, 34.82, 32.06, 31.43, 27.38, 26.64, 22.14. Mass (ESI-MS): m/z calcd. for $C_{44}H_{48}N_5O_4$ $[M+H]^+$, 710.37; found 710.39.

Pep-2: Yield = 72%. ^{1}H NMR (400 MHz, DMSO-d_6) δ (ppm)= 8.85 (d, J= 8.5 Hz, 1H), 8.34 (dd, J= 7.7, 3.2 Hz, 2H), 8.31 – 8.21 (m, 3H), 8.16 – 8.08 (m, 2H), 7.95 (d, J= 9.3 Hz, 1H), 7.86 (d, J= 7.8 Hz, 1H), 7.64 (s, 3H), 7.42 – 7.31 (m, 6H), 7.30 – 7.17 (m, 4H), 7.10 (s, 1H), 4.94 (td, J= 11.6, 10.1, 3.9 Hz, 1H), 4.68 (td, J= 8.6, 4.7 Hz, 1H), 4.25 (td, J= 8.4, 5.1 Hz, 1H), 3.20 – 3.07 (m, 1H),

3.01 – 2.84 (m, 2H), 2.77 (q, J= 6.6 Hz, 2H), 1.72 (t, J= 6.7 Hz, 1H), 1.56 (tt, J= 14.6, 7.2 Hz, 3H), 1.35 (q, J= 15.4, 14.8 Hz, 2H). ^{13}C NMR (101 MHz, DMSO-d_6) δ(ppm)= 173.24, 170.75, 138.18, 137.58, 131.56, 131.53, 130.66, 130.14, 129.33, 129.26, 128.31, 128.17, 128.10, 127.86, 127.60, 127.15, 126.57, 126.34, 125.76, 125.58, 125.06, 124.68, 124.20, 54.86, 53.96, 52.15, 37.47, 37.20, 31.53, 26.67, 22.21. Mass (ESI-MS): m/z calcd. for $C_{41}H_{42}N_5O_4$ $[M+H]^+$: 668.32; found 668.34.

2.4.15.2 Synthesis of other molecules

NDTA, **NDI-2**, **and NDI-3** were prepared the routes shown in Scheme 2.2.

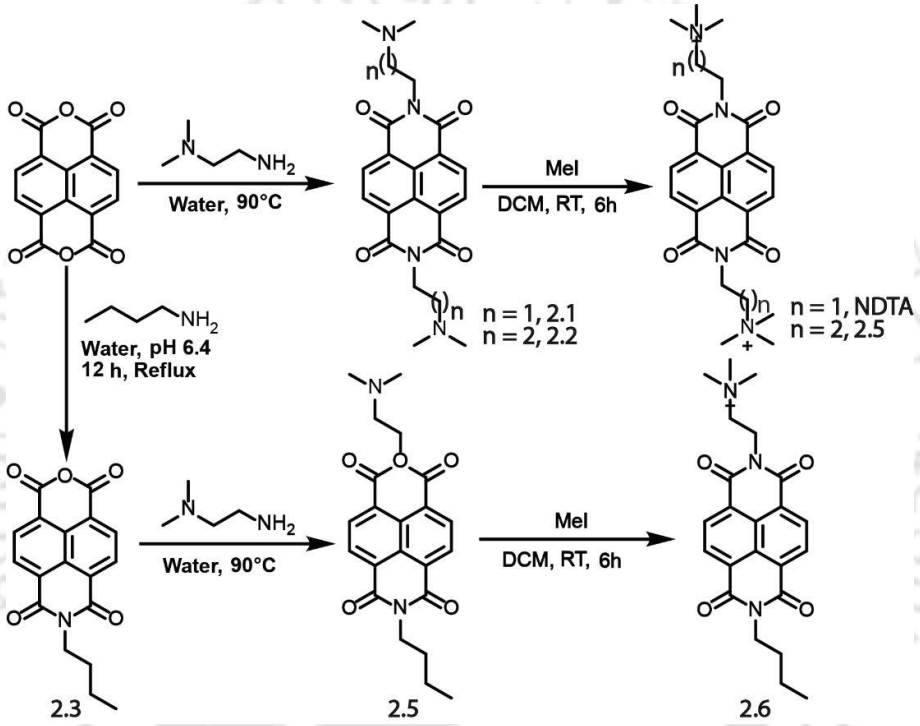

Scheme 2.2 Synthetic routes for **NDTA** and **C_4-NDTA**.

2.3.15.2.1 Compound 2.1

Compound 2.1 was synthesized according to our previously reported procedure.[37] ^{1}H NMR (600 MHz, $CDCl_3$) δ(ppm)= 8.75 (s, 4H), 4.35 (t, J= 6.8 Hz, 4H), 2.67 (t, J= 6.8 Hz, 4H), 2.34 (s, 12H). ^{13}C NMR (151 MHz, $CDCl_3$) δ(ppm) = 165.13, 133.19, 128.80, 79.44, 79.23, 79.02, 59.13, 47.99, 40.85. Mass (ESI-MS): m/z calcd. for $C_{22}H_{25}N_4O_4$ $[M+H]^+$: 409.19 and found 409.19, $[M+2H]^{2+}$: 205.10 and found 205.10.

2.3.15.2.2 Compound 2.2

Compound 2.2 was also synthesized according to our previously reported procedure.[37] Yield = 82%. ^{1}H NMR (400 MHz, $CDCl_3$) δ (ppm)= 8.69 (s, 4H), 4.21 (t, J= 7.6 Hz, 4H), 2.39 (t, J= 7.1 Hz, 4H), 2.19 (s, 12H), 1.88 (p, J= 7.2 Hz, 4H). ^{13}C NMR (100 MHz, $CDCl_3$) δ (ppm) 162.93, 130.99, 126.78, 126.76, 57.37, 45.52, 39.51, 26.12. Mass (ESI-MS): m/z calcd. for $C_{24}H_{29}N_4O_4$ $[M+H]^+$: 437.22 and found 437.22 and for $C_{24}H_{30}N_4O_4$ $[M+2H]^{2+}$: 219.11 and found 219.11.

2.3.15.2.3 Compound 2.3

Compound 2.3 was prepared following our previously published procedure.[51] Yield = 62%. ^{1}H NMR (400 MHz, DMSO-d_6) δ (ppm)= 8.54 (d, J= 7.5 Hz, 2H), 8.18 (d, J= 7.6 Hz, 2H), 4.03 (t, J= 7.6 Hz 2H), 1.62 (p, J= 7.5 Hz, 2H), 1.36 (h, J= 7.3 Hz, 2H), 0.93 (t, J= 7.3 Hz, 3H). ^{13}C NMR (100 MHz, DMSO-d_6) δ (ppm)= 168.45, 162.76, 136.73, 130.04, 129.16, 128.50, 125.44, 124.49, 29.52, 19.76, 13.68.

2.3.15.2.4 Compound 2.4

Compound 2.3 (1 g, 2.85 mmol) was first dissolved in DMF (15 mL) by heating at 60 °C followed by addition of *N, N*-Dimethylethylenediamine (0.44 g, 5.87 mmol). The reaction mixture was heated at 90 °C with stirring for 12 h. The solvent was evaporated under vacuum and the crude residue was suspended in 2:1 water/methanol (100 mL). The obtained solid was thoroughly washed with water by centrifugation and then dried under vacuum to afford 0.8 g (69% yield) of 1b as a deep brown solid. ^{1}H NMR (600 MHz, $CDCl_3$) δ (ppm)= 8.75 (s, 4H), 4.35 (t, J= 6.8 Hz, 2H), 4.20 (t, J= 7.7 Hz, 2H), 2.67 (t, J= 6.8 Hz, 2H), 2.34 (s, 6H), 1.72 (q, J= 7.7 Hz, 2H), 1.46 (q, J= 7.5 Hz, 2H), 0.99 (t, J= 7.4 Hz, 3H). ^{13}C NMR (151 MHz, $CDCl_3$) δ (ppm)= 163.00, 162.88, 131.09, 130.99, 126.78, 126.69, 126.63, 57.05, 45.91, 40.87, 38.73, 30.27, 20.48, 13.97. Mass (ESI-MS): m/z calcd. for $C_{22}H_{24}N_3O_4$ $[M+H]^+$: 394.17, found 394.75.

2.3.15.2.5 NDTA

NDTA was synthesized according to our previously reported procedure.[37] Yield 90%. ^{1}H-NMR (600 MHz, D_2O) δ (ppm)= 3.35 (s, 18H), 3.73 (t, 4H), 4.72 (t, 4H), 8.82 ppm (s, 4H). ^{13}C NMR (151 MHz, DMSO-d_6) δ (ppm)= 33.76, 52.56, 61.89, 126.21, 126.72, 130.92, 164.05 ppm. Mass (ESI-MS): m/z calcd. for $C_{24}H_{30}N_4O_4$ $[M]^{2+}$: 219.11; found, 219.11.

2.3.15.2.6 Compound 2.5

Compound 2.5 (100 mg, 0.094 mmol) and iodomethane (58 mL, 0.94 mmol) were added to DCM (5 mL), and the mixture was stirred for 6 hours. After 5 min. orange coloured precipitate was found and the reaction was continued for another 6 hours. The reaction mixture was centrifuged and the precipitate was washed with DCM for several times. The resulting orange solid was dried under vacuum. Yield 90%.^{1}H NMR (400 MHz, DMSO-d_6) δ(ppm)= 8.71 (s, 4H), 4.50 (t, J= 7.3 Hz, 2H), 4.08 (t, J= 7.4 Hz, 2H), 3.68 – 3.62 (m, 2H), 3.24 (s, 9H), 1.71 – 1.62 (m, 2H), 1.39 (h, J= 7.3 Hz, 2H), 0.95 (t, J= 7.3 Hz, 3H). ^{13}C NMR (100 MHz, DMSO-d_6) δ (ppm) 162.69, 162.54, 130.49, 130.39, 126.57, 126.26, 126.16, 61.65, 52.47, 33.86, 29.52, 19.75, 13.67. Mass (ESI-MS): m/z calcd. for $C_{23}H_{26}N_3O_4$ $[M+H]^+$: 408.19, found 408.73.

2.3.15.2.7 Compound 2.6

Compound 2.6 was synthesized using the same procedure described for Compound 2.5. Yield = 92%. ^{1}H NMR (400 MHz, DMSO-d_6) δ(ppm)= 8.70 (s, 4H), 4.15 (t, J= 6.4 Hz, 4H), 3.56 – 3.43 (m, 4H), 3.06 (s, 18H), 2.21-2.13 (m, 4H). ^{13}C NMR (100 MHz, DMSO-d_6) δ(ppm)= 162.82, 130.47, 126.27, 126.15, 63.19, 52.23, 37.32, 21.54. Mass (ESI-MS): m/z calcd. for $C_{26}H_{34}N_4O_4$ $[M]^{2+}$: 233.13; found, 233.13.

Chapter 3: Light-Induced Syneresis by a Water Insoluble Peptide-Hydrogel and Effective Removal of Small Molecule Waste Contaminants.

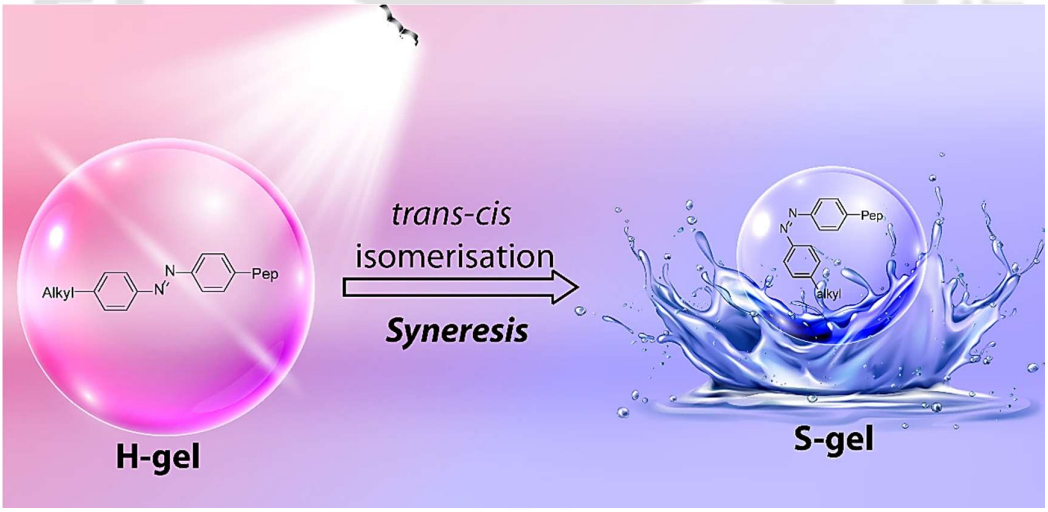

3.1 Introduction

Syneresis is a physicochemical phenomenon whereby the trapped water of a material (mostly hydrogels) is expelled in response to stimuli and thereby the material shrinks to a smaller volume.[195] The discharge of blood serum during the clotting process is a classic example of syneresis.[195] However, reports regarding syneresis or macroscopic volume phase transitions in response to different stimuli are still rare for supramolecular gels. These type of hydrogels exhibit contraction and expulsion of water in response to various stimuli such as pH, metal ions, light, mechanical force, or heat.[104, 105, 167, 196, 197] Such a property can lead to various important applications in the field of material science and the bio-medical field. While an effort was made by Adams and co-workers to propose a rationale behind such behaviour in a supramolecular gel it is still not clear why and when such property could be expected.[198] Banerjee *et al.* reported another interesting case of time-dependent automatic syneresis by a super-hydrogel of lauryl chain appended triphenylalanine.[167] Probably, all the reported hydrogels have come across as serendipitous observations and a proper model could be developed to design such gelators only with the help of more examples and analyses.

In this regard, we have recently reported a peptide[77] capable of forming hydrogels, which remain insoluble in bulk water and exhibited an unusual property as exchange of solvent and solute to and from these hydrogels is highly restricted. Dimerisation of the gelator was found to be critical for this unique property. Inspired by these two previous efforts, herein we have designed an azobenzene-functionalized short peptide (**Azo-KC**) for the formulation of a light-sensitive hydrogel. Unexpectedly, the hydrogel exhibited the unique syneresis phenomena upon the treatment of light. In chapter 1, we have already mentioned the adverse effect of organic dye contaminants on water pollution. Based on the menacing waste-water issues of modern scenarios, this intriguing peptide-based hydrogel might be deployed to remove various organic dyes simply in presence of the UV light for few hours. In the next segment, the detailed analyses and their results regarding the hydrogel have been elaborated.

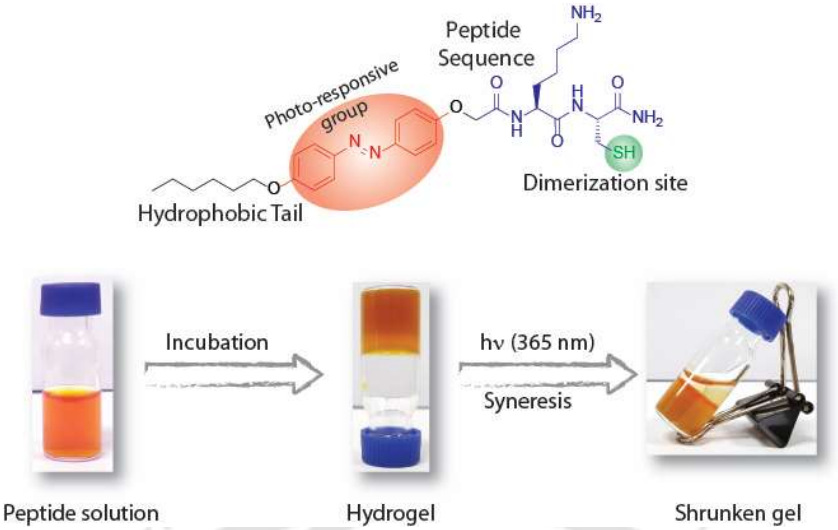

Scheme 3.1 Chemical structure of **Azo-KC** and photographs of the **Azo-KC** solution, hydrogel formed by the solution (H-gel) and syneresis (S-gel) upon irradiation with UV light.

3.2. Results and Discussion

3.2.1. Self-Assembly of the Peptide-Gelator

Chemical structure of the hydrogelator was shown above (Scheme 3.1) which efficiently formed hydrogels under basic conditions. The peptide hydrogelator was prepared at a bulk amount by solution phase peptide synthesis method with properly purification at each steps that has been discussed at the experimental section. An aqueous solution of **Azo-KC** formed a self-supporting hydrogel (H-gel, Scheme 3.1) upon treatment with base (1N NaOH). The minimum gelation concentration (MGC) and gel to sol transition temperature at MGC were found to be 1.15 wt% (16.2 mM) and 57 °C, respectively. Transmission electron microscopic (TEM) analysis shows formation of a network of thin fibers (2-5 nm × ~100 nm, Figure 3.1A). Rheological measurements confirmed a gelled state of the material with a higher storage modulus (G′) compared to its loss modulus (G″) in both amplitude and frequency sweeps (Figure 3.1B and C). While performing the strain-dependent rheology measurement, the hydrogel showed a yield strain and transforms into a quasi-liquid indicating possible thixotropic (injectable) behaviour. A time-dependent strain sweep experiment was performed by alternating the applied strains at a fixed angular frequency. At a higher strain (γ = 1000%), the viscoelastic properties of the material were lost, but were regained almost completely in every successive steps when a lower strain (γ = 0.1%, Figure

3.1D) was applied. This step-strain measurement was cycled four times with excellent recovery, demonstrating thixotropic behaviour by the hydrogel. The hydrogel could easily be injected through a syringe immediately recovering as a gel after shear. Interestingly enough, after the treatment of the UV light (365 nm) to hydrogel, the shrunken gel (S-Gel) exhibited a rise of the G′ and G″ values in both amplitude and frequency sweep experiments indicating the increment of the rigidity of the hydrogel network upon water expulsion.

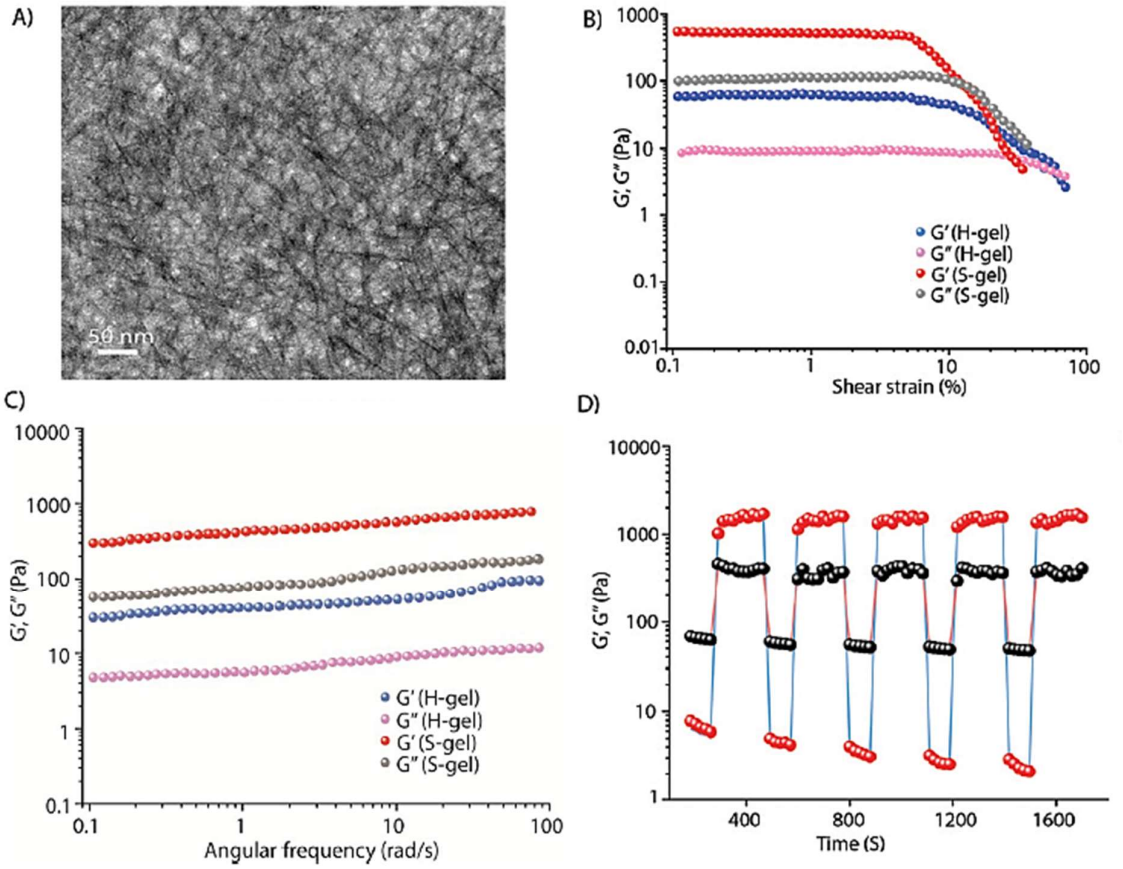

Figure 3.1 (A) FETEM image of the H-gel. (B) And (C) Changes in storage and loss moduli as a function of shear strain for H- and S-gels in amplitude and frequency sweep respectively. (D) The rheological properties of 1.15 wt% H-gel when alternate step strain switched from 1% to 200%.

In line with our previous report, the hydrogel formed by **Azo-KC** was also found to be insoluble in water, additionally, the hydrogel found to be delicately dissolute in presence of different disulfide-bond breakers like TCEP and GSH. A small portion of the hydrogel was placed in bulk water or buffers at different pH values (1-13) and shaken at a constant speed. The bulk medium was analysed over time using UV-Vis spectroscopy to quantify the dissolution (Figure 3.2A and B). In all media, an initial dissolution (up to 11%) was observed,

corresponding to loosely-bound gelator molecules at the surface of the hydrogel. However, in all cases, after 24 h no further dissolution was observed. The extent of dissolution in these media after 7 d are shown in. The hydrogel remained insoluble even after one year of incubation in bulk water.

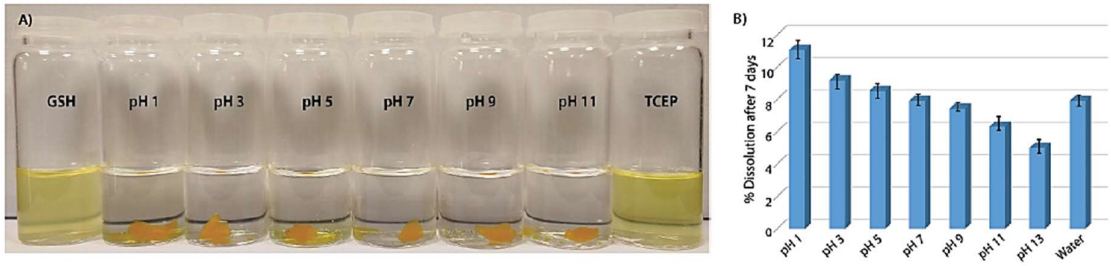

Figure 3.2 (A) Photograph of vials containing different aqueous solutions where small portions of the H-gel were immersed and stirred for 10 min at room temperature. Though the gel remained insoluble in buffers, TCEP and GSH solutions could dissolve the gel completely. (B) % dissolution of the H-gel in buffers of different pH (1-13) after 7 days of incubation at room temperature.

The self-assembly of **Azo-KC** was assisted by the disulfide bridge between two peptides. After 2 h of incubation under basic conditions, only the mass corresponding to the **Azo-KC** dimer was found. Time-dependent HPLC analyses of a diluted solution of **Azo-KC** shown in Figure 3.3A revealed that the dimerisation is complete within 1.5 h. The highly basic medium in this case presumably facilitates oxidation of the Cysteine thiols. To understand the situation in the gel state, a portion of the H-gel was dissolved in DMSO and further diluted with water and analysed using analytical HPLC. More than 99% of the molecules were found to be in the dimer form. To demonstrate the importance of the disulfide linkage towards gelation, the hydrogels were placed into aqueous solutions containing various disulfide bond-breaking agents. In all cases the hydrogel dissolved within minutes. Henceforward, the combination of all these properties like, dual responsiveness (light and reducing agents), syneresis, insolubility and injectability make the hydrogel distinctive amongst all such supramolecular hydrogel reported so far. ^{1}H NMR experiment was carried out on solutions of **Azo-KC** in DMSO-d_6 after 12 h with varying amounts of water. This revealed that both hydrogen bonding and π-π stacking interactions become prominent in the aggregated state. With an increase in water content, the amide-NHs showed down-field shifts while the aromatic protons moved upfield (Figure 3.1B).

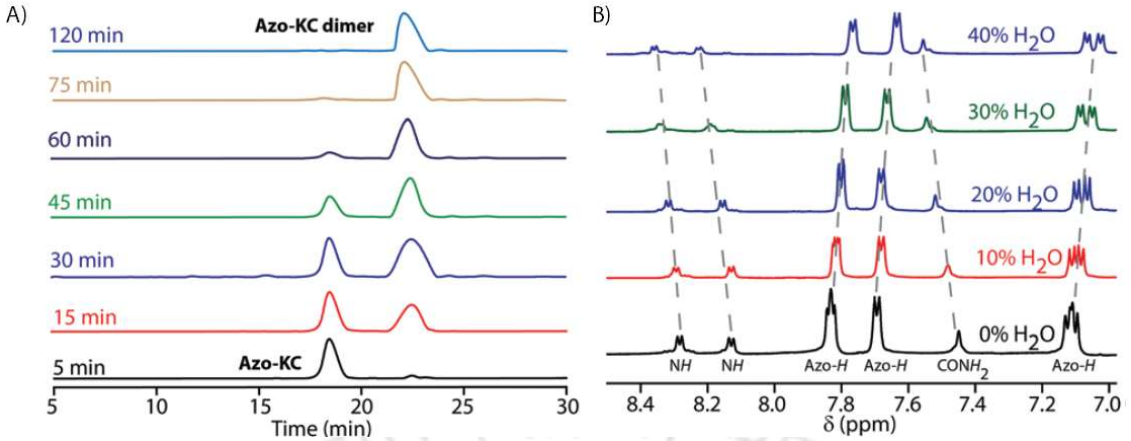

Figure 3.3 (A) Time dependent chromatographic analysis of a 0.01 wt% aqueous solution of **Azo-KC** showing the formation of disulfide linked dimer. (B) ^{1}H NMR spectra of **Azo-KC** dimer in DMSO-d_6 with varying amounts of H_2O.

3.2.2. UV Treatment and Syneresis Phenomenon

The gelator, was designed to embed a light sensitive moiety into a hydrogel by incorporating an "Azo" group, which can undergo "*trans*" to "*cis*" isomerisation upon irradiation with UV light. When irradiated with light (λ = 365 nm), the H-gel displayed shrinkage, expelling water from the hydrogel (Figure 3.4A). This unexpected observation leads us to perform a systematic evaluation of hydrogel syneresis. Quantitative analysis showed that the hydrogel can shrink up to maximum of 50% of its original volume following irradiation with UV light (Figure 3.4A). It is clear from the plot that the shrinkage process is completed within 90 min. HPLC and ESI-MS analyses of the shrunken gel (S-gel) confirm that the constituent molecule of S-gel remains the disulfide linked dimer of **Azo-KC**. The HPLC analyses shows ~ 9:1 distribution of *cis* and *trans* isomers of the dimer in the S-gel sample (Figure 3.4B). To check reversibility of the syneresis process, the shrunken gel was further irradiated with light of 420 nm as well as kept in direct sunlight for several hours with occasional shaking. However, no change in the appearance was observed, which confirmed irreversibility of the process. Water expulsion was also monitored by keeping the H-gel at room temperature for several days. However, no syneresis was observed in this case. Finally, the hydrogel was heated at 45 ^{0}C and only a small portion (~15%) of the total water was expelled from the hydrogel after 2 h of heating. Thus, though heating can cause syneresis in this system, UV light irradiation was found to be a more effective stimulus.

The light induced "*trans*" to "*cis*" structural isomerisation of **Azo-KC** changed the self-assembly state. The UV-Vis absorption spectra of a solution of **Azo-KC** dimer was recorded

at different time intervals while irradiating the solution with light (365 nm). Before irradiation, the molecule showed an absorption maximum at 342 nm (Figure 3.4C), which corresponds to the π-π transition of the *trans*-azobenzene unit. As the sample was irradiated with UV light, a hypsochromic shift was observed in the absorption maxima. After 90 min of irradiation, the absorption maxima was found at 321 nm and the molar extinction coefficient decreased linearly for the respective absorption maxima. Additionally, a new broad peak at 445 nm appeared in the irradiated sample increasing with irradiation time. This new peak is a signature of the *n*–π* transition of *cis*-azobenzene. The CD spectra of the **Azo-KC** hydrogel revealed a bisignated signal in the azobenzene absorption region with a positive to negative crossover point at 324 nm (Figure 3.4D). Additionally, a positive peak at 198 nm and a negative Cotton effect at 222 nm were also observed indicating β-sheet like arrangement of the peptide. The strong exciton-coupled cotton effect at the bisignated peak is a result of supramolecular chirality in the aggregated state.[21] While the secondary conformation of the peptide remained similar for the S-gel, the 250-400 nm region remained CD silent.

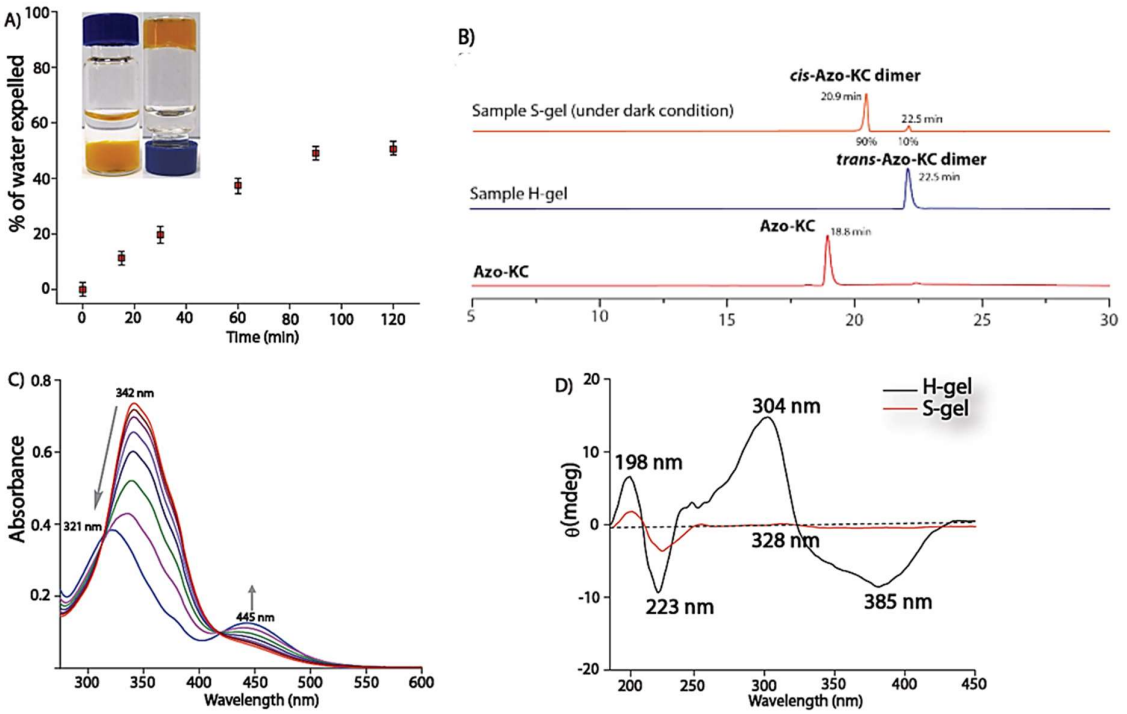

Figure 3.4 (A) % of water expelled from the H-gel during syneresis as a function of duration of the UV-irradiation process. Inset: images of the vials after 2 h of irradiation as in (A) showing the expelled water. (B) Chromatographic analysis of **Azo-KC**, H-gel and S-gel to determine the extent of dimers in the gel states. (C) UV-Vis spectra of a 0.01 wt% 12 h matured aqueous solution of **Azo-KC** (in presence of NaOH) during UV-irradiation. (D) CD spectra of a 0.01 wt% 12 h matured aqueous solution of **Azo-KC** (in presence of NaOH) before and after 2 h of UV-irradiation.

The syneresis observed in this system is an interesting phenomenon, thus gaining mechanistic insight into the system is important for enhanced understanding. The S-gel was analysed using electron microscopy as well as rheology. Interestingly, the S-gel consists of ~ 1 µm long rod-like structures. This morphology clearly differs from the original network of thin fibers observed for the H-gel. The sample after 30 min of exposure to UV light shows a combination of both fibers and rods, which reflects an intermediate state of the morphogenesis process (Figure 3.5A). For the S-gel, both storage and loss moduli were found to be much higher than that of the H-gel (Figure 3.5B). These results suggest a significant alteration takes place in the self-assembly of the gelator molecules upon irradiation with UV light.

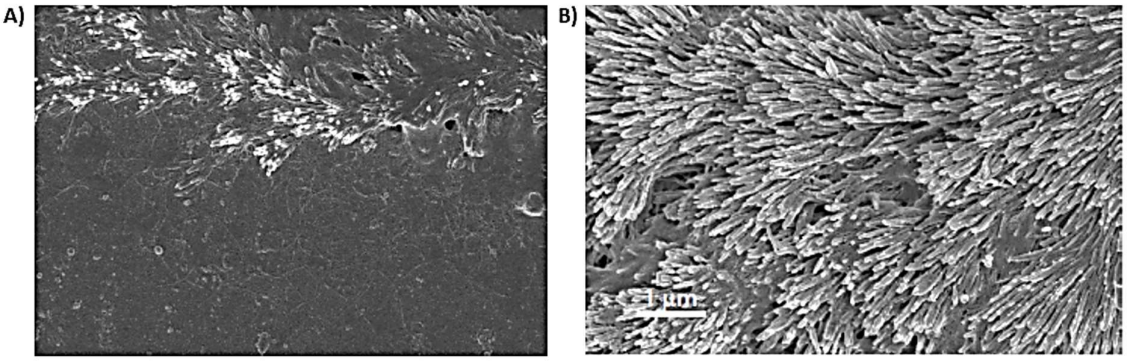

Figure 3.5. (A) FESEM image of H-gel after 30 min of UV-light (365 nm) irradiation showing presence of both rod and fibers, which represents the intermediate state during the syneresis process. (B) FESEM image of the S-gel, only the presence of rod like structures was observed.

FTIR spectra of the as synthesised peptide showed two peaks at 1683 and 1652 cm^{-1}, which were shifted to 1673 and 1639 cm^{-1}, respectively in the H-gel (Figure 3.6A). The observed shifts and peak positions in the H gel indicate possible hydrogen bonding between the neighbouring peptide molecules. However, after syneresis of the hydrogel, the hydrogen bonding interactions are still observed in the IR spectra with two prominent bands at 1677 and 1637 cm^{-1} supporting a β-sheet like arrangement similar to that of the H-gel (Figure 3.6A). Powder XRD analyses of the as synthesised **Azo-KC** and xerogel obtained from the H gel confirmed π-π stacking between the "Azo" groups (interplaner distance of 4.23 Å) in the self-assembled state (Figure 3.6B). PXRD of the xerogel formed from the S-gel showed two π-π stacking interactions (4.16 and 3.79 Å) compared to only a single peak for the H-gel (Figure 3.6B).

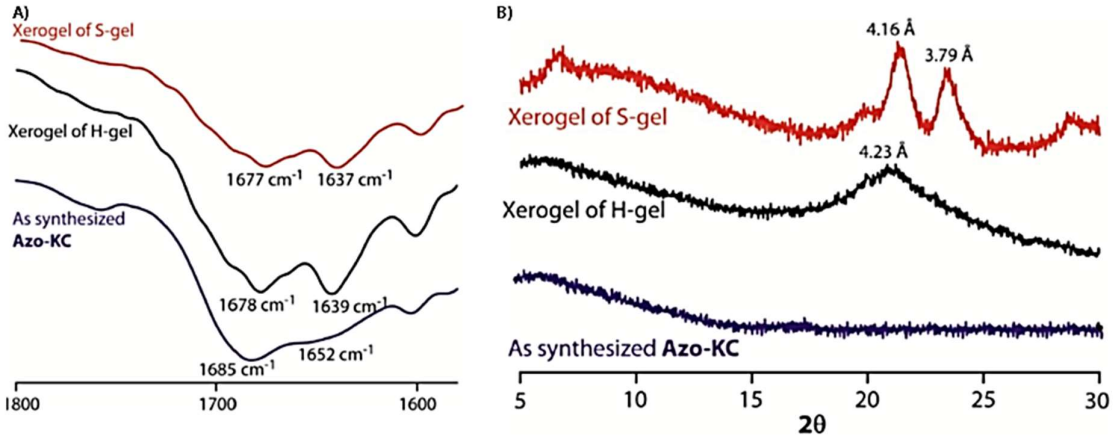

Figure 3.6 (A) Relevant region of the FTIR spectra of as synthesized Azo-KC and xerogels prepared from H-gel and S-gel showing the involvement of hydrogen bonding in the gel state. (B) PXRD of the as synthesized **Azo-KC** and xerogels prepared from H-gel and S-gel showing different π–π interactions in the two gel states.

It is important to note that the transformation in morphology occurs while the system is in an aggregated gel state where the dynamics of the constituent molecules are highly restricted.[199] Crystal to crystal transformation due to photoinduced *trans–cis* isomerisation of azobenzene derivatives has been reported in literature.[200] However, such gel-state morphogenesis is not commonly observed phenomenon.[201]

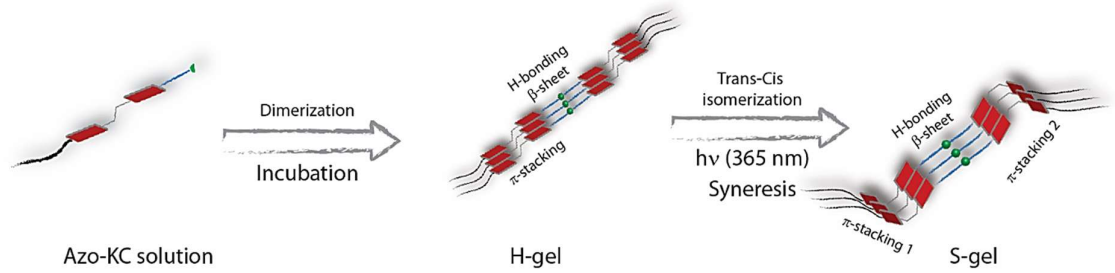

Figure 3.7 Possible molecular arrangements corresponding to different states during hydrogelation and syneresis process.

It is clear that during the *trans–cis* isomerisation, the **Azo-KC** dimer undergoes a significant change in molecular arrangement, which is shown in Figure 3.7. Presumably, the new arrangement in the S-gel requires less water to stabilise the aggregated structure. Thus, the system expels excess water present in the system. Moreover, when exposed to the disulfide bond breaking agents, the S-gel did not get dissolved. This observation also suggested a much stronger packing of the molecules in the S-gel compared to that in H-gel. As a direct consequence, the tightly knitted peptide fibers transferred to the trapped assemble state

which was favourably being separated from the dispersed water of the hydrogel by the assistance of the light-treatment.

3.2.3. Application of the Peptide Hydrogel

We anticipated that light-triggered shrinkage of the H-gel, could be used to entrap toxic small molecules, including dyes, in the S-gel structure. Six different model dyes were tested which were categorised as cationic (Rhodamine B and Methylene blue), anionic (Methyl orange and Eriochrome black T) and neutral (Neutral Red and Nile Red). H-gels (at MGC) were prepared in 20 μM solutions of the model dyes. The H-gels were then subjected to syneresis by irradiation with UV light (365 nm) for 2 h (Figure 3.8A). The expelled water was then analysed using UV-Vis spectroscopy to quantify the concentration of dye expelled. Importantly, the expelled water was found to be free of dye in all cases. Figure 3.8A shows the separation of the methyl orange (MO) from the dye-loaded H-gel. The results of other dyes are reported in the succeeding sections. Furthermore, keeping the gelator concentration fixed at MGC, the limiting concentrations (beyond which small amount of dye came out in the expelled water) of different dyes were also evaluated (Figure 3.8B).

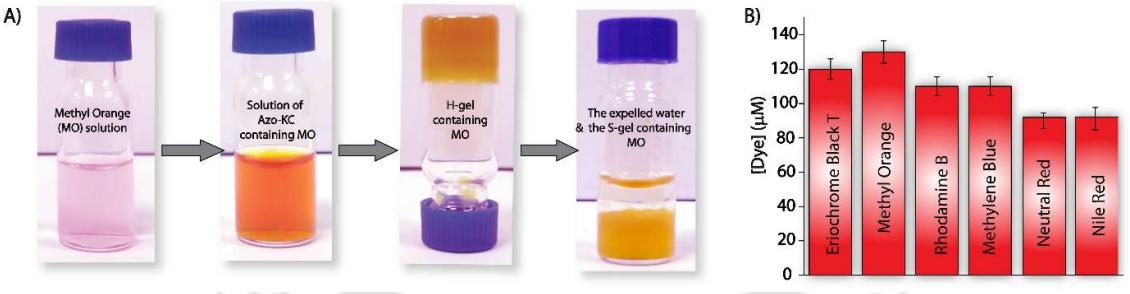

Figure 3.8 (A) Photographs showing MO removal from H-gel upon UV light induced syneresis. (C) Maximum initial dye concentrations for different dyes, which can be completely removed through syneresis of the hydrogel. All measurements were carried out at room temperature.

For MO, the syneresis process could remove the dye completely at or below 120 μM initial dye concentration as analysed by UV-Vis spectroscopy (Figure 3.9). Above this concentration, a small amount of MO was found in the expelled water. For other dyes, the results were similar and are shown in Figure 3.8B.

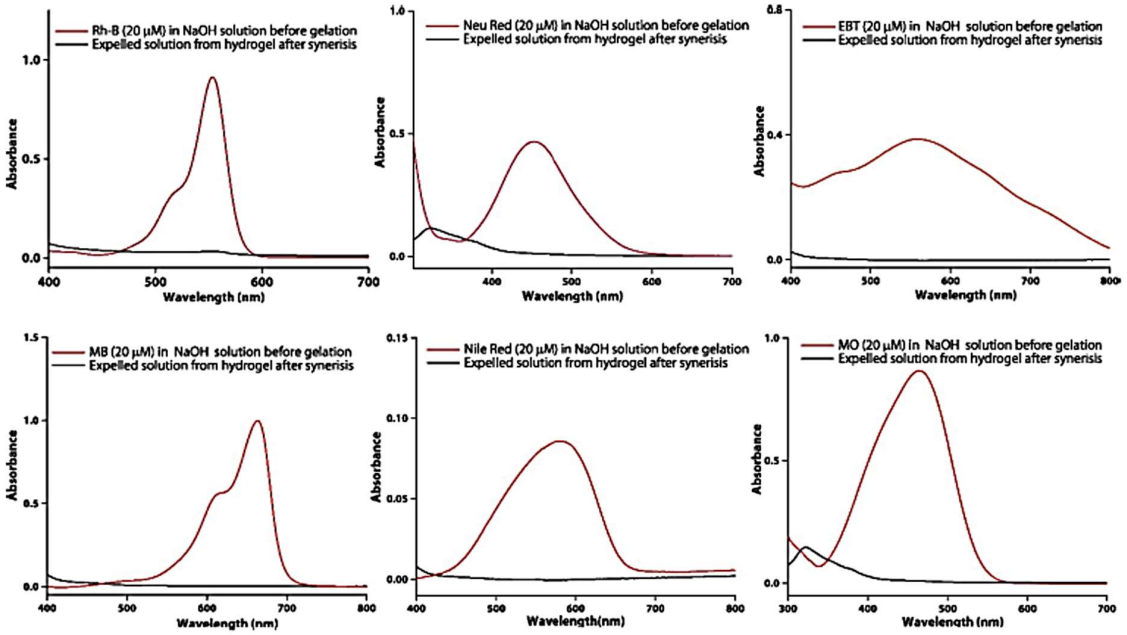

Figure 3.9 The UV-Vis spectra of aqueous (containing NaOH) solutions of various dyes (20 μM) and the expelled water after syneresis of H-gels prepared using 20 μM solutions of the respective dyes.

Apart from the UV-Vis spectroscopy, the dye separation was also scrutinized under HPLC chromatograms. All the expelled solutions from the dye-loaded H-gel were subjected to the HPLC analyses along with the respective dye solution at 20 μM concentration (Figure 3.10). However, results went in support of the previous UV-Vis experiments showing almost full entrapment of all kinds of dyes inside the S-gel network.

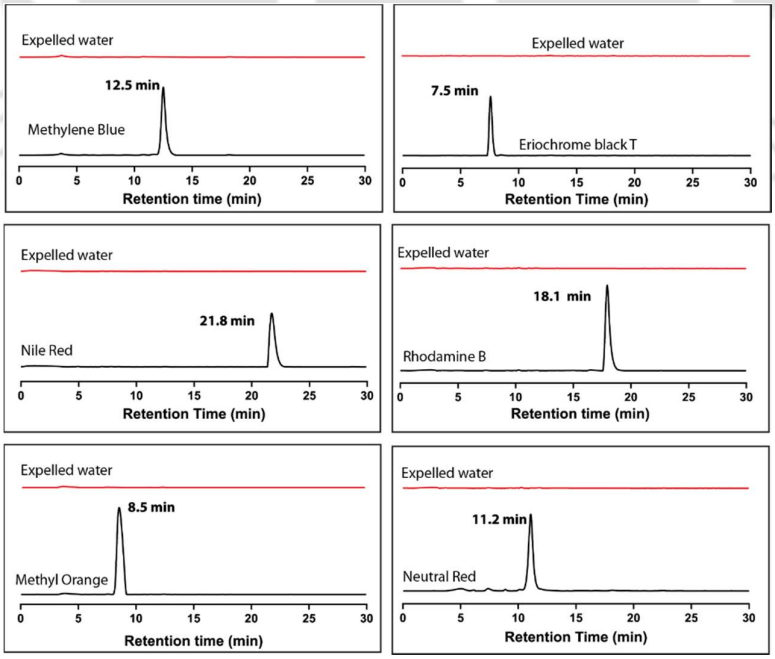

Figure 3.10 The chromatograms of aqueous (containing NaOH) solutions of various dyes (black lines) and the expelled water after syneresis of H-gels (red). All experiments were carried out at room temperature.

3.3 Conclusion

In summary, we have presented a small peptide-based hydrogel, which displayed insolubility in water as well as buffers of different pH (1-13). The hydrogel was found to be thixotropic in nature and uniquely exhibited efficient syneresis upon irradiation with UV light. The syneresis is stimulated through light-induced *trans-cis* isomerisation of the gelator molecule, which rearranged within the gelled state and expel the excess unwanted water. The photo-syneresis process was successfully utilised to efficiently remove model dyes from water which could be certainly one of the most effortless strategies for waste management in recent times.

3.4 Experimental Section

3.4.1 General Materials and Instruments

H-Cys(Trt)NH_2, Fmoc-Lys(Boc)-OH, HBTU and HOBT were procured from GL Biochem, China. All the other chemicals and solvents used were procured from Sigma Aldrich, TCI or Merck, India. To prepare samples, Milli-Q water with a conductivity of less than 2 $mScm^{-1}$ was used. Chromatographic purifications were performed on a Luna 5 µm (C18, 250 × 4.6 mm) column (Phenomenex) using a Dionex Ultimate 3000 HPLC. UV-Vis spectra were recorded on a PerkinElmer Lambda 750 spectrometer. Standard 10 mm-path quartz cuvettes were used for all spectroscopic measurements. ^{1}H NMR, ^{13}C NMR were recorded using a Bruker Ascend 600 MHz (Bruker, Coventry, UK) spectrometer and referenced to deuterated solvents. ESI-MS were performed with a Q-Tof Micro Quadrupole mass spectrophotometer (Micromass). For FTIR, Nicolate iS 10 FTIR spectrometer was used. Circular Dichroism (CD) experiment was performed by using Jasco J-1500 spectropolarimeter. Powder XRD were recorded on a BRUKER D2 Phaser X-Ray diffractometer (30kV, 10mA).

3.4.2 Preparation of Hydrogel

To prepare the hydrogel, 1.5 mg of **Azo-KC** was added in 100 µL of water along with 30 µL of 1 N NaOH solution and shaken to completely dissolve the solid. The solution was kept undisturbed at room temperature for 2 h to get the self-supporting hydrogel. Unless otherwise mentioned, all the studies were performed with 1.15 wt% hydrogel at room temperature.

3.4.3 Determination of Sol–Gel Transition Temperature (T_g)

The gel was placed in a water bath and the bath was heated at a rate of 0.5 °C/min. The temperature at which gel started flowing by inverting the vial was noted as T_g. The experiments were performed in triplicate.

3.4.4 FETEM

5 µL of the samples were cast on the carbon coated Copper grid (300 mesh Cu grid with thick carbon film from Pacific Grid Tech, USA) allowed to air dry for 10 minutes then the excess sample was absorbed by a piece of tissue paper. The sample was further air dried for one day before analysis. Images were taken on a JEOL JEM-2100F microscope.

3.4.5 FESEM

10 µL of the samples were cast on silicon wafers and dried under ambient condition for 24 hours. Images were taken on a Gemini SEM 300 (Sigma Zeiss) instrument.

3.4.6 Rheology

The viscoelastic properties of the hydrogel were characterized using an AntonPaar MCR 102 rheometer equipped with a 20 mm parallel plate (with 0.5 mm zero-gap) measuring system at 25 °C. A strain sweep test was performed to identify the LVR over 0.01 to 100% strain at a fixed oscillatory frequency of 1 rad s^{-1}. Further, the mechanical strength of the gel was determined from oscillatory test i.e. frequency sweep, which was carried out under an appropriate strain (γ= 0.1 %) selected from the LVR with the frequency ranging from 0.1 to 1000 rad s^{-1} at 25 °C. For the injectable behaviour of the gel, time dependent rheology experiment was performed by alternating the applied strain at a fixed angular frequency 1 rad s^{-1}. With the cyclic appearances of the applied strain against time, viscoelastic property was found to be reversible with applied strain (γ = 1000 % to γ = 0.1 %). Injectable behaviour was physically tested by preparing the H-gel in a 1mL syringe. When pressure was applied to the plunger liquid sol was released through the needle which reverted back to the gel state immediately.

3.4.7 Analytical HPLC

Purity of compound 3.6 and **Azo-KC** was checked using analytical HPLC with Luna 5µm (C18) column. Acetonitrile and water with 0.1% TFA was used as the mobile phase. For the time dependent dimerization, a solution of **Azo-KC** maintaining the basic condition by adding appropriate amount of NaOH solution) was incubated at room temperature and at different time, samples were taken and analysed. To analyse the extent of dimerization in the gel state, a small portion of a 24 hours matured hydrogel was taken in minimum amount of DMSO to dissolve it and then diluted in water. This solution was analysed with analytical HPLC and only less than 1% monomer was found in the sample.

3.4.8 Preparation of Stock Solution of Azo-KC Dimer

A 0.5 mM stock solution of **Azo-KC** was prepared in water (containing appropriate amount of NaOH to maintain the basic condition) and incubated for 12 h. This solution was used for UV-Vis and CD experiments.

3.4.9 CD Spectroscopy

The CD spectra of all the samples were recorded at room temperature. The data were collected at 0.5 nm intervals with 2 nm band width. All measurements were done in 0.2 cm path length cuvette with 800 µL sample volume. Each CD profile is an average of 3 scans of the same sample collected at a scan rate 100 nm min^{-1}, with a proper baseline correction from the water medium.

3.4.10 UV-Vis Spectroscopy

The above mentioned **Azo-KC** dimer was diluted with water to maintain a concentration of 0.01 wt% of **Azo-KC** The solution was irradiated with UV-light (365 nm) for 120 min and at different time interval, the UV-Vis spectra were recorded at room temperature.

3.4.11 HPLC and ESI-MS Analyses of Hydrogel Samples

Both H- and S-gels were found to be soluble in DMF. A small portion of these gels were dissolved in minimum amount of DMF and the solutions were further diluted with acetonitrile (to maintain DMF content less than 1%) before analysing the samples by ESI-MS and HPLC.

3.4.12 PXRD Analyses

Both the hydrogel and the light treated shrunken gel were lyophilised inside the 2 mL micro-centrifuge tubes and the lyophilised powders (10 mg each) are taken for the analyses. For the analysis of the unassembled peptide, 10 mg peptide was completely dissolved in 50 µL HFIP and was cast on a clean glass slide. Prior to the experiment, the sample was dried overnight within a vacuum desiccator.

3.4.13 Dissolution Study

The dissolution studies were performed following our previously published protocol.[77] A solution of **Azo-KC** was prepared at MGC containing the required amount of NaOH solution and the sample was equally divided in different vials (100 µL each). After 12 h of incubation, the H-gels were formed and to these samples, 500 µL of water (or buffers of different pH) was added and the samples were shaken (100 rpm) at room temperature. At different times, the aliquots from supernatant bulk aqueous medium were taken out and the presence of the **Azo-KC** dimer was monitored using UV-Vis spectroscopy. Finally, the gels were disrupted completely by the treatment of GSH for 100% dissolution. The % dissolutions were calculated using the cumulative absorbance at λ_{max} (330 nm). For complete dissolution of the hydrogels, similar protocol was applied using aqueous solutions of GSH and Tris(2-carboxyethyl) phosphine (TCEP). In each of these solutions, the H-gel dissolved completely within 5 min.

3.4.14 Buffers Used for the Dissolution Study

HCl-KCl (pH 1); Glycine-HCl (pH 3); Citric Acid-Sodium citrate (pH 5); Tris (hydroxylmethyl) aminomethane - Hydrochloric acid (pH 7 and 9); Sodium hydrogen orthophosphate / Sodium hydroxide (pH 11); Potassium chloride - Sodium hydroxide (pH 13). All buffers were freshly prepared maintaining 20 mM concentration.

3.4.15 Determination of Extent of Water Expulsion during Syneresis

Several samples of the H-gel were prepared (600 µL) in vials and the gel samples were irradiated with UV light (365 nm, 12 lamps of 8 watt) for different time intervals. After irradiation with UV light, the expelled water was carefully taken out and the volume was

measured. Weight of the vials before and after removing the expelled water were also noted. Each experiment was repeated five times to get an average value.

3.4.16 Model Dye Removal Experiments

1 mM stock solutions of the model dyes were prepared in water. From these solutions, appropriate amounts were added to the solutions of **Azo-KC** to maintain a final concentration of the dyes at 20 μM. The solutions were incubated for 12 h to form the H-gels containing these dyes. The samples were then irradiated with UV-light as before when the gels undergo syneresis. The concentrations of the dyes in the expelled water were then monitored using UV-Vis spectroscopy. In another set of experiments, the initial dye concentrations were varied to identify dye removal capacity of the gel. Dyes used are, Methyl Orange (MO), Eriochrome Black T (EBT), Methylene Blue (MB), Rhodamine B (Rh-B), Nile Red (NR), and Neutral Red (Neu R).

3.4.17 Synthetic Routes for the Peptide

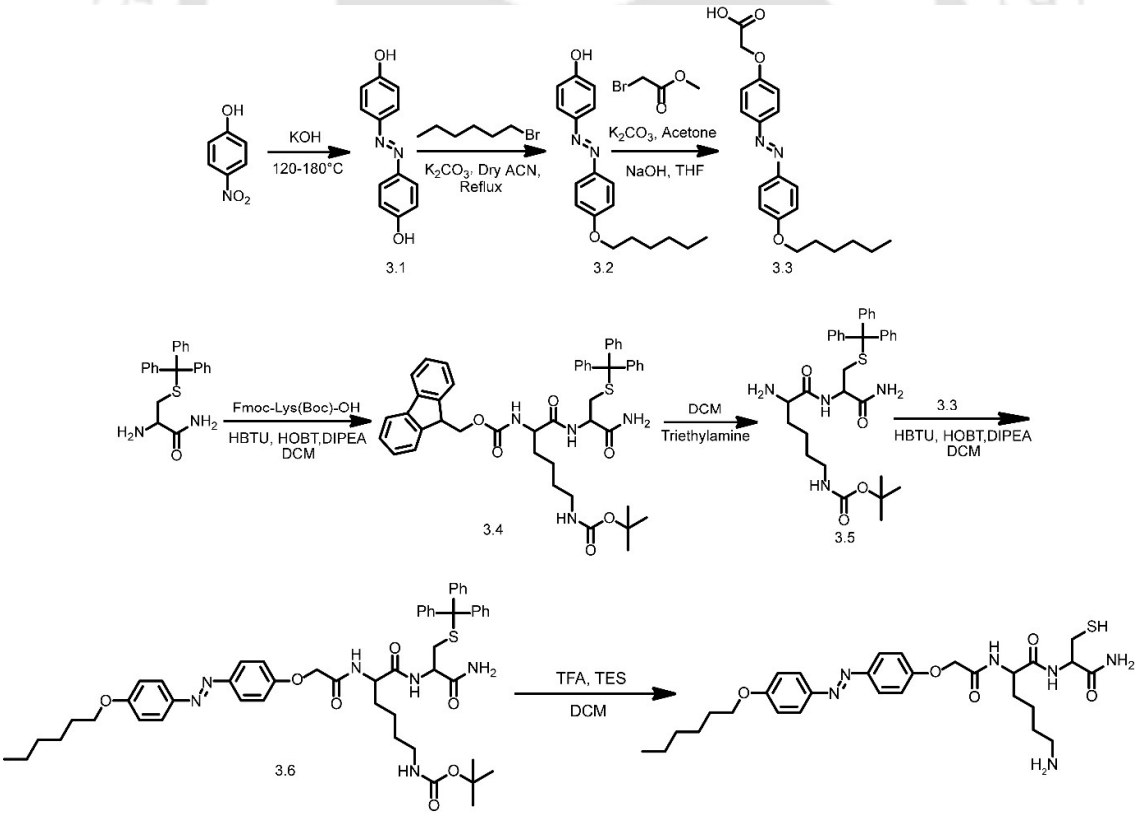

Scheme 3.2 Synthetic steps of the peptide gelator.

3.4.17.1 Synthesis of Compound 3.1

4-Nitrophenol (5 g, 1equiv.) and KOH (25 g, 12.8 equiv.) were taken in a clean 100 mL round bottom flask and was heated at 120 °C for three hours when the mixture turned to yellow. After that, the temperature was gradually increased to 200 °C. The hot brown mixture was cooled at room temperature and the pH was adjusted to 3 by adding dilute HCl. The brown precipitate was thoroughly washed with water and the product was crystallized from methanol (yield = 40%). ^{1}H NMR (600 MHz, DMSO-d_6) δ (ppm)= 10.18 (s, 2H), 7.74 – 7.69 (d, 4H), 6.96 – 6.88 (d, 4H). ^{13}C NMR (151 MHz, DMSO-d_6) δ (ppm)= 160.44, 145.70, 124.63, 116.26. ESI-MS (m/z): calcd. 215.07 for $C_{12}H_{10}N_2O_2$; found, 215.08 for $[M+H]^+$.

3.4.17.2 Synthesis of Compound 3.2

A mixture of compound 3.1 (1.8 g, 1 equiv.) and K_2CO_3 (5.7 g, 5 equiv.) was taken in acetonitrile and stirred for 30 min before hexyl bromide (825 µL, 0.7 equiv.) was added to it. The reaction was refluxed overnight under argon atmosphere. It was then filtered and the solid obtained was thoroughly washed with acetonitrile. The product was purified by column chromatography using ethyl acetate and hexane as mobile phase (yield = 32%). ^{1}H NMR (600 MHz, $CDCl_3$) δ (ppm)= 7.89 – 7.79 (m, 4H), 7.01 – 6.90 (m, 4H), 5.47 (s, 1H), 4.03 (t, J = 6.6 Hz, 2H), 1.86 – 1.77 (m, 2H), 1.52 – 1.44 (m, 2H), 1.35 (dq, J = 7.3, 3.8 Hz, 4H), 1.26 (s, 1H), 0.94 – 0.88 (m, 3H). ^{13}C NMR (151 MHz, $CDCl_3$) δ (ppm)= 161.26, 124.56, 124.54, 124.38, 124.36, 115.80, 115.77, 114.72, 114.70, 77.27, 77.06, 76.84, 68.36, 31.60, 31.58, 29.19, 25.72, 25.70, 22.63, 22.61, 14.08, 14.06. ESI-MS (m/z): calcd. 299.17 for $C_{18}H_{22}N_2O_2$; found, 299.17 for $[M+H]^+$.

3.4.17.3 Synthesis of Compound 3.3

Compound 3.2 (0.825 g, 1 equiv.) was dissolved in acetone in presence of KOH (0.775 g, 5 equiv.) and the solution was stirred for 30 min. Bromo-methyl acetate (550 µL, 2 equiv.) was carefully added to the reaction mixture and was refluxed under argon atmosphere overnight. Completion of the reaction was monitored by TLC. The mixture was concentrated under reduced pressure and the yellow solid was dissolved in DCM and washed with brine. DCM layer was concentrated under reduced pressure to get a yellow product which was dissolved in dry THF with an excess amount of NaOH flakes. Once all the ester was hydrolysed, THF was removed and the product was recovered by acidic

precipitation. The precipitate was thoroughly washed with water and dried (Yield = 99%). ^{1}H NMR (600 MHz, DMSO-d_6) δ(ppm)= 13.13 (s, 1H), 7.88 – 7.78 (m, 4H), 7.10 (m, 4H), 4.80 (s, 2H), 4.06 (t, J= 6.5 Hz, 2H), 1.74 (p, J= 6.8 Hz, 2H), 1.43 (t, J= 7.6 Hz, 2H), 1.32 (m, 4H), 0.91 – 0.86 (m, 3H). ^{13}C NMR (151 MHz, DMSO-d_6) δ(ppm)= 175.14, 166.22, 165.08, 151.69, 151.24, 129.46, 129.26, 73.15, 69.90,3 6.20, 33.78, 33.37, 27.30, 19.15. ESI-MS (m/z): calcd. 357.17 for $C_{20}H_{24}N_2O_4$; found, 357.18 for $[M+H]^+$.

3.4.17.4 Synthesis of Compound 3.4

Fmoc-Lys(Boc)-OH (2.16 g, 1 equiv.), HOBT (0.68 g, 1.1 equiv.) HBTU (0.97 g, 1.1 equiv.) and DIPEA (0.650g, 1.1 equiv.) were taken in dry DCM under argon atmosphere and stirred for 30 min at 0 - 5 °C. H-Cys(Trt)NH2 solution (1.82g, 1 equiv.) in dry DCM, was added to the mixture under cold condition and was allowed to come to room temperature. After 24 h, the reaction mixture was extracted with DCM, washed with brine solution, and the organic layer was dried over anhydrous Na_2SO_4. After evaporating the DCM, the crude mixture was purified using column chromatography. The product obtained was a light yellow solid (yield = 65%). ^{1}H NMR (600 MHz, $CDCl_3$) δ(ppm)= 7.78 (d, J= 7.6 Hz, 2H), 7.59 (dd, J= 7.6, 2.9 Hz, 2H), 7.42 (d, J= 7.8 Hz, 8H), 7.33 – 7.27 (m, 8H), 7.20 (t, J= 7.2 Hz, 3H), 6.66 (s, 1H), 6.35 (s, 1H), 5.83 (s, 1H), 5.57 (s, 1H), 4.39 (d, J= 6.9 Hz, 2H), 4.18 (t, J= 6.9 Hz, 2H), 4.09 (s, 1H), 3.16 – 2.99 (m, 2H), 2.78 (s, 1H), 2.65 – 2.54 (m, 1H), 1.87 (s, 4H), 1.45 (s, 13H), 1.35 (s, 2H); ^{13}C NMR (151 MHz, $CDCl_3$) δ (ppm)= 172.24, 171.89, 144.41, 129.63, 128.19, 127.90, 127.89, 127.25, 127.02, 125.18, 120.12, 67.29, 53.57, 52.02, 47.23, 33.20, 29.78, 28.56, 22.27. MALDI-TOF (m/z): calcd. 812.36 for $C_{48}H_{52}N_4O_6S$; found, 835.43 for $[M+Na]^+$.

3.4.17.5 Synthesis of Compound 3.5

Compound 3.4 (2.43 g, 1 equiv.) was dissolved in DCM (25 mL), to which triethyl amine (5 mL, excess) was added and stirred for 36 h at room temperature. The reaction was stopped when the spot of the starting material disappeared on TLC plate. The reaction mixture was extracted with DCM, washed with brine solution, and the organic layer was dried over anhydrous Na_2SO_4. DCM was evaporated and the product was purified using column chromatography to obtain a white solid (yield = 95%). ^{1}H NMR (600 MHz, $CDCl_3$) δ(ppm)= 7.73 (s, 1H), 7.40 (d, J= 7.8 Hz, 6H), 7.28 (t, J= 7.6 Hz, 6H), 7.21 (t, J= 7.3 Hz, 3H), 6.25 (s, 1H), 5.56 (s, 1H), 4.62 (s, 1H), 3.99 (s, 1H), 3.35 (s, 1H), 3.11 (s, 1H), 3.05 (s, 1H), 2.67 (dd, J= 13.1,

8.1 Hz, 1H), 2.61 (dd, J= 13.0, 5.6 Hz, 1H), 1.76 (s, 1H), 1.42 (s, 13H), 1.37 (t, J= 7.3 Hz, 2H); ^{13}C NMR (151 MHz, $CDCl_3$) δ(ppm)= 175.56, 172.24, 144.41, 129.60, 128.06, 126.89, 67.15, 54.91, 51.73, 46.11, 34.46, 33.11, 29.85, 28.45, 22.75. MALDI-TOF (m/z): calcd. 590.29 for $C_{33}H_{42}N_4O_4S$; found, 613.25 for $[M+Na]^+$.

3.4.17.6 Synthesis of Compound 3.6

Compound 3.3 (0.5 g, 1 equiv.), HOBT (0.2 g, 1.1 equiv.), HBTU (0.585 g, 1.1 equiv.) and DIPEA (0.2 g, 1.1 equiv.) were taken in dry DCM, cooled to 0 °C and stirred for 30 min. Compound 3.5 (0.91 g, 1.1 equiv.) was added to the mixture and the reaction was allowed to come to room temperature and continued to stir overnight. The reaction mixture was then concentrated on a rotary evaporator and the crude mixture was purified by column chromatography using 1% MeOH-DCM as mobile phase (yield = 32%). ^{1}H NMR (600 MHz, $CDCl_3$) δ(ppm)= 7.92 – 7.86 (m, 4H), 7.43 – 7.38 (m, 6H), 7.31 – 7.25 (m, 7H), 7.25 – 7.16 (m, 4H), 7.05 – 6.98 (m, 4H), 6.91 (s, 1H), 6.17 (s, 1H), 5.70 (s, 1H), 4.80 (s, 1H), 4.54 (d, J= 16.1 Hz, 2H), 4.05 (t, J= 6.6 Hz, 2H), 3.11 – 2.96 (m, 2H), 2.75 (dd, J= 13.1, 7.4 Hz, 1H), 2.60 (dd, J= 13.1, 5.5 Hz, 1H), 2.04 (s, 3H), 1.85 – 1.81 (m, 2H), 1.73 – 1.58 (m, 1H), 1.54 – 1.46 (m, 2H), 1.42 (s, 11H), 1.37 (h, J= 3.9 Hz, 4H), 1.32 – 1.26 (m, 2H), 0.96 – 0.90 (m, 3H). ^{13}C NMR (151 MHz, $CDCl_3$) δ(ppm)= 171.15, 168.14, 165.77, 161.50, 158.61, 156.14, 147.96, 146.76, 144.28, 129.54, 128.10, 126.95, 124.54, 115.01, 114.70, 68.36, 67.25, 52.65, 52.17, 40.00, 38.63, 33.18, 31.59, 29.18, 28.46, 25.71, 22.62, 22.37, 14.07. MALDI-TOF (m/z): calcd. 929.45 for $C_{53}H_{64}N_6O_7S$; found, 929.49 for $[M+H]^+$.

3.4.17.7 Synthesis of Azo-KC

Compound 3.6 was taken in 80% TFA in DCM containing 1% TES and stirred at room temperature for 1h. The solvent and TFA was removed under reduced pressure and the crude material was slowly added to cold dry diethyl ether to precipitate Azo-KC. The solid was washed several times with diethyl ether and the purity of the solid was checked by analytical HPLC. Yield = 98%. 1H NMR (600 MHz, DMSO-d_6) δ(ppm)= 8.28 (d, J= 8.0 Hz, 2H), 8.13 (d, J= 8.1 Hz, 1H), 7.88 – 7.79 (m, 4H), 7.61 (s, 2H), 7.45 (s, 1H), 7.23 (s, 2H), 7.12 (dd, J= 13.1, 8.8 Hz, 4H), 4.69 (d, J= 9.7 Hz, 2H), 4.39 – 4.33 (m, 2H), 4.07 (t, J= 6.7 Hz, 2H), 2.97 (s, 4H), 2.76 – 2.72 (m, 2H), 1.74 (d, J= 6.0 Hz, 2H), 1.63 (s, 3H), 1.57 – 1.47 (m, 4H), 1.44 (s, 3H), 1.36 – 1.28 (m, 6H), 1.25 (d, J= 10.4 Hz, 2H), 0.92 – 0.87 (m, 3H). ^{13}C NMR (151 MHz, DMSO-

d_6) δ (ppm)= 161.54, 160.30, 147.13, 146.55, 124.67, 124.48, 115.78, 115.47, 115.45, 68.45, 67.43, 65.37, 55.23, 52.72, 52.43, 39.19, 31.69, 31.44, 29.03, 27.05, 26.54, 25.60, 22.56, 22.51, 15.62, 14.35. MALDI-TOF (m/z): calcd. 587.29 for $C_{29}H_{42}N_6O_5S$; found, 587.30 for $[M+H]^+$.

Chapter 4: Charge Transfer Complexation Aided Control over the Reaction Pathway

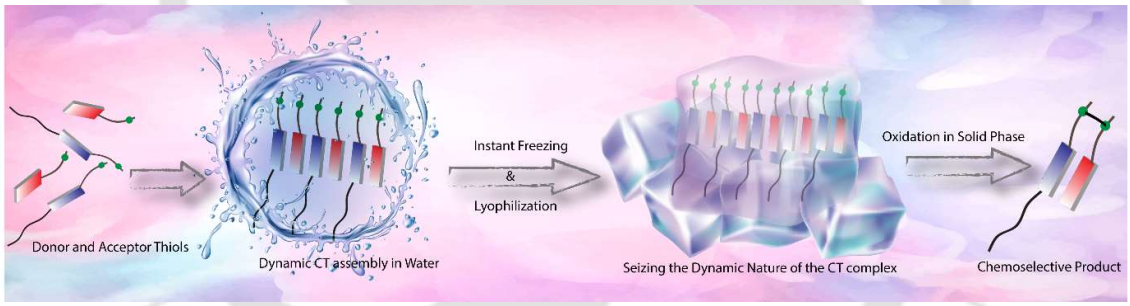

4.1 Introduction

CT assemblies have comprehensively been used in aqueous dynamic combinatorial library to create molecular loops, knots and catenanes.[202-207] In solution, the association constant for D-A assemblies range between 10^1-10^3 M^{-1}.[208, 209] The molecules thus remain in a dynamic motion between the aggregated (CT state) and monomeric state.[210, 211] The dynamic nature of CT complexes does not allow the alternate D-A arrangements to get fully translated to covalently linked D-A when appropriate organic transformation is carried out in solution phase. Any such chemical transformation in solution phase thus result in low yields of the desired products as the dynamicity of constituent molecules also leads to orthogonal assemblies between the same molecules (Scheme 4.1A) resulting into undesired products.[203] In order to obtain highly selective product, the dynamicity of the system need to be regulated. Control over these reactions is often obtained by addition of salts or a template which can be removed once the product is formed.[204, 212-214] Though regulating the reaction pathway could be achieved to a certain extent, these approaches cannot stop the formation of undesired orthogonal products significantly.[204, 212, 213]

We hypothesized that, seizing the dynamic nature of the nano-structures formed by CT interactions may allow one to regulate the reaction pathway. Slow-drying of the solutions certainly affect the aggregation pattern and does not reflect the actual nano-structures formed in the solution.[215] The seizing of dynamicity thus can be achieved by bringing these nano-structures out of the solvent by means of instant freezing followed by drying as in case of lyophilization. Owing to instant freezing, alternate D-A arrangement will remain intact in these nano-structures where the reactive groups will be in close proximity to each other. Allowing them to react in the solid state will effectively lead to the formation of a specific product free of other undesired ones (Scheme 1A). However, we also anticipated that the choice of appropriate CT partners as well as their spatial arrangement in the CT complex will also be equally important to bring the reactive groups at close enough proximity to ensure the reaction in solid state.

To this end, unsymmetrical disulfides are of tremendous pharmaceutical importance and at the same time are synthetically extremely challenging.[216-219] It is worth mentioning that disulfide bond formation is a spontaneous process and can be obtained by simple change in pH of the medium.[220] However, mixing two different thiols result in a mixture of all three combinations. Moreover, there is always a possibility of dynamic disulfide exchange to

occur and that has been exploited widely in dynamic covalent chemistry.[220, 221] Thus, methodologies to prepare asymmetric disulfide generally involve functional groups other than thiols and special reagents/reaction conditions.[216, 217, 222-224] For the present work, we chose thiol (-*SH*) as the reactive group based on these facts and also to develop a simple methodology to create asymmetric disulfide exclusively from two different thiols.

4.2 Results and Discussion

4.2.1 Selection of CT Pair

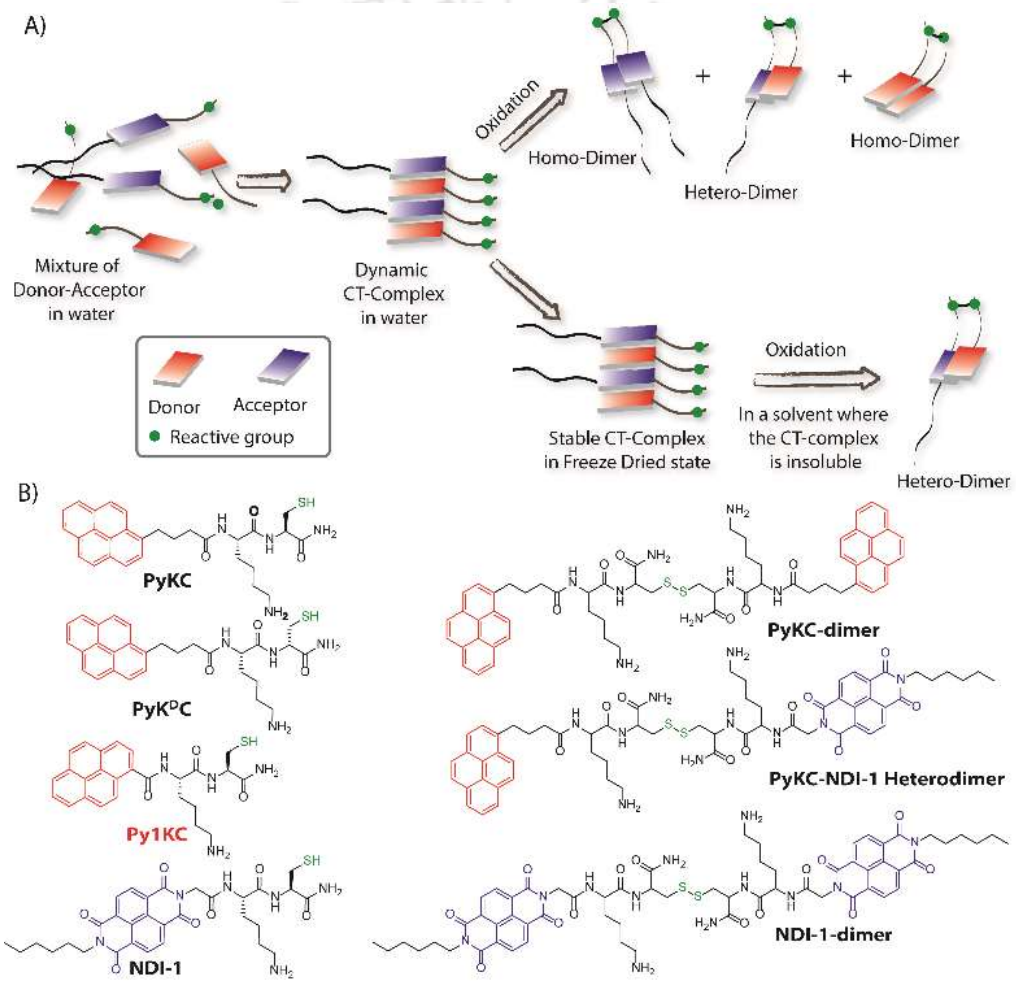

Scheme 4.1 (A) Schematic presentation of the CT-complexation driven protocol to control the chemo-selectivity. (B) Chemical structures of different thiol substrates used for the study and their homo and heterodimers.

To validate the hypothesis, we have taken Py and NDI as the donor and acceptor respectively since they showed strong CT complexation ability.[225] Initially a series (Scheme 4.2) of NDI and Py containing peptide amphiphiles[226] were designed and subjected to DFT calculations to get energy minimized structures of these D-A pairs

in the CT complex states. The molecules were designed in a way to introduce water solubility by incorporating residues like Lysine or Arginine. Presence of Cysteine residues provide the reactive thiol groups for disulfide formation. Incorporation of the hydrophobic tail at one end of NDI moiety ensures that the peptide sequences remain face to face as NDI and Py units form CT complexes (Scheme 4.1A). Amongst all these pairs, **PyKC**[77] and **NDI-1** (Scheme 4.1 and 4.2) were found to have the closest proximity of the -*SH* groups (4.07 Å, Figure 4.1, Table 4.1) in the energy minimized structures of the pairs as obtained from DFT calculations. We envisioned that this distance is close enough to form S-S bond (S-S bond distance is ~2.05 Å) during the planned solid phase oxidation. Moreover, the distance between the π-planes were found to be 3.51 Å indicating possible strong CT interaction between the molecules.

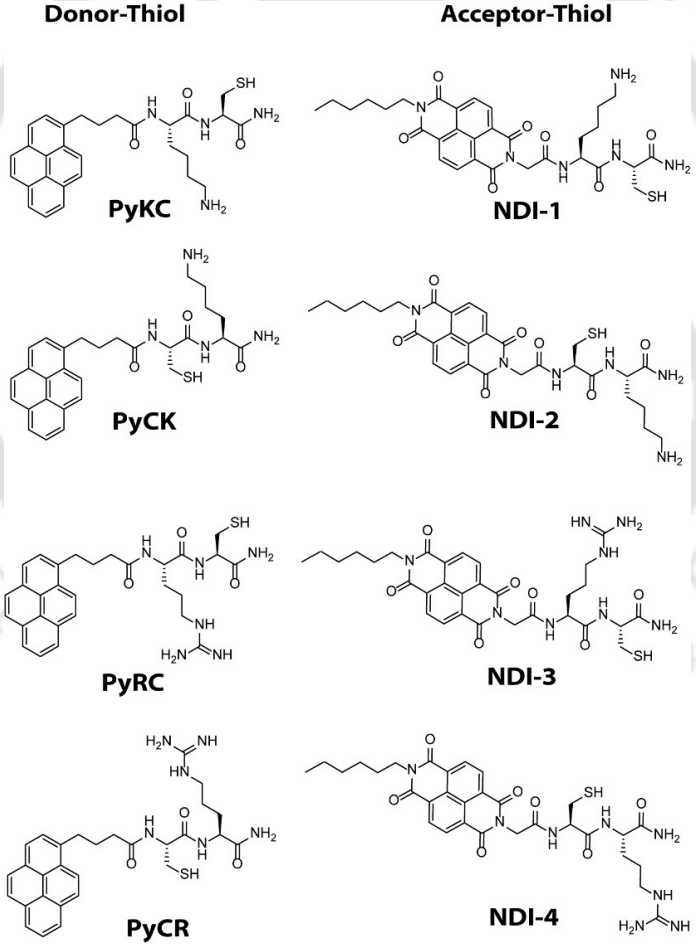

Scheme 4.2 Chemical structures of different NDI and Pyrene containing thiols used for DFT calculations to find the most suitable D-A pair for the study.

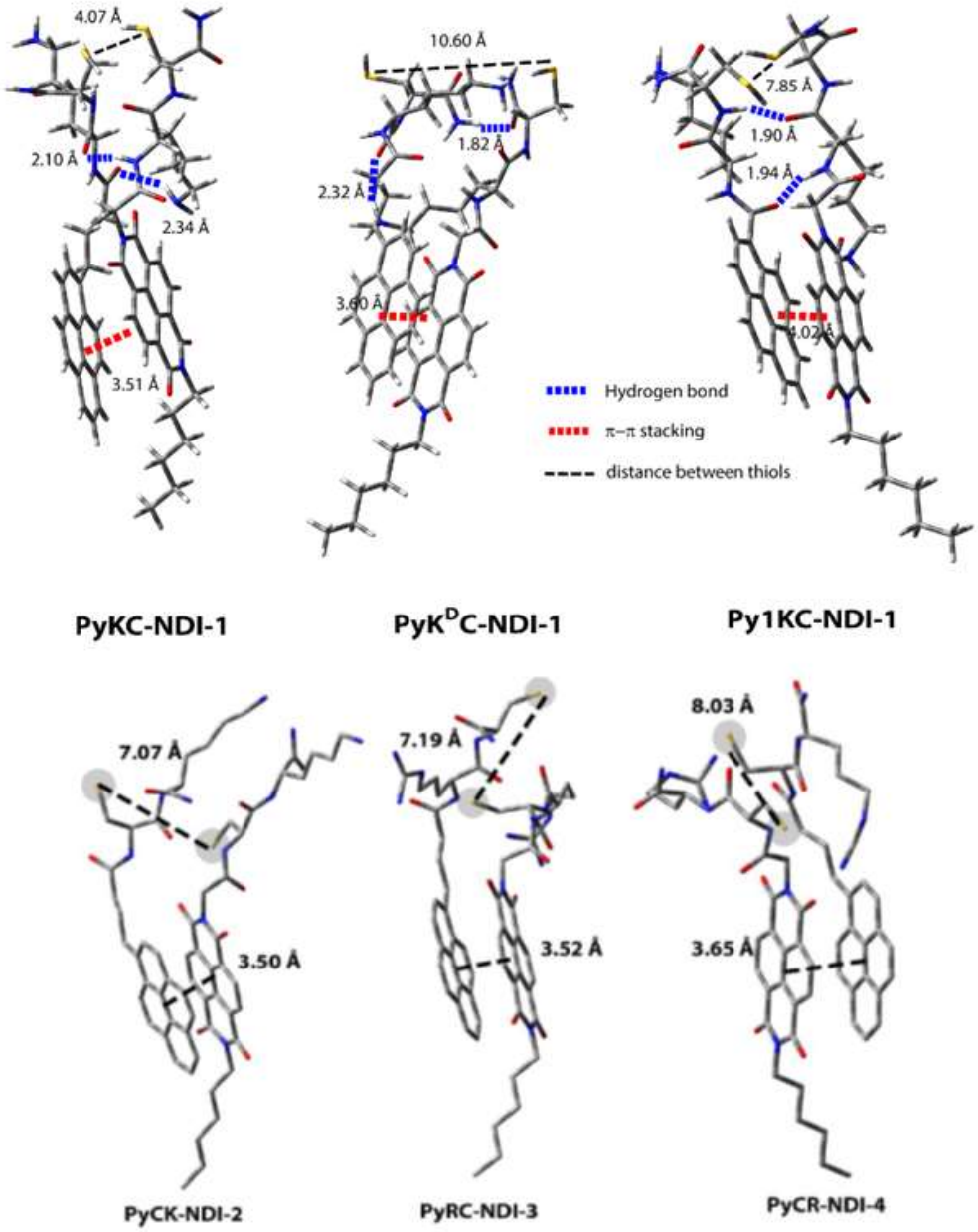

Figure 4.1 Energy minimized structures of different D-A pairs as obtained from DFT calculations showing the distances between the –*SH* groups and between π-rings of the donor and acceptor.

Table 4.1 The distance between the SH groups and π-planes as obtained from the energy minimized CT complexes using DFT calculations.

D-A pair	*SH* – *SH* distance (Å)	π-plane distance (Å)
PyKC – NDI-1	4.07	3.51
PyCK– NDI-2	7.07	3.50
PyRC– NDI-3	7.19	3.52
PyCR– NDI-4	8.03	3.65
PyK^{D}C– NDI-1	10.60	3.60
Py1KC – NDI-1	7.85	4.02

Based on these results, **PyKC** and **NDI-1** were selected and synthesized using solid phase peptide synthesis. Incorporating a lysine unit within the cysteine and interaction building blocks helps in the solubility of the peptides in aqueous medium. The small chain in the **NDI-1** peptide assists to gain the proper orientation of two peptides to stack better and proximate closer spatial arrangement between two sulfhydryl forming disulfide bonds. Two different derivatives of the Pyrene are also attached with KC unit as shown below, these two peptides are kept as conformational competitor for the **PyKC**-**NDI-1** pair and credits the justification for the best CT pair to work with for the best ever synthetic yield at the end.

4.2.2 Analytical Investigation on CT Complexation and Co-Assembly of the Peptides

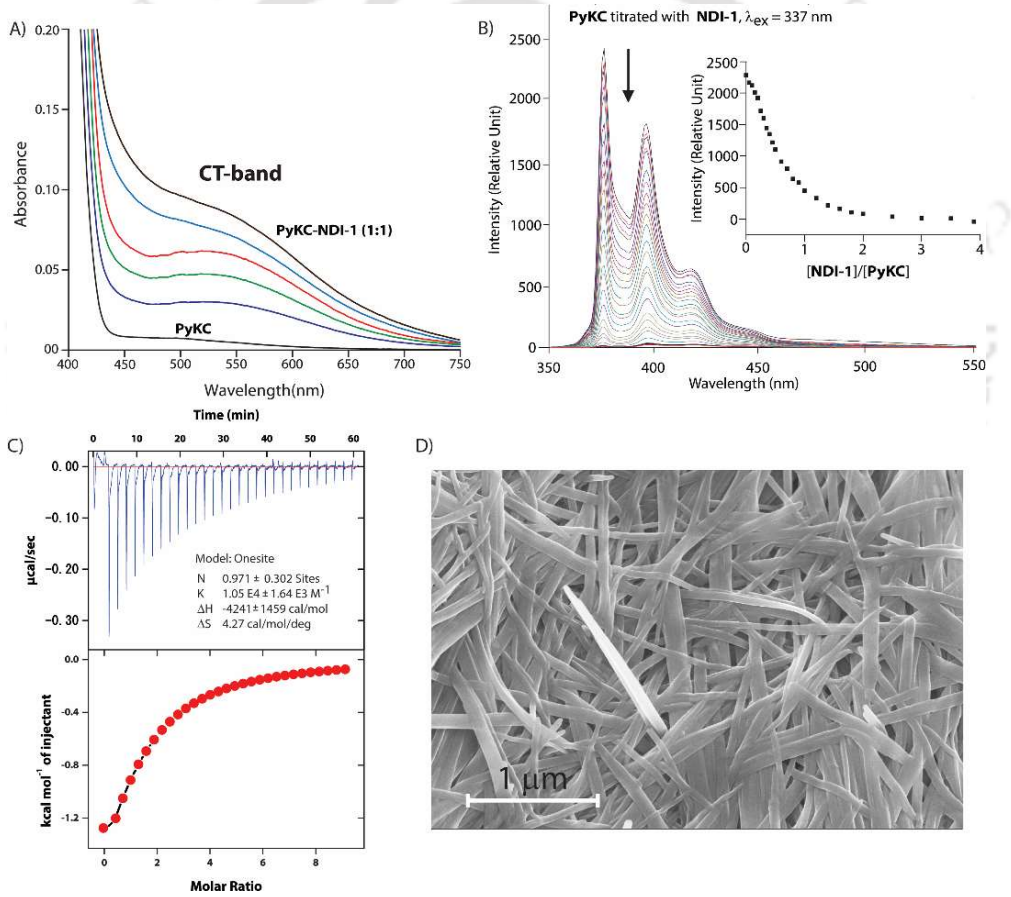

Figure 4.2 (A) UV-Visible spectra of **PyKC** (0.1mM) in presence increasing amounts of **NDI-1** showing the appearance of CT-band. (B) Emission spectra of **PyKC** when titrated with **NDI-1** showing the quenching of the emission. Inset: the changes in emission intensity at 376 nm against the molar ratio of **PyKC** and **NDI-1**. (C) Thermogram (top) and binding isotherm (bottom) of titration of **PyKC** with **NDI-1** at 298 K. (D) FESEM image of a freeze dried sample of an aqueous mixture of **PyKC** with **NDI-1** (1:1) containing 1% TFA.

The CT complexation between these molecules was monitored using UV-visible spectroscopy. As can be seen from Figure 4.2A, an equimolar mixture of the compounds

resulted in appearance of a new broad band at 550 nm which is the characteristic CT-band for Py-NDI pair.[225] A concentration dependent study showed that below 0.05 mM individual concentration, no CT-band could be observed indicating 0.05 mM as the critical concentration below which these molecules probably fail to experience CT interaction. A titration experiment monitored at the pyrene emission maxima (376 nm) of **PyKC** showed a continuous quenching of the emission as the concentration of **NDI-1** increases. A saturation obtained at a molar ratio of 1 suggesting a 1:1 binding between **PyKC** and **NDI-1** (Figure 4.2A and B). ITC data showed a 1:1 complexation as well with an association constant of $(1.05 \pm 0.164) \times 10^4$ M^{-1} (Figure 4.2C)

Moreover, ^{1}H NMR spectra (Figure 4.3A) of the mixture showed prominent up-field shifts along with broadening of the aromatic signals for both the components when they were mixed together in equimolar ratio. These results confirm strong CT interaction between the Py and NDI units of **PyKC** and **NDI-1** respectively. Additionally, some of the amide-NH and NH_2 protons of both the molecules showed down-field shift in the complex form which can only be resulted if they are involved in hydrogen bonding. The intermolecular hydrogen bonding between **PyKC** and **NDI-1** is also prominent from the FTIR spectroscopic analyses of the pure molecules and the complex (Figure 4.3B). Both, **PyKC** and **NDI-1** showed non-hydrogen bonded N-H stretching at 3434 and 3433 cm^{-1} respectively. Whereas, the CT complex of the compounds showed a combination of non-hydrogen bonded and hydrogen bonded stretching at 3433 and 3270 cm^{-1} respectively. Evidence of hydrogen bonding is also present in the amide-I and amide-II stretching region. The prominent amide signals of the parent compounds become a broad peak at ~1663 cm^{-1} which suggests possible intermolecular hydrogen bonding. In this regard, analyses of the CT structure obtained from DFT calculation also suggests possible hydrogen bonding (2.10 Å) between the C=O of the Lys residue of **PyKC** and NH of the Lys residue of **NDI-1** (Figure 4.1).

Another possible hydrogen bond is also found between the side chain NH_2 of Lys (**NDI-1**) and the carbonyl group of the butyric acid residue of **PyKC** (2.34 Å). All these experimental and theoretical calculations strongly suggest multiple intermolecular hydrogen bonding between **PyKC** and **NDI-1**. It is to be noted that the calculated complexation energy value (-43.26 $kcalmol^{-1}$) is relatively higher than that of a typical

CT complex. The presence of these additional stabilizing interactions also explains this higher value.

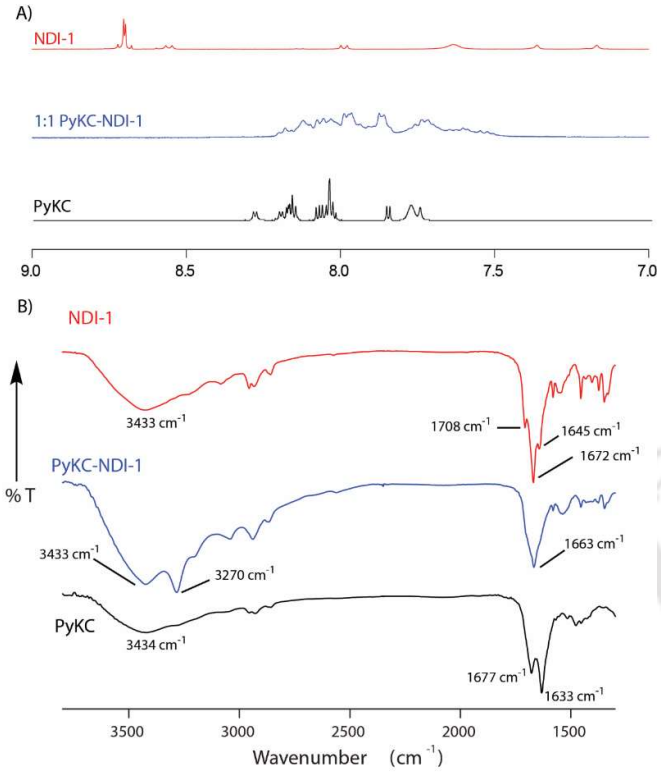

Figure 4.3 (A) ^{1}H NMR spectra (in 10% DMSO-d_6 in D_2O) of **NDI-1**, **PyKC** and a 1:1 mixture of these two compounds showing the up-field shift of aromatic protons of both compounds upon mixing. (Since, the pyrene protons of **PyKC** as well as the NH/NH_2 protons do not appear in D_2O, we took the help of 10% DMSO-d_6). B) FTIR spectra of **PyKC**, **NDI-1** and CT complex of **PyKC** and **NDI-1.**

4.2.3 CT Complexation Assisted Unsymmetrical Disulfide Formation

As the CT-complexation between **PyKC** and **NDI-1** is established, the solution phase disulfide formation of the CT complex was tested. The pH of an equimolar (1 mM) aqueous solution of these two molecules was then adjusted to neutral to allow the disulfide bonding. After 24 hours of incubation under ambient condition the solution was monitored by analytical HPLC using calibration plots of all three possible dimers (Scheme 4.1 and Figure 4.4). Although the formation of heterodimer (**PyKC-NDI-1 heterodimer**) was found to be predominant, other two homo-dimers (**PyKC-dimer** and **NDI-1-dimer**) formed in a substantially good proportion and followed the statistical ratio (2:1:1) of a dynamic system (Scheme 4.1 and Table 4.2).

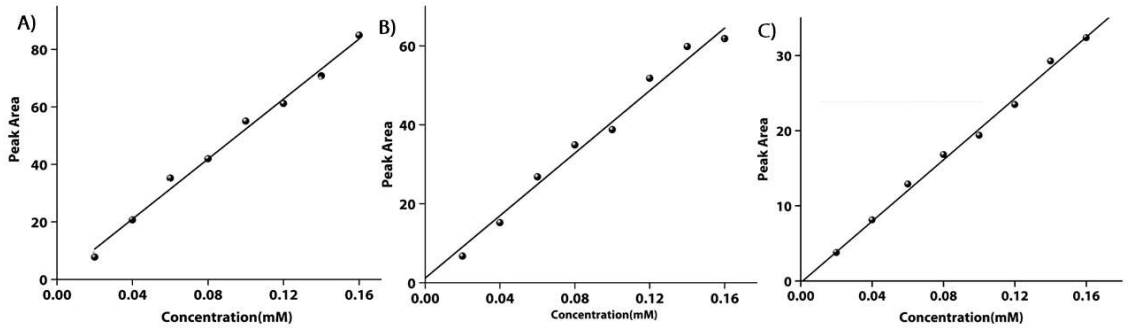

Figure 4.4 Calibration plots of (A) **PyKC-dimer,** (B) **NDI-1 dimer** and (C) **PyKC-NDI-1 heterodimer** respectively.

In order to verify our hypothesis mentioned earlier, the aqueous solution of a 1:1 mixture (in presence of 1% TFA, to prevent disulfide formation (control experiments in the experimental section)[228] of **PyKC** and **NDI-1** (1 mM individual concentrations) was instantly frozen using liquid nitrogen and lyophilized to get the solid. HPLC and ESI-MS analyses of the solid showed absence of any dimer. FESEM images of the dried sample revealed formation of high aspect ratio nano-tapes as can be seen in Figure 4.2D. The nano structure obtained is a result of the CT-interaction between NDI and Py which stacked in an alternate fashion and grown along the long axis. At this point, it was important find a suitable solvent for the planned oxidation reaction using the lyophilized powder.

Table 4.2 Oxygen solubility in various organic solvents.

Reaction condition/solvent	Oxygen Solubility (mol dm^{-3})	Starting concentrations of the donor and acceptor thiols before lyophilization	Time (h)	% heterodimer	% conversion
Aqueous solution	1.22×10^{-3} *a*	1 mM	24	48.9	100
Aerial	-	1 mM	20	98.5	5
Cyclohexane	1.28×10^{-3} *b*	1 mM	20	98.2	100
Cyclohexane	1.28×10^{-3} *b*	0.1 mM	20	98.1	100
Cyclohexane	1.28×10^{-3} *b*	0.01 mM	20	45.5	20
Hexane	2.25×10^{-3} *b*	1 mM	20	98.0	100
Benzene	8.20×10^{-4} *b*	1 mM	20	97.5	71
DCM	7.09×10^{-4} *b*	1 mM	20	97.8	56

a at 298 K and 101.3 kPa; b 298.2 K and 101.3 kPa.

The essential criteria were that the solvent must have sufficiently high oxygen solubility and all of the components and the lyophilized powder must be insoluble in the solvent. A thorough literature survey showed cyclohexane or hexane could be appropriate choices for this purpose as their oxygen solubilities were found to be significantly high (at 298.2 K and 101.3 kPa, 1.28×10^{-3} and 1.25×10^{-3} $moldm^{-3}$ for

cyclohexane and hexane respectively).[229] As expected, no noticeable solubility was observed for both **PyKC**, **NDI-1** as well as lyophilized powder in these two solvents. Based on these observations, the solid nanotapes were then suspended in cyclohexane. After shaking the mixture at 100 rpm at room temperature for 24 hours, the suspension was centrifuged and dried. The material was redissolved in water containing 1% TFA to avoid any further oxidation and immediately analysed by analytical HPLC. Interestingly, a single peak corresponding to the **PyKC-NDI-1 heterodimer** with 98.2% yield (Figure 4.4A) was obtained. ESI-MS of fractions from this peak confirmed the heterodimer formation. Negligible amounts of the homo-dimers (<0.25%) were obtained supporting the successful display of the hypothesis. Further, a time dependent study was performed keeping the experimental conditions unaltered. As can be seen from Figure 4.5A and B, the reaction completes within 20 hours.

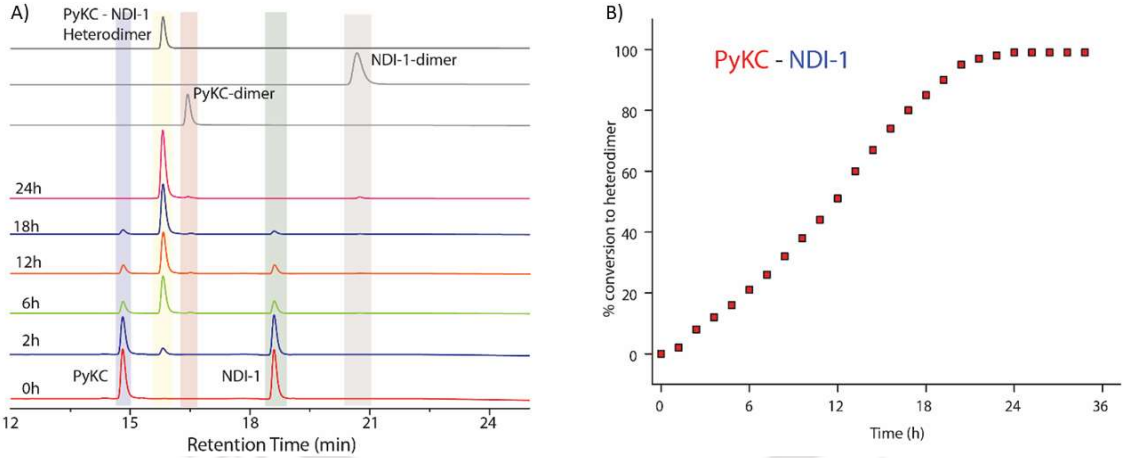

Figure 4.5 (A) Time dependent chromatograms showing the exclusive formation of **PyKC-NDI-1 heterodimer** using the present protocol. (B) % conversion to the heterodimer with time as obtained from (A).

The solid retained its tape like morphology after the reaction (Figure 4.2D). Interestingly, the concentration at which the starting materials were mixed to form CT complexes plays a significant role toward the success of the presented method. At 0.1 mM starting concentration, both, conversion and the chemo-selectivity were similar to that for the 1 mM starting concentration. As we reduced the starting concentration to 0.01 mM, no selectivity toward heterodimer was observed and the overall conversion also dropped to ~ 20% (20 hours, Table 4.2). At this concentration, neither any CT band appeared in the absorption spectra nor could any particular

morphology be seen in the lyophilised solid. The dithiol formation in cyclohexane is definitely assisted by the dissolved oxygen. It is to be noted that the parent compounds as well as their lyophilized CT complex is insoluble in cyclohexane mainly due to the presence of polar Lys residues. However, the hydrophobic segments of the CT complex plausibly make the complex partially dissolved which further strengthen the CT complex. This partial solubilisation does not impart any change in the alternate D-A arrangement and consequently to the morphology but allows the dissolved oxygen molecules to oxidize the thiol groups which are at close proximity.

To further optimize the reaction protocol, other organic solvents (hexane, DCM, benzene) were used in place of cyclohexane.[229] In term of the reaction completion time, cyclohexane and hexane showed similar result while in other solvents the reaction was found to be little slower as the oxygen solubility in these solvents are lower (Table 4.2). To compare with the aerial oxidation, the solid was kept in open air for 24 hours and analysed to observe that though heterodimer was the sole product, only ~5% material was converted within this time frame.

As discussed in the introduction, we assumed that the spatial arrangement of the –*SH* group within CT complex might play a crucial role toward the success of the methodology. To test that, other analogues were prepared (Scheme 4.1B). The stereochemistry of the Cys residue of **PyKC** was reversed to make **PyK^{D}C** and tested by combining it with **NDI-1**; however, CT-band appeared in the UV-Visible spectra and 1:1 binding was observed from fluorescence experiment (Figure 4.6A and B). Further, the spacer between pyrene and peptide sequence is reduced in case of **Py1KC**. Similar to the previous case, 1:1 CT complexation was confirmed from UV-visible and emission experiments (Figure 4.6A and C). Next, powder XRD analyses were performed for all three combinations (Figure 4.6D). The lyophilized powders of both, **PyKC–NDI-1** and **PyK^{D}C–NDI-1** showed strong π-π interactions with similar stacking distances (3.58 and 3.60 Å respectively). However, in case of **Py1KC–NDI-1** pair, the distance was significantly higher (3.93 Å). Due to the absence of any spacer between Py and the peptide unit, for **Py1KC**, the stacking is presumably not as strong

as in the other two cases. To get a confirmed idea, the lyophilised powder of 1:1 mixture of **PyK^{D}C–NDI-1** and **Py1KC–NDI-1** was subjected for FESEM analyses.

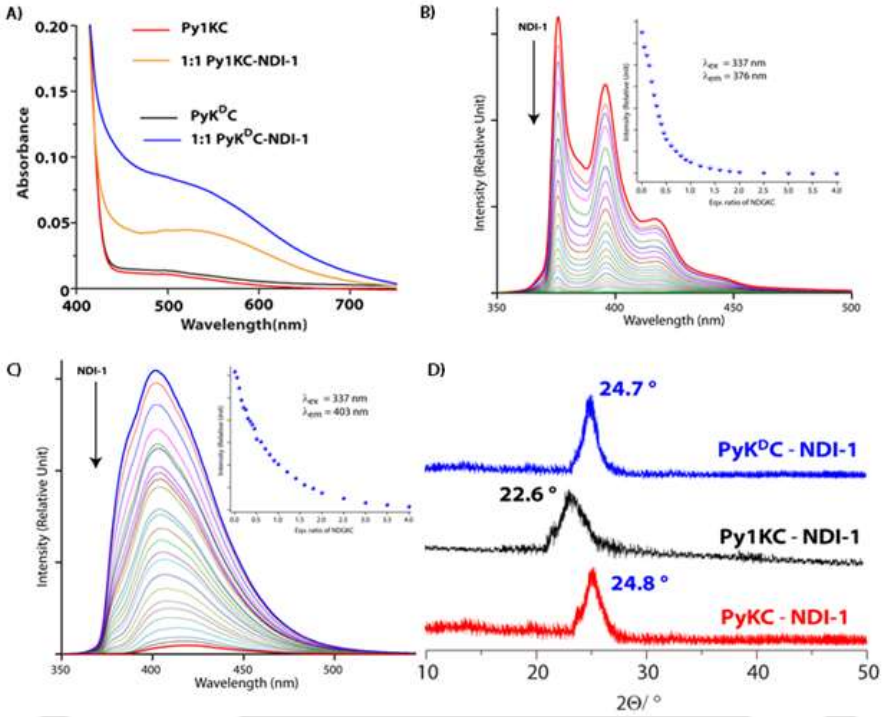

Figure 4.6 (A) UV-Visible spectra of **PyK^{D}C** (1 mM) or **Py1KC** against **NDI-1** showing the appearance of CT-band. (B) Emission spectra of **PyK^{D}C** when titrated with **NDI-1**, (C) Emission spectra of **Py1KC** when titrated with **NDI-1**. In both Insets (B and C): the changes in emission intensity **Py** against different molar ratio. (D) PXRD data of lyophilized 1:1 mixture of **PyKC**+**NDI-1**, **PyK^{D}C**+**NDI-1**, and **Py1KC**+**NDI-1** measured at room temperature.

The microscopic images of the freeze-dried samples showed needle like aggregates for **PyK^{D}C–NDI-1** and small rod like aggregates were observed for **Py1KC-NDI-1** pair (Figure 4.7A and B). These observations indicate possible different aggregation pattern compared to the **PyKC**-**NDI-1** mixture. Importantly, when present protocol was applied for these two combinations, mixture of all three possible products were observed with relatively low conversion rate (3-5% in 24 hours). To get an explanation for the failures in cases of **PyK^{D}C–NDI-1** and **Py1KC–NDI-1** pairs, additionally, the DFT calculations for energy minimized structures of these pairs were performed. The distances between the Py and NDI planes calculated for **PyK^{D}C–NDI-1** was found to be 3.60 Å which is very similar to that obtained from PXRD analyses and close to what found in case of **PyKC–NDI-1** (3.58 Å).

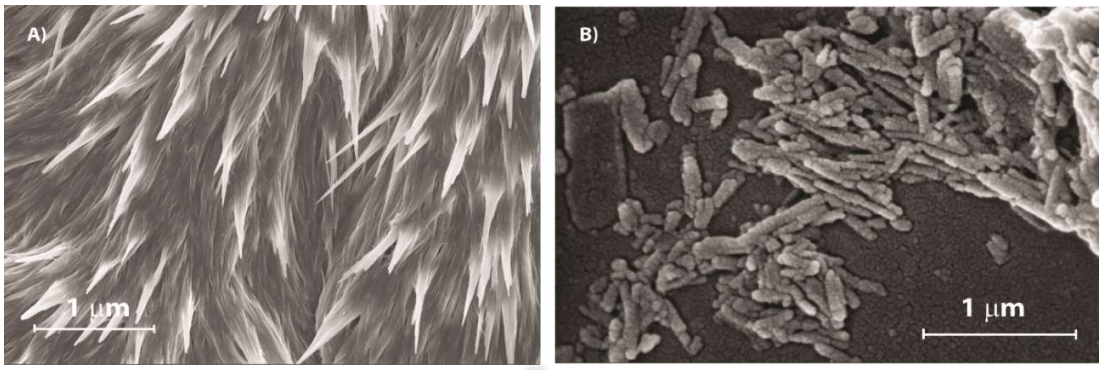

Figure 4.7 (A) and (B) FESEM images of the freeze-dried samples obtained from the combinations of **NDI-1** and (A) **Py^{D}KC** and (B) **Py1KC**.

However, the orientation of the -*SH* groups are entirely in the opposite direction than to that of **PyKC-NDI-1** pair and the distance between the -*SH* groups was found to be considerably high (10.60 Å). In case of **Py1KC**, the π-planes were found to be 4.02 Å apart which is similar to the PXRD data of 3.93 Å. Due to the absence of any spacer, the -*SH* groups are staying far apart with an inter-atomic (S – S) distance of 7.85 Å.

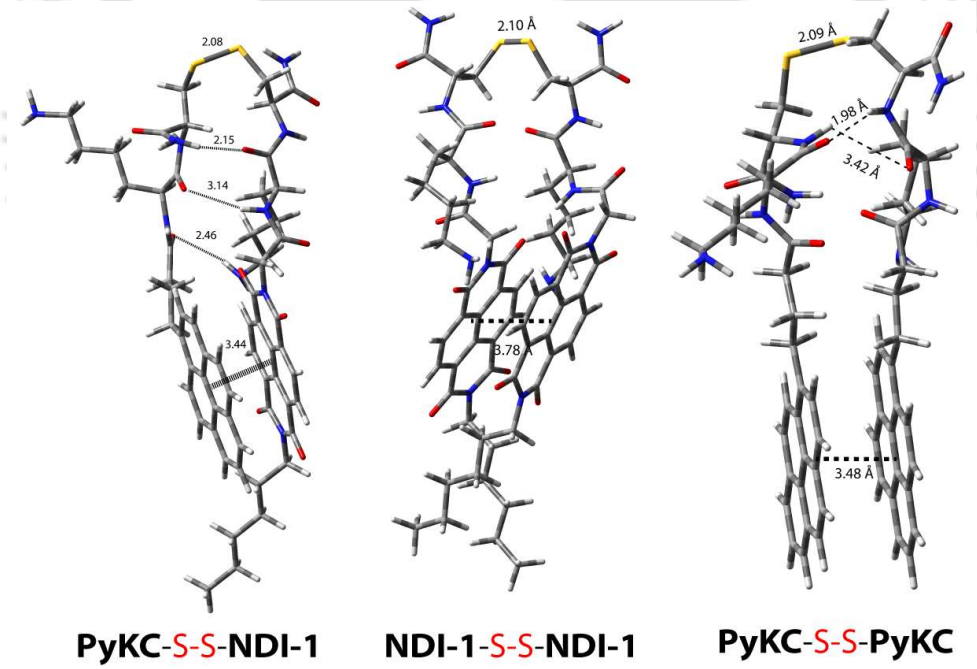

Fig. 4.8 Energy minimized structures of different disulfide linked homo and heterodimers of **PyKC** and **NDI-1** as obtained from DFT calculations.

In order to react in the solid phase, the functional groups must be in close proximity. In case of **PyK^{D}C–NDI-1**, due to the change in stereochemistry of Cys, -*SH* groups are oriented in opposite directions and far from each other which prevent them to form disulfide bonds. On the other hand, owing to the shorter spacer in **Py1KC**, an

unfavourable packing for **Py1KC–NDI-1** keeps the –*SH* groups far apart. All these data explain the lower yield and lack of selectivity observed for these two pairs using the present prototype. It is clear that our initial assumption based on the DFT calculation of **PyKC–NDI-1** pair was valid. The close proximity of the -*SH* groups for **PyKC–NDI-1** allows the solid phase oxidation whereas that is certainly not the case for other two pairs (Figure 4.8). Thus, though CT interactions are present, the other two combinations failed to result in formation of heterodimers selectively. These results evidently demonstrate the critical role of proper orientation of the functional groups in order to successful implementation of the methodology.

4.3 Conclusion

Unsymmetrical disulfides are of tremendous pharmaceutical importance and at the same time are synthetically extremely challenging.[216-219] It is worth mentioning that disulfide bond formation is a spontaneous process and can be obtained by simple change in pH of the medium.[220] However, mixing two different thiols result in a mixture of all three combinations. Moreover, there is always a possibility of dynamic disulfide exchange to occur and that has been exploited widely in dynamic covalent chemistry. Herein, a novel approach is depicted here to control the S-S dimerization reaction pathway utilizing CT interaction. Freezing the dynamicity of CT-aggregates is the key to achieve the control. However, proper orientation and packing of the reacting molecules is essential for the successful execution of the described methodology. Importantly, the new method opens up the possibility to create new molecules which are otherwise difficult to achieve like the asymmetric disulfides depicted here. Although the presented protocol is fundamentally a new concept, it is worth mentioning that the method is limited to only those systems where the thiol groups are at very close proximity. Thus, for effective execution of this method, the D-A complex must obtain a proper molecular orientation. However, we are in the process of utilizing the methodology with other functional groups and the results will be communicated in due course of time.

4.4 Experimental section

4.4.1 General Information and Materials

NDA, n-hexylamine were procured from Sigma Aldrich (USA) and used without further purification. Rink amide MBHA resin and protected amino acids and coupling reagents were obtained from Novabiochem. HPLC-grade solvents were purchased from Spectrochem (India) and Fisher Scientific (India). To prepare samples, Milli-Q water with a conductivity of less than 2 μScm^{-1} was used. Chromatographic purifications were performed on a Luna 5 µm (C18) column (Phenomenex) using a Dionex Ultimate 3000 HPLC. UV-Visible spectra were recorded on a PerkinElmer Lambda 750 spectrometer, while fluorescence measurements were performed on Fluoromax 4 (Horiba, Japan) spectrophotometer. Standard 10 mm-path quartz cuvettes were used for all spectroscopic measurements. ^{1}H NMR, ^{13}C NMR were recorded with a Bruker Ascend 400 MHz (Bruker, Coventry, UK) spectrometer and referenced to deuterated solvents. ESI-MS were performed with a Q-tof-Micro Quadrupole mass spectrophotometer (Micromass).

4.4.2 UV–Visible and Fluorescence Spectroscopic Studies

Super stock solutions of **PyKC**, **PyK^{D}C**, **Py-1-KC** and **NDI-1** were prepared in 5 mL volumetric flasks by weighing appropriate amounts of the compound and dissolving in water containing 1% TFA. These stock solutions were diluted to the concentrations required for the experiment.

4.4.3 FESEM

The freeze dried samples were casted on a carbon tape and the FESEM images were taken on a Gemini SEM 300 (Sigma Zeiss) instrument.

4.4.4 PXRD Analyses

The PXRD of all the samples were measured on a Bruker D2 Phaser X-ray diffractometer (30 kV, 10 mA). The Bragg peak λ was extracted from the XRD data and the layer thickness d could be obtained according to the Bragg equation $d = \lambda/2\sin\theta$, $\lambda = 0.15405$ nm.

4.4.5 ITC Experiments

The formation constants and thermodynamic parameters for the inclusion complexes were determined via isothermal titration calorimetry using a Nano-ITC instrument from MicroCal. **PyKC** solution (0.1 mM, in water containing 1% TFA) was placed in the (volume = 200 mL). **NDI-1** solution in water containing 1% TFA (each injection, 0.5 µL, 2 mM) was injected from a 40 µL syringe at an interval of 2 min into the reaction cell with stirring at 298 K. The first data point was omitted from the data set for curve fitting. All solutions were degassed prior to titration. The data were fitted to a theoretical titration curve using software supplied by Microcal.

4.4.6 DFT Calculations

The M06 family of functions was chosen over other conventional DFT functions as they are proven to be more accurate toward geometries and energy calculations for a variety of dispersion-dominated systems like DNA base-pair stacks and D-A CT complexes.1 HOMO and LUMO orbital energies were obtained using the density functional theory (DFT) at the B3LYP/6-31G (d,p) accuracy level using the Gaussian 09 package of programs.

4.4.7 General Procedure of Hetero-Dimerization

The method described here is for **PyKC-NDI-1** pair.

In a typical experiment, 200 µL solutions of **PyKC** and **NDI-1** (both 1 mM) prepared in water (containing 1% TFA) were mixed and incubated for 12 hours at room temperature. The generation of pink color indicates the formation of charge transfer complex. The solution was then dipped into liquid nitrogen and freeze-dried. 2 mL of cyclohexane was then added to the freeze dried solid and the sample was shaken at 100 rpm at room temperature. Cyclohexane was added to the sample at different time intervals to make up any loss due to evaporation. After the required time period, the samples were centrifuged, solvents were removed and the solid was dried under reduced pressure. The dried samples were then re-dissolved in water (containing 1 % TFA) and analysed using analytical HPLC. The % yield of the different dimers were calculated using calibration curves obtained from the pure samples. For the preparation of **PyKC-NDI-1** heterodimer, the same process was used in a larger scale and the heterodimer was purified using semi-preparative HPLC and

characterized using ESI-MS. ESI-MS calcd. For $[M+H]^+$, $C_{60}H_{71}N_{10}O_{10}S_2^+$: 1155.48, found 1155.48, and 578.24 $[M^{2+}]$.

4.4.8 Syntheses of Materials

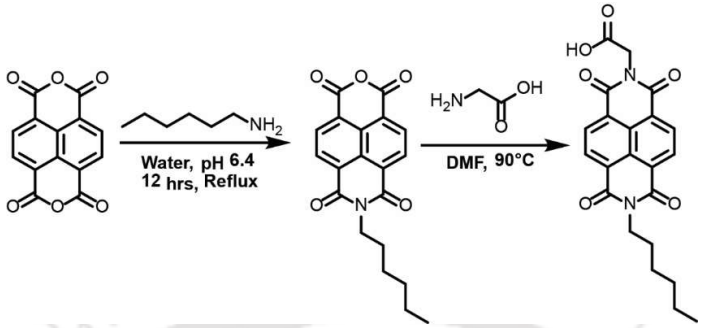

Scheme 4.3 Synthetic scheme for **Hexyl-NDI-Glycine.**

Hexyl-NDI-Glycine

Hexyl-NDI-Glycine was prepared according to our previously reported procedure following the steps mentioned in Scheme S1.[30]

4.4.8.1 Hexyl-NMI

NDA (2.0 g, 7.46 mmol) was taken in a 500 mL round bottom flask and 350 mL of water was added to the solid. 1 M aqueous KOH solution (35 mL) was then added to the mixture and heated with vigorous stirring until the compound completely dissolved. Once the solution became clear, the pH was adjusted to 6.4 by adding 1 M H_3PO_4. To this solution, n-hexyl amine (0.98 ml, 7.46 mmol) was added and the pH of the solution was again adjusted to 6.4 with 1M H_3PO_4. The mixture was refluxed overnight. It was then allowed to cool to room temperature and filtered. To the filtrate, acetic acid (5 mL) was added to afford a solid precipitate, which was then filtered and washed with more water and dried over silica gel under vacuum to get 1.47g (56% yield) of the product as an off-white solid. ^{1}H NMR (DMSO-d_6, 600 MHz): δ (ppm) = 8.56-8.54 (d, J=12Hz, 2H), 8.19-8.18 (d, J= 6Hz, 2H), 4.04-4.01 (t, J= 9Hz, 2H), 1.65-1.61 (m, J= 6Hz, 2H), 1.35-1.28 (m, J= 6Hz, 6H), 0.86- 0.84 (t, J= 6Hz, 3H).

4.4.8.2 Hexyl-NDI-Glycine

Hexyl-NMI (1 g, 2.85 mmol) was first dissolved in DMF (15 mL), by heating at 60 °C followed by the sequential addition of Glycine (0.44 g, 5.87 mmol) and DIPEA (0.98 ml, 5.87 mmol). The reaction mixture was heated at 90 °C with stirring for 12 hours. The solvent was

evaporated under vacuum and the crude residue was suspended in 2:1 water/methanol (100 mL) and the pH of the solution was adjusted to 3 by adding hydrochloric acid (6 N). The obtained solid was thoroughly washed with water by centrifugation and then dried over silica gel under vacuum to afford 0.8 g (69% yield) of 1b as a deep brown solid. ^{1}H NMR (DMSO-d_6, 600 MHz): δ (ppm) = 8.67 (s, 4H), 4.65 (s, *1*H), 4.04-4.02 (t, J = 9Hz, 2H), 1.65-1.61 (m, J = 6Hz, 2H), 1.35-1.28 (m, J = 6Hz, 6H), 0.86-0.84 (t, J = 6Hz, 3H).

4.4.8.3 General Synthesis of the Peptides

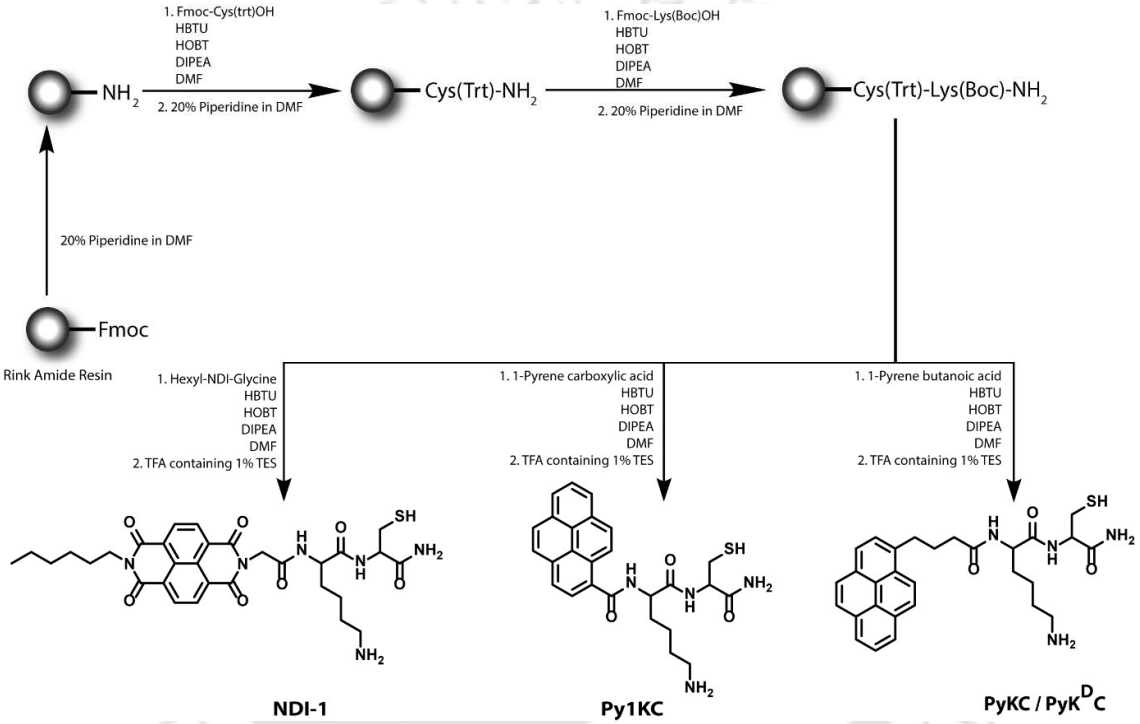

Scheme 4.4 Synthetic routes for **PyKC, PyK^{D}C, Py1KC** and **NDI-1.**

The peptides were synthesized on Rink amide MBHA resin using standard Fmoc (9-fluorenylmethoxycarbonyl) solid phase peptide synthesis (SPPS) method. In a typical coupling, 3 equiv. of protected amino acid (with respect to the loading of the resin), 3 equiv. of HBTU, and 6 equiv. of DIPEA were taken in 5 mL of DMF (for 0.1 mmol scale with respect to the resin loading) and stirred for 5 minutes prior to addition of the mixture to the resin. The reaction mixture was shaken for 60 min and the resin was washed several times with DMF. The Fmoc-deprotection was achieved by treatment of the resin with 20% piperidine/DMF (5 mL, 5 minutes, three times) followed by thorough washing of the resin with DMF. The Fmoc-deprotection and coupling steps were repeated until the designed peptide sequence was obtained. After the final Fmoc deprotection, the peptide loaded resin

was washed several times with DMF followed by DCM and dried under reduced pressure. The dried resin was then treated with a mixture of 95% TFA in DCM containing 1% TES and stirred for 1 hour. The resin was finally washed with DCM several times. The cleavage cocktail and the washings combined were concentrated to a minimum volume on a rotary evaporator. The cleaved peptide was then precipitated from cold dry ether, centrifuged and lyophilized to get the crude peptide. For **PyK^{D}C**, Fmoc-D-Cys(Trt)-OH was coupled as the first amino acid of the sequence followed by similar procedure as mentioned above. Purification was done in a semi-preparative HPLC using a Luna 5 µm (C18) column (Phenomenex) with a programme of acetonitrile and water starting at 5% acetonitrile to reach 30% after 5 min and continued to reach 100% at 40 min.

4.4.8.4 Characterisation of NDI-1

Yield = 70%. ^{1}H NMR (400 MHz, DMSO-d_6) δ (ppm)= 8.74 – 8.66 (m, 4H), 8.62 – 8.52 (br, 1H), 7.99 (br, J = 8.1 Hz, 1H), 7.63 (s, 2H), 7.36 (s, 1H), 4.84 – 4.70 (m, 2H), 4.33 (tt, J = 7.9, 4.5 Hz, 2H), 4.07 (t, J = 7.5 Hz, 2H), 2.78 (s, 5H), 2.24 (s, 1H), 1.76 – 1.63 (m, 2H), 1.37 (s, 4H), 1.38 – 1.27 (m, 1H), 1.31 (s, 4H), 0.91 – 0.83 (m, 3H).^{13}C NMR (100 MHz, DMSO-d_6) δ (ppm)= 171.87, 171.79, 163.06, 162.99, 131.17, 130.94, 127.16, 126.75, 126.35, 55.29, 52.92, 43.12, 31.41, 27.79, 27.03, 26.62, 26.51, 22.55, 22.43, 14.37. Mass (ESI-MS): m/z calcd. For $C_{31}H_{38}N_6O_7S$ $[M+H]^+$, 639.29; found 639.25.

4.4.8.5 Characterisation of PyKC

^{1}H NMR (DMSO-d_6, 400 MHz): δ (ppm)= 8.39 (d, J = 9.3 Hz, 1H), 8.28 (m, 2H), 8.23 (m, 2H), 8.14 (d, J = 2.0 Hz, 2H), 8.07 (t, J = 7.6 Hz, 1H), 7.97 (t, J = 8.2 Hz, 2H), 7.66 (s, 3H), 7.29 (s, 1H), 7.20 (s, 1H), 4.39 – 4.21 (m, 2H), 2.90 – 2.66 (m, 4H), 2.29 (m, 3H), 2.03 (p, J = 7.3 Hz, 2H), 1.69 (m, 1H), 1.55 (m, 3H), 1.35 (d, J = 35.3 Hz, 2H). ^{13}C NMR (100 MHz, DMSO-d_6): δ (ppm)= 172.96, 172.31, 171.87, 137.06, 131.36, 130.90, 129.78, 128.06, 127.93, 127.70, 126.99, 126.63, 125.42, 125.26, 124.03, 55.06, 53.19, 39.18, 35.29, 32.71, 31.44, 28.00, 27.10, 26.58, 22.82. ESI-MS calcd. for $[M+H]^+$, $C_{29}H_{34}N_4O_3S$: 519.24, found: 519.24 (m/z)

4.4.8.6 Characterisation of PyK^{D}C

^{1}H NMR (400 MHz, DMSO-d_6): δ (ppm)= 8.37 (m, 1H), 8.31 – 8.17 (m, 5H), 8.15 (m, 3H), 8.13 – 8.02 (m, 1H), 7.95 (d, J = 7.8 Hz, 1H), 7.67 (s, 3H), 7.41 (s, 1H), 7.26 (s, 1H), 4.38 – 4.18 (m, 2H),

2.89 (m, 1H), 2.74 (s, 3H), 2.32 (t, J= 7.3 Hz, 2H), 2.30 (s, 1H), 2.22 (t, J= 8.4 Hz, 1H), 2.01 (t, J= 7.5 Hz, 2H), 1.67 (s, 1H), 1.55 (m, 3H), 1.36 (m, 7.6 Hz, 2H).

4.4.8.7 Characterisation of Py1KC

^{1}H NMR (400 MHz, DMSO-d_6): δ (ppm)= 8.92 (d, J= 7.5 Hz, 1H), 8.54 (d, J= 9.3 Hz, 1H), 8.42 (s, 1H), 8.36 (dd, J= 7.7, 4.1 Hz, 3H), 8.31 – 8.21 (m, 3H), 8.20 (d, J= 7.9 Hz, 1H), 8.14 (m, 2H), 7.70 (s, 3H), 7.53 (s, 1H), 7.29 (s, 1H), 4.68 – 4.58 (m, 1H), 4.46 (m, 1H), 2.93 (dd, J= 13.5, 5.0 Hz, 1H), 2.88 – 2.79 (m, 3H), 1.85 (s, 2H), 1.72 – 1.48 (m, 2H), 1.54 (s, 2H).

4.4.8.8 PyKC-dimer

The **PyKC**-dimer was prepared by incubating **PyKC** solution in pH 8 buffer for 72 hours followed by lyophilisation and purity check by analytical HPLC and ESI-MS. No further purification was needed and the yield was more than 99.5%. Calibration plots were made by injecting samples of different concentration and their respective peak areas from analytical HPLC. ESI-MS calcd. for $[M+H]^+$, $C_{58}H_{66}N_8O_6S_2^+$: 1035.4580, found: 1035.4576, and 518.2320 $[M^{2+}]$.

4.4.8.9 NDI-1-dimer

The disulfide linked dimer of **NDI-1** was prepared by incubating **NDI-1** solution in pH 8 buffer for 72 hours followed by lyophilisation and purity check by analytical HPLC and ESI-MS. No further purification was needed and the yield was more than 99%. Calibration plots were made by injecting samples of different concentration and their respective peak areas from analytical HPLC. ESI-MS calcd. for $[M+H]^+$, $C_{62}H_{75}N_{12}O_{14}S_2^+$:1275.50, found: 1275.49, and 638.25 $[M^{2+}]$.

4.4.8.10 Heterodimer

The donor and acceptor solutions were mixed to maintain the molar ratio of 1:1 followed by changing the pH to 8 by addition of NaOH solution and the mixtures were incubated at room temperature for 72 hours. The mixtures were analysed by analytical HPLC and the peaks corresponding to the heterodimers were identified by analysing the ESI-MS of the fractions. These two dimers were not isolated for calibration curves. However, the % conversions during the reactions using the presented methodology were calculated from the disappearance of the starting materials. Retention times of different molecules when

eluted with a gradient of acetonitrile in water starting from 5% ACN/H_2O to reach 30% ACN/H_2O after 5 min and continued to reach 100% ACN at 40 min on a Luna 5 μm (C18) column (Phenomenex) at a flow rate of 1 mL min^{-1} using Dionex Ultimate 3000 analytical HPLC.

Table 4.3 Retention time of different monomers and dimers of the peptide.

Compound	R_T (min)
PyKC /PyK^DC	14.8
NDI-1	18.9
PyKC-dimer/ PyK^DC-dimer	17.4
NDI-1-Dimer	20.9
PyKC-NDI-1 Heterodimer/ PyK^DC-NDI-1 Heterodimer	16.9
Py1KC	15.4
Py1KC-Dimer	18.0
Py1KC-NDI-1 Heterodimer	17.2

4.4.9 Control Experiments

4.4.9.1 To check the Disulfide Formation in Aqueous 1% TFA Solution

Both **PyKC** and **NDI-1** were dissolved in aqueous 1% TFA solution separately as well as in 1:1 molar ratio. All three samples were incubated at room temperature for 24 hours and then analysed by HPLC and ESI-MS. No detectable dimerization was obtained in any of these three solutions. Based on these results, the initial solutions of the monomers were prepared in aqueous 1% TFA solutions to prevent any dimerization.

4.4.9.2 To Check any Dimerization in Cyclohexane without Lyophilisation of the CT Complexes

Both as synthesized powdered **PyKC** and **NDI-1** were suspended in cyclohexane separately as well as in 1:1 molar ratio. All three samples were incubated at room temperature for 24h and then centrifuged, solids were dried and dissolved in 1% TFA solutions. These solutions were analysed by HPLC and ESI-MS. No detectable dimerization was obtained in any of these three solutions.

4.4.9.3 To Check the Solubility of the Building Blocks in Cyclohexane

Both **PyKC** and **NDI-1** were suspended (10 mg) in cyclohexane/hexane (10 mL) and the suspensions were sonicated for 30 minutes. After that the suspensions were centrifuged at 12000 rpm for 10 mins. 100 μL of the supernatant cyclohexane samples were pipetted out, dried and to that 50 mL of water was added and the solutions were analysed by HPLC and

ESI-MS. No trace of the monomers was found in any case suggesting insolubility of the monomers in cyclohexane.

Chapter 5: Protection and Glutathione Responsive Delivery of Proteins by an Ultrashort Peptide Hydrogel

5.1 Introduction

Protein and peptide-based therapeutics offer the ability to treat diseases such as protein deficiency or mutations, cancer, microbial infections, autoimmune disorders, psoriasis, and diabetes, to name a few.[230] The number of marketed protein drugs for the treatment of these diseases are growing rapidly and seventy percent of the top selling drugs fall under this category.[231] However, the majority of these drugs are targeting extracellular proteins such as cell membrane proteins or secretory proteins. These extracellular proteins have only a minor share of the total protein content in humans. There are several diseases like protein deficiency or mutations that are typically termed as "undruggable" by small therapeutic molecules.[232] Treatment for these diseases require intracellular targeting by protein/peptide therapeutics which is extremely challenging as permeation of the cell membrane is an uphill task. Techniques and methodologies that can efficiently deliver protein/hormone/small peptide therapeutics inside the cells and even to a particular organelle is thus of extreme importance.[232]

A plethora of carriers for intracellular delivery of proteins and peptides have been charted in the last decade that includes, dendrimers,[233, 234] metal nanoparticles,[235] silica nanostructures,[236] protein-based vehicles,[237, 238] lipid-based systems,[239, 240] metal-organic frameworks,[241-243] fluorous masks,[244] virus-like particles,[245] DNA composites,[246] vesicles,[247] nanotubes,[248] nanoneedles, polymers,[249, 250] hydrogels[232, 251] to name a few. These delivery vehicles show great potential toward the cytosolic delivery of proteins and peptides. However, several issues require proper attention. To begin with, protection of the encapsulated biomolecules from denaturing effect is essential as the delivered proteins must serve their function within the cytosol. Often, covalent modifications are made to the proteins in order to conjugate with the carriers. Specific tags are attached to the proteins in order to reinforce the binding with the vehicle. Similarly, dynamic covalent linkages are also utilized to directly conjugate with the carrier. These covalent modifications result in loss of activities significantly.

To encounter these shortfalls of available delivery vehicles, the supramolecular hydrogel is an attractive alternative. Several peptide-based hydrogels are reported with the ability of cellular protein delivery. However, it is essential to comprehend that protein delivery with hydrogel is technically limited to topical applications unless the hydrogel is injectable/thixotropic in nature. The cargo loaded hydrogel can be injected at the site of

treatment/tumour. Even only the thixotropic nature alone does not serve the purpose as after injecting the protein-loaded hydrogel, the gel may get washed out in the biofluid present at the site. Thus an injectable and water-insoluble hydrogel could possibly overcome the issues. Additionally, the hydrogel must be sensitive to the extracellular environment or to a biomolecule present at the site in order to release the cargo.

In this context, we have recently reported an ultrashort peptide hydrogelator with the ability to form a gel in water that remains insoluble in water and HBS (human blood serum).[77] However, the **PyKC** hydrogel is responsive to GSH. Additionally, we have shown that the very tightly knitted network of the **PyKC** hydrogel is capable of encapsulate and protect proteins from external denaturing effects for a long time without any significant loss of protein activity. Considering the shortcomings of the hydrogel-based protein delivery systems, we envisioned that **PyKC** hydrogel could be a potential candidate for efficient protein delivery. Another essential criterion for the success of such delivery vehicles is that the hydrogel should adhere to the tissue. However, the **PyKC** hydrogel does not fulfil the criteria (as observed from other unpublished studies). To resolve this issue, we have prepared another short peptide (**PyKRGD**) containing a known cell adhesive unit, RGD.

5.2 Results and Discussion

5.2.1 Composite Hydrogelation

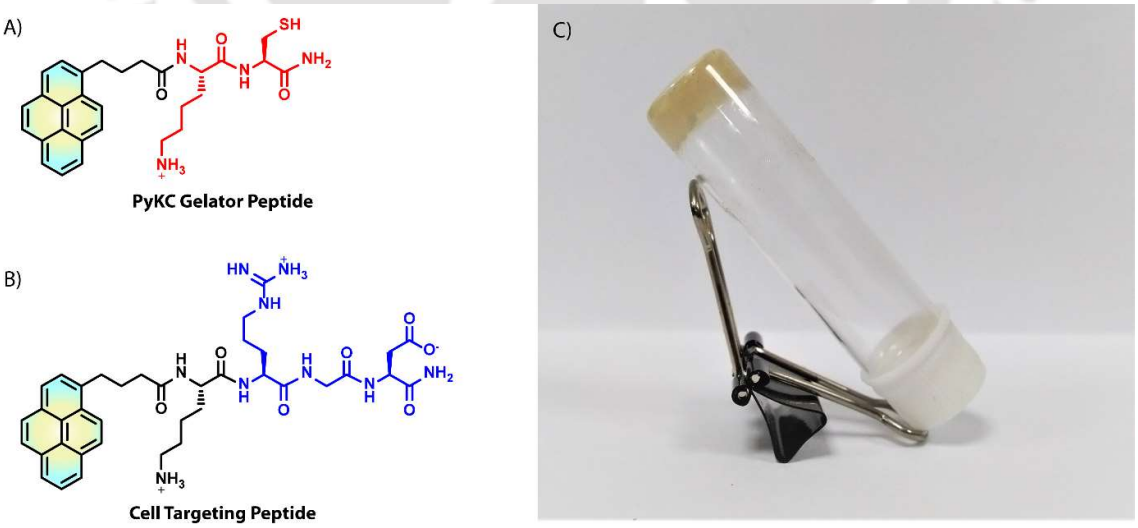

Figure 5.1 (A) and (B) Chemical structures of the peptides and (C) Picture of the composite hydrogel.

All peptides were synthesized using the solid-phase peptide synthesis method followed by HPLC purification. The gelation procedure was kept similar to our previous report. For

hydrogelation[77], the required amount of **PyKC** was dissolved in 20 mM pH 8 Tris buffer, followed by the required amount of **PyKRGD** (1% respect to PyKC using a previously prepared stock solution of **PyKRGD**). The homogeneous solution turned into a transparent self-supported hydrogel after 12 hours of incubation. The minimum gelation concentration was observed to be 0.5 wt%. The presence of dimer of **PyKC** was demonstrated by both ESI-MS and HPLC analyses. The detailed mechanism of the cysteine dimerization mediated hydrogelation was demonstrated in the earlier report by both analytical and theoretical experiments.[77]

Next, the gel to sol transition temperature (T_g) was recorded by the ball dropping method. The transition started at 50 °C and can be considered as the T_g of the composite hydrogel. The hydrogel showed insolubility in various aqueous media as well as in other water-miscible organic mediums. We were curious to know whether there is any effect on this property by **PyKRGD**. A dissolution test was performed in buffers of different pH. As shown in Figure 5.2, a maximum of 15% dissolution of the hydrogel within the first seven days was observed in all these buffers. Relatively higher dissolution is observed in acidic buffers due to the protonation of the amine groups present in the gel network. Interestingly, as expected, TCEP and GSH could dissolve the hydrogel entirely within 10 mins. The response toward these disulfide bond breaking is encouraging toward using the composite hydrogel for protein delivery.

Figure 5.2 (A) RhB containing 1 wt% composite hydrogel has been dispersed in various pH and water after stirring for 30 mins, (B) % of dissolution in various solvents.

The morphology of the composite hydrogel was then checked using FETEM, FESEM and AFM techniques. All the techniques showed similar network like morphology of the composite hydrogel. A tightly knitted network of thin fibres was seen under microscopes. The network pattern, as well as the dimensions (~15 nm x 200 nm) of the fibres closely, matches with that of **PyKC** hydrogel.[77]

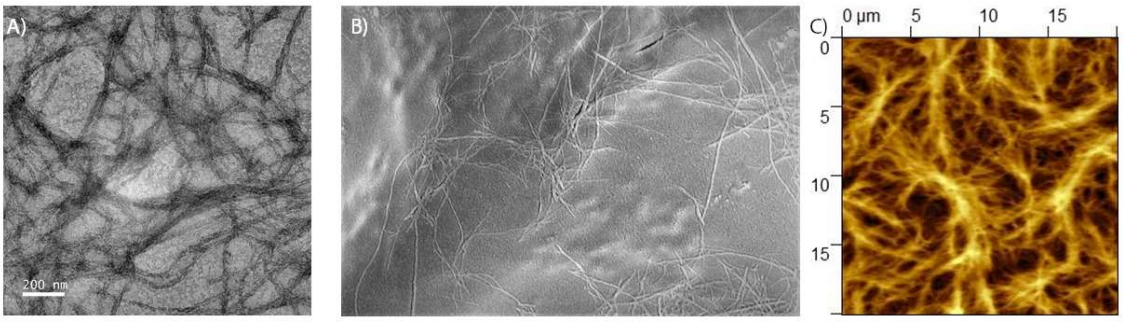

Figure 5.3 Microscopic images taken from the composite hydrogel. (A) FETEM, (B) FESEM, and (C) AFM images, respectively.

Rheological analyses were conducted to get insights into the mechanical properties of the composite hydrogel. In the strain sweep experiment, the gel was found to retain its viscoelastic property up to 10% strain under the fixed angular frequency of 1 rad s^{-1} at 25 °C (Figure 5.4A). The composite hydrogel showed gel behaviour within the range of 0.07-25%; beyond that region, the gel moved to the sol domain. The gel was found to be frequency-independent over the applied region of 0.1–100 rad s^{-1}, confirmed from the frequency sweep experiment, where both G′ and G″ values were higher, and the gap between these two parameters was relatively high over the entire region (Figure 5.4B).

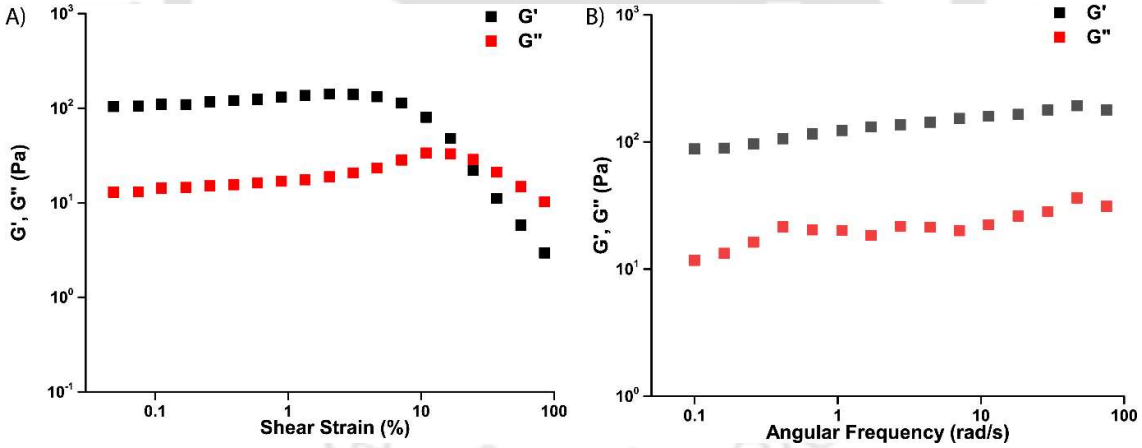

Figure 5.4 Different rheological experiments, (A) Stain sweep, (B) Angular Sweep.

Using hydrogels as a delivery vehicle is limited to topical applications unless they are thixotropic and injectable in nature. The thixotropic property of the composite hydrogel was then evaluated. A time-dependent strain sweep was performed by alternating the applied strains at a fixed angular frequency of 1 rad s^{-1} (Figure 5.5C). At a higher strain (γ = 100%), the gel loses its viscoelastic property. Interestingly, in every successive step, it regains its initial viscoelastic nature almost completely while coming back to a lower strain. For having such recovering tendency, the gel can be classified as a self-healing or

thixotropic material. In the present case, when a strain (γ = 100%) much higher than the yield strain (γ = 10%) is applied, the sol state appears (G″ > G′); however, when a strain (γ = 0.1%) much lower than the yield strain is applied on that deformed gel, it goes back to its initial gel state (G′ > G″, G′ ~ 103 Pa). To further check the injectability of the composite hydrogel, the hydrogel was prepared in a syringe, and upon pressing the piston, the hydrogel turns into a liquid and comes out of the needle (Figure 5.5D). The liquid instantly returns to the gel state after release. Interestingly enough, a dye-loaded hydrogel did not release any colour while injecting it into a physiological buffer (pH 7.4, 20 mM PBS). It clearly refers to the fact that the hydrogel retains its gel property after the injection and also retains its insoluble behaviour. The injectability and the insolubility of the hydrogel are crucial in order to use them for local delivery of drug/therapeutics. The injectability allows the therapeutic loaded hydrogel to be injected at the site of infection/tumour. On the other hand, the insolubility ensures that the hydrogel will stay at the site of injection and will not be washed out by the biofluid.

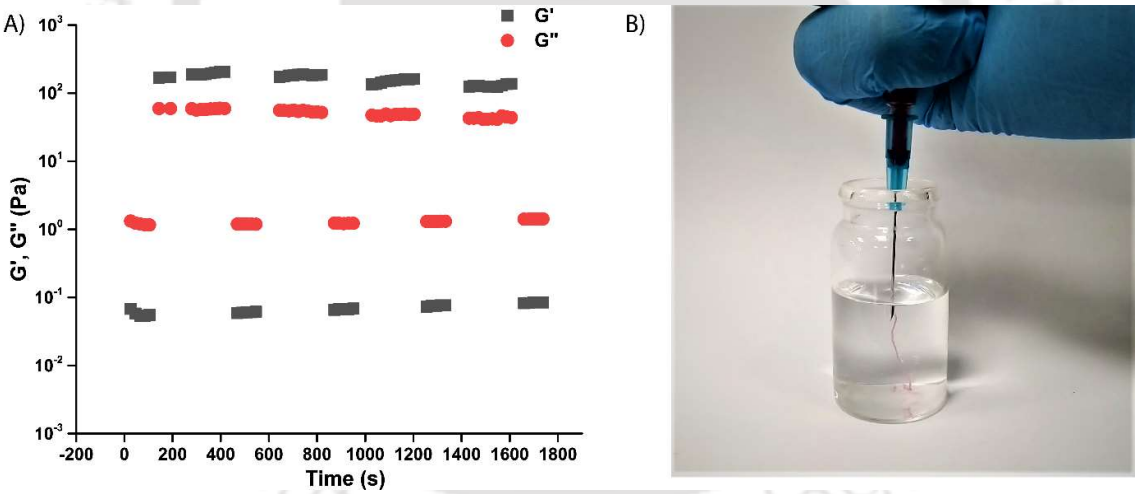

Figure 5.5 (A) the continuous step strain measurements for the thixotropic property. (B) Photograph showing injectability property of the hydrogel.

5.2.2 GSH-mediated Protein Release

To evaluate the sensitivity of the composite hydrogel toward GSH, an in-vitro protein study was performed as a function of time and GSH concentration. Various proteins have been tagged with FITC fluorophores (Table 5.1). The CD spectra of the tagged proteins were compared with the native proteins to confirm almost no change in the protein structures.

Table 5.1 Detailed list of tagged proteins

Protein	Fluorophore	Short Name	λ_{ex}	λ_{em}	Mol Wt.
BSA	FITC	BSA-FITC	498 nm	530 nm	66.5 kda
CR Lipase	FITC	CR-Lipase-FITC	495 nm	580 nm	30 kda
RNase A	FITC	RNase A-FITC	495 nm	529 nm	13.7 kda
Histone	FITC	Histone-FITC	495 nm	521 nm	55 kda

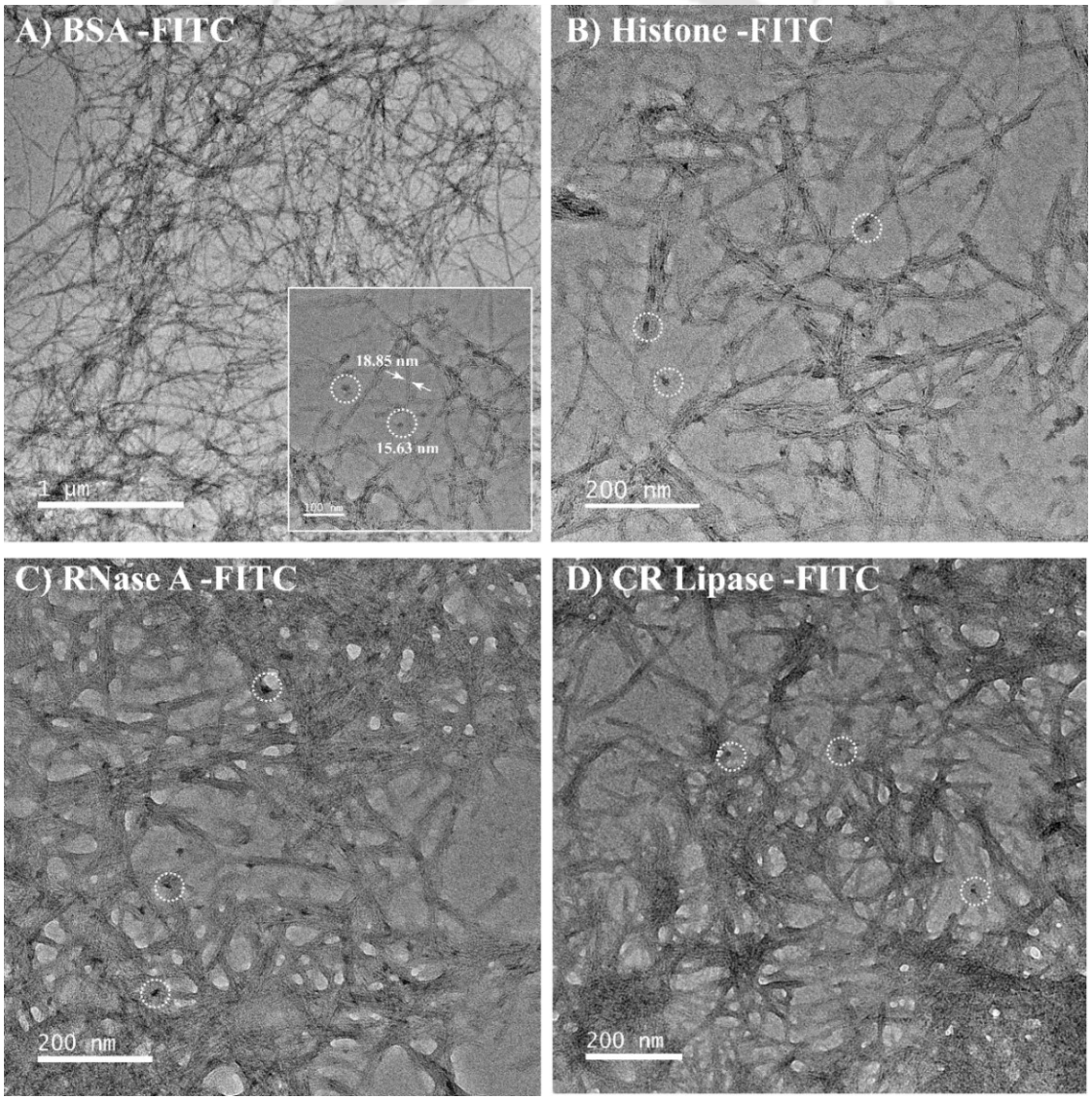

Figure 5.6 FETEM images of the entrapped proteins inside the fibrilar network of the composite hydrogel. (A) BSA-FITC, (B) Histone-FITC, (C) RNase A and (D) CR lipase.

Next, the protein-loaded hydrogels were prepared by mixing and incubating the stock solutions of the protein, **PyKRGD** and the required amount of **PyKC** while keeping the ratio of 1 wt% **PyKC**, 0.1 wt% **PyKRGD** and 0.1 wt% protein. The encapsulation of the proteins inside the fibrilar network of the hydrogel was confirmed by FETEM images where black dots corresponding to the proteins were observed throughout the fibrillar network of the composite hydrogel (Figure 5.6A-D).

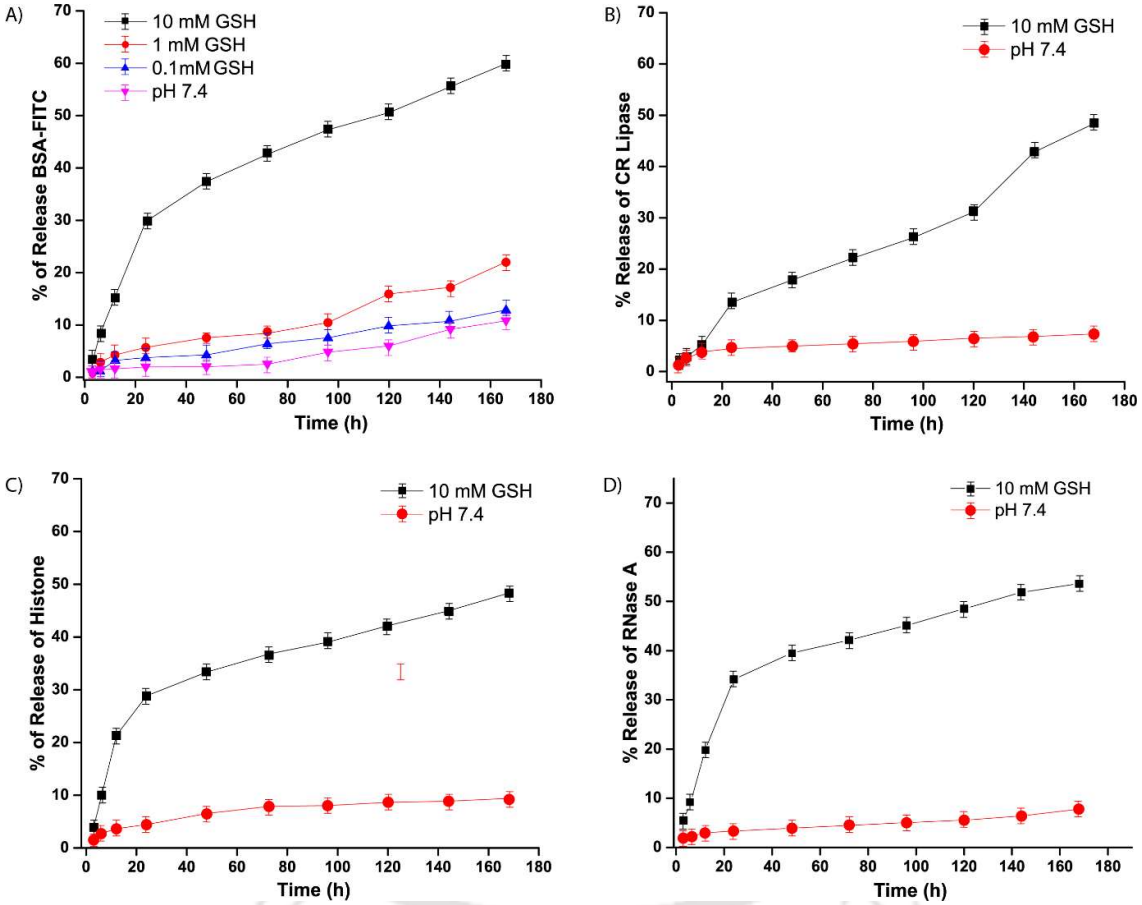

Figure 5.7 Release profile of the various proteins upon Glutathione (GSH) treatment, (A) BSA-FITC with different concentrations of GSH, (B) CR lipase, (C) Histone, and (D) RNase A, respectively.

For GSH concentration-dependent release study, FITC-tagged BSA (BSA-FITC) was chosen as the model protein. To monitor the protein release from the hydrogel in response to GSH, the protein-loaded hydrogels were immersed in solutions of GSH of varying concentrations (to 10 mM). The supernatant GSH solutions were taken out from time to time, and the amount of released proteins was estimated following the max absorbance. As shown in Figure 5.7A, even after seven days, less than 10% protein was released in the presence of 0.1 mM GSH. Though very similar, the marginally higher release was observed compared to

the buffer with no GSH. As the concentration increased from 0.1 mM to 1 mM, the extent of release also enhanced significantly. In 10 mM GSH, ~ 30% release was observed within the first 24 hours (Figure 5.7A). After that, a sustained release profile was observed, and more than 60% of the protein was released over a period of seven days.

ESI-MS analyses of the supernatant samples showed the presence of **PyKC** monomer and **PyKRGD** peptides. The amount of the peptides was determined using HPLC analyses and was found to be ~50% of the originally used peptides to prepare the composite hydrogel. It is also worth mentioning that after seven days of incubation in the GSH solution, the volume of the hydrogel reduced significantly (close to half of the original volume) as determined visually. The other proteins were then subjected to release study using 10 mM GSH as the release media. In all cases, similar to BSA-FITC, sustained release of the proteins was observed with maximum release of more than 50% of the trapped protein within seven days were observed (Figure 5.7B, C and D).

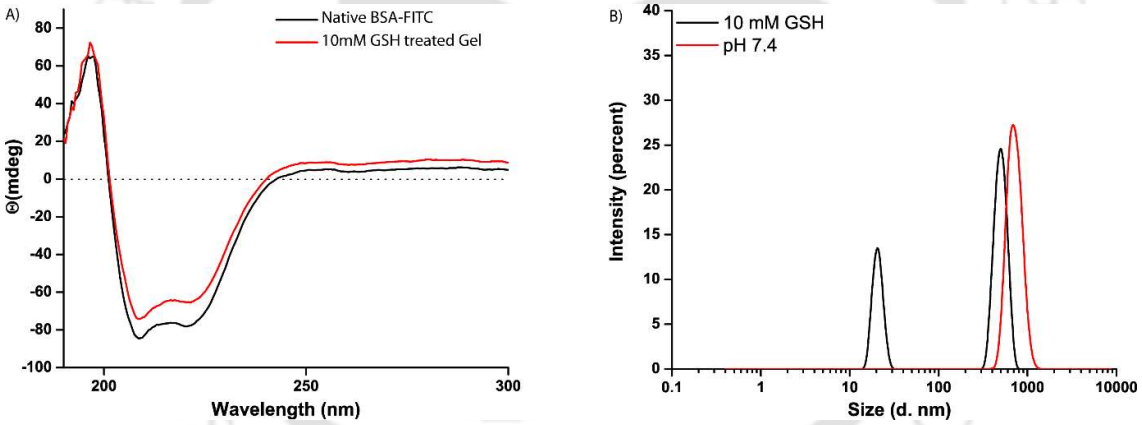

Figure 5.8 (A) CD analysis of the released solution and native BSA-FITC, (B). DLS analysis shows the arrival of a new peak near 20 nm after GSH mediated release.

For successful application of protein delivery, the released proteins must retain their structural integrity and inherent activity. A matured BSA-FITC loaded hydrogel was treated with 10 mM GSH solution for seven days, and the CD profile of the supernatant solution was recorded and compared with the CD spectrum of a solution of BSA in 10 μM GSH containing the required amount (equivalent to 50% dissolution of 1 wt% composite hydrogel) of **PyKC** and **PyKRGD**. The released protein showed an almost similar CD profile to that of the native protein. These results align with our previous experience with **PyKC** hydrogel and prove that the entrapment and treatment with GSH could not impart any noticeable change in

protein folding (Figure 5.8A). DLS analysis from the same supernatant reveals the presence of 20 nm-sized particles that represent the trapped proteins having a dimensional resemblance with the previous FETEM images of the protein-loaded hydrogel (Figure 5.8B).

The composite hydrogel of **PyKC–PyKRGD** thus passed all the prerequisites for its application as a protein delivery vehicle. However, before exploring the protein release studies, the cytocompatibility of **PyKC** was tested against three different cell lines, 293A, SW480 and MCF7 cells, respectively. Different concentrations (1 μM to 100 μM) of **PyKC** was tested using an MTT assay over 24 hours. Notably, the gelator was found to be nontoxic even at 100 μM concentration for all three cell lines (Figure 5.8).

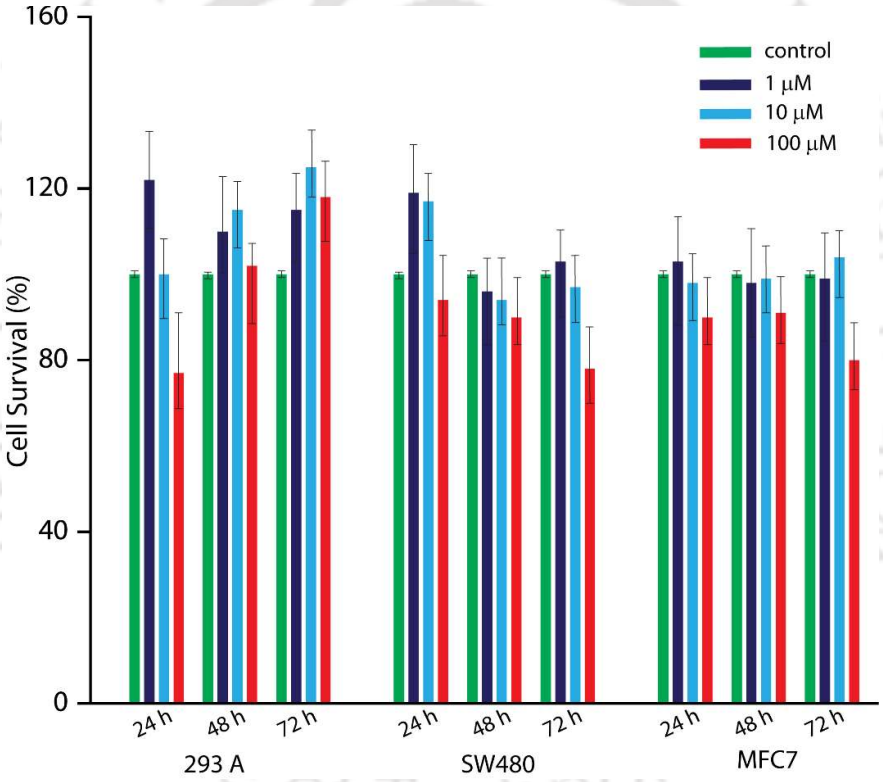

Figure 5.8 Cytotoxicity studies of **PyKC** on different cell lines.

5.3 Conclusion

In this work, we have successfully developed a composite hydrogel by combining two different short peptides, **PyKC** and **PyKRGD**. The characterization of the composite gel shows that the presence of **PyKRGD** in the mixture could not impart much changes in the gel character of **PyKC**. Importantly, like **PyKC**, the composite gel also showed insolubility in

aqueous buffers of varying pH and thixotropic and injectability–property. Moreover, the hydrogel showed a response to GSH which breaks the hydrogel by breaking the disulfide linkages of **PyKC** dimer. **PyKC** was found to be nontoxic to different cell lines. Based on these results, the composite hydrogel was used for in-vitro protein release studies using four different fluorophore labelled proteins in response to GSH concentration. In the presence of 10 mM GSH, a sustained release of ~ 50% of the loaded proteins within seven days were observed.

We aim to extend the work further with the cellular release of various proteins, hormones and peptides. However, due to the COVID-19 pandemic, the intracellular delivery studies could not be finished on time. These experiments are remaining underway and we anticipate to show some promising outcomes.

5.4 Experimental Section

5.4.1 General Information and Materials

Rink amide MBHA resin, Fmoc-Cys(Trt)OH, Fmoc-Lys(Boc)-OH, Fmoc-Asp(Otbu)-OH, Fmoc-Arg(Pbf)-OH, Fmoc-Gly-OH, HBTU and HOBT were procured from GL Biochem, China. Bovine serum albumin, Lipases from *Candida rugosa* and Histone from calf thymus Trypsin, Rhodamine B, 1-Pyrenebutyric acid and TES, GSH, HPLC-grade DMF and TFA, DCM, and ACN were purchased from Sigma Aldrich. Bovine Pancreatic RNase A was acquired from SRL chemicals. For the preparation of samples for different analyses, Milli-Q water with a conductivity of less than 2 mS cm^{-1} was used. Chromatographic purifications were performed on a Luna 5 µm (C18, 250x10 mm) column (Phenomenex) whereas, analytical HPLC were performed on a Luna 5 µm (C18, 250 × 4.6 mm) column (Phenomenex) using a Dionex Ultimate 3000 HPLC. UV-Vis spectra were recorded on a PerkinElmer Lambda 750 spectrometer, while fluorescence measurements were performed on a Fluoromax 4 (Horiba) spectrophotometer. Standard 10 mm-path quartz cuvettes were used for all spectroscopic measurements. ^{1}H NMR, ^{13}C NMR were recorded with a Bruker Ascend 600 MHz (Bruker, Coventry, UK) spectrometer and referenced to deuterated solvents. ESI-MS were performed with a Q-Tof Micro Quadrupole mass spectrophotometer (Micromass). FETEM images were taken using JEOL JEM-2100F microscope. AFM images were taken on

Nanosurf Flex-Axiom (Nanosurf, Switzerland). CD experiments were performed by using Jasco J-1500 spectropolarimeter**.**

5.4.2 Preparation of Hydrogel

The hydrogel was prepared at 1 wt% (1 mg per 100 µL) with respect to **PyKC**. 2 mg **PyKC** peptide was dissolved 150 µL of freshly prepared pH 8 Tris buffer (20mM). A fresh stock solution of **PyKRGD** was prepared by taking 2 mg in 1mL of pH 8 Tris buffer (20mM). The required volume of **PyKRGD** solution was mixed properly with the gelator solution to keep the concentration of **PyKC** and **PyKRGD** as 1 wt% and 0.01 wt% respectively the volume was made up with the buffer. The solution was incubated at room temperature for 24 hours for complete gelation.

5.4.3 Determination of Sol–Gel Transition Temperature (T_g)

The hydrogel samples were placed in a water bath and the bath was heated at a rate of 0.5 °Cmin^{-1}. The temperature at which the hydrogel started melting was noted by manually inspecting the samples for free flow. The experiments were performed in triplicate and the results were obtained within ± 0.5 °C.

5.4.4 FESEM, FETEM and AFM

10 mL of the gel samples were placed on silicon wafer (for FESEM and AFM) or a carbon coated TEM grid (for FETEM) and the samples were dried under ambient conditions before the measurements.

5.4.5 Rheology

The rheological measurements of the hydrogel were completed on a MCR 102 rheometer (Anton Paar) with a 20 mm parallel plate at 25 °C with a bandgap of 0.3 mm. The LVR was identified first by a strain sweep test over a range from 0.01 to 100% strain at a fixed oscillatory frequency of 1 rad s^{-1}. The oscillatory test (frequency sweep) was carried out under a strain (γ) of 0.1%.

5.4.6 CD Spectroscopy

The CD spectra of all the samples were recorded at room temperature. The data were collected at 0.5 nm intervals with a 2 nm bandwidth. All measurements were done in 0.2 cm path length cuvette with 800 mL sample volume. Each CD profile is an average of 3 scans of the same sample collected at a scan rate of 100 nm min^{-1}, with a proper baseline correction from the respective solvents. The CD spectra of the native protein and the tagged protein solution were recorded maintaining the enzyme concentration at 5-10 μM. For the protein release study, the CD spectra were recorded from the GSH (50 mM) treated protein-loaded hydrogel (0.1 mg protein in 100 μL hydrogel at 1 wt% concentration) after proper dilution by the Tris buffer.

5.4.7 DLS Experiments

The particle sizes of the assemblies were obtained at 298 K using a 632.8 nm He–Ne laser using Zetasizer Nano-ZS90 (Malvern). The stock solution for the protein release study was prepared by dissolving a 100 μL protein-loaded hydrogel into 1 mL GSH solution (50 mM). Gentle centrifugation resulted in separating the colored supernatant solution, which was also filtered through 0.4-micron filters before each measurement. All the measurements were performed in triplicates.

5.4.8 Peptide Synthesis Protocols

The peptides were synthesized on Rink amide MBHA resin using standard Fmoc (9-fluorenylmethoxycarbonyl) solid-phase peptide synthesis (SPPS) protocol. The synthetic protocols of the **PyKC** peptide were already discussed in the fourth chapter. For **PyKRGD**, similar procedure was used and was synthesized following Scheme 5.2. (Yield = 70%) MALDI-TOF: m/z calcd. for $C_{38}H_{51}N_9O_7^+$ $[M]^+$, 744.873; found 744.854. ^{1}H NMR (600 MHz, DMSO-d_6) δ (ppm)= 8.37 (d, J= 9.0 Hz, 1H), 8.26 (t, J= 6.8 Hz, 2H), 8.21 (t, J= 9.1 Hz, 2H), 8.18 – 8.15 (m, 1H), 8.12 (d, J= 3.3 Hz, 2H), 8.10 (d, J= 6.9 Hz, 1H), 8.07 – 8.01 (m, 2H), 7.93 (d, J= 7.7 Hz, 1H), 7.69 (s, 2H), 7.59 (s, 1H), 7.25 (s, 1H), 7.13 (s, 1H), 4.48 (d, J = 6.3 Hz, 1H), 4.32 – 4.23 (m, 2H), 3.73 (dd, J= 19.5, 5.3 Hz, 2H), 3.35 – 3.26 (m, 4H), 3.07 (d, J= 6.0 Hz, 2H), 2.74 (d, J= 5.9 Hz, 3H), 2.29 (t, J= 7.1 Hz, 2H), 2.00 (d, J= 7.8 Hz, 2H), 1.72 – 1.62 (m, 2H), 1.51 (d, J= 5.2 Hz, 6H), 1.31 (d, J= 7.7 Hz, 2H). ^{13}C NMR (151 MHz, DMSO-d_6) δ (ppm)= 173.00, 172.75, 172.48, 172.31, 172.22, 169.00, 158.91, 158.70, 157.19, 137.02, 131.35, 130.88, 129.77, 128.61,

128.04, 127.92, 127.68, 126.99, 126.63, 125.42, 125.26, 124.70, 124.60, 123.98, 52.76, 52.71, 49.84, 42.40, 40.85, 39.18, 36.65, 35.27, 32.68, 31.63, 29.51, 28.02, 27.11, 25.40, 22.87.

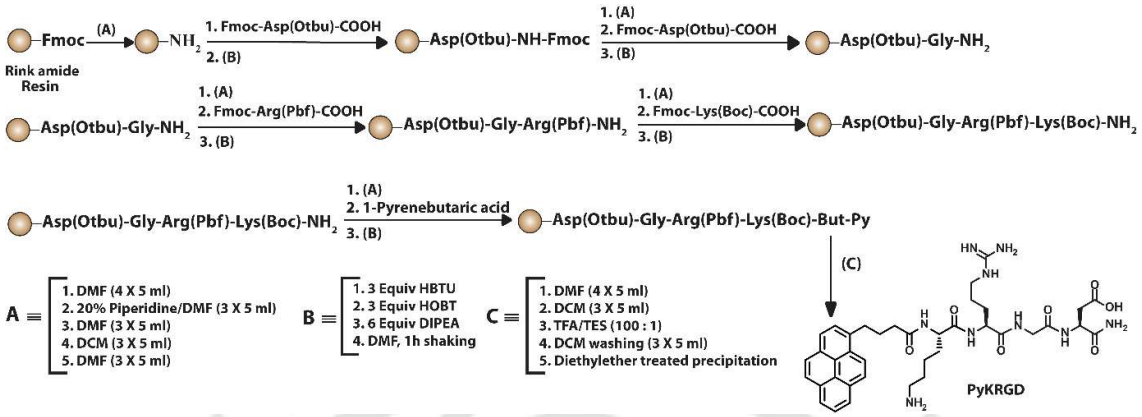

Scheme 5.1 Schematic route for **PyKRGD** synthesis.

5.4.9 Fluorophore Tagging on Proteins

In a typical procedure**,** 5 mg of the protein was dissolved in 1 mL of 100 mM $NaHCO_3$-Na_2CO_3 buffer solution (pH 9). The required amount (3-5 mg) of FITC was dissolved in 50 µL anhydrous DMF and transferred into the stirred solution of the protein. The stirring was further continued for 3 hours in the dark. Then, the reaction mixtures were taken in an activated dialysis membrane (cut-off: 14,000). The mixture was dialyzed against cold buffer solution with proper time to time refilling until the green emission of the unreacted FITC was fully diminished. Lastly, the mixture was dialyzed against the cold milli-Q water for the complete removal of the salts. The tagged proteins were obtained after freeze-drying the dialyzed protein solution. MALDI, UV, Fluorescence measurements confirmed the attachment of the fluorophores towards the proteins.

5.4.10 Dissolution Study

In a typical experiment, several samples of 100 µL composite hydrogels were prepared in 20 mM Tris buffer, pH 8, keeping the concentrations of **PyKC** and **PyKRGD** as one wt% and 0.01 wt%, respectively. After 24 hours incubation at room temperature, 1 mL of different buffers were added to these samples and tapped to disperse the hydrogel into the buffers. The samples were then kept horizontally over a shaker and shaken at 100 rpm at room temperature. At different times, aliquots of the supernatants were replaced with the same amounts of fresh buffers to keep the overall volume intact. This investigation was continued

for one week. The aliquots were diluted with the same bulk solvent/solution before recording their absorption at λ_{max} (352 nm). The % dissolutions were calculated considering the absorption of a freshly prepared solution of **PyKC** and **PyKRGD** (1 wt% and 0.01 wt% respectively in 20 mM Tris buffer (pH 8) and similarly diluted). All experiments were performed in triplicate.

5.4.11 In-vitro Release Study

In all cases, the composite hydrogel was prepared following a similar protocol as mentioned earlier, except that the required amount of buffer solutions that were added to fill up the volume contained 0.1 mg of the respective protein. The hydrogels were incubated in the dark before using them for the release studies. To these protein-loaded hydrogels, 1 mL reduced GSH solution (0.1 or 1 or 10 mM) were carefully added, and the centrifuge tube was carefully shaken to disperse the hydrogel into the GSH solution. The sample was then kept on horizontally on a shaker and shaken slowly (100 rpm). Before taking the sample for measurements, the sample was centrifuged to bring the gel to the bottom of the centrifuge tube and allowed to stand for 5 mins. The aliquots were taken from the supernatant solution, an equal volume of fresh GSH solutions were added. The same process was repeated every time. The collected samples were analysed by measuring the absorbance of the tagged proteins at their respective λ_{max} (Table 1). For the 100% release, the protein-loaded hydrogel (similar concentration and volume) was completely dissolved in 1 mL 100 mM GSH solution by mechanical stirring, and the absorbance of the solution was recorded. The cumulative release was calculated using the absorbance values at a different time and the 100% release. Control release studies were carried out in pH 7.4 buffer. All experiments were done in triplicate.

Appendix

(NMR, Mass and HPLC of Synthesized Compounds)

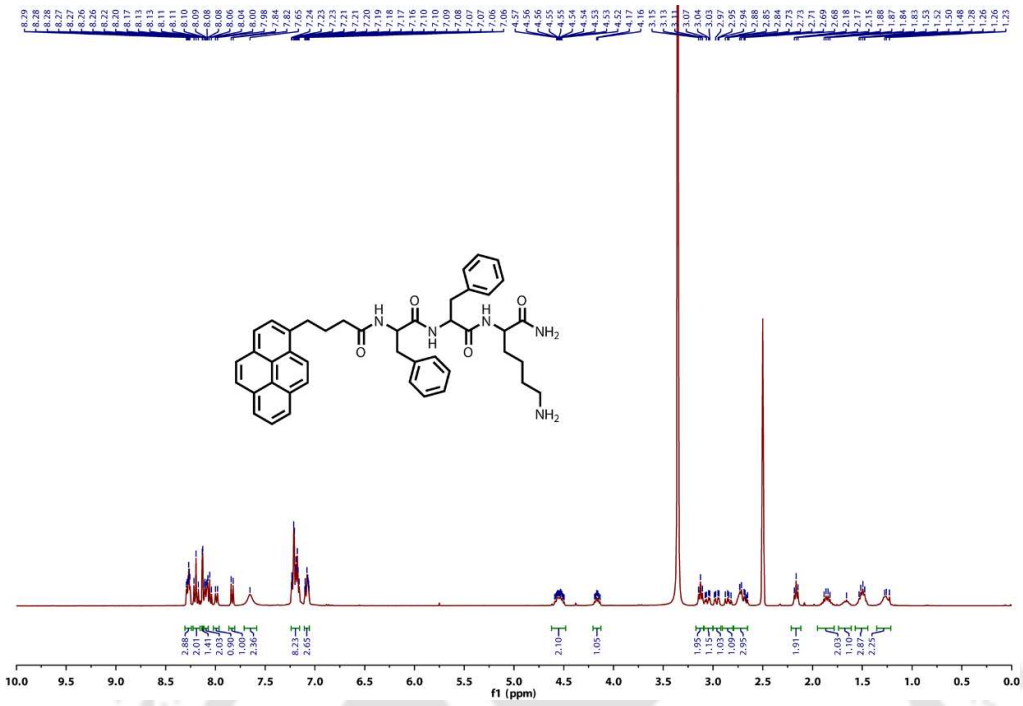

Figure 6.1 [1]H NMR spectrum of **PyFFK** in DMSO-d_6.

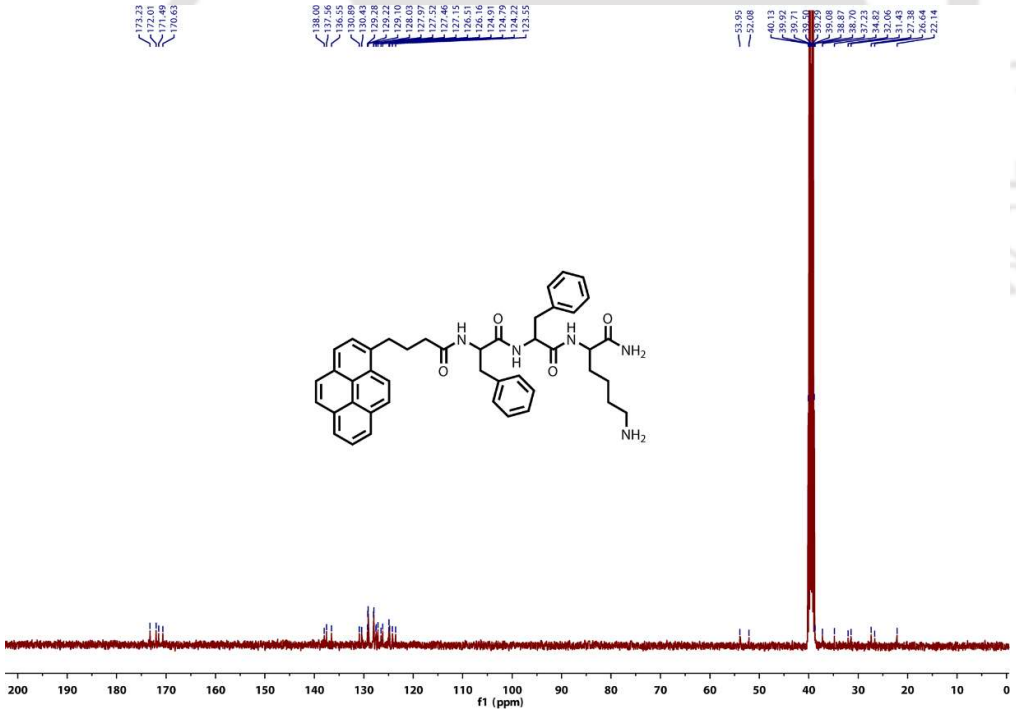

Figure 6.2 [13]C NMR spectrum of **PyFFK** in DMSO-d_6.

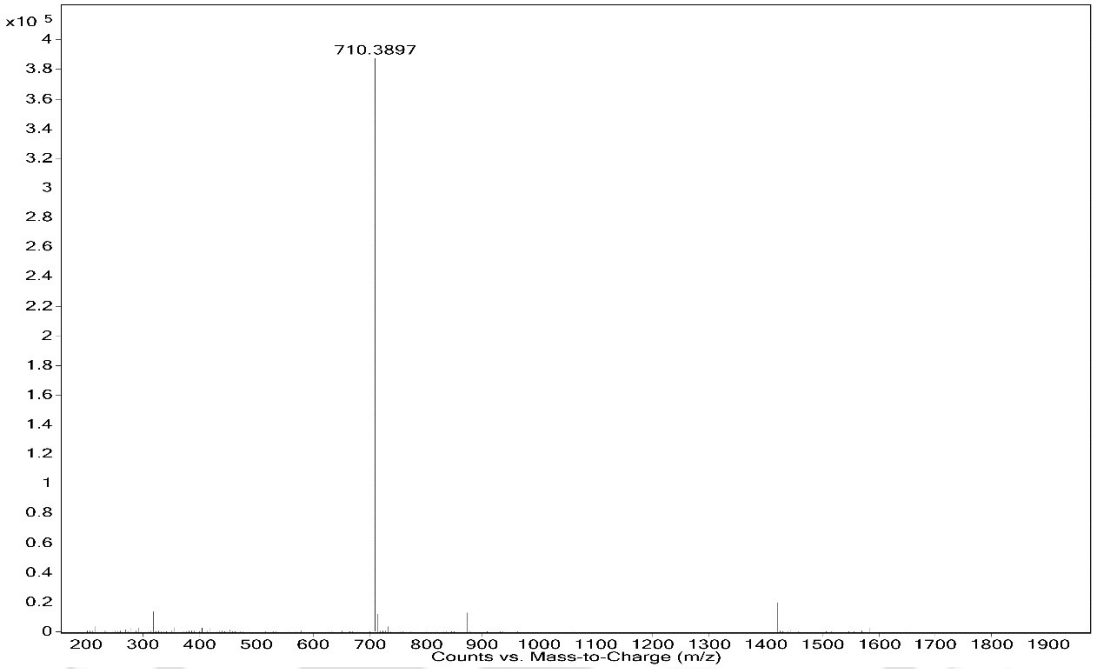

Figure 6.3 ESI-MS of **PyFFK**.

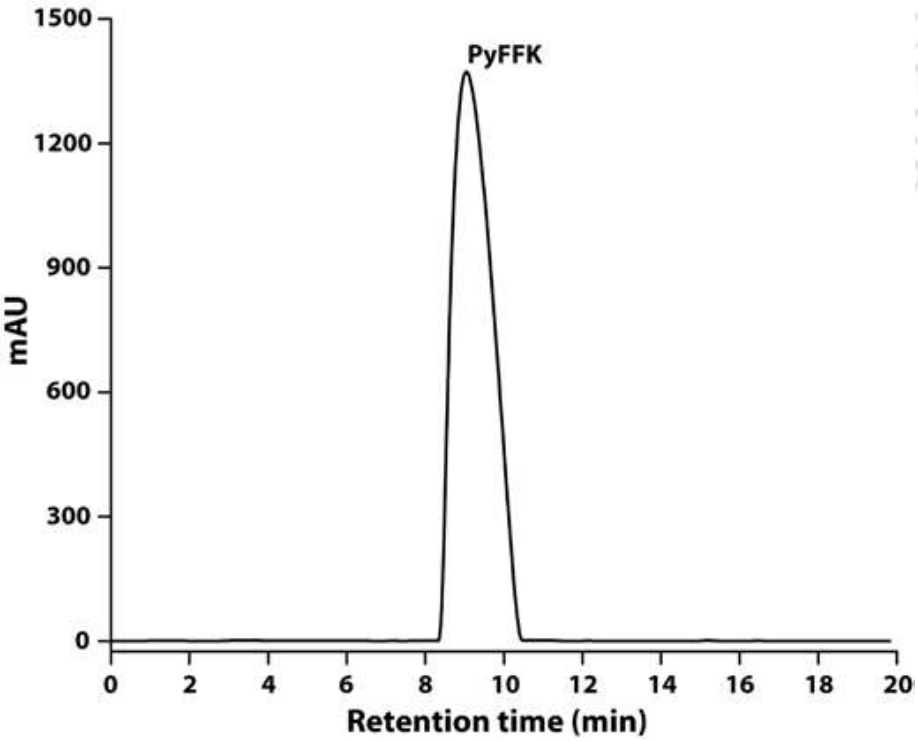

Figure 6.4 Analytical HPLC chromatogram of **PyFFK**.

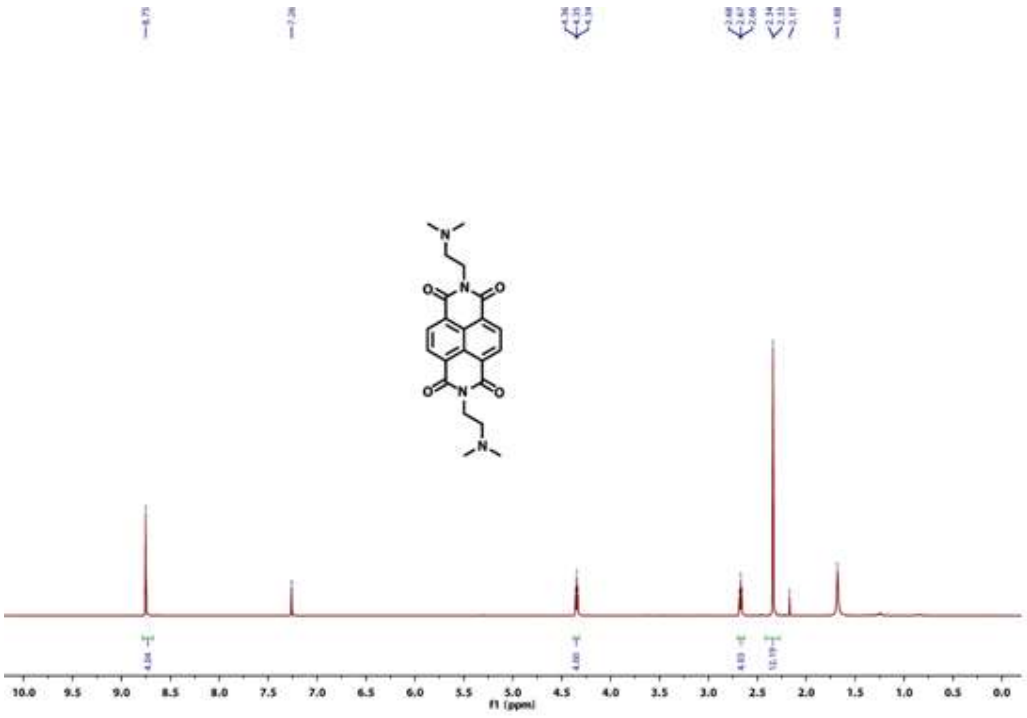

Figure 6.5 ^{1}H NMR spectrum of **Compound 2.1** in $CDCl_3$.

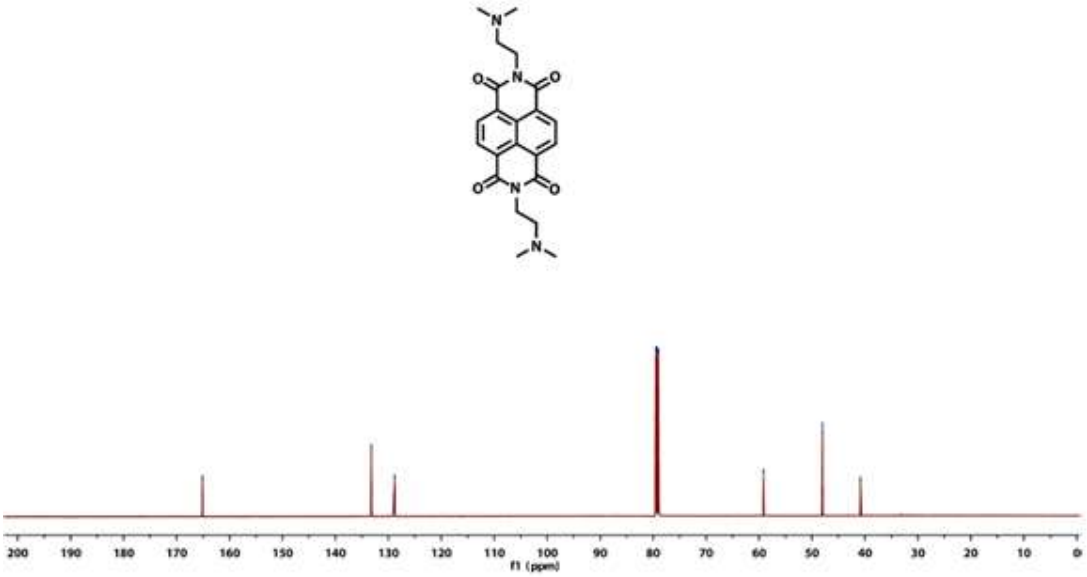

Figure 6.6 ^{13}C NMR spectrum of **Compound 2.1** in $CDCl_3$.

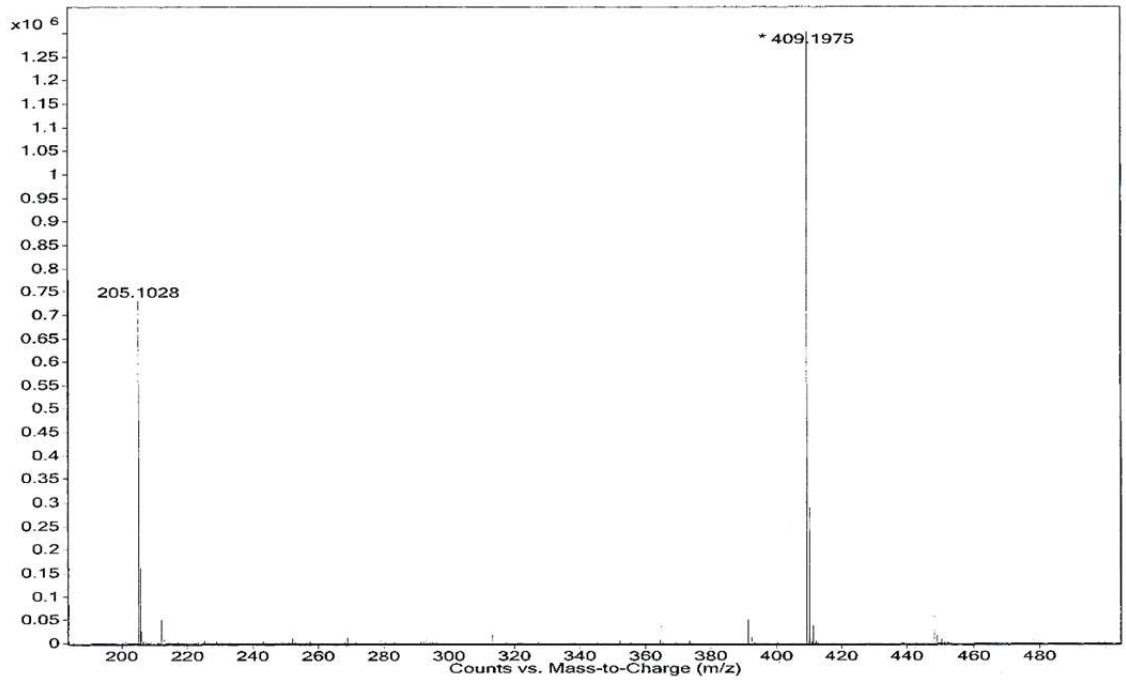

Figure 6.7 ESI-MS of **Compound 2.1**.

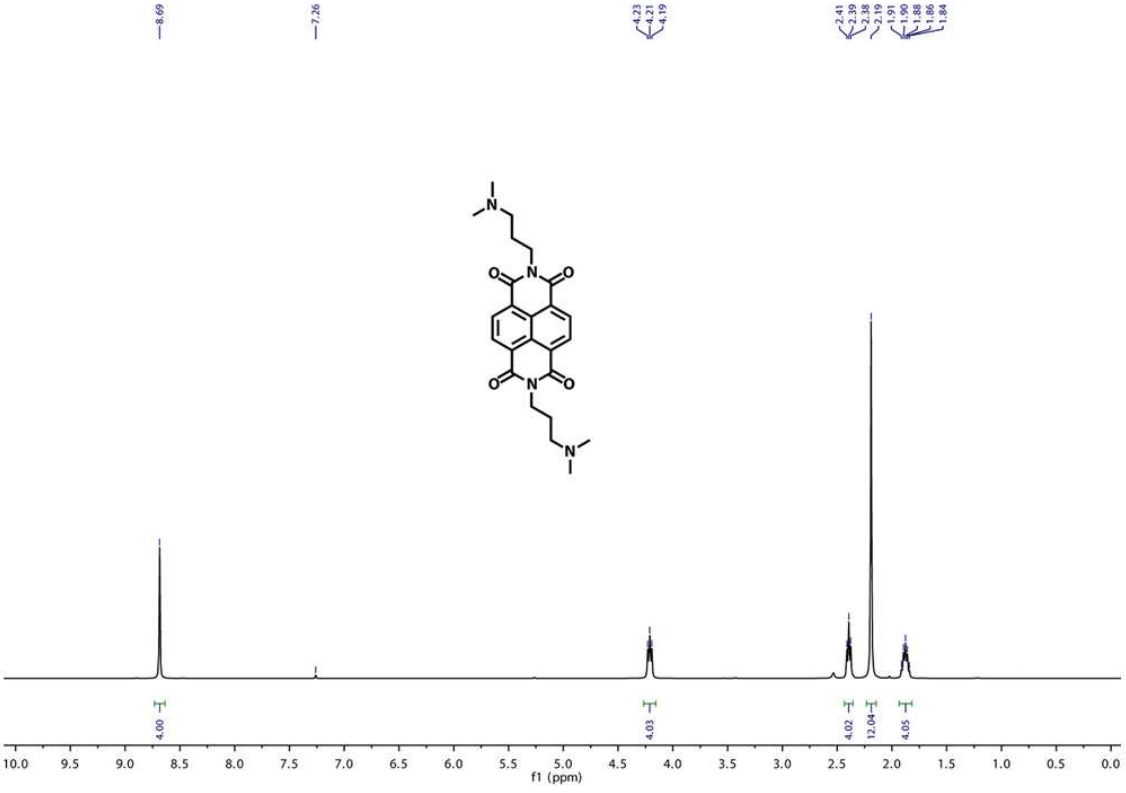

Figure 6.8 ^{1}H NMR spectrum of **Compound 2.2** in $CDCl_3$.

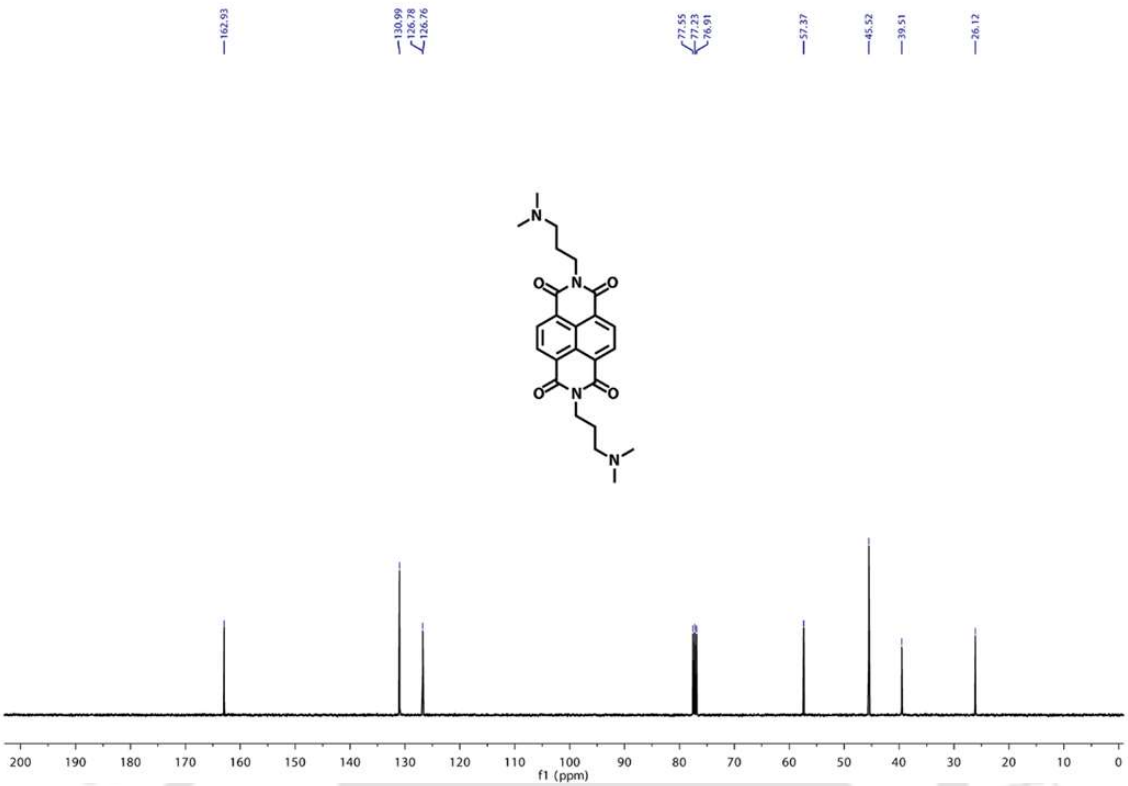

Figure 6.9 ^{13}C NMR spectrum of **Compound 2.2** in $CDCl_3$.

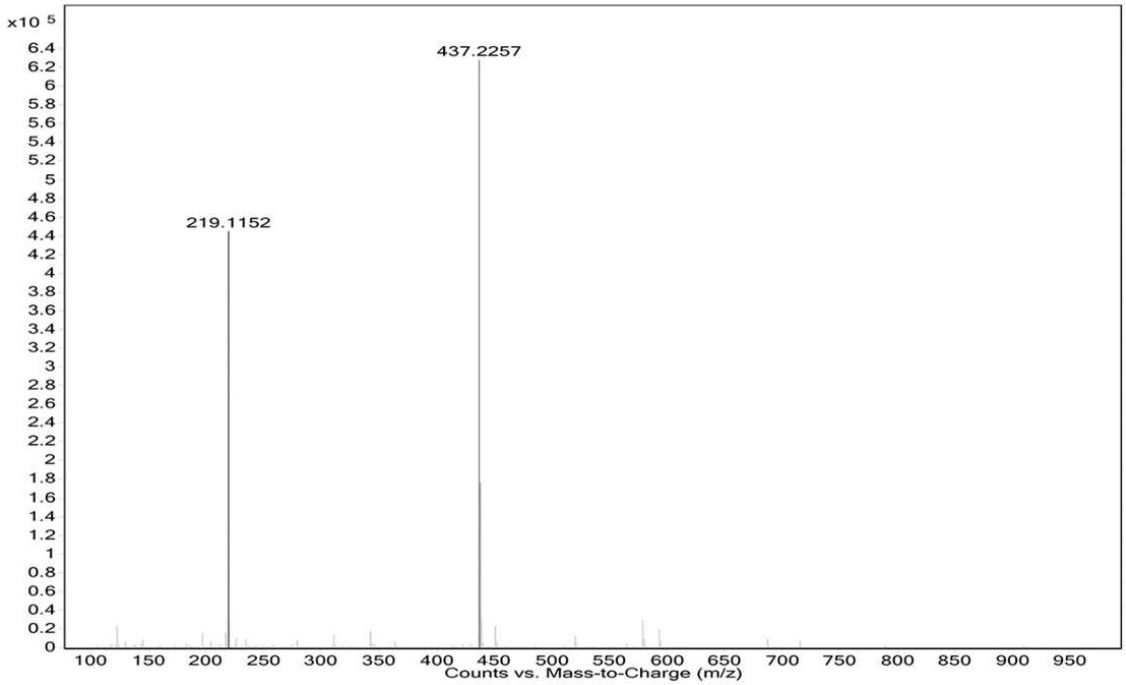

Figure 6.10 ESI-MS of **Compound 2.2**.

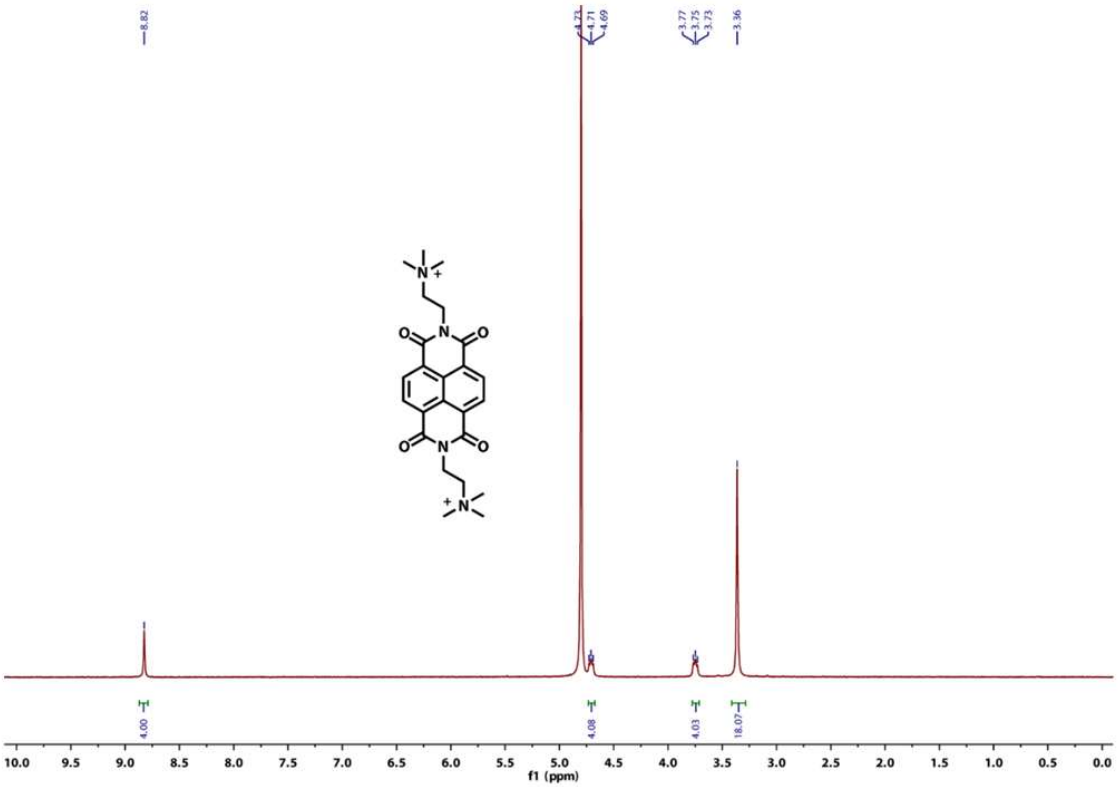

Figure 6.11 ^{1}H NMR spectrum of **NDTA** in D_2O.

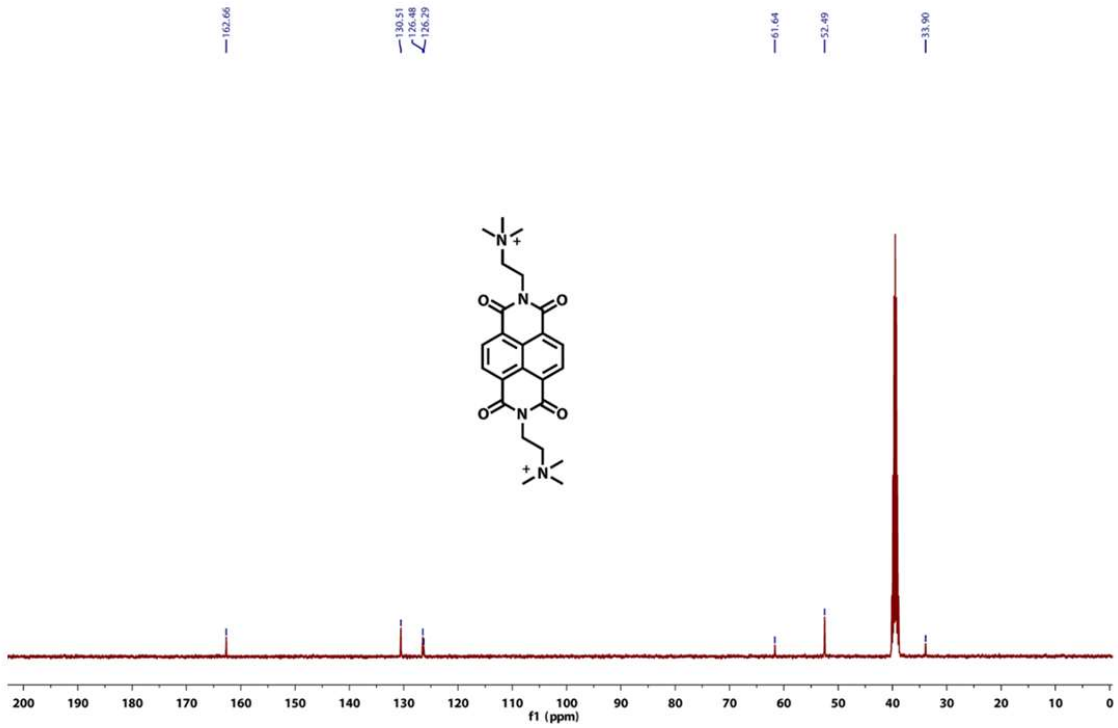

Figure 6.12 ^{13}C NMR spectrum of **NDTA** in D_2O.

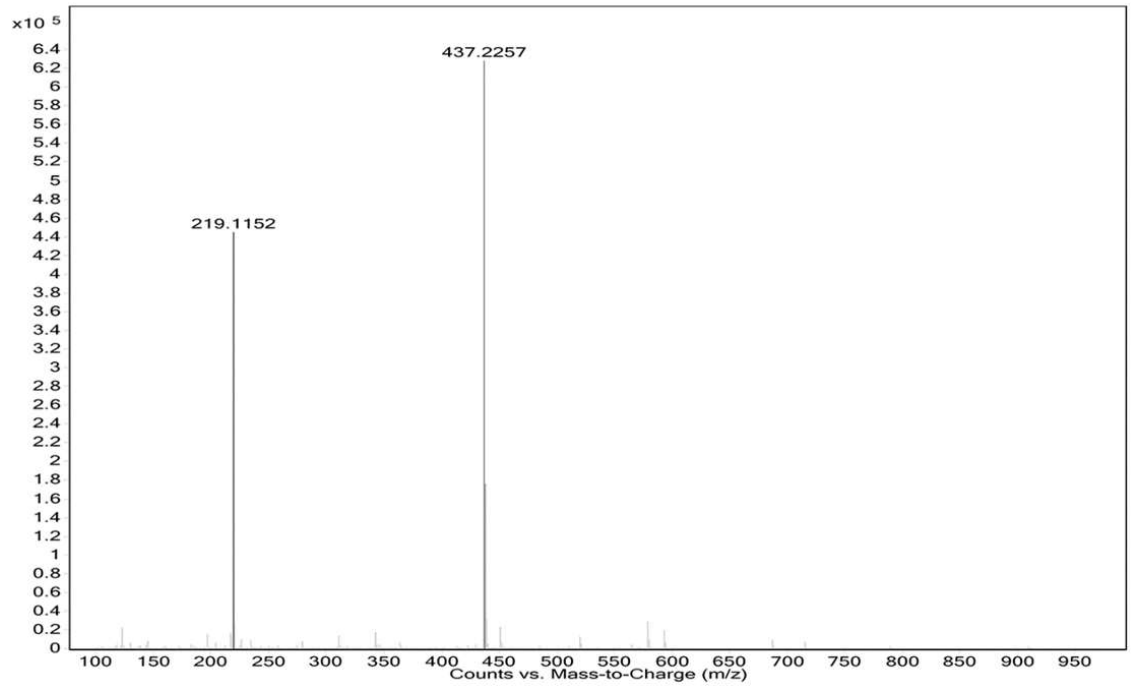

Figure 6.13 ESI-MS spectrum of **NDTA**.

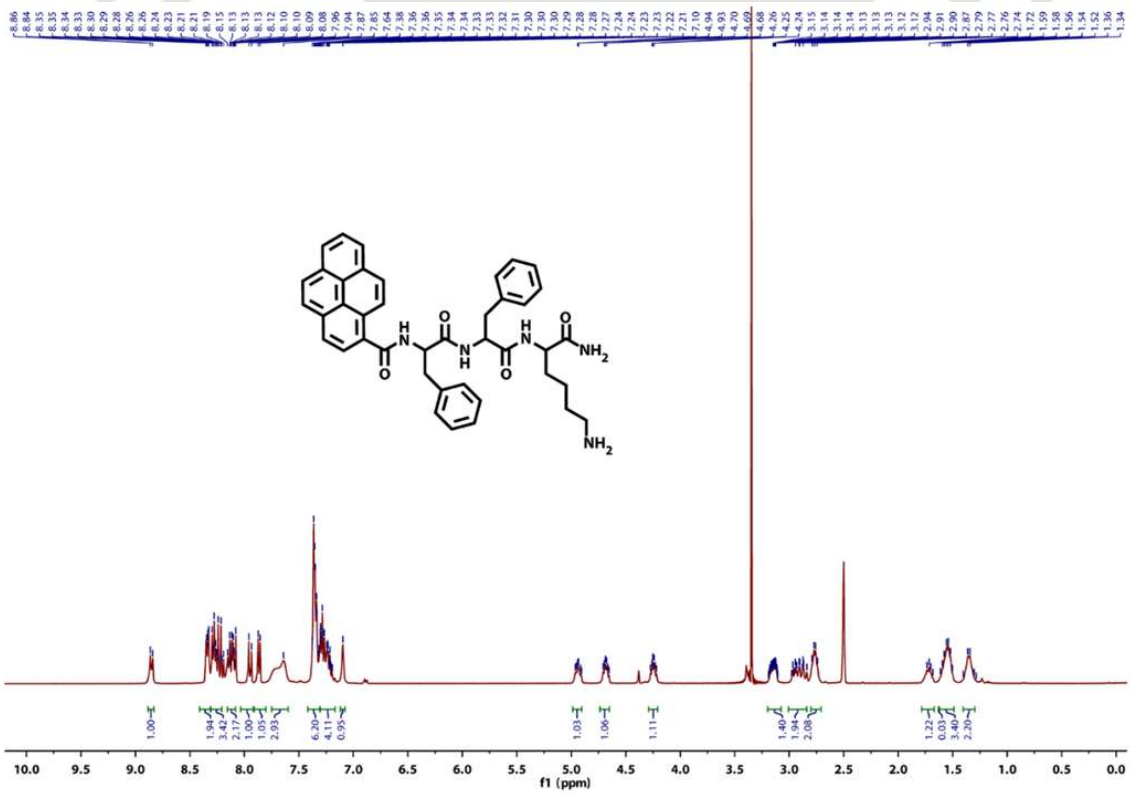

Figure 6.14 ^{1}H NMR spectrum of **Pep-2** in DMSO-d_6.

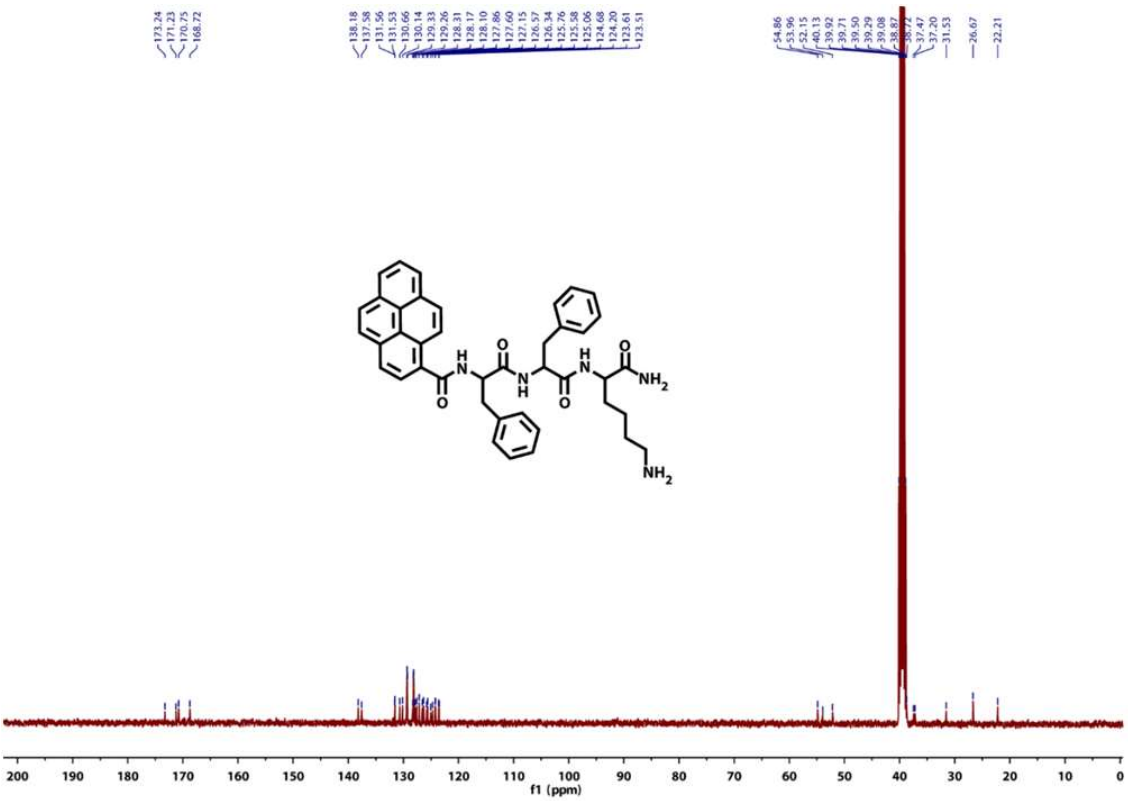

Figure 6.15 ^{13}C NMR spectrum of **Pep-2** in DMSO-d_6.

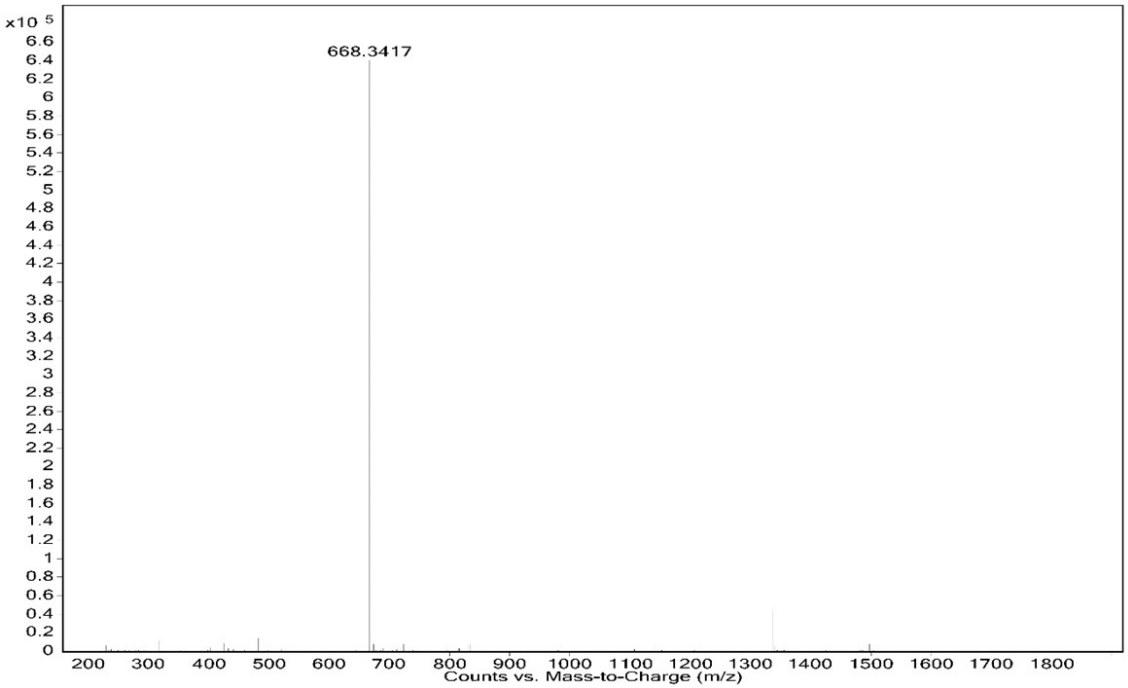

Figure 6.16 ESI-MS spectrum of **Pep-2**.

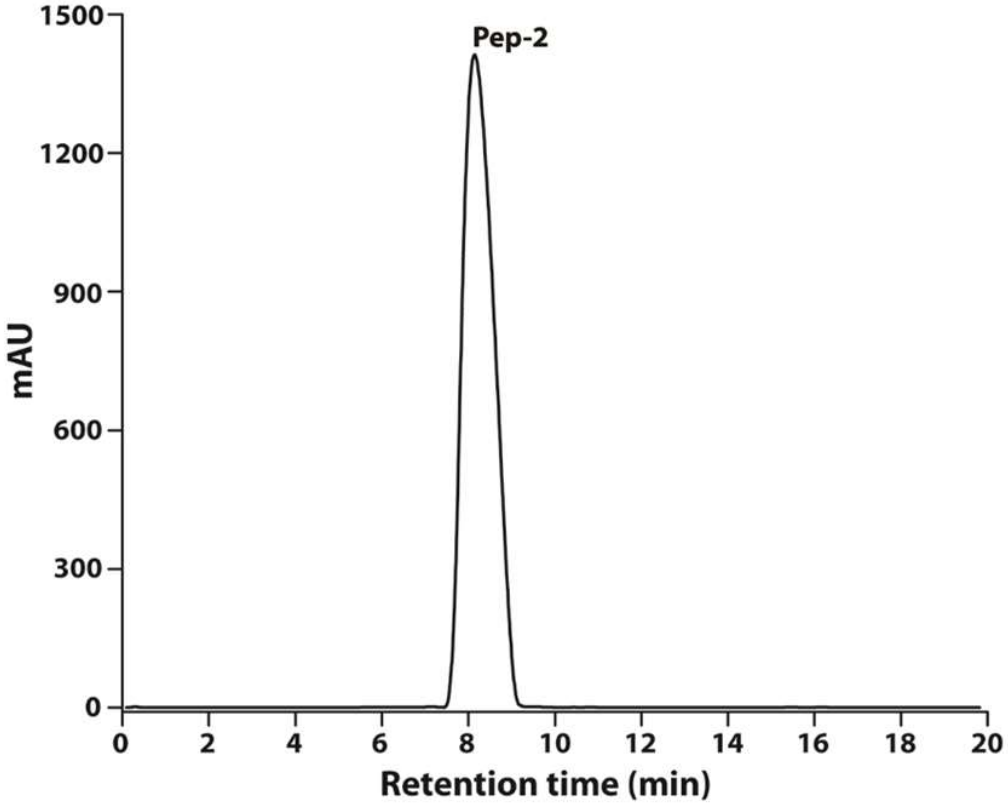

Figure 6.17 Analytical HPLC chromatogram of **Pep-2**.

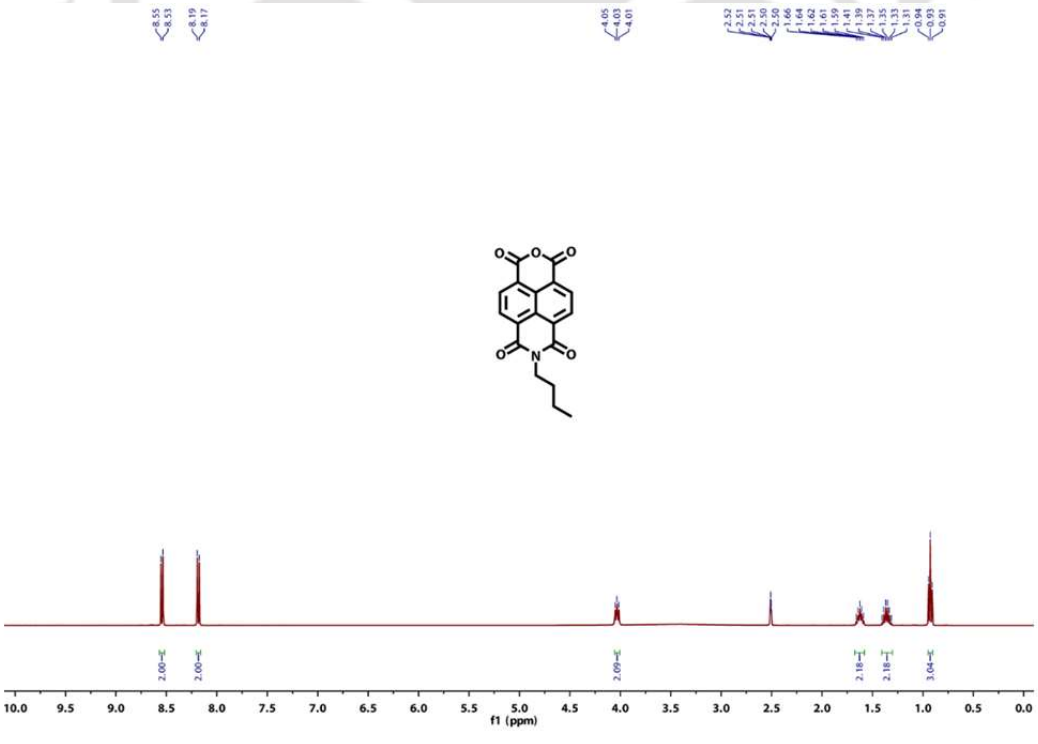

Figure 6.18 ^{1}H NMR spectrum of **Compound 2.3** in DMSO-d_6.

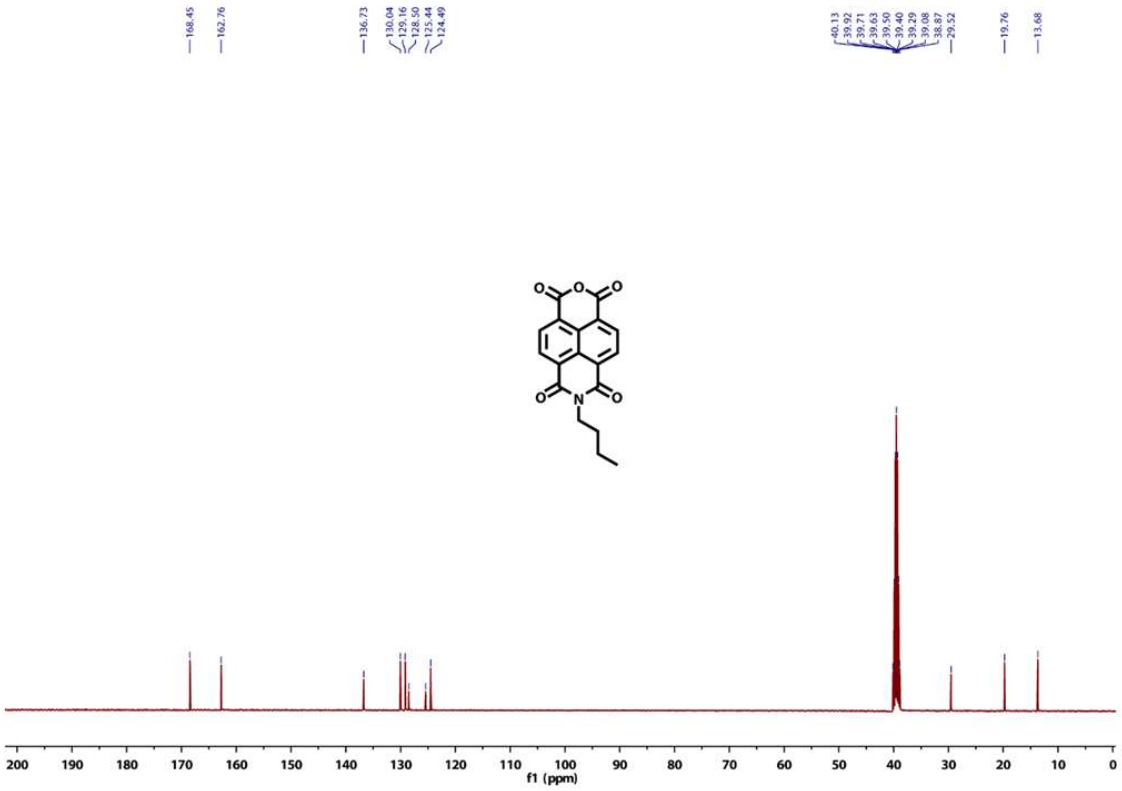

Figure 6.19 ^{13}C NMR spectrum of **Compound 2.3** in DMSO-d_6.

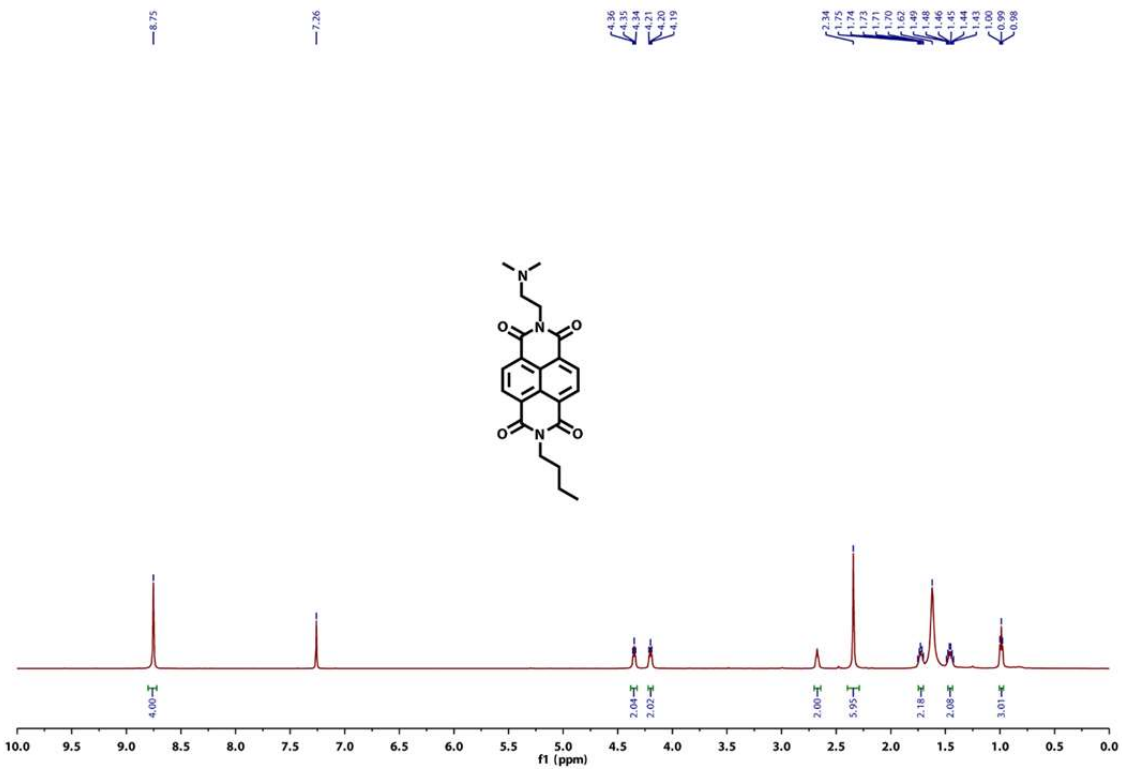

Figure 6.20 ^{1}H NMR spectrum of **Compound 2.4** in $CDCl_3$.

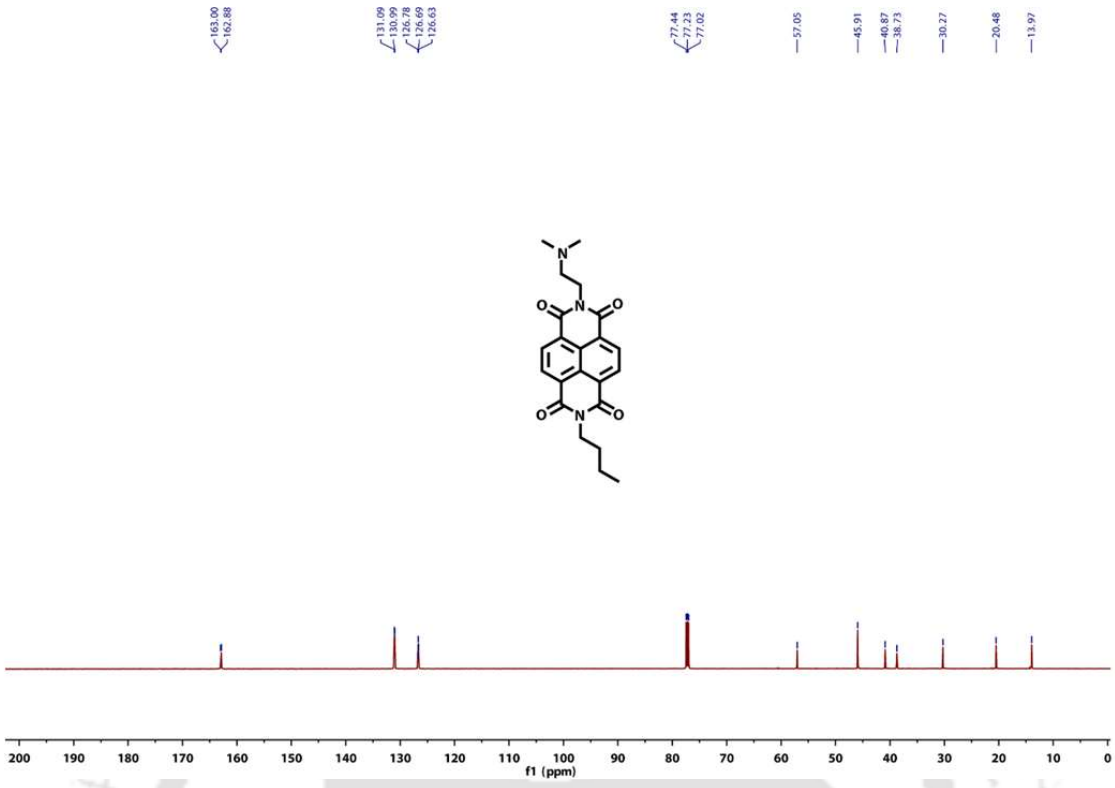

Figure 6.21 ^{13}C NMR spectrum of **Compound 2.4** in $CDCl_3$.

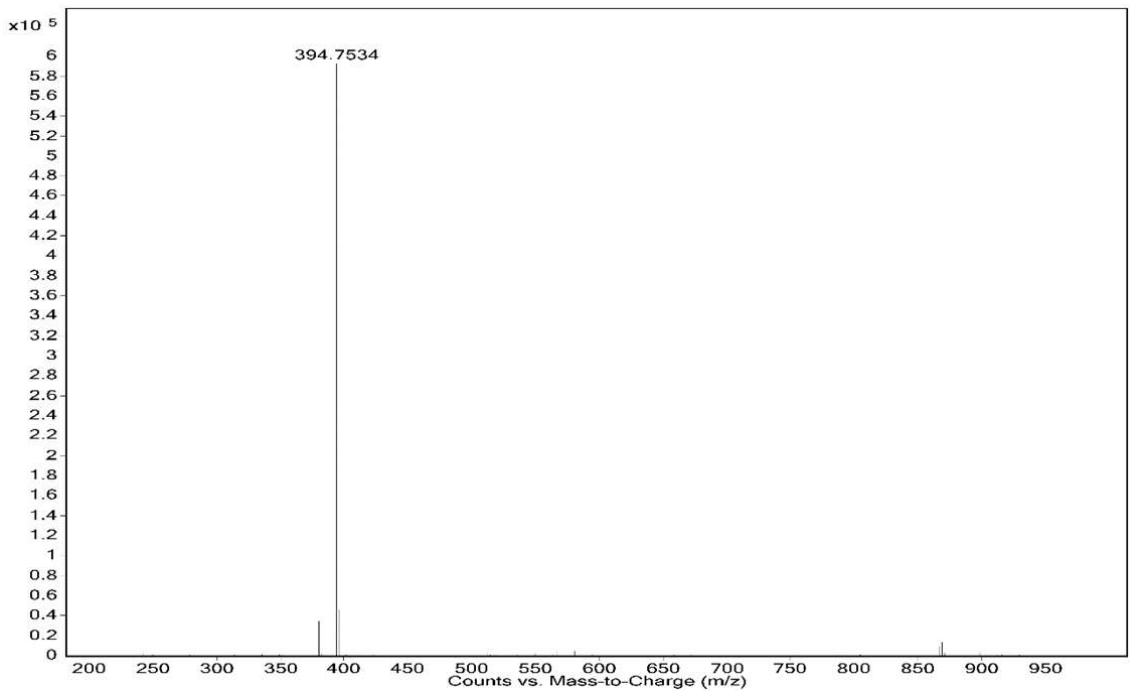

Figure 6.22 ESI-MS spectrum of **Compound 2.4**.

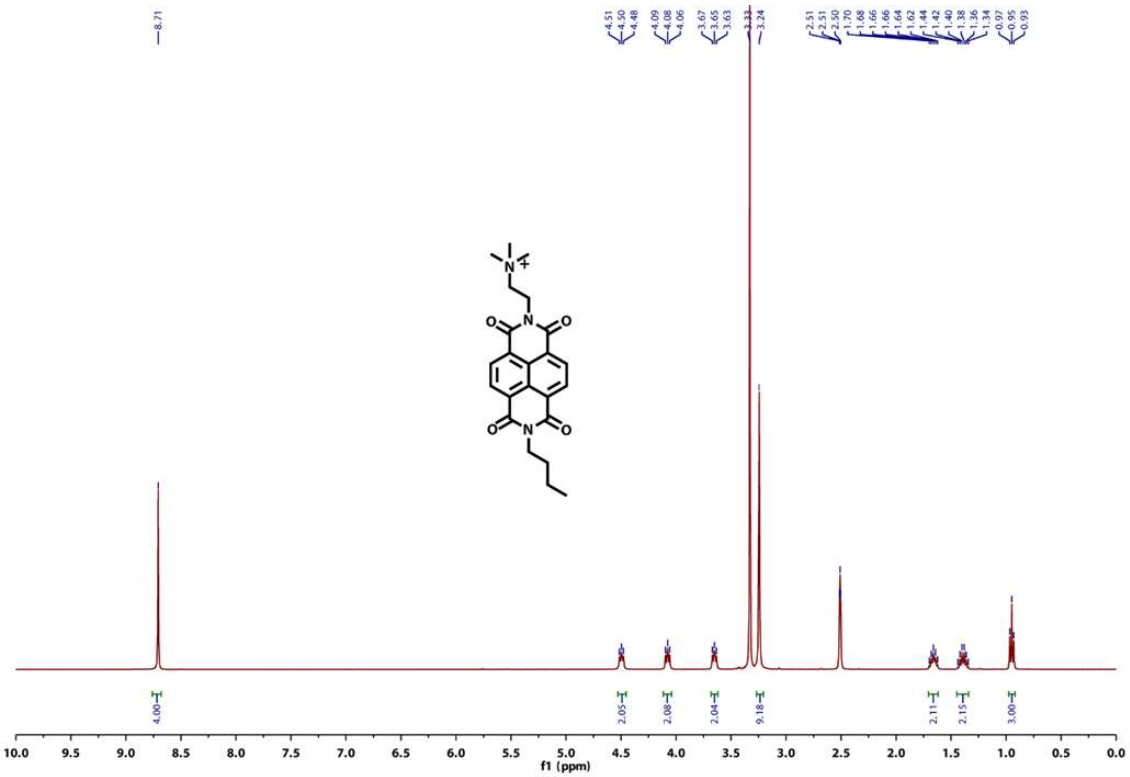

Figure 6.23 ^{1}H NMR spectrum of **Compound 2.5** in $CDCl_3$.

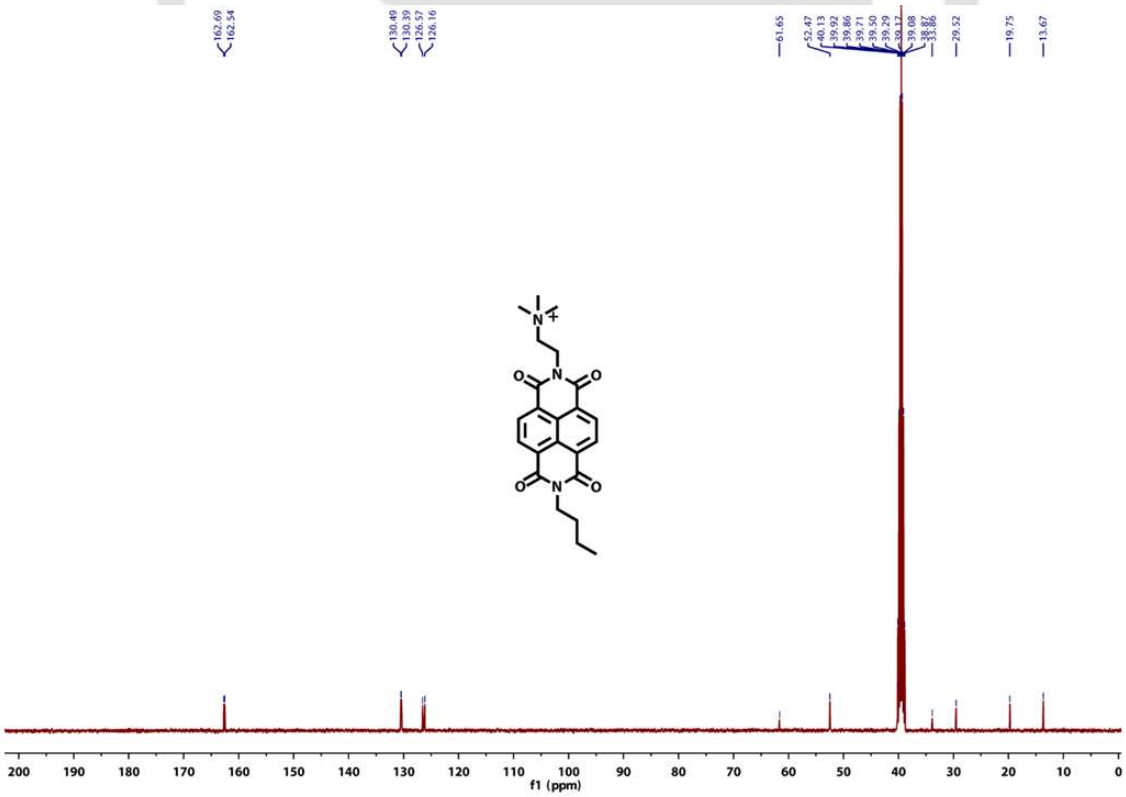

Figure 6.24 ^{13}C NMR spectrum of **Compound 2.5** in $CDCl_3$.

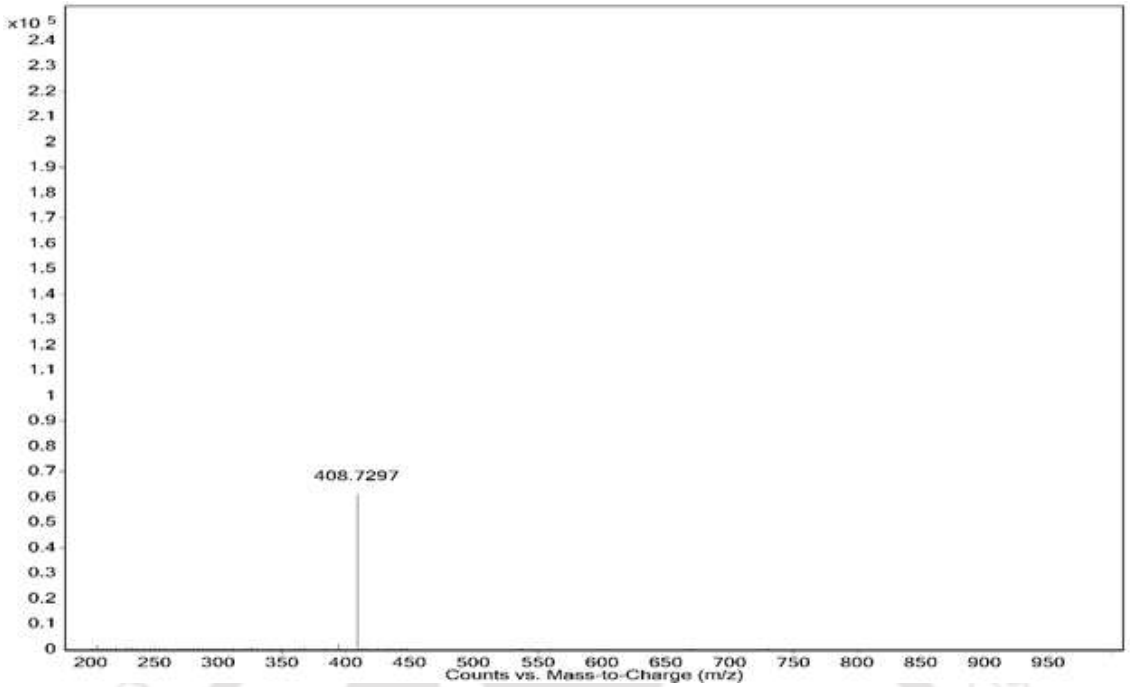

Figure 6.25 ESI-MS spectrum of **Compound 2.5**.

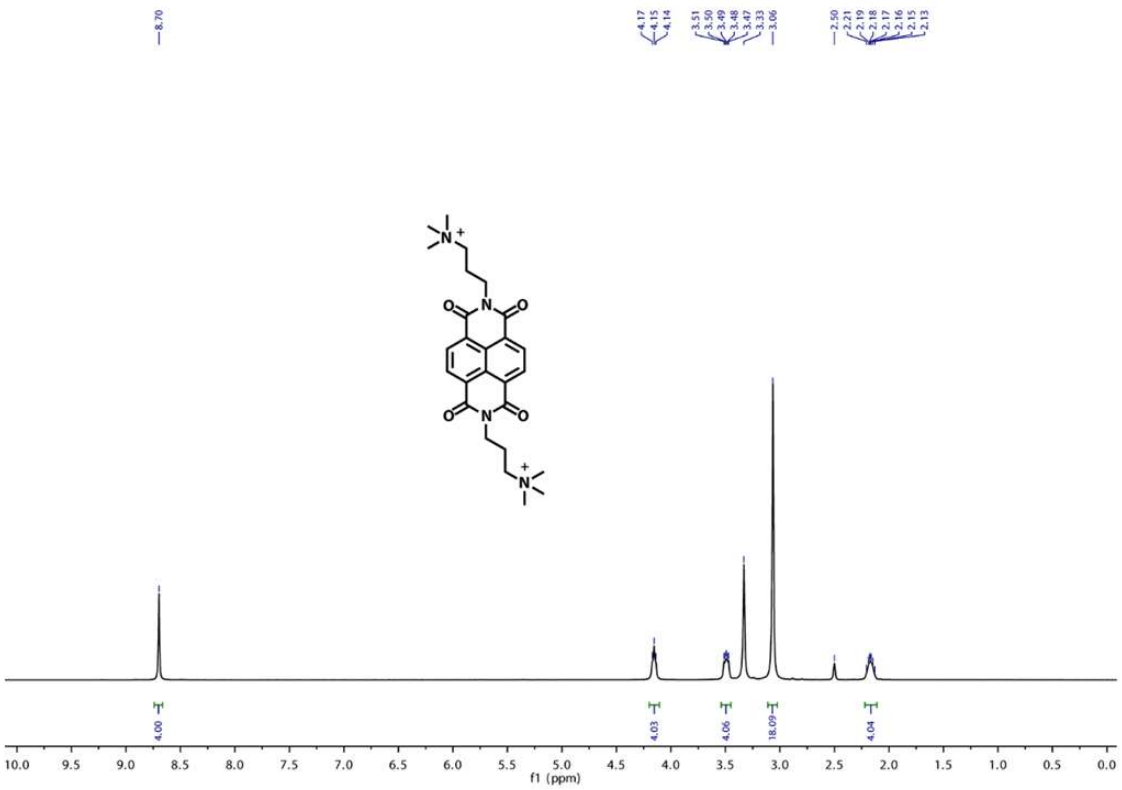

Figure 6.26 ^{1}H NMR spectrum of **Compound 2.6** in DMSO-d_6.

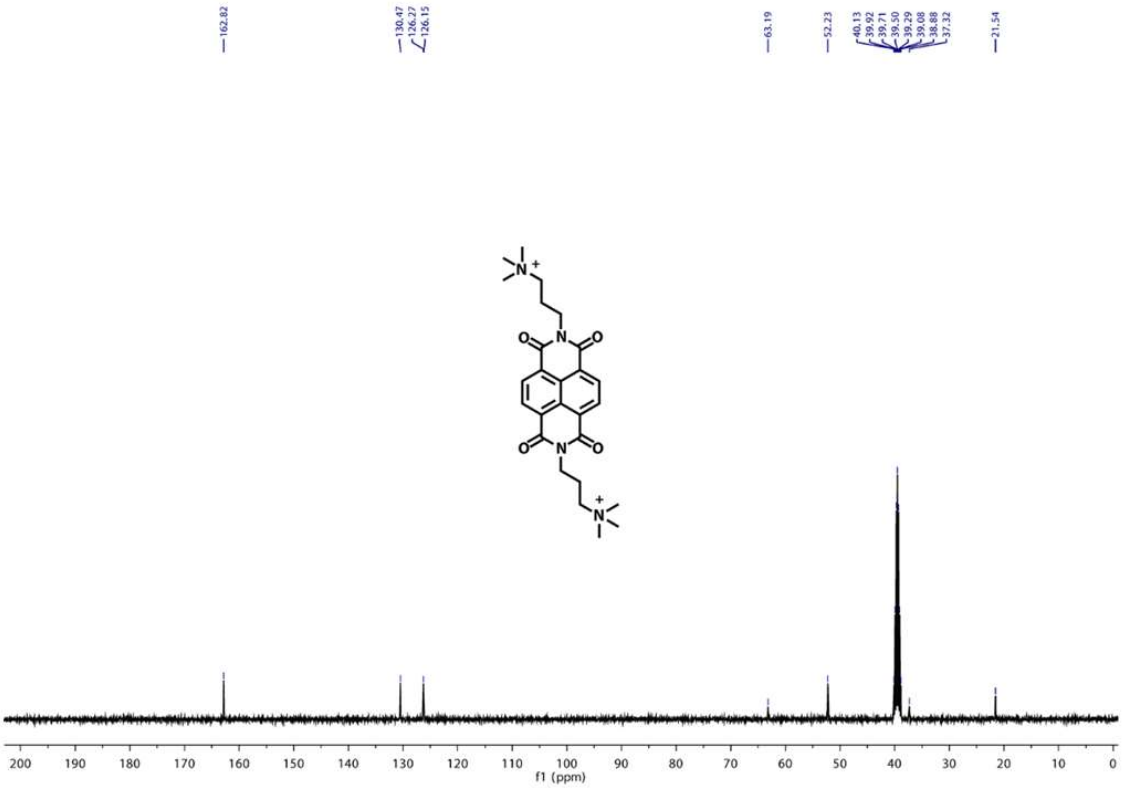

Figure 6.27 ^{13}C NMR spectrum of **Compound 2.6** in DMSO-d_6.

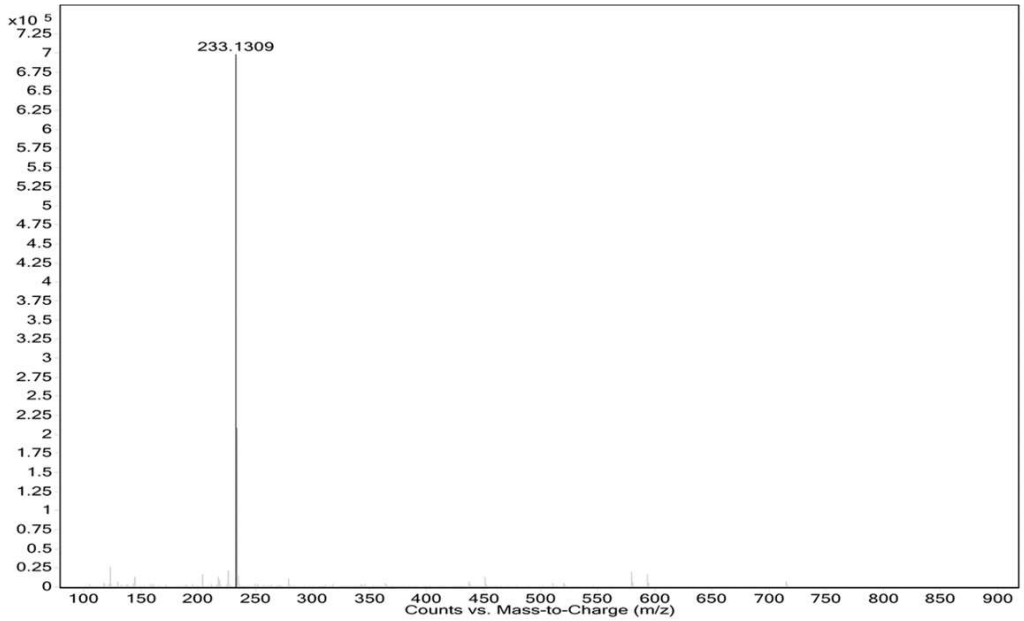

Figure 6.28 ESI-MS of **Compound 2.6**.

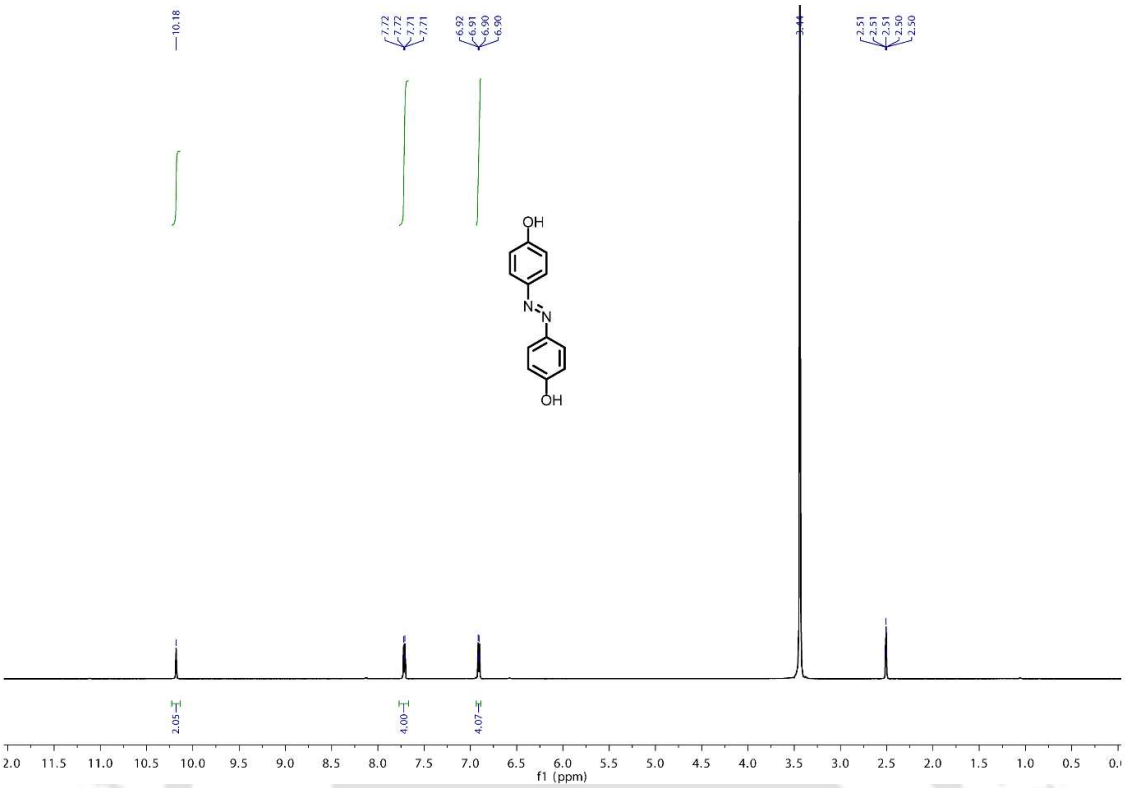

Figure 6.29 ^{1}H NMR spectrum of **Compound 3.1** in $CDCl_3$.

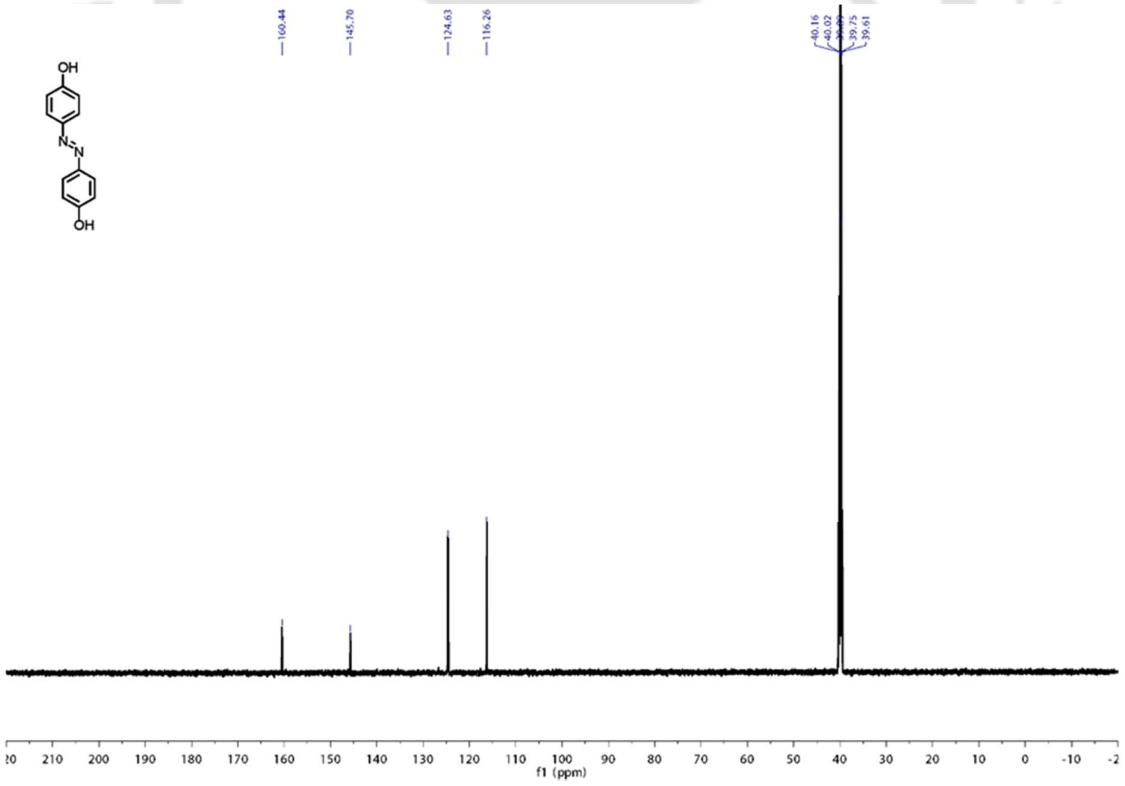

Figure 6.30 ^{13}C NMR spectrum of **Compound 3.1** in $CDCl_3$.

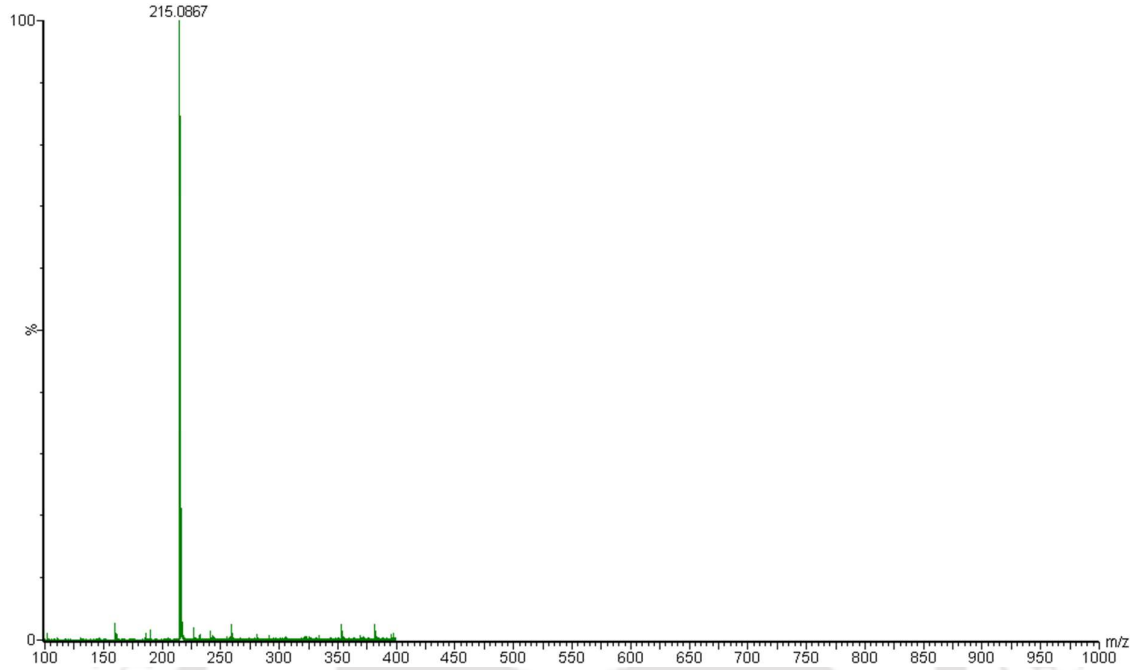

Figure 6.31 LC-MS of **Compound 3.1**.

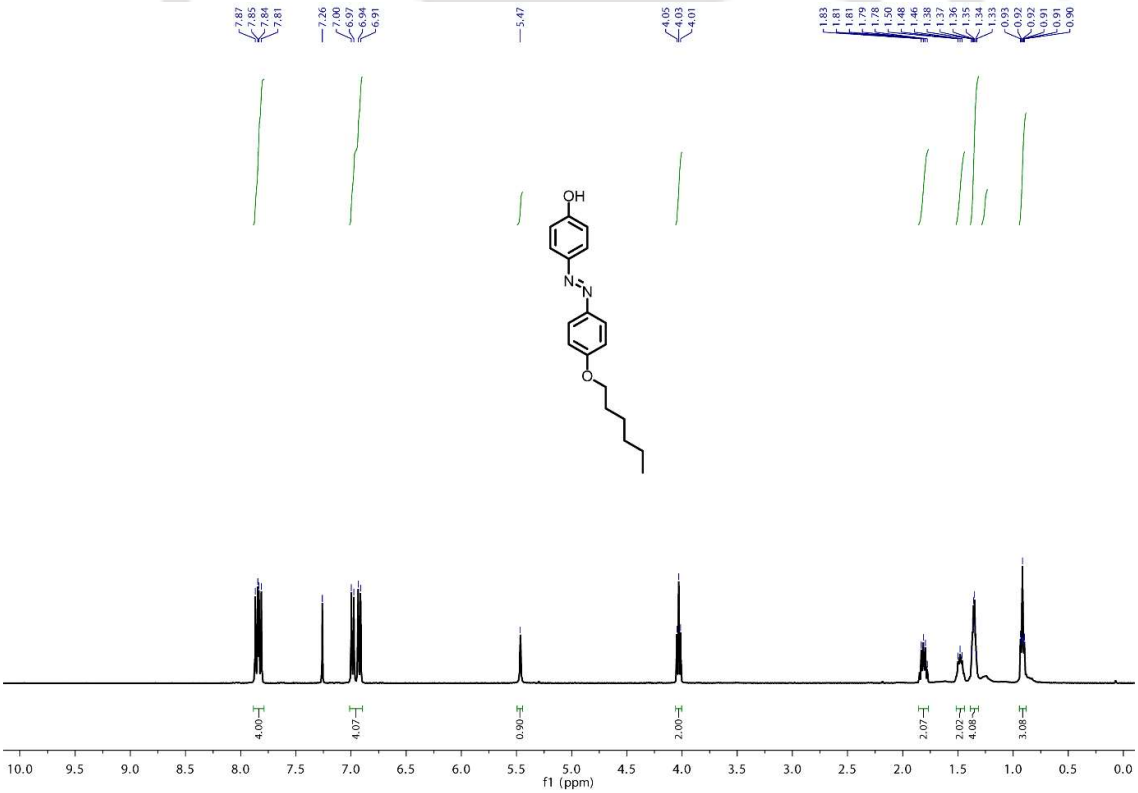

Figure 6.32 ^{1}H NMR spectrum of **Compound 3.2** in $CDCl_3$.

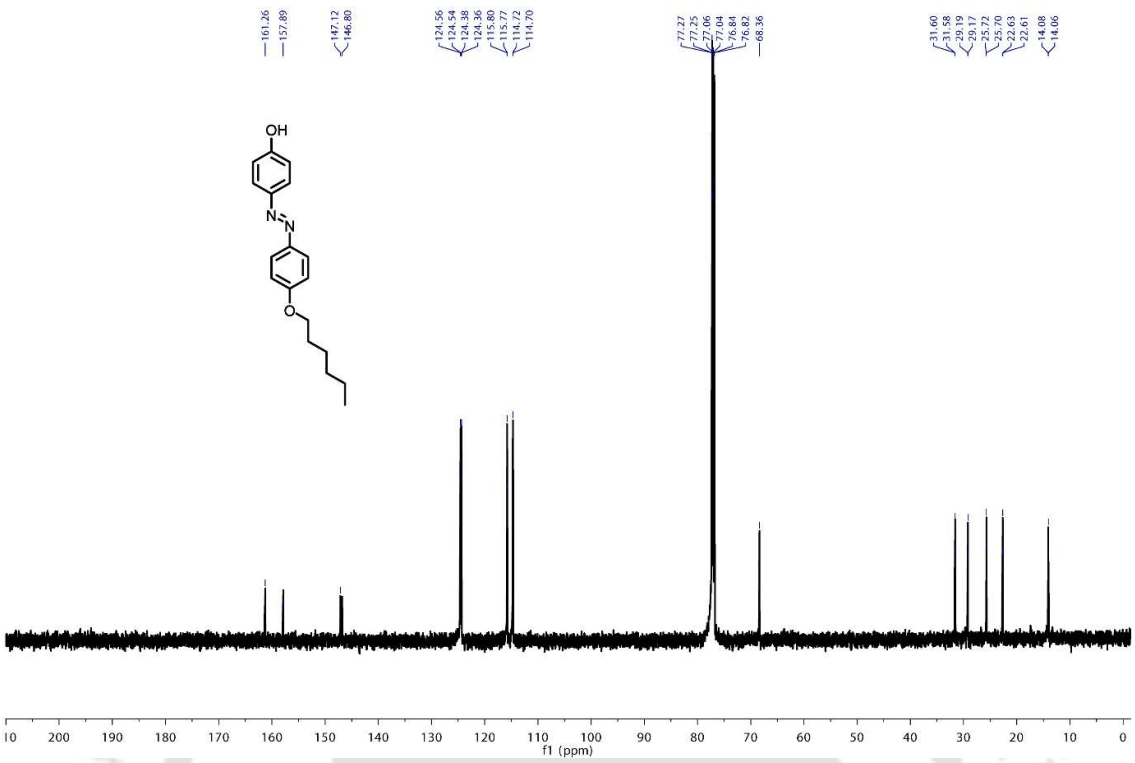

Figure 6. 33 ^{13}C NMR spectrum of **Compound 3.2** in $CDCl_3$.

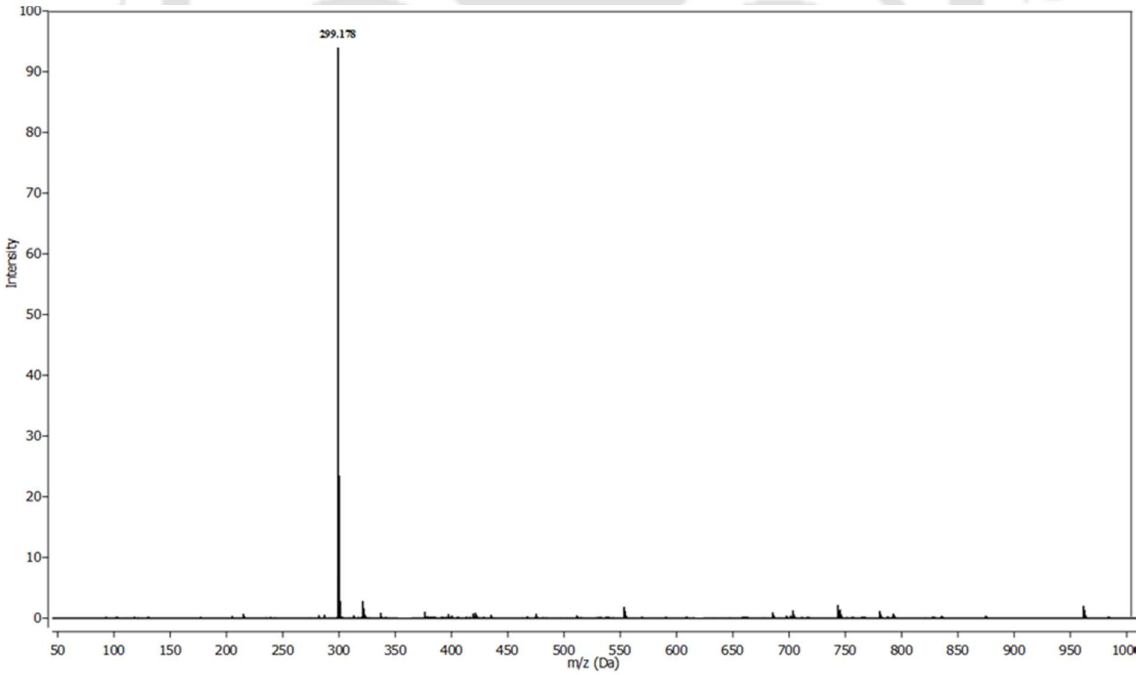

Figure 6.34 ESI-MS of **Compound 3.2**.

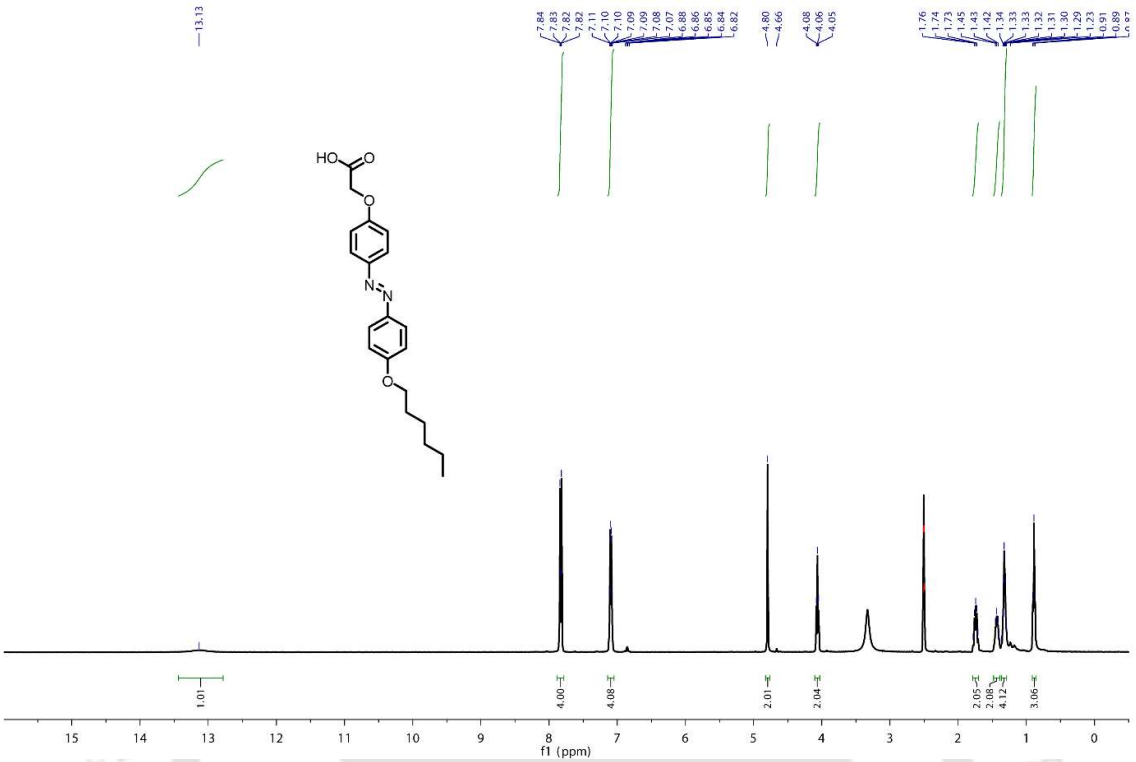

Figure 6.35 ^{1}H NMR spectrum of **Compound 3.3** in DMSO-d_6.

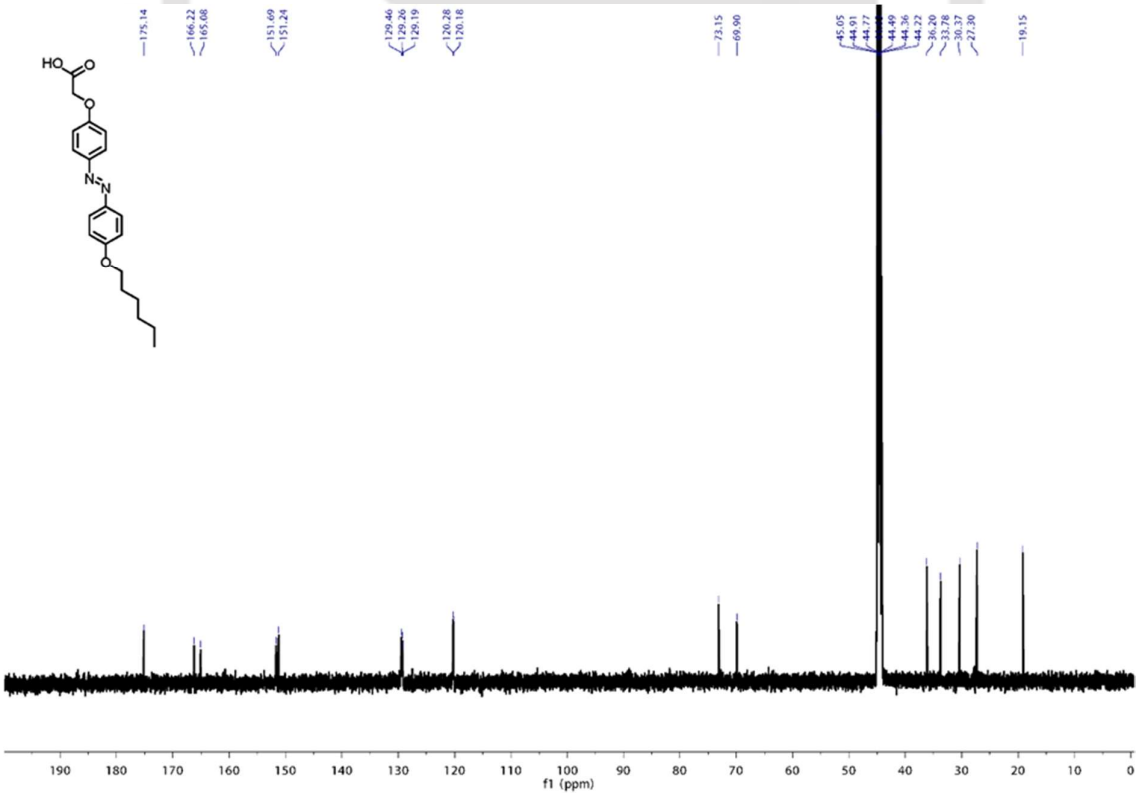

Figure 6.36 ^{13}C NMR spectrum of **Compound 3.3** in DMSO-d_6.

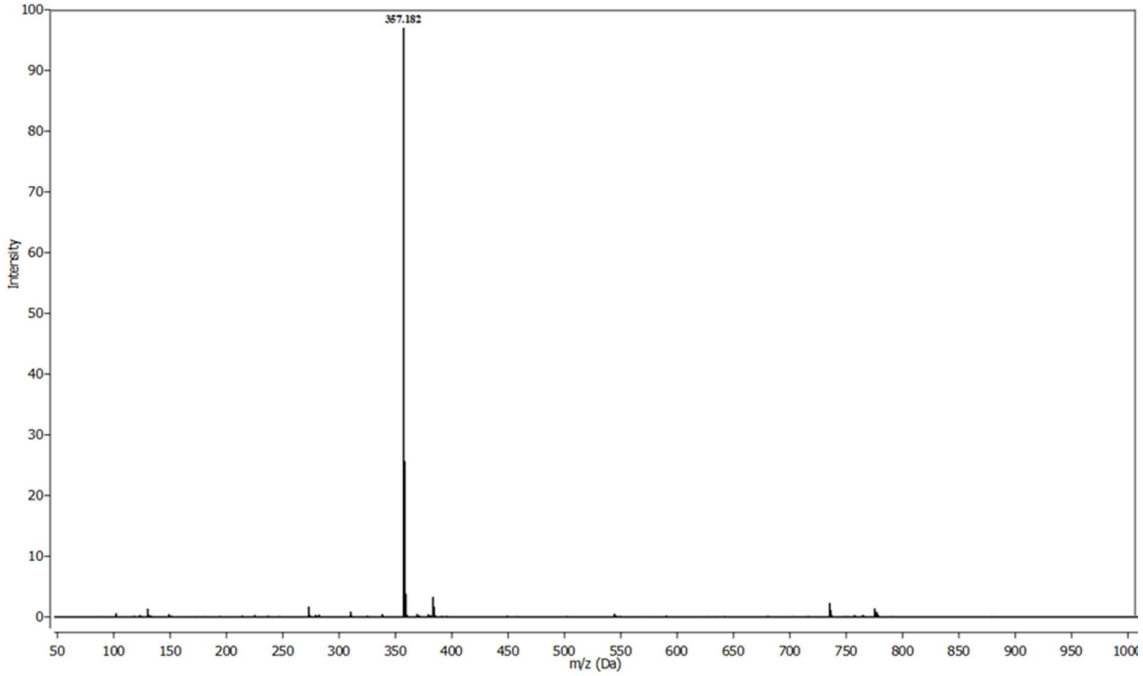

Figure 6.37 ESI-MS of **Compound 3.3**.

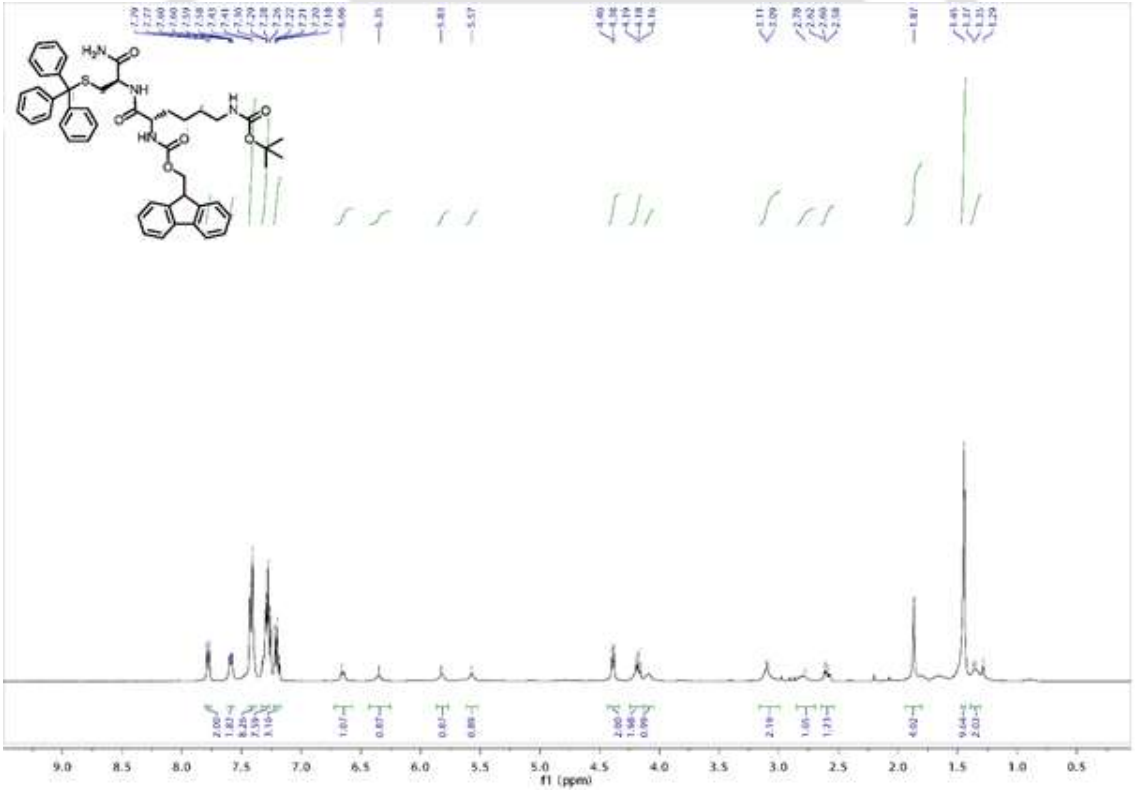

Figure 6.38 ^{1}H NMR spectrum of **Compound 3.4** in $CDCl_3$.

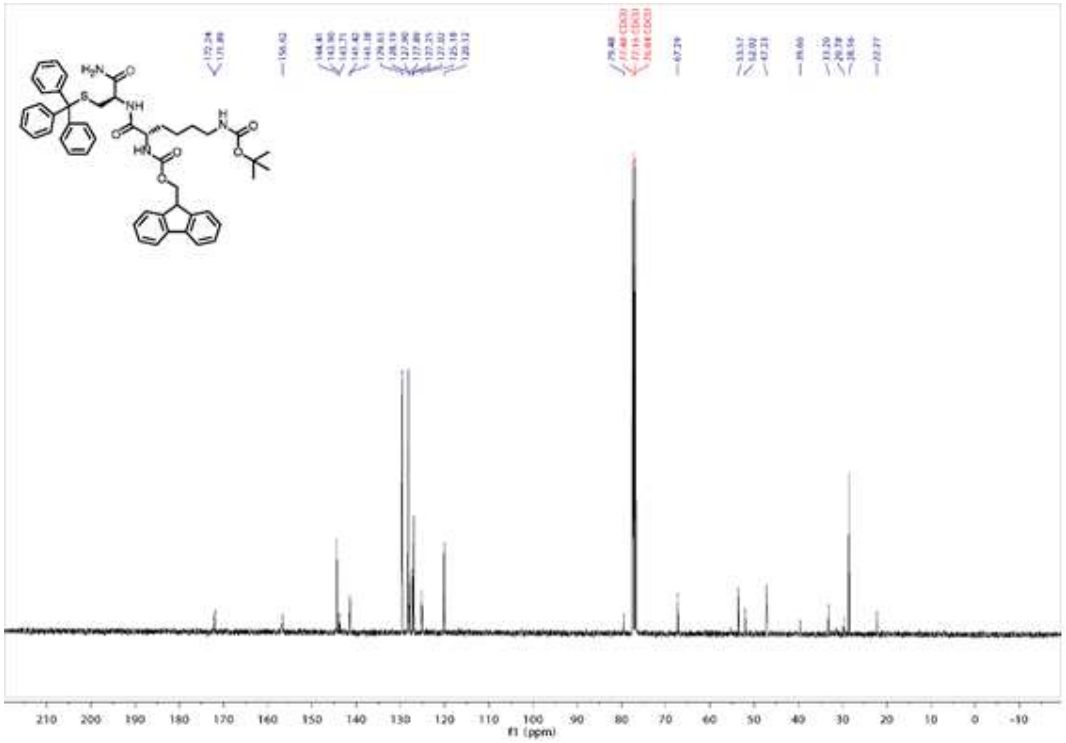

Figure 6.39 ^{13}C NMR spectrum of **Compound 3.4** in $CDCl_3$.

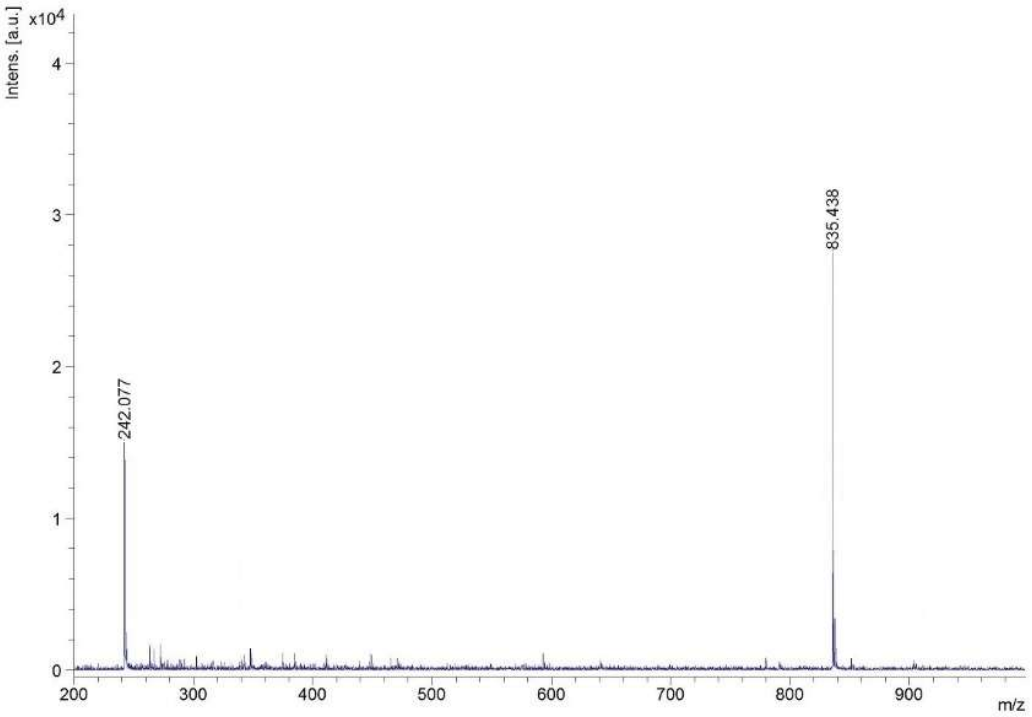

Figure 6.40 MALDI-TOF-MS of **Compound 3.4.**

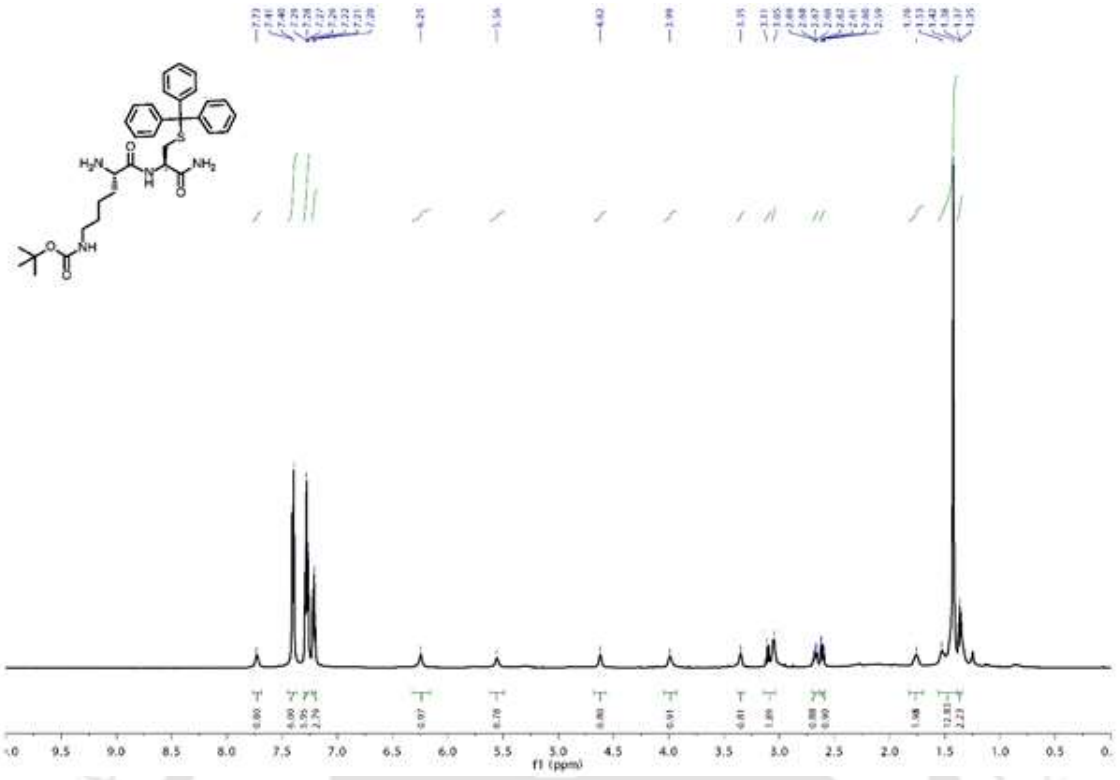

Figure 6.41 ^{1}H NMR spectrum of **Compound 3.5** in $CDCl_3$.

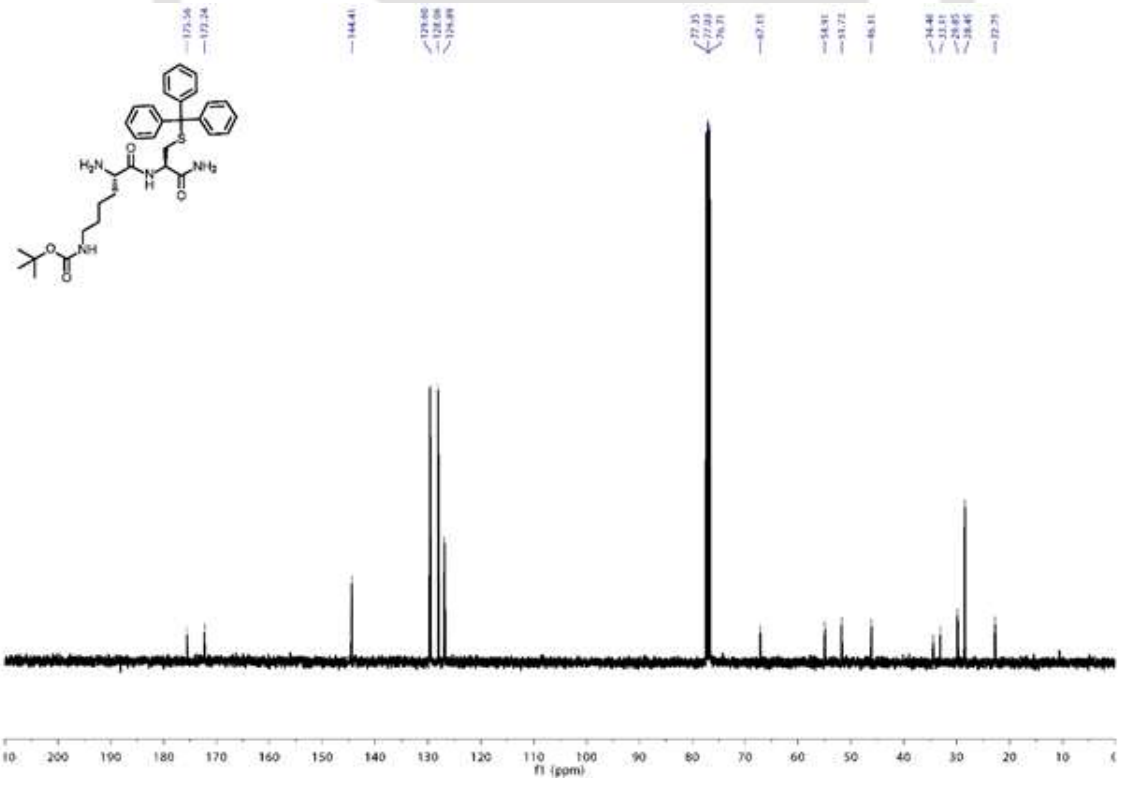

Figure 6.42 ^{13}C NMR spectrum of **Compound 3.5** in $CDCl_3$.

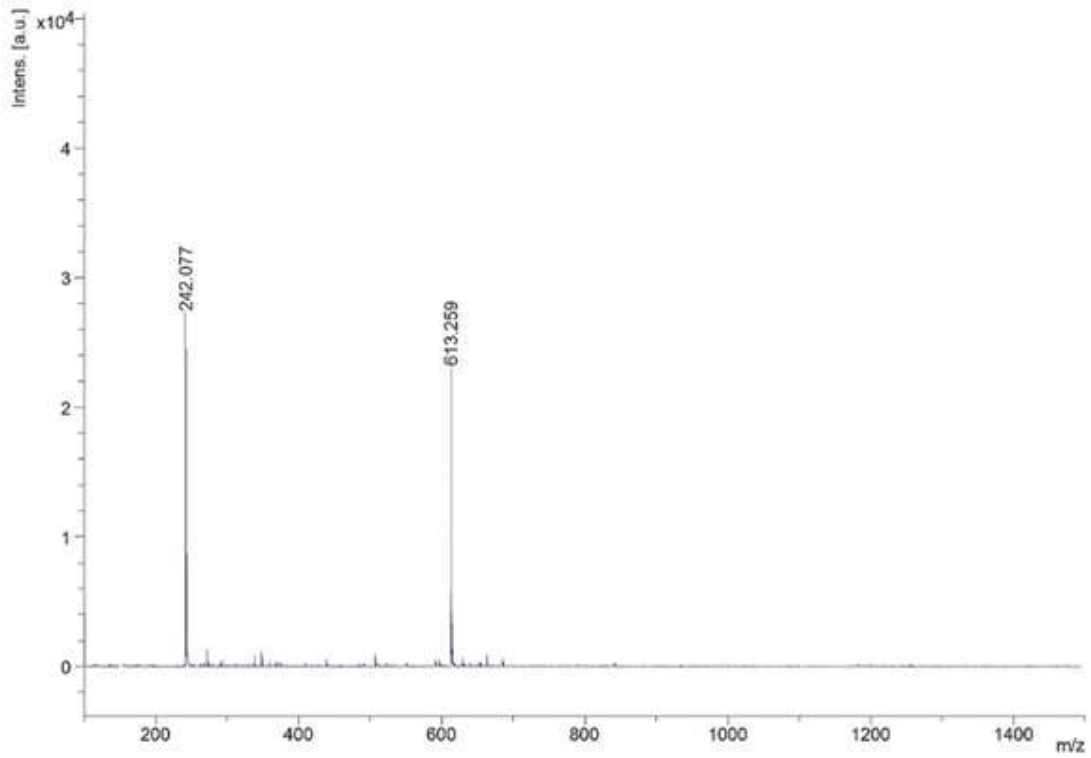

Figure 6.43 MALDI-TOF-MS of **Compound 3.5.**

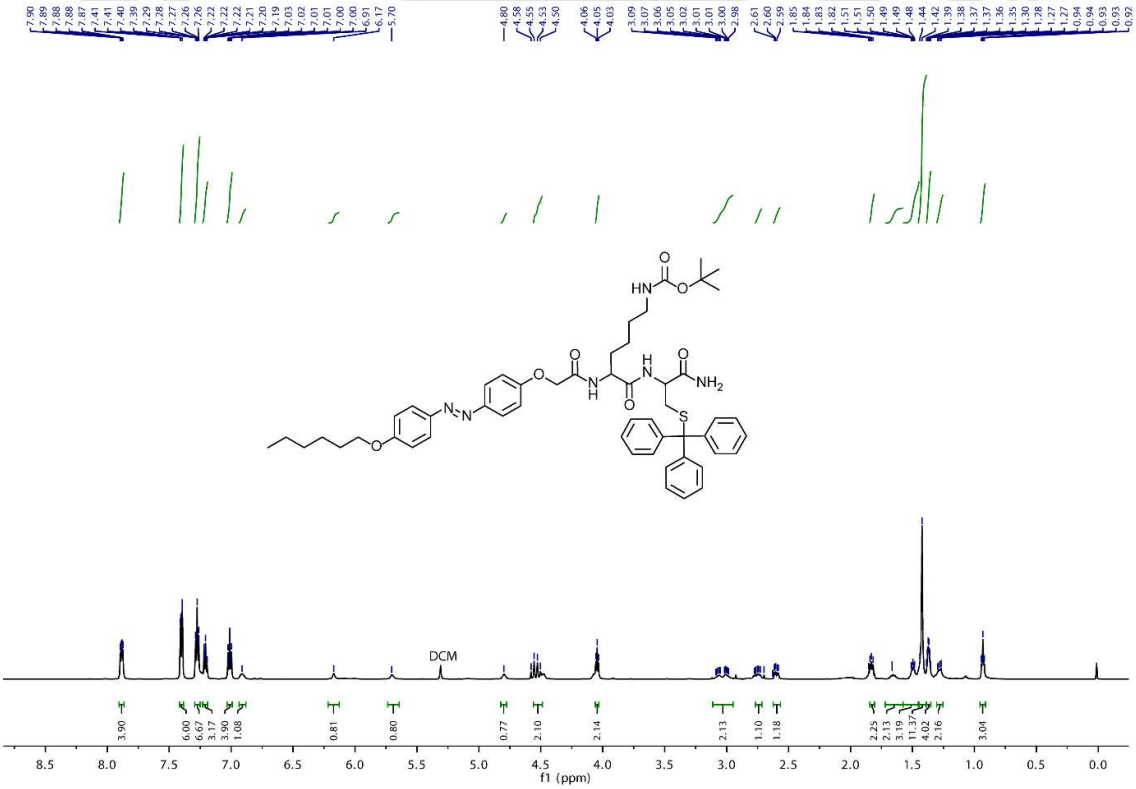

Figure 6.44 ^{1}H NMR spectrum of **Compound 3.6** in $CDCl_3$.

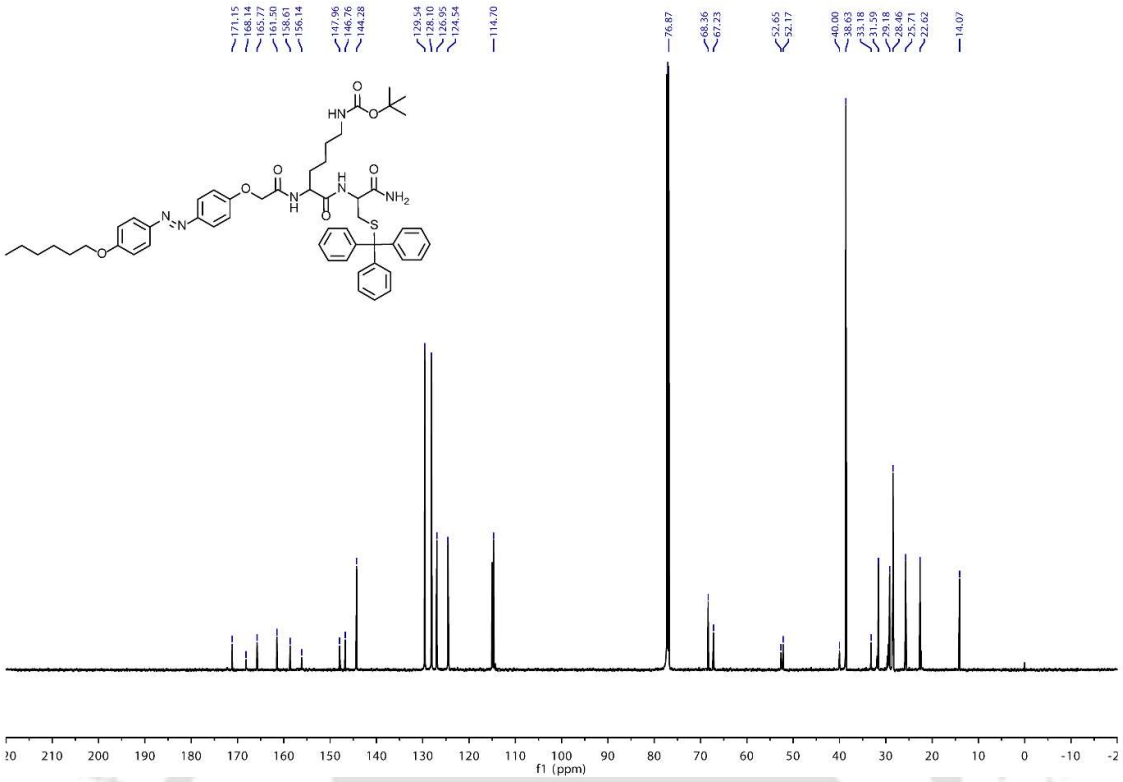

Figure 6.45 ^{13}C NMR spectrum of **Compound 3.6** in $CDCl_3$.

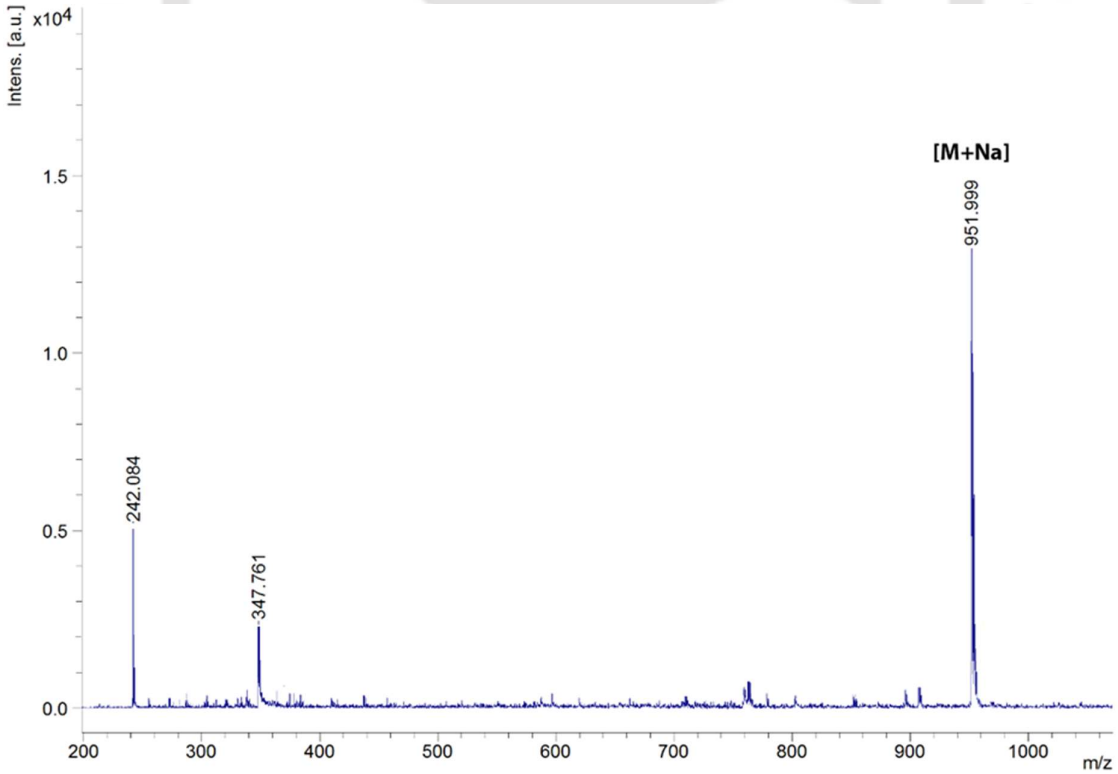

Figure 6.46 MALDI-TOF-MS of **Compound 3.6.**

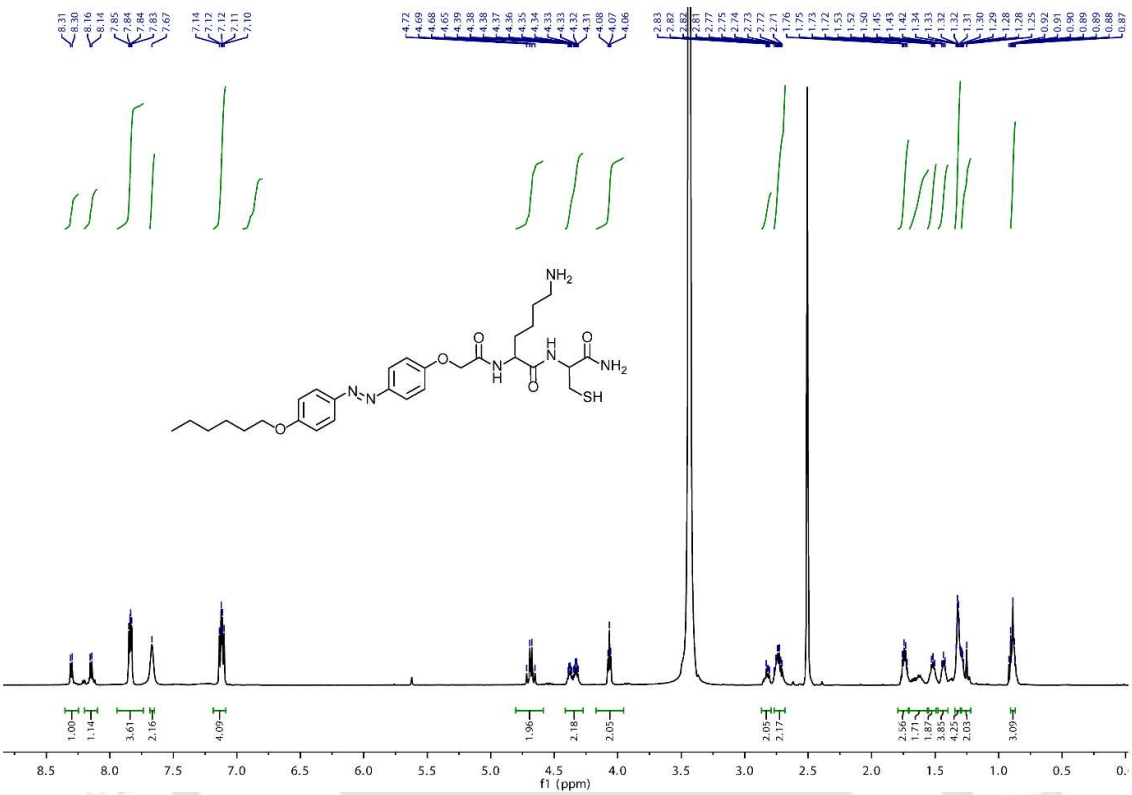

Figure 6.47 ^{1}H NMR spectrum of **AzoKC** in DMSO-d_6.

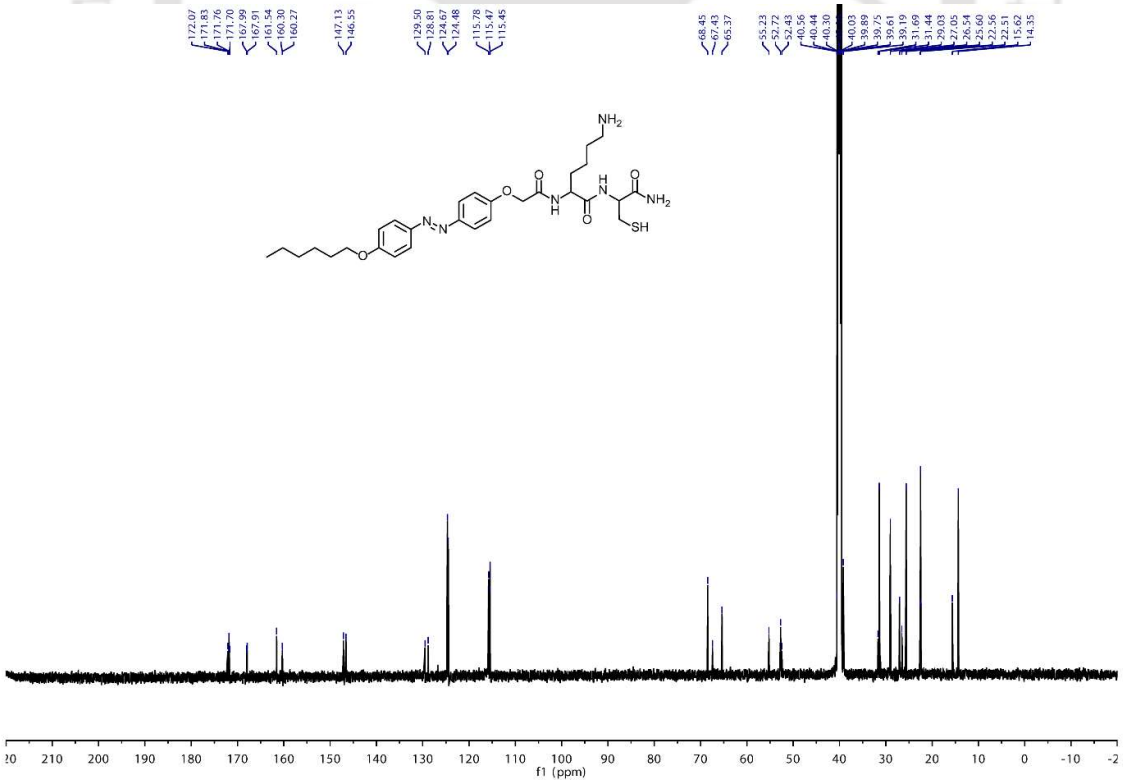

Figure 6.48 ^{13}C NMR spectrum of **AzoKC** in DMSO-d_6.

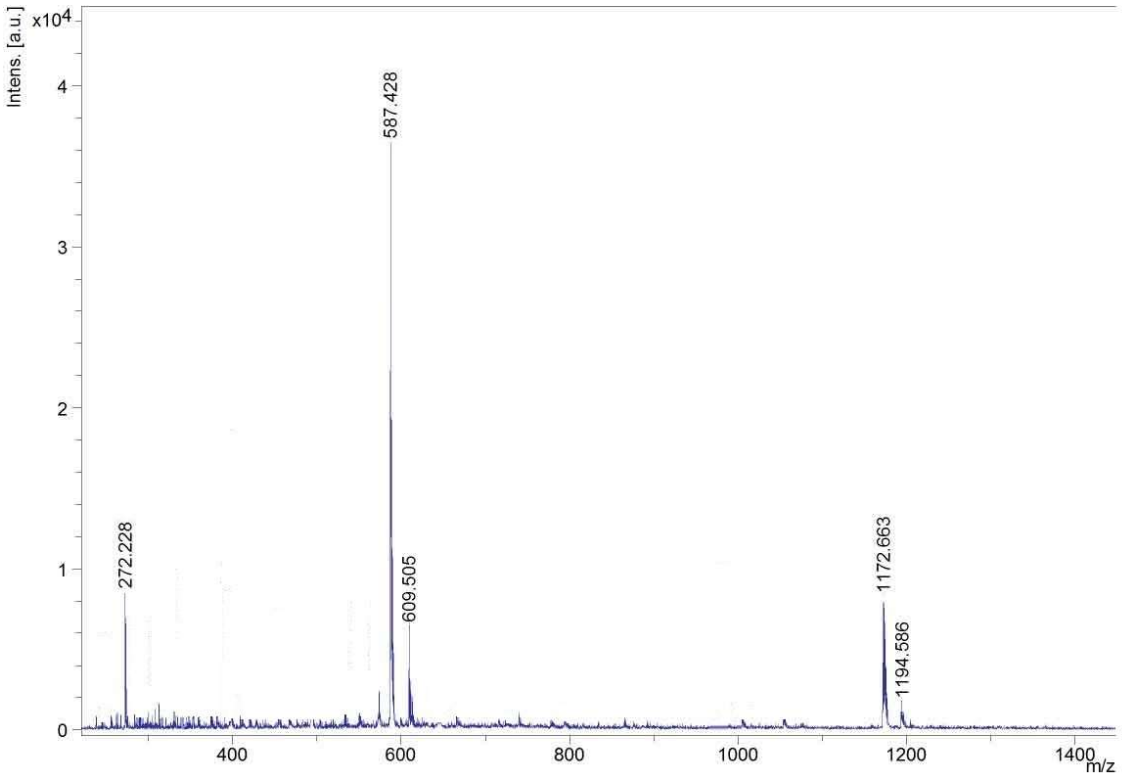

Figure 6.49 MALDI-TOF-MS of **AzoKC.**

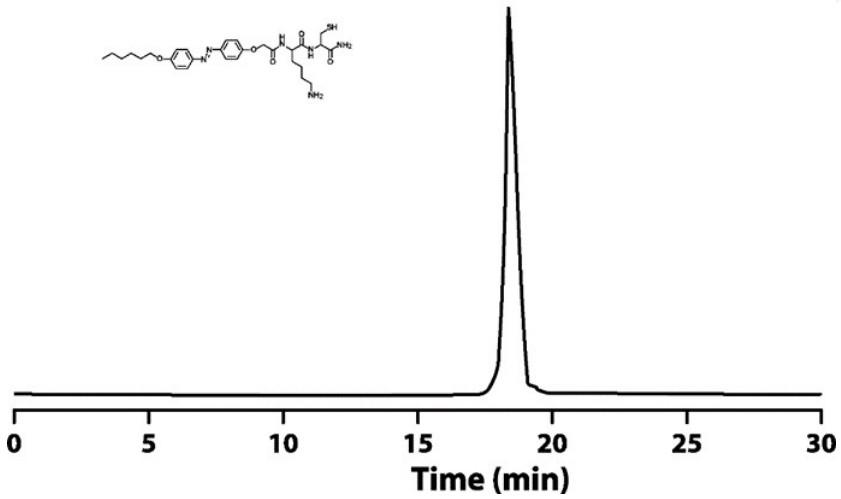

Figure 6.50 Analytical HPLC chromatogram of **AzoKC**.

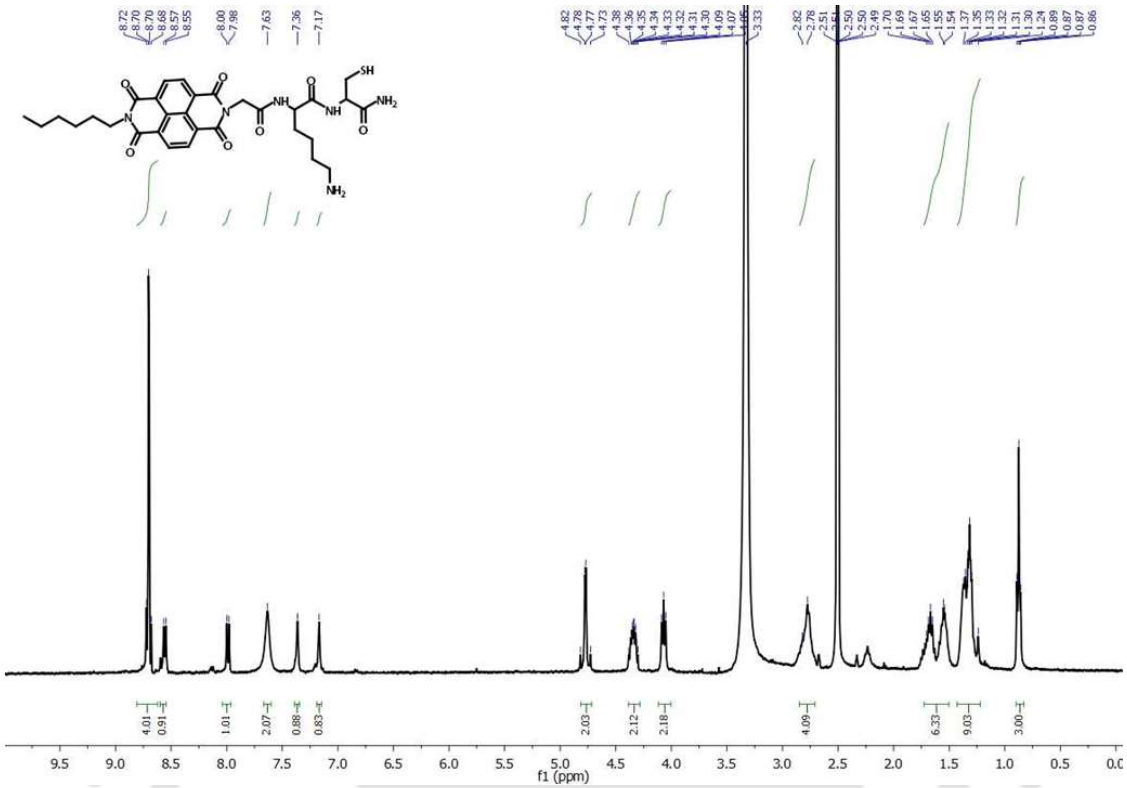

Figure 6.51 ^{1}H NMR spectrum of **NDI-1** in DMSO-d_6.

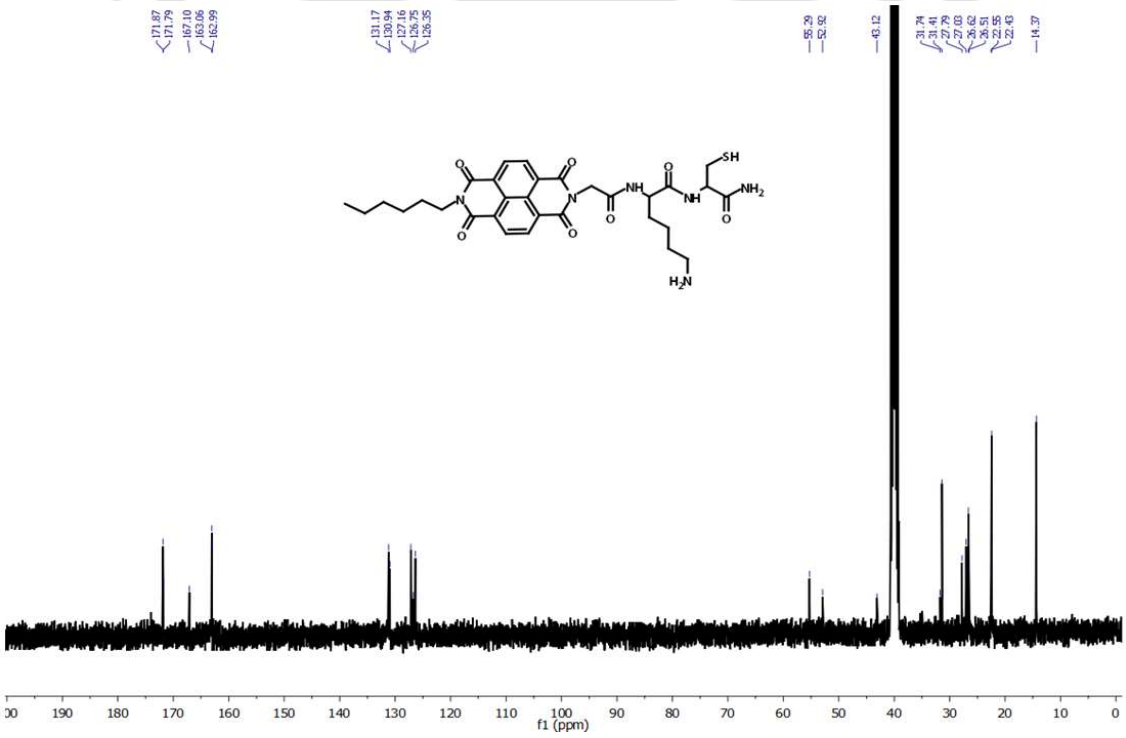

Figure 6.52 ^{13}C NMR spectrum of **NDI-1** in DMSO-d_6.

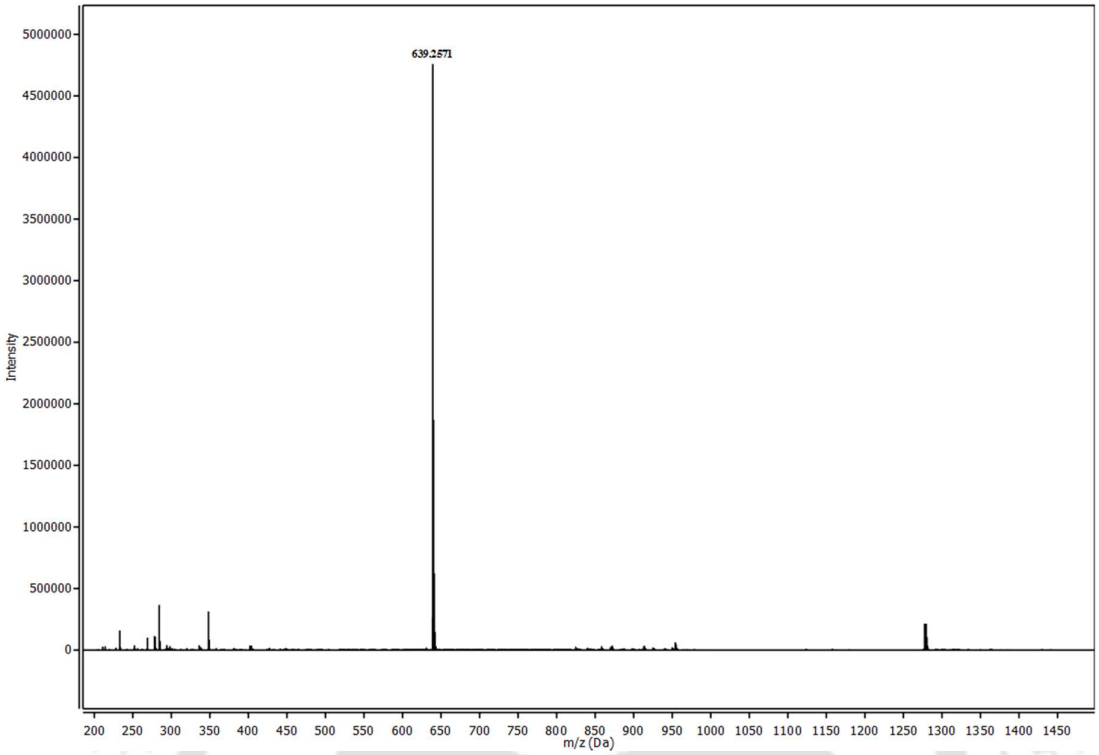

Figure 6.53 ESI-MS of **NDI-1**.

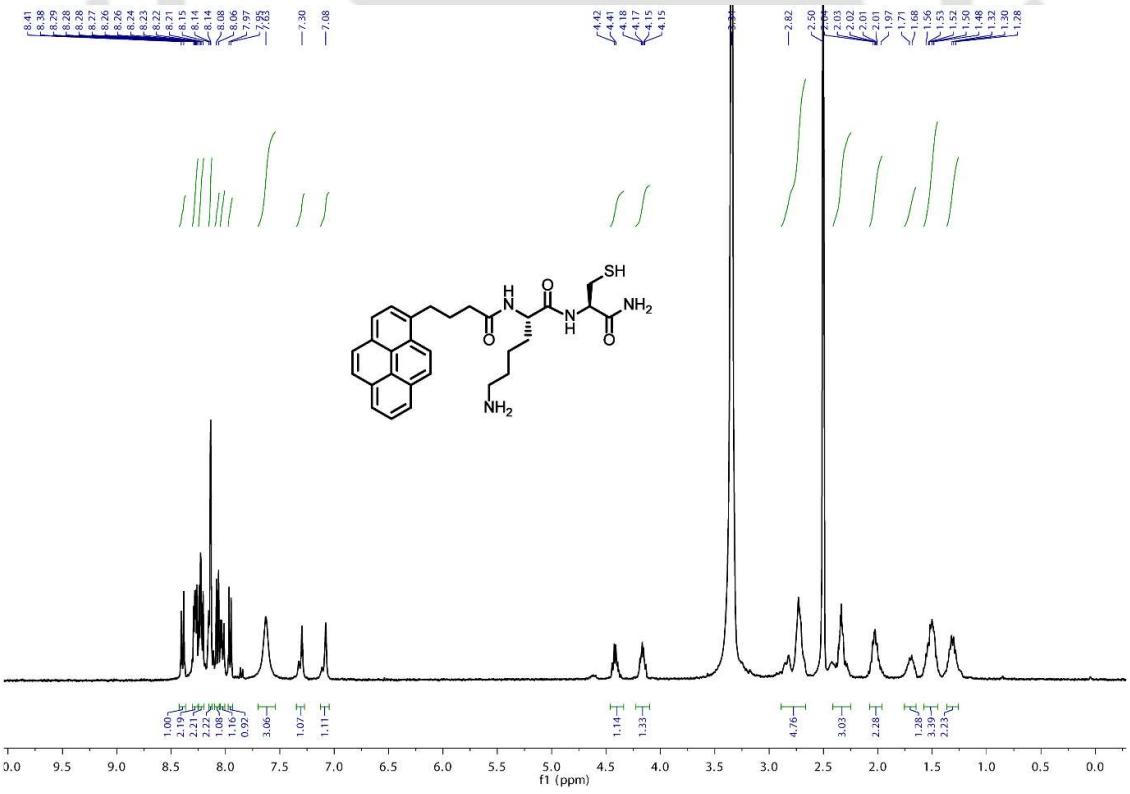

Figure 6.54 ^{1}H NMR spectrum of **PyKC** in DMSO-d_6.

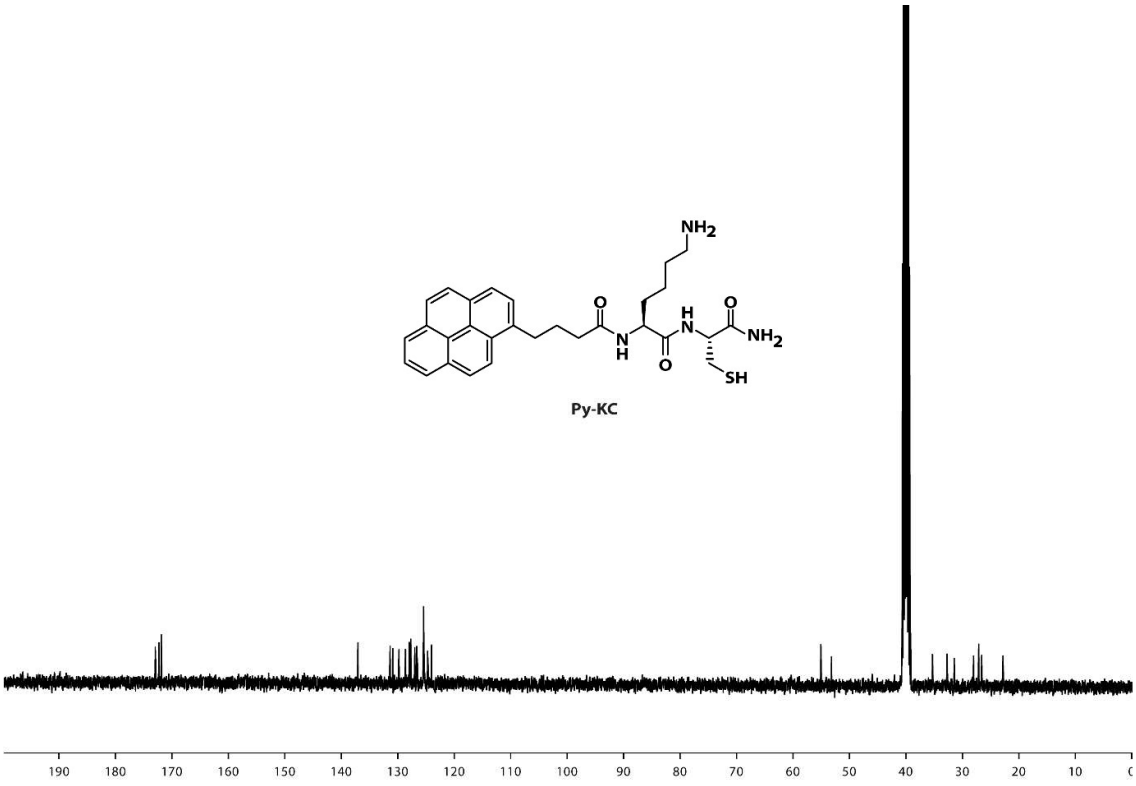

Figure 6.55 ^{13}C NMR spectrum of **PyKC** in DMSO-d_6.

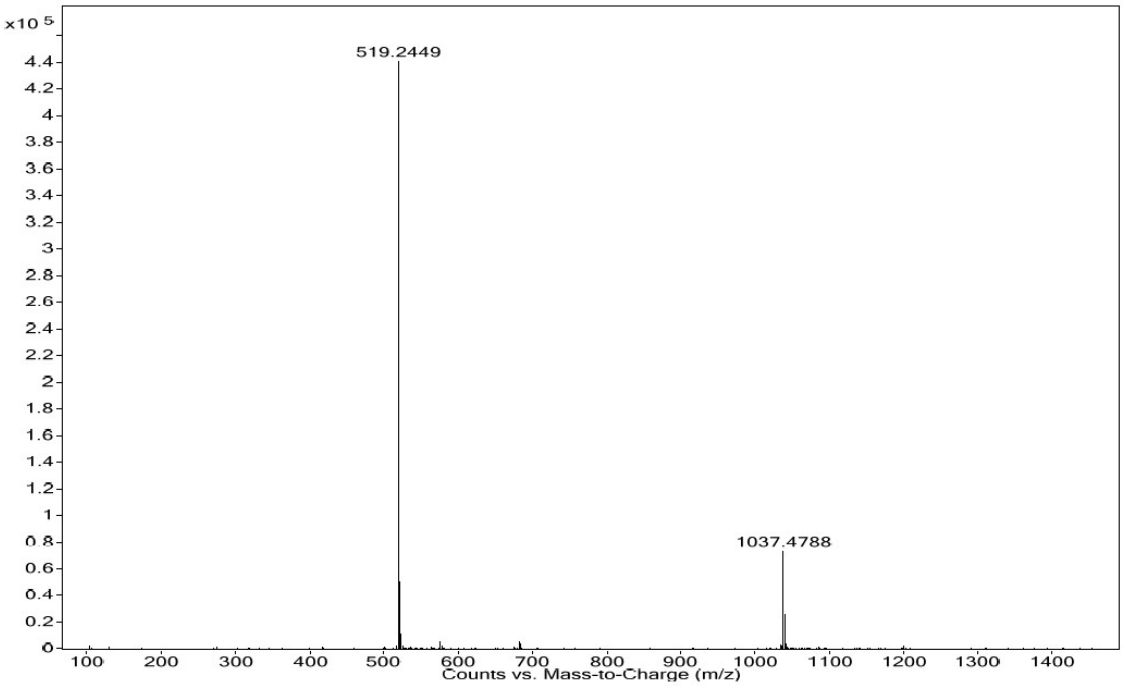

Figure 6.56 ESI-MS of **PyKC**.

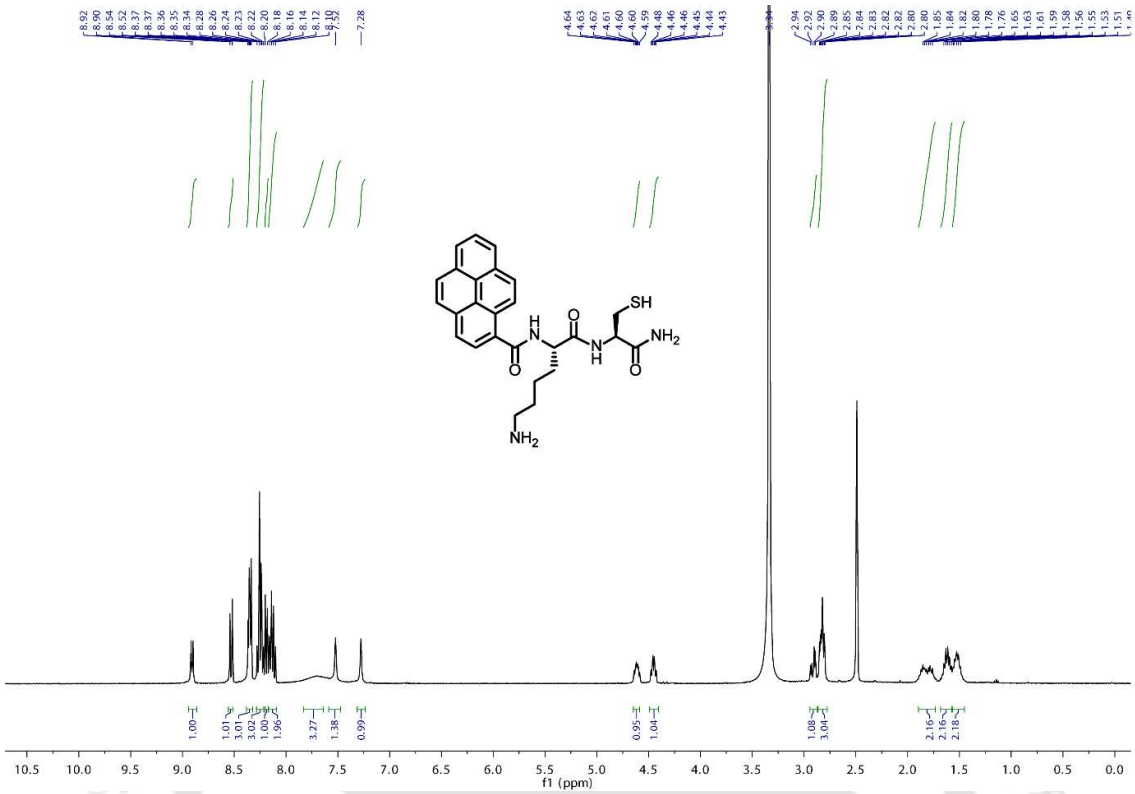

Figure 6.57 ^{1}H NMR spectrum of **Py1KC** in DMSO-d_6.

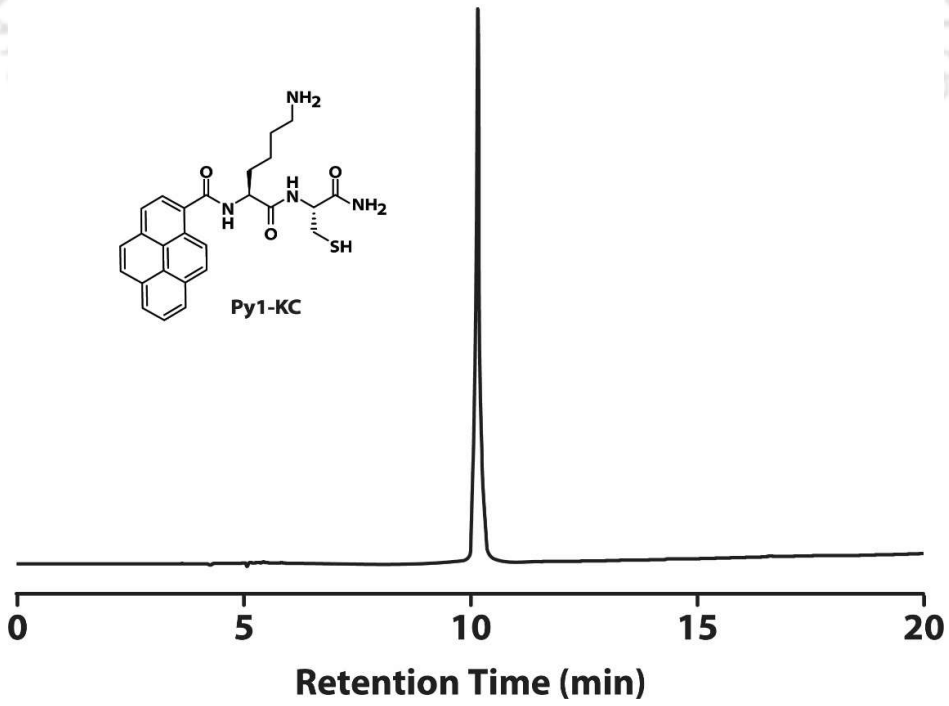

Figure 6.58 Analytical HPLC chromatogram of **Py1KC**.

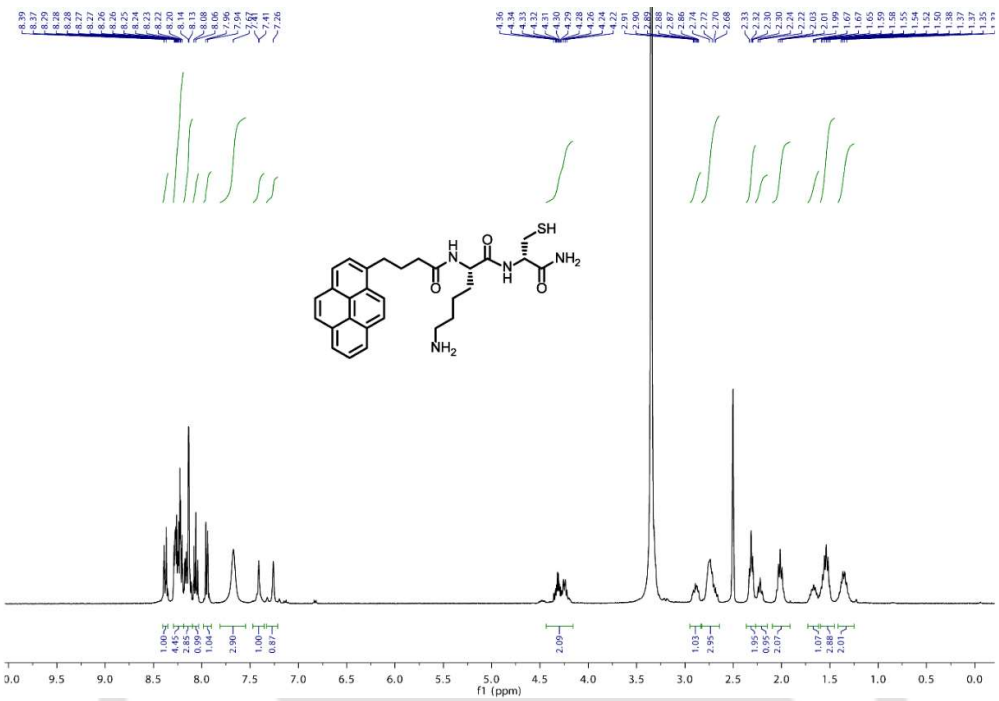

Figure 6.59 ^{1}H NMR spectrum of **Py1KC** in DMSO-d_6.

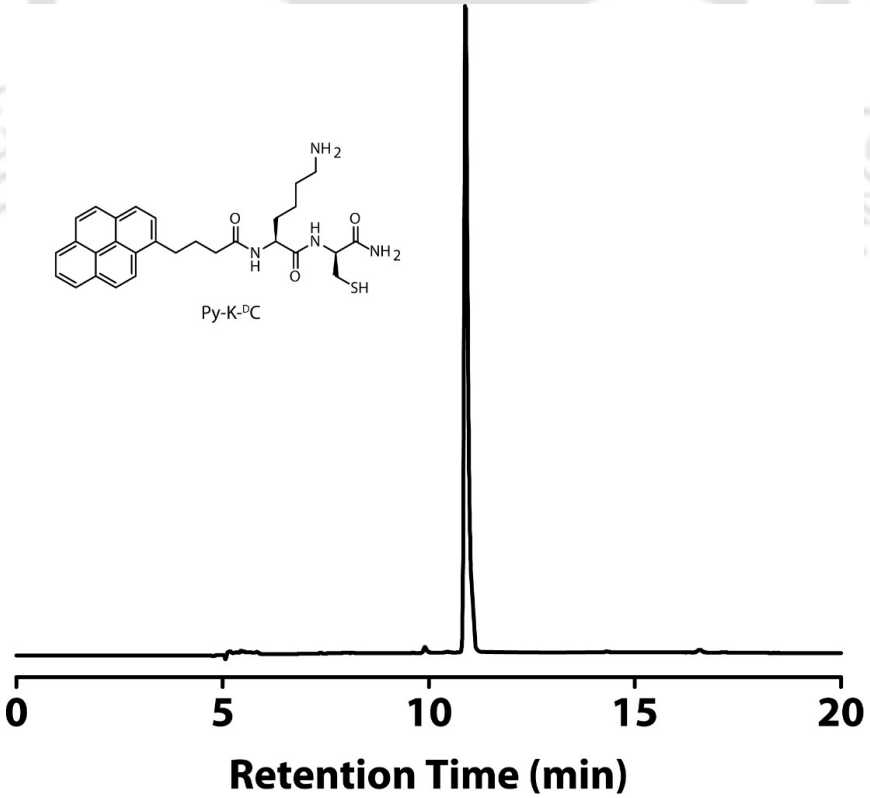

Figure 6.60 Analytical HPLC chromatogram of **PyK^{D}C**.

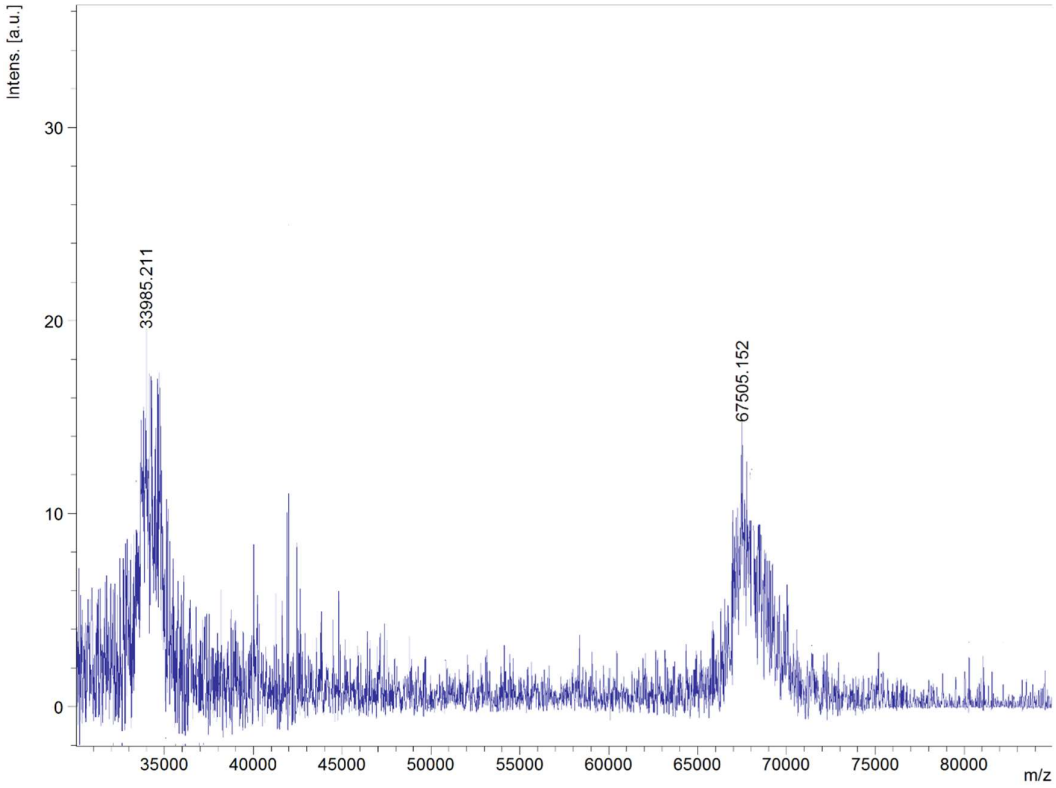

Figure 6.61 MALDI-TOF of **BSA-FITC**.

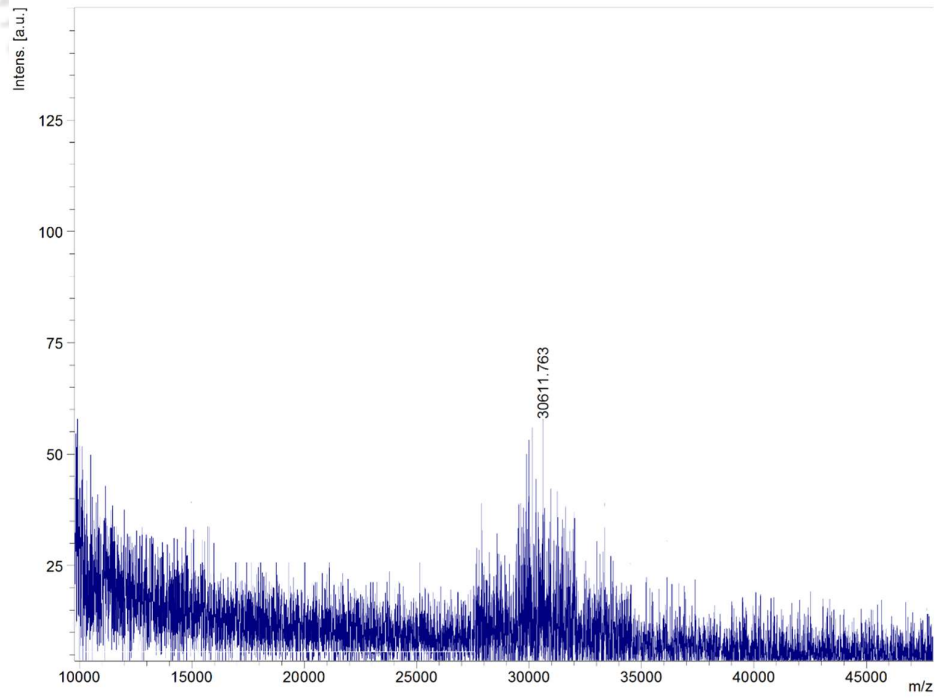

Figure 6.62 MALDI-TOF of **CR Lipase-FITC**.

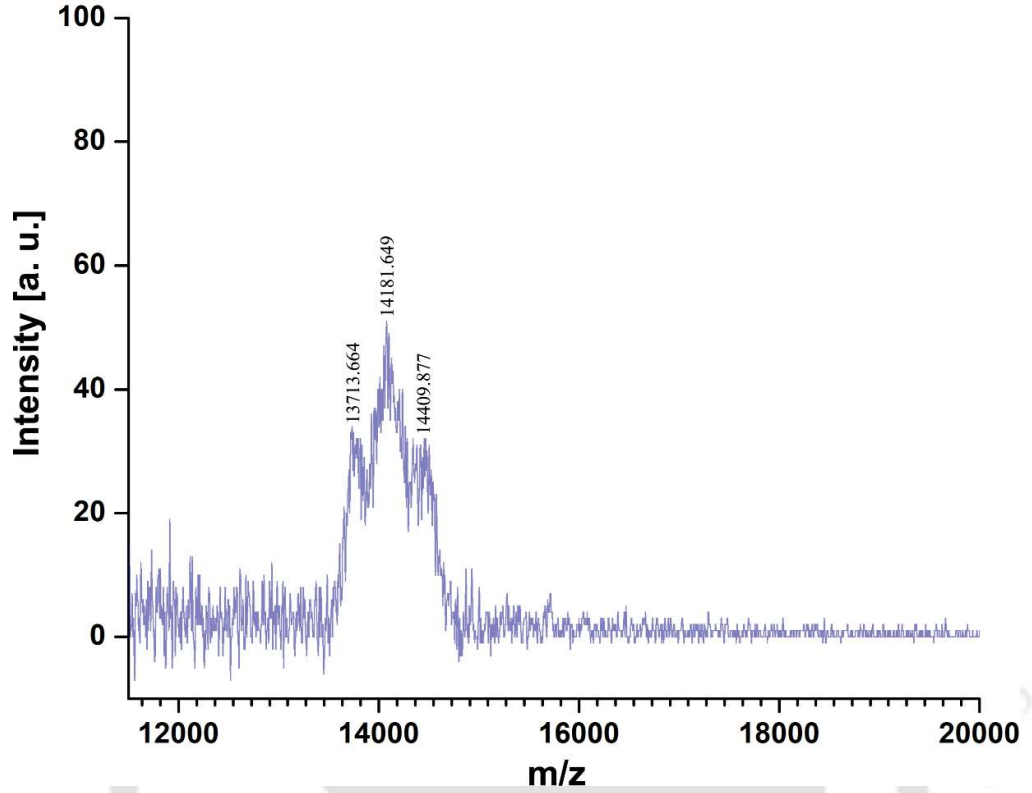

Figure 6.63 MALDI-TOF of **RNase A-FITC**.

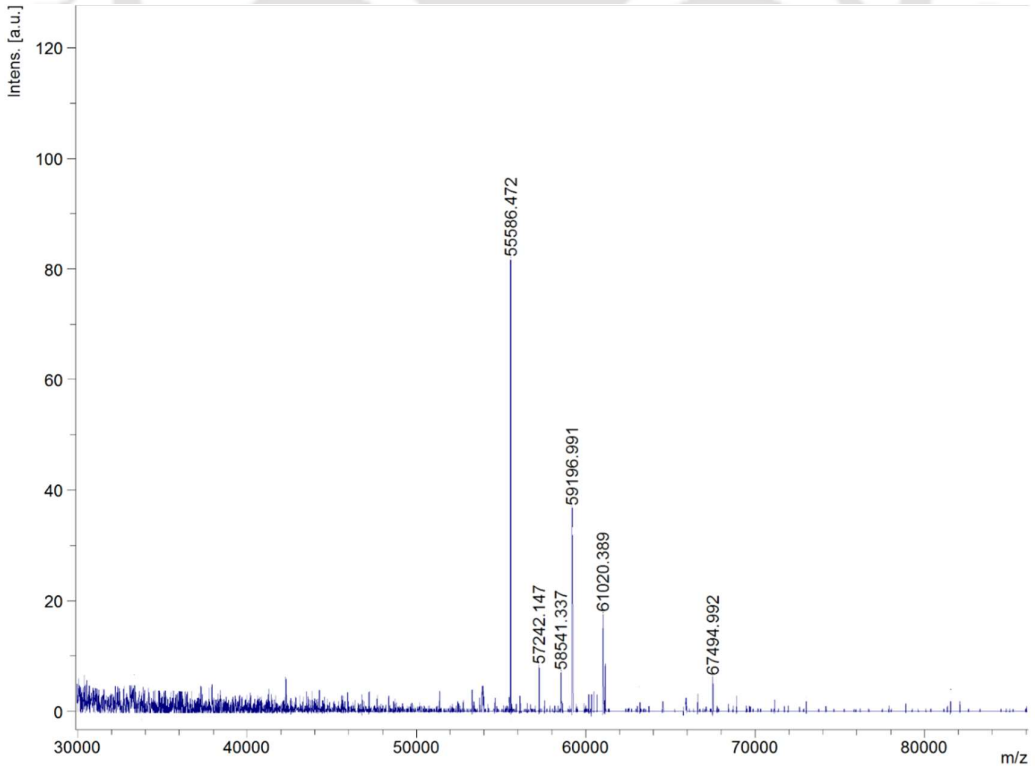

Figure 6.64 MALDI-TOF of **Histone-FITC**.

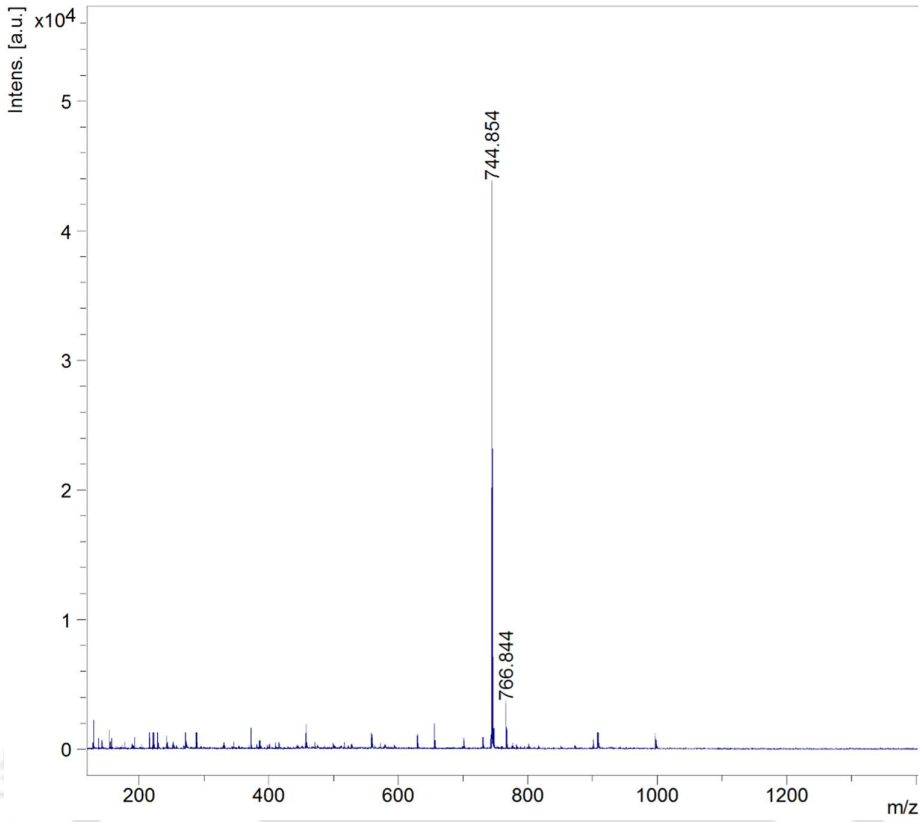

Figure 6.65 MALDI-TOF of **PyKRGD.**

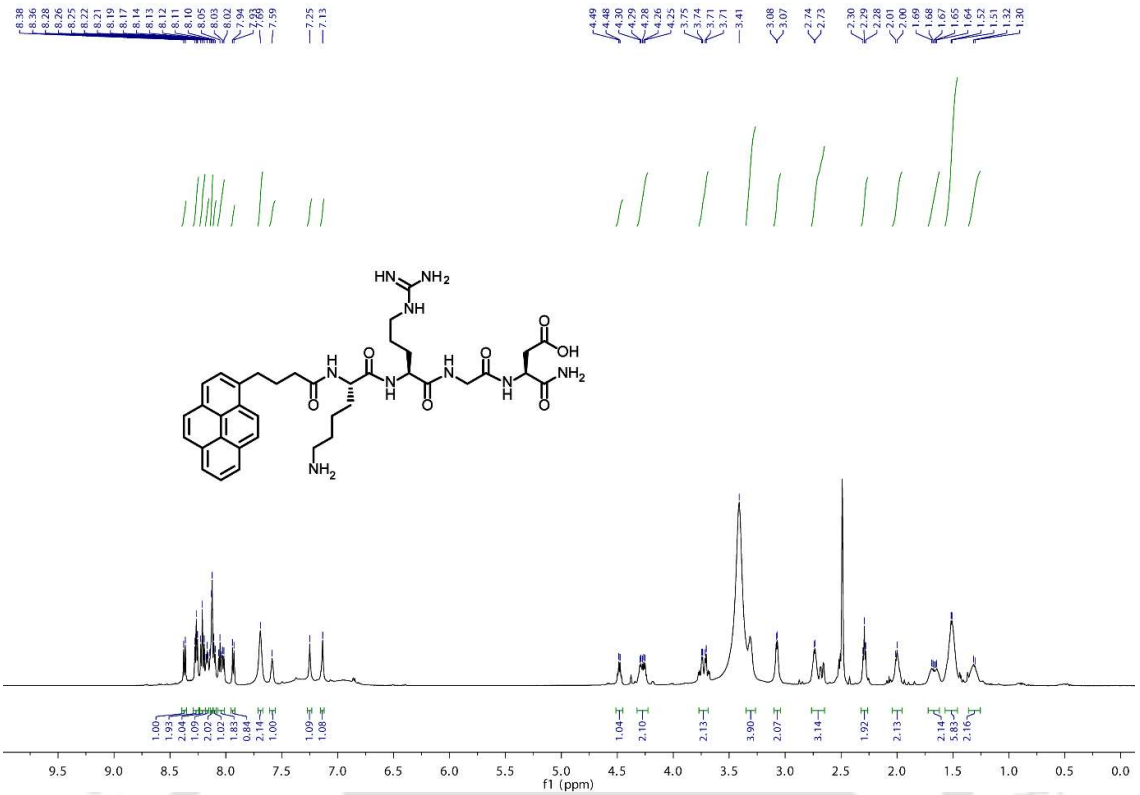

Figure 6.66 ^{1}H NMR spectrum of **PyKRGD** in DMSO-d_6.

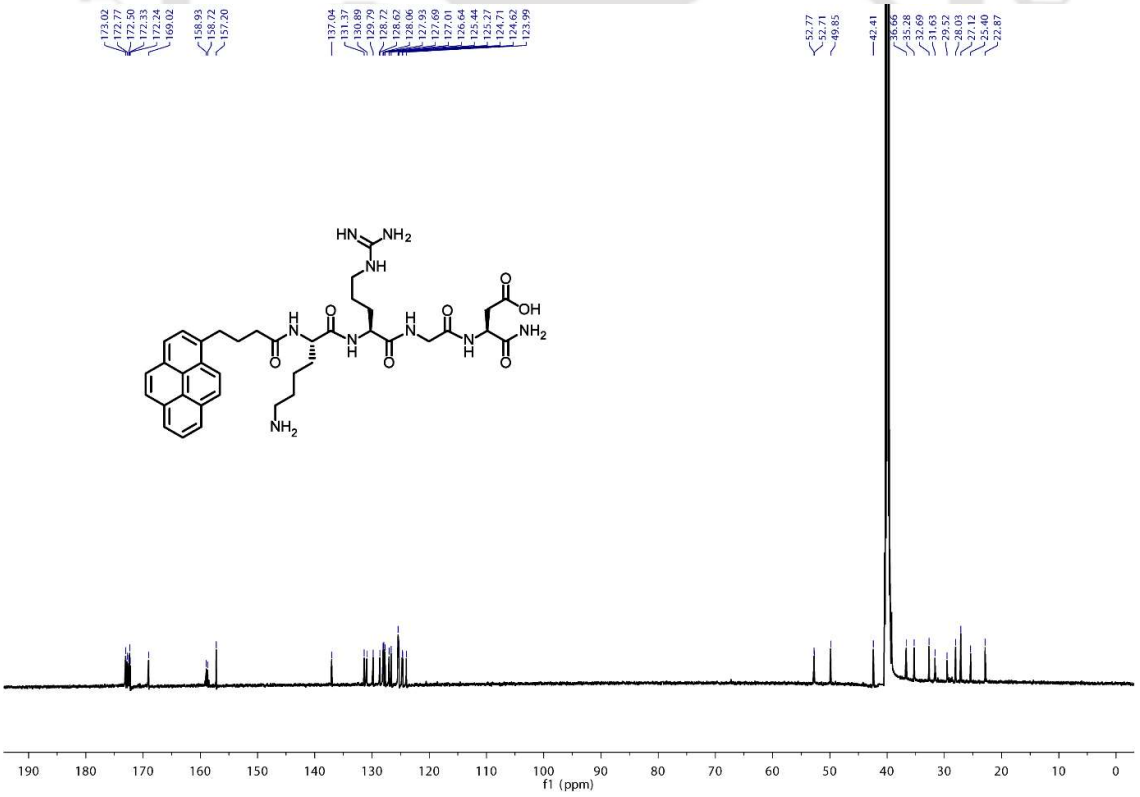

Figure 6.67 ^{13}C NMR spectrum of **PyKRGD** in DMSO-d_6.

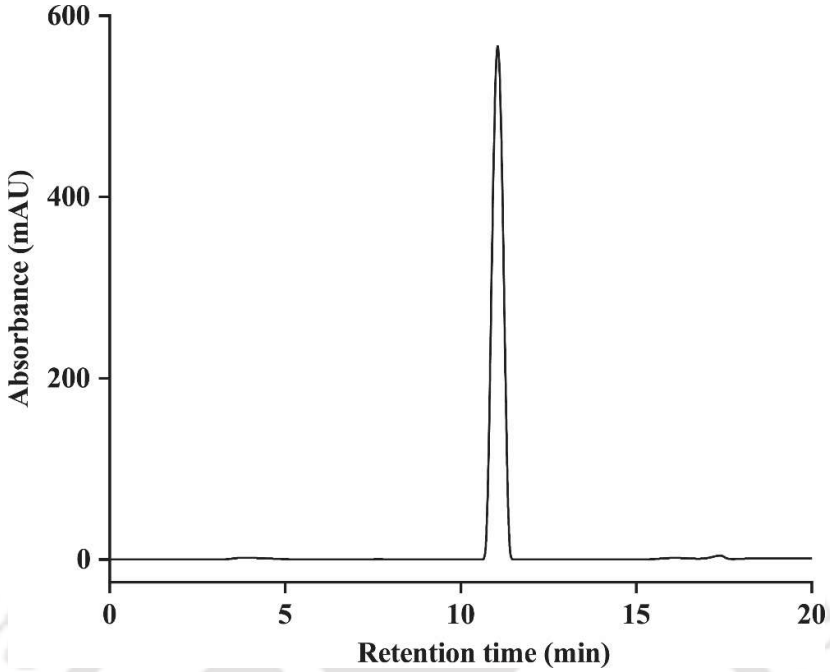

Figure 6.68 Analytical HPLC chromatogram of **PyKRGD**.

References

1. Desiraju, G. R., *Nature* **2001,** *412* (6845), 397-400.
2. Toste, F. D., *Acc. Chem. Res* **2018,** *51*, 2980-2981.
3. Steed, J. W.; Atwood, J. L., *Supramolecular chemistry*. John Wiley & Sons: 2013.
4. Damodaran, S.; Parkin, K. L., Amino acids, peptides, and proteins. In *Fennema's food chemistry*, CRC Press: 2017; pp 235-356.
5. Ding, X.; Zhao, H.; Li, Y.; Lee, A. L.; Li, Z.; Fu, M.; Li, C.; Yang, Y. Y.; Yuan, P., *Adv. Drug Deliv. Rev.* **2020**, *160*, 78-104.
6. Li, J.; Mooney, D. J., *Nat. Rev. Mater.* **2016,** *1*, 1-17.
7. Ardoña, H. A. M.; Tovar, J. D., *Bioconjugate Chem.***2015,** *26*, 2290-2302.
8. Dasgupta, A.; Mondal, J. H.; Das, D., *RSC Adv.* **2013,** *3*, 9117-9149.
9. Mondal, J. H.; Ahmed, S.; Das, D., *Langmuir* **2014,** *30*, 8290-8299.
10. Dasgupta, A.; Das, D., *Langmuir* **2019,** *35*, 10704-10724.
11. Hendricks, M. P.; Sato, K.; Palmer, L. C.; Stupp, S. I., *Acc. Chem. Res.* **2017,** *50*, 2440-2448.
12. Jiao, D.; Geng, J.; Loh, X. J.; Das, D.; Lee, T.-C.; Scherman, O. A., *Angew. Chem. Int. Ed.* **2012,** *51*, 9633-9637.
13. Mondal, J. H.; Ahmed, S.; Ghosh, T.; Das, D., *Soft Matter* **2015,** *11*, 4912-4920.
14. Dowari, P.; Das, S.; Pramanik, B.; Das, D., *Chem. Commun.* **2019,** *55*, 14119-14122.
15. Smith, J. A.; Pease, L. G.; Kopple, K. D., *Crit. Rev. Biochem.* **1980,** *8*, 315-399.
16. Marqusee, S.; Baldwin, R. L., *Proc. Nat. Acad. Sci.* **1987,** *84*, 8898.
17. Liebmann, T.; Rydholm, S.; Akpe, V.; Brismar, H., *BMC Biotechnol.* **2007,** *7*, 1-11.
18. Tang, C.; Ulijn, R. V.; Saiani, A., *Langmuir* **2011,** *27*, 14438-14449.
19. Shi, J.; Gao, Y.; Yang, Z.; Xu, B., *Beilstein J. Org. Chem.* **2011,** *7*, 167-172.
20. Ou, C.; Zhang, J.; Zhang, X.; Yang, Z.; Chen, M., *Chem. Commun.* **2013,** *49*, 1853-1855.
21. Huang, Y.; Qiu, Z.; Xu, Y.; Shi, J.; Lin, H.; Zhang, Y., *Org. Biomol. Chem.* **2011,** *9*, 2149-2155.
22. Zhang, Y.; Yang, Z.; Yuan, F.; Gu, H.; Gao, P.; Xu, B., *J. Am. Chem. Soc.* **2004,** *126* , 15028-15029.
23. Eakins, G. L.; Gallaher, J. K.; Keyzers, R. A.; Falber, A.; Webb, J. E. A.; Laos, A.; Tidhar, Y.; Weissman, H.; Rybtchinski, B.; Thordarson, P., *J. Phys. Chem. B* **2014,** *118*, 8642-8651.
24. Jalani, K.; Kumar, M.; George, S. J., *Chem. Commun.* **2013,** *49*, 5174-5176.
25. Jain, A.; Dhiman, S.; Dhayani, A.; Vemula, P. K.; George, *Nat. Commun.* **2019,** *10*, 450.
26. Wang, C.; Guo, Y.; Wang, Z.; Zhang, X., *Langmuir* **2010,** *26*, 14509-14511.
27. Shin, Y.-g. K.; Newton, M. D.; Isied, S. S., *J. Am. Chem. Soc.* **2003,** *125*, 3722-3732.
28. Yu, J.; Horsley, J. R.; Abell, A. D., *RSC Adv.* **2017,** *7*, 42370-42378.
29. Bartocci, S.; Berrocal, J. A.; Guarracino, P.; Grillaud, M.; Franco, L.; Mba, M., *Chem. Eur. J.* **2018,** *24*, 2920-2928.
30. Dougherty, D. A., The cation– π interaction. *Acc. Chem. Res.* **2013,** *46* (4), 885-893.
31. Kumar, K.; Woo, S. M.; Siu, T.; Cortopassi, W. A.; Duarte, F.; Paton, R. S., *Chem. Sci.* **2018,** *9* (10), 2655-2665.
32. Li, J.; Mooney, D. J., *Nat. Rev. Mater.* **2016,** *1*, 1-17.
33. Ma, J. C.; Dougherty, D. A., *Chem. Rev.* **1997,** *97*, 1303-1324.
34. Mahadevi, A. S.; Sastry, G. N., *Chem. Rev.* **2013,** *113*, 2100-2138.
35. Pless, S. A.; Galpin, J. D.; Frankel, A.; Ahern, C. A., *Nat. Commun.* **2011,** *2*, 1-9.
36. Torrice, M. M.; Bower, K. S.; Lester, H. A.; Dougherty, D. A., *Proc. Nat. Acad. Sci.* **2009,** *106*, 11919-11924.
37. Xiu, X.; Puskar, N. L.; Shanata, J. A. P., *Nature* **2009,** *458*, 534-537.
38. Petersen, F. N.; Jensen, M.; Nielsen, C. H., *Biophys. J.* **2005,** *89*, 3985-96.
39. Sunner, J.; Nishizawa, K.; Kebarle, P., *J. Phys. Chem. A* **1981,** *85* , 1814-1820.
40. Meot-Ner, M.; Deakyne, C. A., *J. Am. Chem. Soc.* **1985,** *107*, 474-479.
41. Dougherty, D. A., *Science* **1996,** *271*, 163-168.
42. Gebbie, M. A.; Wei, W.; Schrader, A. M., *Nat. Chem.* **2017,** *9*, 473-479.
43. Yamada, S.; Yamamoto, N.; Takamori, E., *J. Org. Chem.* **2016,** *81*, 11819-11830.
44. Smith, M. S.; Lawrence, E. E. K.; Billings, W. M.; Larsen, K. S.; Bécar, N. A., *ACS Chem. Biol.* **2017,** *12*, 2535-2537.
45. Woolfson, D. N.; Ryadnov, M. G., *Curr. Opin. Chem. Biol.* **2006,** *10*, 559-567.
46. Aggeli, A.; Bell, M.; Boden, N.; N. Keen, J.; C. B. McLeish, T.; Nyrkova, I.; Radford, S. E.; Semenov, A., *J. Mater. Chem.* **1997,** *7*, 1135-1145.
47. Aggeli, A.; Bell, M.; Boden, N.; Carrick, L. M.; Strong, A. E., *Angew. Chem. Int. Ed.* **2003,** *42*, 5603-5606.
48. Aggeli, A.; Nyrkova, I. A.; Bell, M.; Harding, R.; Carrick, L.; McLeish, T. C. B.; Semenov, A. N.; Boden, N., *Proc. Natl. Acad. Sci.* **2001,** *98*, 11857-11862.
49. Rapaport, H.; Grisaru, H.; Silberstein, T., *Adv. Funct. Mater.* **2008,** *18*, 2889-2896.

50. Yokoi, H.; Kinoshita, T.; Zhang, S., *Proc. Natl. Acad. Sci.* **2005,** *102*, 8414-8419.
51. Kisiday, J.; Jin, M.; Kurz, B.; Hung, H.; Semino, C.; Zhang, S.; Grodzinsky, A. J., *Proc. Natl. Acad. Sci.* **2002,** *99*, 9996-10001.
52. Clarke, D. E.; Parmenter, C. D. J.; Scherman, O. A., *Angew. Chem. Int. Ed.* **2018,** *57*, 7709-7713.
53. Schneider, J. P.; Pochan, D. J.; Ozbas, B.; Rajagopal, K.; Pakstis, L.; Kretsinger, J., *J. Am. Chem. Soc.* **2002,** *124*, 15030-15037.
54. Geisler, I. M.; Schneider, J. P., *Adv. Funct. Mater.* **2012,** *22*, 529-537.
55. Ozbas, B.; Kretsinger, J.; Rajagopal, K.; Schneider, J. P.; Pochan, D. J., *Macromolecules* **2004,** *37*, 7331-7337.
56. Pochan, D. J.; Schneider, J. P.; Kretsinger, J.; Ozbas, B.; Rajagopal, K.; Haines, L., *J. Am. Chem. Soc.* **2003,** *125*, 11802-11803.
57. Haines, L. A.; Rajagopal, K.; Ozbas, B.; Salick, D. A.; Pochan, D. J.; Schneider, J. P., *J. Am. Chem. Soc.* **2005,** *127*, 17025-17029.
58. Vázquez-González, M.; Willner, I., *Angew. Chem. Int. Ed.* **2020,** *59*, 15342-15377.
59. Willner, I., Stimuli-controlled hydrogels and their applications. *Acc. Chem. Res* **2017,** *50*, 657-658.
60. Yoshida, R.; Okano, T., Springer: 2010; pp 19-43.
61. Shah, A.; Malik, M. S.; Khan, G. S.; Nosheen, E.; Iftikhar, F. J.; Khan, F. A.; Shukla, S. S.; Akhter, M. S.; Kraatz, H. B.; Aminabhavi, T. M., Stimuli-responsive peptide-based biomaterials as drug delivery systems. *Chemical Engineering Journal* **2018,** *353*, 559-583.
62. Hoque, J.; Sangaj, N.; Varghese, S., Stimuli-Responsive Supramolecular Hydrogels and Their Applications in Regenerative Medicine. *Macromolecular Bioscience* **2019,** *19*, 1800259.
63. Schneider, J. P.; Pochan, D. J.; Ozbas, B.; Rajagopal, K.; Pakstis, L.; Kretsinger, J., *J. Am. Chem. Soc* **2002,** *124*, 15030-15037.
64. Zhang, C.; Shafi, R.; Lampel, A.; MacPherson, D.; Pappas, C. G.; Narang, V.; Wang, T.; Maldarelli, C.; Ulijn, R. V., *Angew. Chem. Int. Ed.* **2017,** *129*, 14703-14707.
65. Jayawarna, V.; Ali, M.; Jowitt, T. A.; Miller, A. F.; Saiani, A.; Gough, J. E.; Ulijn, R. V., *Adv. Mater.* **2006,** *18*, 611-614.
66. Tang, C.; Smith, A. M.; Collins, R. F.; Ulijn, R. V.; Saiani, A., *Langmuir* **2009,** *25*, 9447-9453.
67. Zhao, Y.; Yokoi, H.; Tanaka, M.; Kinoshita, T.; Tan, T., *Biomacromolecules* **2008,** *9*, 1511-1518.
68. Wang, J.; Chen, X.-Y.; Zhao, Y.; Yang, Y.; Wang, W.; Wu, C.; Yang, B.; Zhang, Z.; Zhang, L.; Liu, Y., *ACS nano* **2019,** *13*, 11686-11697.
69. Liu, Y.; Yang, Y.; Wang, C.; Zhao, X., *Nanoscale* **2013,** *5*, 6413-6421.
70. Ghosh, G.; Barman, R.; Sarkar, J.; Ghosh, S., *J. Phy. Chem. B* **2019,** *123*, 5909-5915.
71. Meng, D.; Zhang, P.; Zhang, L.; Wang, H.; Ho, C.-T.; Li, S.; Shahidi, F.; Zhao, H., *J. Funct. Foods.* **2017,** *37*, 467-479.
72. Di Meo, S.; Reed, T. T.; Venditti, P.; Victor, V. M., *Oxid. Med. Cell. Longev.* **2016,** *2016,* 1245049.
73. Sun, Z.; Li, Z.; He, Y.; Shen, R.; Deng, L.; Yang, M.; Liang, Y.; Zhang, Y., *J. Am. Chem. Soc* **2013,** *135*, 13379-13386.
74. Sun, Z.; Deng, L.; Gan, H.; Shen, R.; Yang, M.; Zhang, Y., *Biosens. Bioelectron.* **2013,** *39*, 215-219.
75. Wojciechowski, J. P.; Martin, A. D.; Thordarson, P., *J. Am. Chem. Soc* **2018,** *140*, 2869-2874.
76. Arrick, B. A.; Nathan, C. F., *Cancer Res.* **1984,** *44* (10), 4224-4232.
77. Singha, N.; Srivastava, A.; Pramanik, B.; Ahmed, S.; Dowari, P.; Chowdhuri, S.; Das, B. K.; Debnath, A.; Das, D., *Chem. Sci.* **2019,** *10* (23), 5920-5928.
78. Shi, Y.; Wang, J.; Wang, H.; Hu, Y.; Chen, X.; Yang, Z., *PLoS One* **2014,** *9*, e106968.
79. Zhu, Y.; Wang, L.; Li, Y.; Huang, Z.; Luo, S.; He, Y.; Han, H.; Raza, F.; Wu, J.; Ge, L., *Biomater. Sci.* **2020,** *8*, 5415-5426.
80. Zheng, D.; Gao, Z.; Xu, T.; Liang, C.; Shi, Y.; Wang, L.; Yang, Z., *Nanoscale* **2018,** *10*, 21459-21465.
81. Peddie, V.; Abell, A. D., *J. Photochem. Photobiol. C* **2019,** *40*, 1-20.
82. Beharry, A. A.; Woolley, G. A., *Chem. Soc. Rev.* **2011,** *40*, 4422-4437.
83. Renner, C.; Moroder, L., *ChemBioChem* **2006,** *7*, 868-878.
84. Wang, G.; Zhang, J., *J. Photochem. Photobiol. C* **2012,** *13*, 299-309.
85. Sisido, M.; Ishikawa, Y.; Itoh, K.; Tazuke, S., *Macromolecules* **1991,** *24*, 3993-3998.
86. Huang, Y.; Qiu, Z.; Xu, Y.; Shi, J.; Lin, H.; Zhang, Y., *Org. Biomol. Chem.* **2011,** *9*, 2149-2155.
87. Boonyarattanakalin, S.; Hu, J.; Dykstra-Rummel, S. A.; August, A.; Peterson, B. R., *J. Am. Chem. Soc* **2007,** *129*, 268-269.
88. Li, X.; Gao, Y.; Kuang, Y.; Xu, B., *Chem. Commun.* **2010,** *46*, 5364-5366.
89. Doran, T. M.; Ryan, D. M.; Nilsson, B. L., *Polym. Chem.* **2014,** *5*, 241-248.

90. Zhang, X.; Dong, C.; Huang, W.; Wang, H.; Wang, L.; Ding, D.; Zhou, H.; Long, J.; Wang, T.; Yang, Z., *Nanoscale* **2015,** *7*, 16666-16670.
91. Yamamoto, H.; Kitsuki, T.; Nishida, A.; Asada, K.; Ohkawa, K., *Macromolecules* **1999,** *32*, 1055-1061.
92. Chivers, P. R. A.; Dookie, R. S.; Gough, J. E.; Webb, S. J., *Chem. Commun.* **2020,** *56*, 13792-13795.
93. Chen, C.; Zhang, Y.; Hou, Z.; Cui, X.; Zhao, Y.; Xu, H., *Biomacromolecules* **2017,** *18*, 3563-3571.
94. Gao, J.; Zheng, W.; Kong, D.; Yang, Z., *Soft Matter* **2011,** *7*, 10443-10448.
95. Li, X.; Li, J.; Gao, Y.; Kuang, Y.; Shi, J.; Xu, B., *J. Am. Chem. Soc* **2010,** *132*, 17707-17709.
96. Li, X.; Fu, M.; Wu, J.; Zhang, C.; Deng, X.; Dhinakar, A.; Huang, W.; Qian, H.; Ge, L., *Acta Biomater.* **2017,** *51*, 294-303.
97. Zhang, Y.; Gu, H.; Yang, Z.; Xu, B., *J. Am. Chem. Soc* **2003,** *125*, 13680-13681.
98. Pan, S.; Luo, S.; Li, S.; Lai, Y.; Geng, Y.; He, B.; Gu, Z., *Chem. Commun.* **2013,** *49* (73), 8045-8047.
99. Deming, T. J., *Soft Matter* **2005,** *1*, 28-35.
100. Nowak, A. P.; Breedveld, V.; Pine, D. J.; Deming, T. J., *J. Am. Chem. Soc* **2003,** *125*, 15666-15670.
101. Chakraborty, P.; Tang, Y.; Yamamoto, T.; Yao, Y.; Guterman, T.; Zilberzwige-Tal, S.; Adadi, N.; Ji, W.; Dvir, T.; Ramamoorthy, A.; Wei, G.; Gazit, E., *Adv. Mater.* **2020,** *32*, 1906043.
102. Hiew, S. H.; Mohanram, H.; Ning, L.; Guo, J.; Sánchez-Ferrer, A.; Shi, X.; Pervushin, K.; Mu, Y.; Mezzenga, R.; Miserez, A., *Adv. Sci.* **2019,** *6*, 1901173.
103. Duan, P.; Qin, L.; Zhu, X.; Liu, M., *Chem. Eur. J.* **2011,** *17*, 6389-6395.
104. Qin, L.; Duan, P.; Xie, F.; Zhang, L.; Liu, M., *Chem. Commun.* **2013,** *49*, 10823-10825.
105. Xie, F.; Qin, L.; Liu, M., *Chem. Commun.* **2016,** *52*, 930-933.
106. Bal, S.; Das, K.; Ahmed, S.; Das, D., *Angew. Chem. Int. Ed.* **2019,** *131*, 250-253.
107. Horch, R. E., Future perspectives in tissue engineering:'Tissue Engineering'review series. *J. Cell. Mol. Med.* **2006,** *10*, 4-6.
108. Dhandayuthapani, B.; Yoshida, Y.; Maekawa, T.; Kumar, D. S., Polymeric scaffolds in tissue engineering application: a review. *Int. J. Polym. Sci.* **2011,** *2011,* 290602.
109. Langer, R.; Vacanti, J. P., *Science* **1993,** *260*, 920.
110. Atala, A., *Br. Med. Bull.* **2011,** *97*, 81-104.
111. Atala, A., *J. Endourol.* **2000,** *14*, 49-57.
112. Ott, H. C.; Matthiesen, T. S.; Goh, S.-K.; Black, L. D.; Kren, S. M.; Netoff, T. I., *Nat. Med.* **2008,** *14*, 213-221.
113. Whitney, G. A.; Mera, H.; Weidenbecher, M.; Awadallah, A.; Mansour, J. M.; Dennis, J. E., *BioResearch Open Access* **2012,** *1*, 157-165.
114. Wang, Y.; Uemura, T.; Dong, J.; Kojima, H.; Tanaka, J.; Tateishi, T., *Tissue Eng.* **2003,** *9*, 1205-1214.
115. Petite, H.; Viateau, V.; Bensaid, W.; Meunier, A.; de Pollak, C.; Bourguignon, M.; Oudina, K.; Sedel, L.; Guillemin, G., *Nat. Biotechnol.* **2000,** *18*, 959-963.
116. Kim, M. J.; Kim, J.-H.; Yi, G.; Lim, S.-H.; Hong, Y. S.; Chung, D. J., *Macromol. Res.* **2008,** *16*, 345-352.
117. Langelaan, M. L. P.; Boonen, K. J. M.; Polak, R. B.; Baaijens, F. P. T.; Post, M. J.; van der Schaft, D. W. J., *Trends food Sci. Technol.* **2010,** *21*, 59-66.
118. Honda, M. J.; Imaizumi, M.; Tsuchiya, S.; *J. Oral Sci.* **2010,** *52*, 541-552.
119. Drury, J. L.; Mooney, D. J., *Biomaterials* **2003,** *24*, 4337-4351.
120. Lee, K. Y.; Mooney, D. J., *Chem. Rev.* **2001,** *101*, 1869-1880.
121. Ding, X.; Zhao, H.; Li, Y.; Lee, A. L.; Li, Z.; Fu, M.; Li, C.; Yang, Y. Y.; Yuan, P., *Adv. Drug Deliv. Rev.* **2020,** *160*, 78-104.
122. Liu, X.; Wang, X.; Wang, X.; Ren, H.; He, J.; Qiao, L.; Cui, F.-Z., *Acta Biomater.* **2013,** *9*, 6798-6805.
123. Zhang, S.; Lockshin, C.; Herbert, A.; Winter, E.; Rich, A., *The EMBO journal* **1992,** *11*, 3787-3796.
124. Luo, Z.; Yue, Y.; Zhang, Y.; Yuan, X.; Gong, J.; Wang, L.; He, B.; Liu, Z.; Sun, Y.; Liu, J., *Biomaterials* **2013,** *34*, 4902-4913.
125. Liu, W.; Wong-Noonan, S.; Pham, N. B.; Pradhan, I.; Spigelmyer, A.; Funk, R.; Nedzesky, J.; Cohen, H.; Gawalt, E. S.; Fan, Y.; Meng, W. S., *Acta Biomater.* **2019,** *88*, 211-223.
126. Castillo Diaz, L. A.; Elsawy, M.; Saiani, A.; Gough, J. E.; Miller, A. F., *J. Tissue Eng.* **2016,** *7*, 2041731416649789.
127. Misawa, H.; Kobayashi, N.; Soto-Gutierrez, A.; Chen, Y.; Yoshida, A.; Rivas-Carrillo, J. D.; *Cell transplant.* **2006,** *15*, 903-910.
128. Hartgerink, J. D.; Beniash, E.; Stupp, S. I., *Science* **2001,** *294*, 1684-1688.
129. Rosen, H.; Abribat, T., *Nat. Rev. Drug Discov.* **2005,** *4*, 381-385.
130. Langer, R., *Nature* **1998,** *392*, 5-10.
131. Tran, S.; DeGiovanni, P.-J.; Piel, B.; Rai, P., *Clin. Transl. Med.* **2017,** *6*, 1-21.

132. Raizada, A.; Bandari, A.; Kumar, B., *Int. J. Pharm. Res. Dev* **2010,** *2* (8), 9-20.
133. Mondal, S.; Das, S.; Nandi, A. K., *Soft Matter* **2020,** *16*, 1404-1454.
134. Kuang, Y.; Shi, J.; Li, J.; Yuan, D.; Alberti, K. A.; Xu, Q.; Xu, B., *Angew. Chem. Int. Ed.* **2014,** *126*, 8242-8245.
135. Li, J.; Gao, Y.; Kuang, Y.; Shi, J.; Du, X.; Zhou, J.; Wang, H.; Yang, Z.; Xu, B., *J. Am. Chem. Soc* **2013,** *135*, 9907-9914.
136. Yang, C.; Chu, L.; Zhang, Y.; Shi, Y.; Liu, J.; Liu, Q.; Fan, S.; Yang, Z.; Ding, D.; Kong, D., *ACS Appl. Mater. Interfaces* **2015,** *7*, 2735-2744.
137. Xu, X. D.; Liang, L.; Chen, C. S.; Lu, B.; Wang, N. l.; Jiang, F. G.; Zhang, X. Z.; Zhuo, R. X., *ACS Appl. Mater. Interfaces* **2010,** *2*, 2663-2671.
138. Koutsopoulos, S.; Unsworth, L. D.; Nagai, Y.; Zhang, S., *Proc. Natl. Acad. Sci.* **2009,** *106*, 4623-4628.
139. Medina, S. H.; Li, S.; Howard, O. M. Z.; Dunlap, M.; Trivett, A.; Schneider, J. P.; Oppenheim, J. J., *Biomaterials* **2015,** *53*, 545-553.
140. Haines-Butterick, L.; Rajagopal, K.; Branco, M.; Salick, D.; Rughani, R.; Pilarz, M.; Lamm, M. S.; Pochan, D. J.; *Proc. Natl. Acad. Sci.* **2007,** *104* (19), 7791-7796.
141. Timmermans, S. B. P. E.; van Hest, J. C. M., *Curr. Opin. Colloid Interface Sci.* **2018,** *35*, 26-35.
142. Vriezema, D. M.; Comellas Aragonès, M.; Elemans, J. A. A. W.; Cornelissen, J. J. L. M.; Rowan, A. E.; Nolte, R. J. M., *Chem. Rev.* **2005,** *105*, 1445-1490.
143. Rodriguez-Llansola, F.; Escuder, B.; Miravet, J. F., *J. Am. Chem. Soc* **2009,** *131*, 11478-11484.
144. Gao, Y.; Zhao, F.; Wang, Q.; Zhang, Y.; Xu, B., *Chem. Soc. Rev.* **2010,** *39*, 3425-3433.
145. Hawkins, K.; Patterson, A. K.; Clarke, P. A.; Smith, D. K., *J. Am. Chem. Soc* **2020,** *142*, 4379-4389.
146. Wang, Q.; Yang, Z.; Zhang, X.; Xiao, X.; Chang, C. K.; Xu, B., *Angew. Chem. Int. Ed.* **2007,** *46*, 4285-4289.
147. Wang, Q.; Yang, Z.; Ma, M.; Chang, C. K.; Xu, B., *Chem. Eur. J.* **2008,** *14*, 5073-5078.
148. Chatterjee, A.; Afrose, S. P.; Ahmed, S.; Venugopal, A.; Das, D., *Chem. Commun.* **2020,** *56*, 7869-7872.
149. Chatterjee, A.; Mahato, C.; Das, D., *Angew. Chem. Int. Ed.* **2021,** *60*, 202-207.
150. Reja, A.; Afrose, S. P.; Das, D., *Angew. Chem. Int. Ed.* **2020,** *59*, 4329-4334.
151. Santoso, S.; Hwang, W.; Hartman, H., *Nano Let.* **2002,** *2*, 687-691.
152. Armstrong, C. T.; Boyle, A. L.; Bromley, E. H. C., Faraday Discuss. **2009,** *143*, 305-317.
153. Fairman, R.; Åkerfeldt, K. S., Peptides as novel smart materials. *Curr. Opin. Struct. Biol.* **2005,** *15*, 453-463.
154. Reches, M.; Gazit, E., *Science* **2003,** *300*, 625-627.
155. Nanda, J.; Biswas, A.; Adhikari, B.; Banerjee, A., *Angew. Chem. Int. Ed.* **2013,** *52*, 5041-5045.
156. Ahmed, S.; Mondal, J. H.; Behera, N.; Das, D., *Langmuir* **2013,** *29*, 14274-14283.
157. Conte, M. P.; Lau, K. H. A.; Ulijn, R. V., *ACS Appl. Mater. Interfaces* **2017,** *9*, 3266-3271.
158. Rueda, N.; Dos Santos, J. C. S.; Ortiz, C.; Torres, R.; Barbosa, O.; Rodrigues, R. C., *Chem. Rec.* **2016,** *16*, 1436-1455.
159. Yang, Y.; Zeng, J.; Gao, C.; Krull, U. J., *Biosens. Bioelectron.* **2003,** *18*, 311-317.
160. Zhu, X.; Ma, Y.; Zhao, C.; Lin, Z.; Zhang, L.; Chen, R.; Yang, W., *Langmuir* **2014,** *30*, 15229-15237.
161. Campbell, E. C.; Grant, J.; Wang, Y.; Sandhu, M.; Williams, R. J.; Nisbet, D. R.; Perriman, A. W.; Lupton, D. W.; Jackson, C. J., *Adv. Biosyst.* **2018,** *2*, 1700240.
162. Wang, J.; Miao, X.; Fengzhao, Q.; Ren, C.; Yang, Z.; Wang, L., *RSC Adv.* **2013,** *3*, 16739-16746.
163. Hickling, C.; Toogood, H. S.; Saiani, A.; Scrutton, N. S.; Miller, A. F., *Macromol. Rapid Commun.* **2014,** *35*, 868-874.
164. Ben-Zvi, O.; Grinberg, I.; Orr, A. A.; Noy, D.; Tamamis, P.; Yacoby, I.; Adler-Abramovich, L., *ACS Nano* **2021,** *15*, 6530-6539.
165. Okesola, B. O.; Smith, D. K., *Chem. Soc. Rev.* **2016,** *45*, 4226-4251.
166. Sinha, V.; Chakma, S., *J. Environ. Chem. Eng.* **2019,** *7*, 103295.
167. Basak, S.; Nandi, N.; Paul, S.; Hamley, I. W.; Banerjee, A., *Chem. Commun.* **2017,** *53*, 5910-5913.
168. Sunner, J.; Nishizawa, K.; Kebarle, P., *J. Phys. Chem.* **1981,** *85*, 1814-1820.
169. Meot-Ner, M.; Deakyne, C. A., *J. Am. Chem. Soc.* **1985,** *107*, 474-479.
170. Dougherty, D. A., Science **1996,** *271* (5246), 163-168.
171. Gebbie, M. A.; Wei, W.; Schrader, A. M.; Cristiani, T. R.; Dobbs, H. A.; Idso, M.; Chmelka, B. F., *Nat. Chem.* **2017**, *9*, 473-479.
172. Yamada, S.; Yamamoto, N.; Takamori, E., *J. Org. Chem.* 2016, *81*, 11819-11830.
173. Chen, W.; Elfeky, S. A.; Nonne, Y.; Male, L.; Ahmed, K.; Amiable, C.; Axe, P.; Yamada, S.; James, T. D.; Bull, S. D., *Chem. Commun.* **2011**, *47*, 253-255.
174. Luo, J.; Chen, K.; Yin, P.; Li, T.; Wan, G.; Zhang, J.; Ye, S.; Bi, X.; Pang, Y.; Wei, Y., *Angew. Chem. Int. Ed.* **2018**, *130*, 4131-4136.

175. Garel, L.; Lozach, B.; Dutasta, J. P.; Collet, A., *J. Am. Chem. Soc.* **1993**, *115*, 11652-11653.
176. Collet, E.; Lemée-Cailleau, M.-H.; Buron-Le Cointe, M.; Cailleau, H.; Wulff, M.; Luty, T.; Koshihara, S.-Y.; Meyer, M.; Toupet, L.; Rabiller, P., *Science* **2003**, 300, 612-615.
177. Tayi, A. S.; Shveyd, A. K.; Sue, A. C. H.; Szarko, J. M.; Rolczynski, B. S.; Cao, D.; Kennedy, T. J.; Sarjeant, A. A.; Stern, C. L.; Paxton, W. F.; Wu, W.; Dey, S. K.; Fahrenbach, A. C.; Guest, J. R.; Mohseni, H.; Chen, L. X.; Wang, K. L.; Stoddart, J. F.; Stupp, S. I., *Nature* **2012,** *488*, 485-489.
178. Pandeeswar, M.; Senanayak, S. P.; Narayan, K. S.; Govindaraju, T., Multi-stimuli-responsive charge-transfer hydrogel for room-temperature organic ferroelectric thin-film devices. *J. Am. Chem. Soc.* **2016**, *138*, 8259-8268.
179. Sagade, A. A.; Rao, K. V.; George, S. J.; Datta, A.; Kulkarni, G. U., A charge transfer single crystal field effect transistor operating at low voltages. *Chem. Commun.* **2013,** *49*, 5847-5849.
180. Vijay, D.; Sastry, G. N., The cooperativity of cation–π and π–π interactions. *Chem. Phys. Lett.* **2010,** *485* , 235-242.
181. Das, A.; Ghosh, S., *Angew. Chem. Int. Ed.* **2014,** *53*, 2038-2054.
182. Shaw, J. S.; Vaiyapuri, R.; Parker, M. P.; Murray, C. A.; Lim, K. J. C.; Pan, C.; Knappert, M.; Cardin, C. J.; Greenland, B. W.; Grau-Crespo, R., *Chem. Sci.* **2018,** *9*, 4052-4061.
183. Kumar, N. S. S.; Gujrati, M. D.; Wilson, J. N., *Chem. Commun.* **2010,** *46*, 5464-5466.
184. Yeh, M. Y.; Lin, H. C., *Phys. Chem. Chem. Phys.* **2014,** *16*, 24216-24222.
185. Gujrati, M. D.; Kumar, N. S. S.; Brown, A. S.; Captain, B.; Wilson, J. N., *Langmuir* **2011,** *27* , 6554-6558.
186. Jeena, M. T.; Palanikumar, L.; Go, E. M.; Kim, I.; Kang, M. G.; Lee, S.; Park, S.; Choi, H.; Kim, C.; Jin, S. M., *Nat. Commun.* **2017,** *8*, 1-10.
187. Madhu, C.; Roy, B.; Makam, P.; Govindaraju, T., *Chem. Commun.* **2018,** *54*, 2280-2283.
188. Molla, M. R.; Ghosh, S., *Chem. Eur. J.* **2012,** *18* (32), 9860-9869.
189. Kumpulainen, T.; Lang, B.; Rosspeintner, A.; *Chem. Rev.* **2017,** *117*, 10826-10939.
190. Du, X.; Zhou, J.; Shi, J.; Xu, B., *Chem. Rev.* **2015,** *115*, 13165-13307.
191. Dasgupta, A.; Mondal, J. H.; Das, D., *RSC Advs* **2013,** *3* (24), 9117-9149.
192. Singha, N.; Gupta, P.; Pramanik, B.; Ahmed, S.; Dasgupta, A.; Ukil, A.; Das, D., *Biomacromolecules* **2017,** *18*, 3630-3641.
193. Gao, L.; Gao, Y.; Lin, Y.; Ju, Y.; Yang, S.; Hu, J., *Chem. Asian J.* **2016,** *11*, 3430-3435.
194. Das, D.; Dasgupta, A.; Roy, S.; Mitra, R. N.; Debnath, S.; Das, P. K., *Chem. Eur. J.* **2006,** *12*, 5068-5074.
195. Pearse, M. J.; Mackinlay, A. G., Biochemical aspects of syneresis: a review. *J. Dairy Sci.* **1989,** *72*, 1401-1407.
196. Conte, M. P.; Singh, N.; Sasselli, I. R.; Escuder, B.; Ulijn, R. V., Metastable hydrogels from aromatic dipeptides. *Chem. Commun.* **2016,** *52* (96), 13889-13892.
197. Zhou, S. L.; Matsumoto, S.; Tian, H. D.; Yamane, H.; Ojida, A.; Kiyonaka, S.; Hamachi, I., *Chem. Eur. J.* **2005,** *11*, 1130-1136.
198. Castilla, A. M.; Wallace, M.; Mears, L. L. E.; Draper, E. R.; Doutch, J.; Rogers, S.; Adams, D. J., *Soft Matter* **2016,** *12*, 7848-7854.
199. Singha, N.; Das, B. K.; Pramanik, B.; Das, S.; Das, D., *Chem. Sci.* **2019,** *10*, 10035-10039.
200. Bushuyev, O. S.; Corkery, T. C.; Barrett, C. J.; Friščić, T., *Chem. Sci.* **2014,** *5*, 3158-3164.
201. Wang, Y.; de Kruijff, R. M.; Lovrak, M.; Guo, X.; Eelkema, R.; van Esch, J. H., *Angew. Chem. Int. Ed.* **2019,** *58*, 3800-3803.
202. Au-Yeung, H. Y.; Pantoş, G. D.; Sanders, J. K. M., *Angew. Chem. Int. Ed.* **2010,** *49*, 5331-5334.
203. Cougnon, F. B. L.; Ponnuswamy, N.; Jenkins, N. A.; Pantoş, G. D.; Sanders, J. K. M., *J. Am. Chem. Soc.* **2012,** *134*, 19129-19135.
204. Cougnon, F. B. L.; Jenkins, N. A.; Pantoş, G. D.; Sanders, J. K. M., *Angew. Chem. Int. Ed.* **2012,** *51*, 1443-1447.
205. Cougnon, F. B. L.; Sanders, J. K. M., *Acc. Chem. Res.* **2012,** *45*, 2211-2221.
206. Spruell, J. M.; Coskun, A.; Friedman, D. C.; Forgan, R. S.; Sarjeant, A. A.; Trabolsi, A.; Fahrenbach, A. C.; Barin, G.; Paxton, W. F.; Dey, S. K.; Olson, M. A.; Benítez, D.; Tkatchouk, E.; Colvin, M. T.; Carmielli, R.; Caldwell, S. T.; Rosair, G. M.; Hewage, S. G.; Duclairoir, F.; Seymour, J. L.; Slawin, A. M. Z.; Goddard Iii, W. A.; Wasielewski, M. R.; *Nat. Chem.* **2010,** *2*, 870.
207. Coskun, A.; Spruell, J. M.; Barin, G.; Fahrenbach, A. C.; Forgan, R. S.; Colvin, M. T.; Carmieli, R.; Benítez, D.; Tkatchouk, E.; Friedman, D. C.; Sarjeant, A. A.; Wasielewski, M. R.; Goddard, W. A.; *J. Am. Chem. Soc.* **2011,** *133*, 4538-4547.
208. Molla, M. R.; Ghosh, S., *Chem. Eur. J.* **2012,** *18*, 9860-9869.
209. Zaini, R.; Orcutt, A. C.; Arnold, B. R., *Photochem. Photobiol.* **1999,** *69*, 443-447.

210. Wang, J.-Y.; Yan, J.; Ding, L.; Ma, Y.; Pei, J., *Adv. Funct. Mater.* **2009,** *19*, 1746-1752.
211. Wang, C.; Yin, S.; Chen, S.; Xu, H.; Wang, Z.; Zhang, X., *Angew. Chem. Int. Ed.* **2008,** *47*, 9049-9052.
212. Corbett, P. T.; Sanders, J. K. M.; Otto, S., *J. Am. Chem. Soc.* **2005,** *127*, 9390-9392.
213. Au-Yeung, H. Y.; Pantoş, G. D.; Sanders, J. K. M., *Proc. Natl. Acad. Sci.* **2009,** *106*, 10466-10470.
214. Au-Yeung, H. Y.; Dan Pantoş, G.; Sanders, J. K. M., *J. Am. Chem. Soc.* **2009,** *131*, 16030-16032.
215. Mears, L. L. E.; Draper, E. R.; Castilla, A. M.; Su, H.; Zhuola; Dietrich, B.; Nolan, M. C.; Smith, G. N.; Doutch, J.; Rogers, S.; Akhtar, R.; Cui, H.; Adams, D. J., *Biomacromolecules* **2017,** *18*, 3531-3540.
216. Huang, P.; Wang, P.; Tang, S.; Fu, Z.; Lei, A., *Angew. Chem. Int. Ed.* **2018,** *57*, 8115-8119.
217. Hunter, R.; Caira, M.; Stellenboom, N., *J. Org. Chem.* **2006,** *71*, 8268-8271.
218. Dethe, D. H.; Srivastava, A.; Dherange, B. D.; Kumar, B. V., *Adv. Synth. Catal.* **2018,** *360*, 3020-3025.
219. Qiu, X.; Yang, X.; Zhang, Y.; Song, S.; Jiao, N., *Org. Chem. Front.* **2019,** *6*, 2220-2225.
220. Black, S. P.; Sanders, J. K. M.; Stefankiewicz, A. R., *Chem. Soc. Rev.* **2014,** *43*, 1861-1872.
221. Corbett, P. T.; Leclaire, J.; Vial, L.; West, K. R.; Wietor, J.-L.; Sanders, J. K. M.; Otto, S., *Chem. Rev.* **2006,** *106*, 3652-3711.
222. Dou, Y.; Huang, X.; Wang, H.; Yang, L.; Li, H.; Yuan, B.; Yang, G., *Green Chem.* **2017,** *19*, 2491-2495.
223. Xiao, X.; Xue, J.; Jiang, X., *Nat. Commun.* **2018,** *9*, 2191.
224. Schäfer, O.; Barz, M., *Chem. Eur. J.* **2018,** *24*, 12131-12142.
225. Pramanik, B.; Ahmed, S.; Singha, N.; Das, B. K.; Dowari, P.; Das, D., *Langmuir* **2019,** *35*, 478-488.
226. Dasgupta, A.; Das, D., *Langmuir* **2019,** *35* (33), 10704-10724.
227. Singha, N.; Srivastava, A.; Pramanik, B.; Ahmed, S.; Dowari, P.; Chowdhuri, S.; Das, B. K.; Debnath, A.; Das, D., *Chem. Sci.* **2019,** *10*, 5920-5928
228. Scheraga, H. A.; Wedemeyer, W. J.; Welker, E., In *Methods in Enzymology*, Nicholson, A. W., Ed. Academic Press: 2001; Vol. 341, pp 189-221.
229. Sato, T.; Hamada, Y.; Sumikawa, M.; Araki, S.; Yamamoto, H., *Ind. Eng. Chem. Res.* **2014,** *53*, 19331-19337.
230. Lee, Y.-W.; Luther, D. C.; Kretzmann, J. A.; Burden, A.; Jeon, T.; Zhai, S.; Rotello, V. M., *Theranostics* **2019,** *9*, 3280-3292.
231. Urquhart, L., *Nat. Rev. Drug Discov.* **2019**.
232. Vermonden, T.; Censi, R., *Chem. Rev.* **2012,** *112*, 2853-2888.
233. Liu, C.; Wan, T.; Wang, H.; Zhang, S.; Ping, Y.; Cheng, Y., *Sci. Advances* **2019,** *5*, eaaw8922.
234. Ren, L.; Lv, J.; Wang, H.; Cheng, Y., *Angew. Chem. Int. Ed.* **2020,** *59*, 4711-4719.
235. Ghosh, P.; Yang, X.; Arvizo, R.; Zhu, Z.-J.; Agasti, S. S.; Mo, Z., *J. Am. Chem. Soc.* **2010,** *132*, 2642-2645.
236. Cha, B. G.; Jeong, J. H.; Kim, J., *ACS Cent. Sci.* **2018,** *4*, 484-492.
237. Kuan, S. L.; Ng, D. Y. W.; Wu, Y.; Förtsch, C.; Barth, H.; *J. Am. Chem. Soc.* **2013,** *135*, 17254-17257.
238. Yan, M.; Du, J.; Gu, Z.; Liang, M.; Hu, Y.; Zhang, W.; Priceman, S.; Wu, L.; Zhou, Z. H.; Liu, Z.; Segura, T.; Tang, Y.; Lu, Y., *Nat. Nanotechnol.* **2010,** *5*, 48-53.
239. Chang, J.; Chen, X.; Glass, Z.; Gao, F.; Mao, L.; Wang, M.; Xu, Q., *Acc. Chem. Res.* **2019,** *52*, 665-675
240. Wang, M.; Alberti, K.; Sun, S.; Arellano, C. L.; Xu, Q., *Angew. Chem. Int. Ed. Engl.* **2014,** *53*, 2893-8.
241. Chen, T.-T.; Yi, J.-T.; Zhao, Y.-Y.; Chu, X., *J. Am. Chem. Soc.* **2018,** *140*, 9912-9920.
242. Wang, S.; Chen, Y.; Wang, S.; Li, P.; Mirkin, C. A.; Farha, O. K., *J. Am. Chem. Soc.* **2019,** *141*, 2215-2219.
243. Cheng, G.; Li, W.; Ha, L.; Han, X.; Hao, S.; Wan, Y.; Wang, Z.; Dong, F.; Zou, X.; Mao, Y.; Zheng, S. Y., *J. Am. Chem. Soc.* **2018,** *140*, 7282-7291.
244. Sloand, J. N.; Nguyen, T. T.; Zinck, S. A.; Cook, E. C.; Zimudzi, T. J.; Showalter, S. A.; Glick, A. B.; Simon, J. C.; Medina, S. H., *ACS Nano* **2020,** *14*, 4061-4073.
245. Kaczmarczyk, S. J.; Sitaraman, K.; Young, H. A.; Hughes, S. H.; Chatterjee, D. K., *Proc. Natl. Acad. Sci.* **2011,** *108*, 16998-17003.
246. Kim, E.; Zwi-Dantsis, L.; Reznikov, N.; Hansel, C. S.; Agarwal, S.; Stevens, M. M., *Adv. Mater.* **2017,** *29* , 1701086.
247. Wang, Q.; Yu, J.; Kadungure, T.; Beyene, J.; Zhang, H.; Lu, Q., *Nat. Commun.* **2018,** *9* , 1-7.
248. Wang, M.; Yu, S.; Wang, C.; Kong, J., *ACS Nano* **2010,** *4* (11), 6483-6490.
249. Kretzmann, J. A.; Luther, D. C.; Evans, C. W.; Jeon, T.; Jerome, W.; Gopalakrishnan, S.; Lee, Y. W.; Norret, M.; Iyer, K. S.; Rotello, V. M., *J. Am. Chem. Soc.* **2021,** *143*, 4758-4765.
250. Wen, J.; Anderson, S. M.; Du, J.; Yan, M.; Wang, J.; Shen, M.; Lu, Y.; Segura, T., *Adv. Mater.* **2011,** *23*, 4549-53.
251. Li, Y.; Wang, F.; Cui, H., *Bioeng. Trans. Med.* **2016,** *1*, 306-322.

Publications

1. Bapan Pramanik, Sahnawaz Ahmed, Rupam Roy, **Basab Kanti Das**, Nilotpal Sinha and Debapratim Das, A DNA-NDI hybride to effiently detect histone in parts per trillion (ppt) level. *ChemeistrySelect* 2017, 2, 8911-8916.

2. Bapan Pramanik, Sahnawaz Ahmed, Nilotpal Singha, **Basab Kanti Das**, Payel Dowari and Debapratim Das, Unorthodox combination of cation-π and charge- transfer interactions within a donor-acceptor pair. *Langmuir* **2019**, 35, 478-488.

3. Nilotpal Singha, Arpita Srivastava, Bapan Pramanik, Sahnawaz Ahmed, Payel Dowari, Sumit Chowdhury, **Basab Kanti Das**, Ananya Debnath and Debapratim Das, Unusual confinement property of a water insoluble small peptide hydrogel. *Chem. Sci.* **2019**, 10, 5920-5928.

4. **Basab Kanti Das,** Nilotpal Singha, Bapan Pramanik, Saurav Das and Debapratim Das* Freeze the dynamicity: Charge transfer complexation assisted control over reaction pathway. *Chem. Sci.* **2019**, 10, 10035-10039.

5. **Basab Kanti Das**, Bapan Pramanik, Sumit Chowdhuri, Oren A. Scherman and Debapratim Das* Light-triggered syneresis of a water insoluble peptide-hydrogel effectively removes small molecule waste contaminants**.** *Chem. Commun***. 2020**, 56, 3393-3396.

Conferences

1. FRONTIERS IN CHEMICAL SCIENCES 2018

2. National Conference on Surfactants, Emulsions and Biocolloids (NATCOSEB-XIX).

3. International Conference on Advanced Nanomaterials and Nanotechnology (ICANN2019). (Got ACS Best poster award)

4. WORKSHOP CUM SYMPOSIUM ON Bio-inspired Nanomaterials for Environmental Applications. (Sponsored by UKEIRI and DST).

Also participated in

5. FRONTIERS IN CHEMICAL SCIENCES 2016

6. Systems chemistry Symposium 2020.

7. Chemical Science for Drug Discovery & Therapy 2020, VNIT Nagpur.

8. Systems chemistry Symposium 2021.